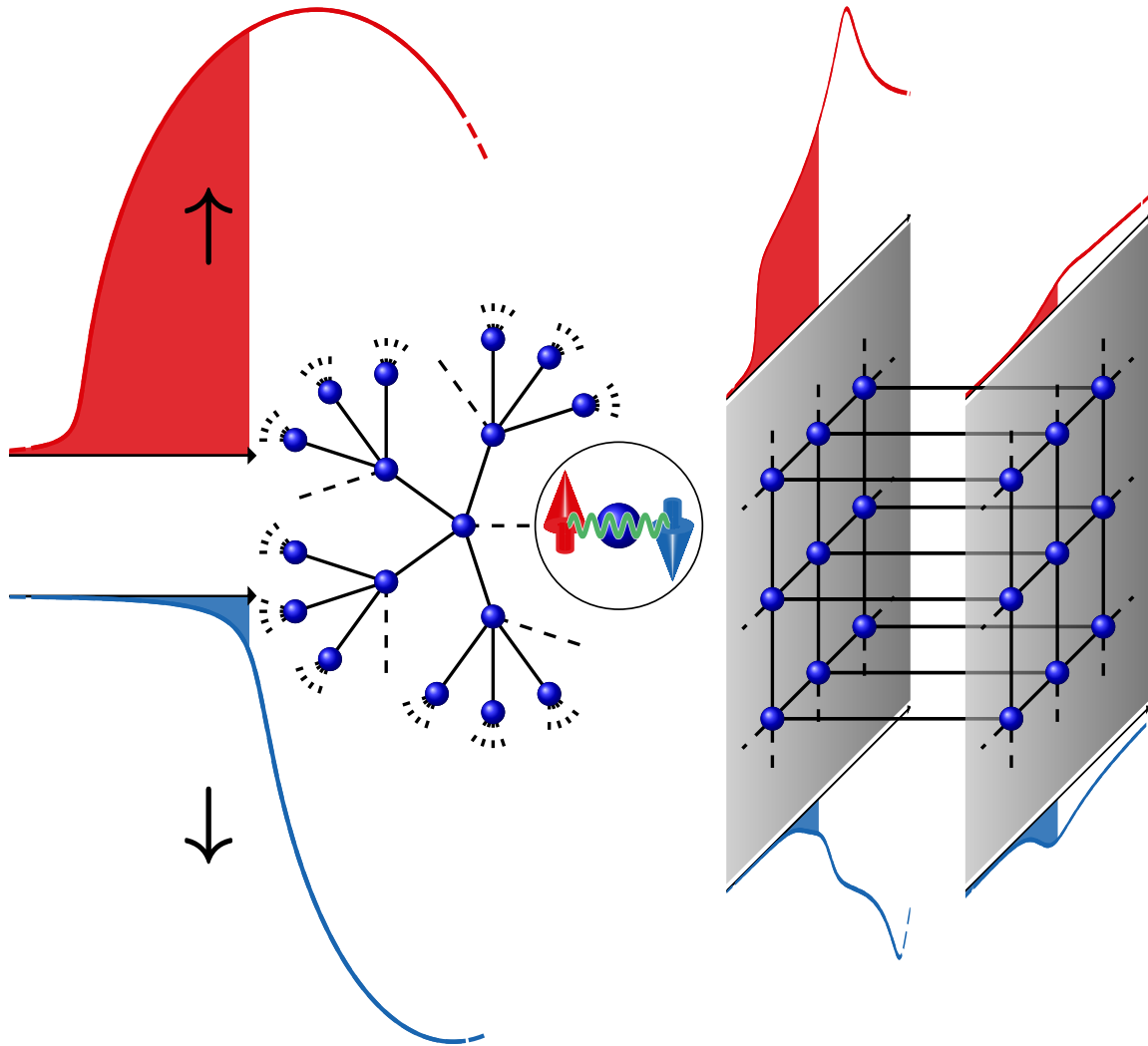


Electronic correlations in inhomogeneous model systems

Numerical simulation of spectra and transmission



Andreas Weh



Universität Augsburg
Institut für Physik

Electronic correlations in inhomogeneous model systems

Numerical simulation of spectra and transmission

Dissertation

zur Erlangung des akademischen Grades
Dr. rer. nat.

eingereicht an der
Mathematisch-Naturwissenschaftlich-Technischen Fakultät
der Universität Augsburg

von
Andreas Weh

Augsburg, April 2022

Erster Gutachter:

Prof. Dr. Ulrich Eckern

Zweiter Gutachter:

Prof. Dr. Liviu Chioncel

Dritter Gutachter:

Prof. Dr. Wolfgang von der Linden

Tag der mündlichen Prüfung:

29. Juni 2022

Preface

Parts of this thesis have already been published in the references [W1–W4], including most of the results and in part the corresponding theory. The content of these references might appear verbatim or adjusted for this thesis.¹ I indicate such content by adding the reference in the headings. The figure on the title page is adapted from the key image used for reference [W2].

Most results of this thesis are of numerical nature. They were generated applying existing impurity solvers. For finite temperatures, I used a (slightly adjusted) continuous-time quantum Monte Carlo code in hybridization expansion (CT-HYB) written by Junya Otsuki (unpublished), as well as the ‘`w2dynamics`’ code [C1]. The analytic continuation was mostly performed applying self-written Padé algorithms [C2], further the sparse modeling tool ‘`SpM`’ [C3] was employed. The analytic continuation was also compared to the ‘`ΩMaxent`’ maximum entropy code [C4] and a stochastic optimization code [C5]. For zero-temperature real-frequency results, I used the ‘`ForkTPS`’ code (unpublished) largely written by Daniel Bauernfeind, which is based on ‘`ITensor`’ [C6] and integrated in ‘`TRIQS`’ [C7]. I packaged most of the additional algorithms and post-processing algorithms, which I wrote in the course of this thesis, as the ‘`GfTool`’ code [C2].

¹Reprinted content of reference [W3] with permission from Weh et al., Phys. Rev. B **104**, 045127 (2021).
Copyright © 2021 by the American Physical Society.

Contents

Preface	v
Contents	ix
1. Introduction	1
1.1. Modeling correlated electrons	1
1.2. Numerical techniques	2
1.3. Application to half-metals	2
Outline	4
2. Lattice and impurity models	5
2.1. Hubbard model	5
2.1.1. Particle-hole symmetry	6
2.1.2. Limit of strong interaction: t - J model	7
2.1.3. Extensions of the single-band Hubbard model	8
2.2. Single impurity Anderson model	8
2.2.1. Limit of strong interaction: Kondo model	10
3. Local electronic interaction	11
3.1. Dynamical mean-field theory	11
3.1.1. Self-energy of the impurity model	16
3.1.2. Beyond the single-site approximation	17
4. Continuous-time quantum Monte Carlo	19
4.1. Hybridization expansion of the partition function	20
4.1.1. Segment picture of the local Hamiltonian	21
4.1.2. Monte Carlo sampling of segment configurations	23
4.1.3. Evaluation of determinants	25
4.1.4. Sampling of Green's function	27
4.1.5. Negative sign and error estimate	31
4.2. Analytic continuation	32
4.2.1. Padé approximants	36
4.2.2. Pole-based Padé approximants	37
4.2.3. Numerical example: Bethe Green's function	43
5. Tensor network methods	47
5.1. Tensor representation of quantum states	48
5.1.1. Low rank approximation of a tensor network	50
5.1.2. Iterative compression of tensor trains	52
5.2. Tensor representation of operators	53
5.3. Two-site density matrix renormalization group	57

5.4.	Subspace expansion for single-site methods	59
5.5.	Density matrix in tensor trains	60
5.6.	Time-dependent variational principle	62
5.6.1.	Dirac-Frenkel time-dependent variational principle	62
5.6.2.	Projection onto tangent space of tensor trains	63
5.6.3.	Single-site time-dependent variational principle	66
6.	Multicomponent alloys: substitutional disorder [W3]	71
6.1.	Tight-binding Hamiltonian [W3]	72
6.2.	Propagator expansion and the \mathcal{T} -matrix	74
6.3.	Diagonal disorder: coherent potential approximation	76
6.3.1.	Local effective medium	77
6.3.2.	Derivation of the coherent potential approximation	80
6.4.	Generalization to off-diagonal disorder[W3]	82
6.4.1.	Component space and extended space [W3]	82
6.4.2.	Effective medium theory	86
6.4.3.	Local approximation	87
6.4.4.	Self-consistency equation	88
6.4.5.	Efficient calculation: diagonal structure in k -points [W3]	89
6.4.6.	Self-consistency with renormalized indicator tensors [W3]	92
6.4.7.	Limit of independent components [W3]	94
7.	Electronic correlation in alloys	97
7.1.	The local CPA+DMFT approach for off-diagonal disorder [W3]	97
7.2.	Numerical results [W3]	98
7.2.1.	Non-interacting limit [W3]	99
7.2.2.	Alloy components with equal interaction strengths [W3]	101
7.2.3.	Alloy components with different interaction strengths [W3]	102
7.2.4.	Combined effect of diagonal and off-diagonal disorder [W3]	103
8.	Half-metals in layered systems [W2]	107
8.1.	Revisiting the bulk [W2]	107
8.2.	Half-metals in bilayers [W2]	111
8.3.	Summary [W2]	114
9.	Electronic transport through a correlated magnetic layer [W4]	119
9.1.	Generic transport model [W4]	119
9.1.1.	Diagonalizing the leads	122
9.1.2.	Meir–Wingreen formula for the transmission	124
9.2.	Results [W4]	127
9.2.1.	Non-interacting central layer [W4]	127
9.2.2.	Effect of lattice mismatch	131
9.2.3.	Local electronic interaction in the central region [W4]	134
9.3.	Summary [W4]	136
10.	Conclusion and outlook	137

A. Matsubara sum and Fourier transform	141
A.1. Matsubara and Fourier sum	143
A.1.1. Example: occupation of the single-pole Green's function	143
A.1.2. Truncation error estimate	145
A.1.3. Treatment of high-frequency behavior	146
A.1.4. Gibbs oscillation of Fourier sum	148
A.1.5. Truncation as approximate Fermi function	148
A.2. Fourier integral	152
B. Laplace transform	159
B.1. Test cases: analytic examples	159
B.2. Discretization	160
B.3. Truncation	162
B.4. Expansion to the real axis	163
B.4.1. Examples	164
B.5. Padé-Fourier approximation	167
B.5.1. Quadratic Hermite-Padé approximant	173
B.6. Linear prediction	175
B.6.1. Validity for Green's functions	175
B.6.2. Linear prediction coefficients	177
B.6.3. Pole-structure of Green's function from prediction roots	178
B.6.4. Linear prediction z -transform	179
B.7. Comparison	182
Acronyms	187
Own publications	189
Codes	191
Bibliography	193
Acknowledgments	209

1. Introduction

1.1. Modeling correlated electrons

If two objects or events cannot be described independently, we call them correlated. Mathematically, the expectation value of correlated quantities A and B does not factorize:

$$\langle AB \rangle \neq \langle A \rangle \langle B \rangle.$$

Physically, correlations are caused by interactions between objects. We experience correlation effects in our everyday life. Driving on a crowded street, the cars cannot be described independently. As the cars get closer, they (or rather their drivers) start to interact, and traffic jams can emerge. While an independent car could drive as fast as the speed limit allows, many interacting cars might come to a complete standstill.

In condensed matter physics, correlated electron systems show many fascinating features. A prime example is the metal-to-Mott-insulator transition [1–3], which cannot be described by the single-particle picture employed in band theory. Other exciting phenomena include heavy fermions, colossal magnetoresistance, and Fermi liquid instabilities. Correlated electron systems exhibiting such properties are also very interesting for applications in electronic devices, as these properties are tunable. The phase diagrams are typically complex, showing many different phases.

While many-body systems of correlated electrons are exciting and show promising physical properties, they are difficult to treat theoretically. While density functional theory [4–7] is extremely successful for weakly correlated systems, it fails for strongly correlated systems like Mott insulators, which are incorrectly predicted to be metallic. But even abandoning first-principles methods for realistic materials, treating seemingly simple models instead, the many-body problem remains hard. Analytical solutions are typically only available for one-dimensional systems (and sometimes in the opposite limit of infinite dimensions). Likewise, numerical solutions are often very limited due to the exponential growth of the Hilbert space with the system size. The complexity of the many-body problem of correlated electrons necessitates the study of simplified models. With the progress of non-perturbative treatment and numerical methods, models are nowadays routinely used to supplement first-principles calculations based on density functional theory with correlations. This is termed density functional theory + dynamical mean-field theory, or, if the local density approximation is used as exchange-correlation functional, LDA+DMFT. Such first-principles calculations can predict material properties, which can save time compared to synthesizing materials.

Additionally, modeling can provide further insight into correlation effects. While real materials exhibit an intricate interplay of many different constituents and their interactions, models allow reducing the problem of identifying the essential physics. This is crucial to our understanding of the physical origin. Besides the academic interest, this, in turn, helps to improve methods to describe real materials and is significant to designing new materials with favorable properties, like room temperature superconductors.

1.2. Numerical techniques

As mentioned above, solving the many-body problem is a formidable task. Already the quantum three-body problem cannot be solved analytically; thus, solving the problem of many interacting electrons in solids seems like a futile endeavor. Therefore, we turn to powerful computers and employ numerical techniques.

We focus on solving the Hubbard model. In principle, the task is clear: We write the Hubbard Hamiltonian in a many-particle basis and diagonalize the matrix; this is termed exact diagonalization [8]. Due to the exponential growth of the Hilbert space and, therefore, the matrix dimensions with system size, this approach is limited to extremely small systems. Using iterative diagonalization procedures like Lanczos [9] allows treating larger matrices; due to the exponential scaling, the treatable system size remains however small. Instead of directly solving the lattice problem, the dynamical mean-field theory can be employed. This amounts to solving a simpler, effective impurity problem that is determined self-consistently.

The impurity problem can be directly solved using quantum Monte Carlo (QMC) algorithms, which are based on sampling contributions to the partition function formulated in the action formalism [10, 11]. The early Hirsch–Fye [12] algorithm is based on a discretization in imaginary time. Nowadays, more accurate continuous-time quantum Monte Carlo algorithms without a time discretization are employed [13]. While Monte Carlo algorithms avoid the exponential scaling with system size and can treat infinitely large baths, they are plagued by the so-called fermionic sign problem and restricted to imaginary times. Real-time versions exist also [14, 15], but they face a dynamical sign problem [16].

Alternatively, Hamiltonian-based methods can be applied by discretizing the bath of the effective impurity model. For small numbers of bath sites, the impurity problem can be solved by employing exact diagonalization [8, 9]. The numerical renormalization group [17, 18] is tailored to impurity models and does not suffer from restricted numbers of bath sites. It employs a logarithmic discretization, providing accurate results around the Fermi level. However, the resolution at higher energies is poor. Tensor network methods [19, 20] based on the density matrix renormalization group by White [21, 22] can treat large numbers of bath sites. The discretization is arbitrary, allowing for good resolution also at higher energies. Typically, these methods are limited to zero temperature.

1.3. Application to half-metals

The term half-metal refers to materials that exhibit a metallic spin channel while the other spin channel is insulating. In a one-particle band picture, this corresponds to a finite value of the spectral function at the Fermi level for the metallic spin channel, while the other spin channel shows a band gap. In half-metallic electrodes, a fully spin-polarized current can be produced, and fascinating effects arise, such as giant magnetoresistance in tunnel magnetoresistance devices [23]. Thus, half-metals have a high potential for spintronic applications [23, 24].

First-principles calculations using density-functional theory [4–7] identified a number of bulk half-metals, including Heusler alloys [25] (e.g., NiMnSb, FeMnSb, Mn₂VAl), double perovskites, transition-metal oxides (e.g., CrO₂), chalcogenides, and pnictides

(e.g., CrAs, VAs). Some of these materials could be experimentally realized. Spin fluctuations are crucial to metallic ferromagnets [26]. In half-metallic ferromagnets, incoherent nonquasiparticle states were found in the vicinity of the Fermi level [23, 27, 28]. Their tails depolarize the spectral function as they cross the Fermi level. For applications, not only the bulk but in particular interfaces are of interest, as giant magnetoresistance in the current perpendicular to the planes can be produced for interfaces of ferromagnetic and nonmagnetic metals [29–31].

Outline

Chapter 2 introduces the Hubbard model and the single-impurity Anderson model to describe interacting electrons; the Hamiltonians and their parameters are presented.

Chapter 3 discusses the dynamical mean-field theory algorithm, which is used to treat local electronic interactions. The derivation based on the cavity construction is given. Chapters 4 and 5 describe two complementary numerical methods to solve the single-impurity Anderson model necessary for the dynamical mean-field theory. Chapter 4 outlines the action based continuous-time quantum Monte Carlo algorithm, presenting the hybridization expansion. Quantum Monte Carlo uses an imaginary time representation, thus an analytic continuation is necessary to obtain the spectra. This chapter focuses on the Padé algorithm; a variant of the algorithm is given, which calculates the position of the poles instead of the polynomial coefficients. Chapter 5 gives a schematic introduction into tensor networks algorithms, emphasizing the diagrammatic representation. The density matrix renormalization group algorithm to obtain the ground state, as well as the time-dependent variational principle to perform the time evolution are presented.

Chapter 6 introduces the formalism for substitutional disorder in non-interacting model systems. First, the local coherent potential approximation is derived, which treats diagonal disorder, that is disorder in the on-site energies. Next, the approximation is extended to the Blackman–Esterling–Berk formulation, which provides the generalization to off-diagonal disorder, that is disorder affecting the hopping amplitudes. Chapter 7 combines the dynamical mean-field theory algorithm introduced in chapter 3 with the Blackman–Esterling–Berk formulation introduced in chapter 6 to treat electronic correlation and disorder on the same level within a single-site approximation. Numerical examples for paramagnetic systems are provided.

Chapter 8 discusses model half-metallic ferromagnets considering a Bethe lattice as well as layered square-lattice structures. Chapter 9 models the transport through a barrier made of a single interacting half-metallic ferromagnet layer. The transmission is calculated using the Meir–Wingreen formalism, and its spin-polarization is analyzed.

Appendices A and B describe the numerical treatment of the transformation between time and frequency, necessary for the dynamical mean-field theory algorithm. Appendix A discusses the Fourier transform on the imaginary axis for finite temperatures, while appendix B explains the Laplace transform from real times to real frequencies.

2. Lattice and impurity models

2.1. Hubbard model

The Hubbard model [32], also introduced by Gutzwiller [33] and Kanamori [34], was proposed to describe transition-metal monoxides with partially filled d -bands, which are anti-ferromagnetic insulators. It is also appropriate for f -electrons in rare earth metals, with even narrower bands. The Hubbard model describes the competition between itinerant band and localized atomic character of electrons. Despite its formal simplicity, it shows a rich phase diagram. The Jülich book series on correlated electrons provides an excellent overview of the Hubbard model [35–37].

The Hubbard model is described by a lattice Hamiltonian, which considers the part of the Coulomb interaction local in Wannier space. While the bare Coulomb interaction is long ranged, the screened effective interaction is short ranged and the local term dominates [32]. Considering only the local interaction can be interpreted as ‘perfect screening’ or be considered simply as an approximation taking only the most dominant terms into account. In Wannier space, the Hamiltonian reads

$$\hat{H} = \sum_{i\sigma} (\epsilon_{i\sigma} - \mu) \hat{n}_{i\sigma} - \sum_{ij\sigma} t_{ij} \hat{c}_{i\sigma}^\dagger \hat{c}_{j\sigma} + \sum_i U_i \hat{n}_{i\uparrow} \hat{n}_{i\downarrow}, \quad (2.1)$$

where $\epsilon_{i\sigma}$ is the on-site energy, μ the chemical potential, t_{ij} the hopping amplitude, and U_i the local Hubbard interaction. The fermionic creation and annihilating operators at site i for spin σ are $\hat{c}_{i\sigma}^\dagger$ and $\hat{c}_{i\sigma}$ respectively; the number operator is denoted $\hat{n}_{i\sigma} = \hat{c}_{i\sigma}^\dagger \hat{c}_{i\sigma}$. The hopping amplitudes are purely off-diagonal $t_{ii} = 0$, and Hermitian $t_{ij} = t_{ji}^*$. Often, the hopping of electrons is restricted to nearest neighbors only, as the hopping amplitudes decay rapidly. For the spatially homogeneous system, the parameters $\epsilon_{i\sigma}$ and U_i are independent of the site i and t_{ij} depends only on the distance $t_{ij} = t(|\mathbf{r}_i - \mathbf{r}_j|)$. In this case, the non-interacting part can be diagonalized by a lattice Fourier transform. The hopping term yields the dispersion $\epsilon_{\mathbf{k}}$:

$$\sum_{\mathbf{k}} \epsilon_{\mathbf{k}} \hat{n}_{\mathbf{k}\sigma} = \sum_{ij} t_{ij} \hat{c}_{i\sigma}^\dagger \hat{c}_{j\sigma}; \quad (2.2)$$

in the following we omit the boldface notation for the vector \mathbf{k} . In k -space, the Hubbard Hamiltonian for a homogeneous system reads

$$\hat{H} = \sum_{k\sigma} (\epsilon_{\mathbf{k}} + \epsilon_{\sigma} - \mu) \hat{n}_{k\sigma} + U \frac{1}{N} \sum_{kk'q} \hat{c}_{k+q\uparrow}^\dagger \hat{c}_{k\uparrow} \hat{c}_{k'-q\downarrow}^\dagger \hat{c}_{k'\downarrow}, \quad (2.3)$$

the interaction is a spin- and k -conserving scattering term.

In the non-interacting limit $U_i = 0$, the Hamiltonian is diagonal in the basis of k -states $[\hat{H}, \hat{n}_{k\sigma}] = 0$. In the localized atomic limit $t_{ij} = 0$, on the other hand, the sites are independent, and the Hamiltonian is diagonal in the particle number basis $[\hat{H}, \hat{n}_{i\sigma}] = 0$.

The kinetic term and the interaction term do not commute, reflecting the competition between the itinerant band and the localized atomic character of the electrons. An exact solution has only been obtained for the one-dimensional case by Lieb and Wu [38], and Essler et al. [39]. In the opposite limit of infinite coordination, significant simplifications arise. These simplifications yield the dynamical mean-field theory (DMFT) discussed in chapter 3.

The Hubbard model succeeds in explaining the Mott transition at half-filling [40]. Band theory incorrectly predicts a conducting metal, but for strong interaction the system is (Mott) insulating. Furthermore, the Hubbard model can also explain ferromagnetism of itinerant electrons [41].

The prototypical realization of the Hubbard model is SrVO₃, with its 3d¹ configuration of one vanadium per unit cell [42–44]. The Hubbard model has gained further experimental relevance, as it can be realized in form of optical lattices [45, 46].

2.1.1. Particle-hole symmetry

We consider the effect of interchanging particles and holes in the Hubbard Hamiltonian, compare [36]. We define a particle-hole transformation T'_{ph} as interchanging all creation and annihilating operators

$$T'_{\text{ph}} \hat{c}_{i\sigma}^\dagger = \hat{c}_{i\sigma}. \quad (2.4)$$

Thus, the particle-hole transformation changes the number operator to $T'_{\text{ph}} \hat{n}_{i\sigma} = 1 - \hat{n}_{i\sigma}$; this corresponds to replacing occupied sites by empty ones, and empty sites by filled ones. Applying this particle-hole transformation to the Hamiltonian yields

$$T'_{\text{ph}} \hat{H} = - \sum_{i\sigma} (\epsilon_{i\sigma} + U_i - \mu) \hat{n}_{i\sigma} + \sum_{ij\sigma} t_{ij} \hat{c}_{i\sigma}^\dagger \hat{c}_{j\sigma} + \sum_i U_i \hat{n}_{i\uparrow} \hat{n}_{i\downarrow} + \sum_{i\sigma} (\epsilon_{i\sigma} + \frac{U_i}{2} - \mu). \quad (2.5)$$

The last summand can be neglected, as constant terms have no physical relevance. The particle-hole transformed Hubbard Hamiltonian has the same structure as the original Hamiltonian eq. (2.1), only the sign of the hopping amplitudes, t_{ij} , and the on-site energies, $\epsilon_{i\sigma}$, changes, and the on-site energies are shifted by the interaction U_i . This means, the particle-hole transformation amounts to replacing the parameters

$$(\epsilon_{i\sigma} - \mu) \rightarrow -(\epsilon_{i\sigma} + U_i - \mu) \quad t_{ij} \rightarrow -t_{ij} \quad U_i \rightarrow U_i, \quad (2.6)$$

or equivalently, writing the Hamiltonian in a parametrized form

$$T'_{\text{ph}} \hat{H}(\epsilon_{i\sigma} - \mu, t_{ij}, U_i) = \hat{H}(-\epsilon_{i\sigma} - U_i + \mu, -t_{ij}, U_i) + \sum_{i\sigma} (\epsilon_{i\sigma} + \frac{U_i}{2} - \mu). \quad (2.7)$$

We focus on the specific case of a bipartite lattice with nearest-neighbor hopping only. In this case, the hopping term always connects sites from the two different sublattices \mathcal{A} and \mathcal{B} . To compensate the minus sign appearing for the hopping amplitudes, we define a slightly different particle-hole transformation. We use a staggering function, adding a sign for one sublattice, say \mathcal{A} :

$$T_{\text{ph}} \hat{c}_{i\sigma}^\dagger = (-1)^{1_{\mathcal{A}}(i)} \hat{c}_{i\sigma}, \quad (2.8)$$

where $1_{\mathcal{A}}(i)$ is the indicator function $1_{\mathcal{A}}(i) = 1$ if $i \in \mathcal{A}$ and $1_{\mathcal{A}}(i) = 0$ else. Local quantities are not affected by this sign-change, but the hopping terms pick up an additional minus sign. Thus, the Hamiltonian transforms as follows:

$$T_{\text{ph}}\hat{H}(\epsilon_{i\sigma} - \mu, t_{ij}, U_i) = \hat{H}(-\epsilon_{i\sigma} - U_i + \mu, t_{ij}, U_i) + \sum_{i\sigma} (\epsilon_{i\sigma} + \frac{U_i}{2} - \mu); \quad (2.9)$$

only the on-site energy is modified. We identify the choice of parameters $\epsilon_{i\sigma} + U_i/2 - \mu = 0$ as particle-hole symmetry:

$$T_{\text{ph}}\hat{H}(-U_i/2, t_{ij}, U_i) = \hat{H}(-U_i/2, t_{ij}, U_i); \quad (2.10)$$

such a Hamiltonian is invariant under the particle-hole transformation. This implies that the system is half-filled $n_{i\sigma} = 1/2$. Often, such a Hubbard Hamiltonian is written in the form

$$\begin{aligned} \hat{H} &= \sum_{i\sigma} (\epsilon_{i\sigma} - \mu) \hat{n}_{i\sigma} - \sum_{\langle i,j \rangle \sigma} t_{ij} \hat{c}_{i\sigma}^\dagger \hat{c}_{j\sigma} + \sum_i U_i (\hat{n}_{i\uparrow} - \frac{1}{2})(\hat{n}_{i\downarrow} - \frac{1}{2}) \\ &= \sum_{i\sigma} (\epsilon_{i\sigma} - \mu - U_i/2) \hat{n}_{i\sigma} - \sum_{\langle i,j \rangle \sigma} t_{ij} \hat{c}_{i\sigma}^\dagger \hat{c}_{j\sigma} + \sum_i U_i \hat{n}_{i\uparrow} \hat{n}_{i\downarrow} + \frac{1}{4} \sum_i U_i \end{aligned} \quad (2.11)$$

as in this case the particle-hole symmetry is fulfilled for the condition $\epsilon_{i\sigma} - \mu = 0$, that is for a vanishing on-site term, independent of the interaction strength U_i . The bracket $\langle i, j \rangle$ denotes that the sum is only over nearest-neighbors sites.

This discussion applies only to bipartite lattices with nearest-neighbor hopping only, which have a symmetric density of states (DOS). In such a case the sign change $t_{ij} \rightarrow -t_{ij}$ mentioned for the particle-hole transform T'_{ph} does not affect densities. The occupation is the expectation value

$$\langle \hat{n}_{i\sigma} \rangle = \frac{1}{\mathcal{Z}} \text{Tr} \hat{n}_{i\sigma} e^{-\beta \hat{H}}. \quad (2.12)$$

Only terms with an equal number of creation and annihilating operators at every site contribute to the trace. Thus, if we expand the exponential in eq. (2.12), we only have to consider closed loops of hopping terms, as the hopping t_{ij} is the only non-local term. For an even number of hopping terms, evidently the change of sign has no effect. For the bipartite lattice with nearest-neighbor hopping only, all loops have even numbers of hopping terms. Including next-nearest-neighbor hopping, or consider different lattice structures like the triangular lattice, this is not the case anymore.

2.1.2. Limit of strong interaction: t - J model

In the limit of strong interaction, the double occupation $\langle n_{i\uparrow} n_{i\downarrow} \rangle$ is suppressed. The Schrieffer–Wolff transformation provides a systematic way to eliminate terms in orders of t/U and project the Hamiltonian onto a low-energy subspace without double occupations [47–49]. We consider the case of less than or equal half filling, nearest-neighbor

hopping, and, to simplify formulas, vanishing on-site energy $\epsilon_i = 0$. The unitary transformation yields up to order $\mathcal{O}(t/U^2)$ the effective Hamiltonian [49]

$$\begin{aligned} \hat{H}_{\text{eff}} = & -t \sum_{\langle ij \rangle \sigma} (1 - \hat{n}_{i\bar{\sigma}}) \hat{c}_{i\sigma}^\dagger \hat{c}_{j\sigma} (1 - \hat{n}_{j\bar{\sigma}}) + \left(\frac{2t^2}{U} \right) \sum_{\langle ij \rangle} [\hat{\mathbf{S}}_i \cdot \hat{\mathbf{S}}_j - \frac{1}{4} (1 - \hat{n}_{i\downarrow}) \hat{n}_{i\uparrow} \hat{n}_{j\downarrow} (1 - \hat{n}_{j\uparrow})] \\ & + \frac{t^2}{U} \sum_{\langle i,j,l \rangle \sigma} (1 - \hat{n}_{i-\sigma}) \hat{c}_{i\sigma}^\dagger (1 - \hat{n}_{j\sigma}) \hat{c}_{j-\sigma}^\dagger \hat{c}_{j\sigma} (1 - \hat{n}_{j-\sigma}) \hat{c}_{l-\sigma} (1 - \hat{n}_{l\sigma}) \\ & + \frac{t^2}{U} \sum_{\langle i,j,l \rangle \sigma} (1 - \hat{n}_{i-\sigma}) \hat{c}_{i\sigma}^\dagger (1 - \hat{n}_{j\sigma}) \hat{n}_{j-\sigma} \hat{c}_{l\sigma} (1 - \hat{n}_{l-\sigma}), \end{aligned} \quad (2.13)$$

where $\hat{\mathbf{S}}_i$ is the vector of spin operators $\hat{\mathbf{S}}_i = \sum_{\nu\mu} \hat{c}_{i\nu}^\dagger \boldsymbol{\sigma}_{\nu\mu} \hat{c}_{i\mu}$, with the vector of Pauli matrices $\boldsymbol{\sigma}$. The coefficient of the second term is denoted $J := 2t^2/U$. The second line corresponds to a pair hopping, the third to a hopping over a site occupied by an electron of opposite spin-flip.

Exactly at half filling, hopping is not possible anymore, as there are no empty sites in the subspace without double occupations; all sites are singly occupied $\langle \hat{n}_i \rangle = 1$. Thus, the t - J model reduces to the anti-ferromagnetic Heisenberg model

$$\hat{H}_{\text{eff}} = J \sum_{\langle i,j \rangle} \left[\hat{\mathbf{S}}_i \cdot \hat{\mathbf{S}}_j - \frac{1}{4} \right]. \quad (2.14)$$

This effective model describes to the Mott insulating state.

2.1.3. Extensions of the single-band Hubbard model

For the description of most realistic materials, multiple orbitals are essential. Thus, it is necessary to extend the Hubbard Hamiltonian accordingly from a single band to multiple orbitals.

A different extension of the Hubbard model is to allow for random on-site energies or hopping amplitudes; this is referred to as Anderson-Hubbard model [50, 51]. Also, short-ranged interaction can be added, this is called the extended Hubbard model [52–54].

2.2. Single impurity Anderson model

The single-impurity Anderson model (SIAM) was proposed by Anderson [55] to describe the occurrence of localized magnetic moments for iron-group ions in a nonmagnetic host metal. The model assumes a single local impurity, embedded into a bath of conduction electrons. The Hamiltonian reads

$$\hat{H} = \sum_{\sigma} \epsilon_{\sigma} \hat{d}_{\sigma}^{\dagger} \hat{d}_{\sigma} + U \hat{d}_{\uparrow}^{\dagger} \hat{d}_{\uparrow} \hat{d}_{\downarrow}^{\dagger} \hat{d}_{\downarrow} + \sum_{k\sigma} \epsilon_{k\sigma} \hat{c}_{k\sigma}^{\dagger} \hat{c}_{k\sigma} + \sum_{k\sigma} [V_{k\sigma} \hat{c}_{k\sigma}^{\dagger} \hat{d}_{\sigma} + V_{k\sigma}^* \hat{d}_{\sigma}^{\dagger} \hat{c}_{k\sigma}], \quad (2.15)$$

where $\hat{d}_{\sigma}^{\dagger}$ and \hat{d}_{σ} are the creation and annihilation operators for the impurity site, which was assumed to be a d -orbital; $\hat{c}_{k\sigma}^{\dagger}$ and $\hat{c}_{k\sigma}$ are the creation and annihilation operators for

the free conduction electrons of the host metal, the bath, which were assumed to be s -orbitals. The on-site energy of the impurity is ϵ_σ , the (Hubbard) U is the local interaction for the impurity site, $\epsilon_{k\sigma}$ is the dispersion of the bath, and $V_{k\sigma}$ is the hybridization strength between bath and impurity.

The bath in the SIAM is non-interacting, thus the bath degrees of freedom can be integrated out yielding an effective model for the impurity. This can conveniently be done using the action formalism [10, 11]. We split the action of the SIAM into the local, the bath, and the hybridization action

$$S_{\text{imp}} = S_{\text{loc}} + S_{\text{bath}} + S_{\text{hyb}}, \quad (2.16)$$

$$S_{\text{loc}} = \int_0^\beta d\tau \sum_\sigma \left[d_\sigma^+(\tau) (\partial_\tau + \epsilon_\sigma) d_\sigma(\tau) + U d_\uparrow^+(\tau) d_\uparrow(\tau) d_\downarrow^+(\tau) d_\downarrow(\tau) \right], \quad (2.17)$$

$$S_{\text{bath}} = \int_0^\beta d\tau \sum_{k\sigma} c_{k\sigma}^+(\tau) (\partial_\tau + \epsilon_{k\sigma}) c_{k\sigma}(\tau), \quad (2.18)$$

$$S_{\text{hyb}} = \int_0^\beta d\tau \sum_{k\sigma} \left[c_{k\sigma}^+(\tau) V_{k\sigma} d_\sigma(\tau) + d_\sigma^+(\tau) V_{k\sigma}^* c_{k\sigma}(\tau) \right], \quad (2.19)$$

where $d_\sigma^+(\tau)$ and $d_\sigma(\tau)$ are the Grassmann fields of the impurity site, and $c_{k\sigma}^+(\tau)$ and $c_{k\sigma}(\tau)$ are the Grassmann fields of the bath sites. The partition function reads

$$\mathcal{Z}_{\text{imp}} = \int \prod_\sigma \mathcal{D}[d_\sigma^+, d_\sigma] e^{-S_{\text{loc}}} \int \prod_{k\sigma} \mathcal{D}[c_{k\sigma}^+, c_{k\sigma}] e^{-S_{\text{bath}} - S_{\text{hyb}}} \quad (2.20)$$

The action is quadratic in the non-interacting bath degrees. The Fourier transform from imaginary-time to Matsubara frequencies replaces the differentiation $\partial_\tau \rightarrow -i\omega_n$, introducing the frequency dependent Grassmann fields $c_{k\sigma n}^+$, where n indicates the fermionic Matsubara frequency. The Gaussian Grassmann integral [11] for the bath degrees yields

$$\begin{aligned} \int \prod_{k\sigma n} \mathcal{D}[c_{k\sigma n}^+, c_{k\sigma n}] \exp \left(\sum_{k\sigma n} c_{k\sigma n}^+ [i\omega_n - \epsilon_{k\sigma}] c_{k\sigma n} - \sum_{k\sigma n} [c_{k\sigma n}^+ V_{k\sigma} d_{\sigma n} + d_{\sigma n}^+ V_{k\sigma}^* c_{k\sigma n}] \right) \\ = \mathcal{Z}_{\text{bath}} \exp \left(\sum_{k\sigma n} d_{\sigma n}^+ V_{k\sigma}^* [i\omega_n - \epsilon_{k\sigma}]^{-1} V_{k\sigma} d_{\sigma n} \right). \end{aligned} \quad (2.21)$$

The bath partition function $\mathcal{Z}_{\text{bath}}$ is of no physical relevance as it only affects the absolute magnitude of the partition function but not physical observables. It only acts as normalization factor. Formally, it can be expressed as the determinant of the diagonal matrix \mathbf{h} :

$$\mathcal{Z}_{\text{bath}} = \prod_{k\sigma n} [i\omega_n + \epsilon_{k\sigma}] = \det \mathbf{h}, \quad \text{with} \quad (\mathbf{h})_{k\sigma n; k'\sigma'n'} = \delta_{k\sigma n; k'\sigma'n'} (i\omega_n + \epsilon_{k\sigma}) \quad (2.22)$$

The Grassmann integral eq. (2.21) defines the hybridization function $\Delta_\sigma(i\omega_n)$, which encapsulates the effect of the bath sites on the impurity

$$\Delta_\sigma(i\omega_n) = \sum_k \frac{|V_{k\sigma}|^2}{i\omega_n - \epsilon_{k\sigma}}, \quad (2.23)$$

$$\Delta_\sigma(\tau) = \sum_k |V_{k\sigma}|^2 \times \begin{cases} f(\epsilon_{k\sigma}) e^{-\epsilon_{k\sigma}\tau} & \text{if } \tau \in (-\beta, 0), \\ -[1 - f(\epsilon_{k\sigma})] e^{-\epsilon_{k\sigma}\tau} & \text{if } \tau \in (0, \beta). \end{cases} \quad (2.24)$$

The hybridization function can also be expressed as sum over the Green's functions $g_{k\sigma}(i\omega_n)$ for an isolated bath site (locators)

$$\Delta_\sigma(i\omega_n) = \sum_k |V_{k\sigma}|^2 g_{k\sigma}(i\omega_n) \quad \text{with} \quad g_{k\sigma}(i\omega_n) = \frac{1}{i\omega_n - \varepsilon_{k\sigma}}. \quad (2.25)$$

Its high-frequency asymptote is $\Delta_\sigma(i\omega_n) \sim \frac{1}{i\omega_n} \sum_k |V_{k\sigma}|^2$. The impurity sites can therefore be described by the effective action

$$S_{\text{eff}}[\mathbf{d}^+, \mathbf{d}] = \int_0^\beta d\tau \left[\sum_\sigma d_\sigma^+(\tau) (\partial_\tau + \epsilon_\sigma) d_\sigma(\tau) + U d_\uparrow^+(\tau) d_\uparrow(\tau) d_\downarrow^+(\tau) d_\downarrow(\tau) \right] \\ + \int_0^\beta d\tau \int_0^\beta d\tau' \sum_\sigma d_\sigma^+(\tau) \Delta_\sigma(\tau - \tau') d_\sigma(\tau'), \quad (2.26)$$

where the vectorial notation \mathbf{d}^+ and \mathbf{d} denotes the dependence of the action on the set of Grassman fields $\mathbf{d}^+ = \{d_\sigma^+(\tau)\}$ and $\mathbf{d} = \{d_\sigma(\tau)\}$ respectively. We identify the quadratic term as the inverse of the non-interacting impurity Green's function

$$G_{0\sigma}^{-1}(i\omega_n) = i\omega_n - \epsilon_\sigma - \Delta_\sigma(i\omega_n), \quad (2.27)$$

such that the effective action can be written

$$S_{\text{eff}}[\mathbf{d}^+, \mathbf{d}] = \sum_n d_{\sigma n}^+ G_{0\sigma}^{-1}(i\omega_n) d_{\sigma n} + S_U \quad (2.28)$$

where S_U is the interaction part of the local action.

2.2.1. Limit of strong interaction: Kondo model

Like for the Hubbard model, we consider the limit of strong interaction by projecting onto the low-energy subspace without double occupation on the impurity site. The transformation is named after Schrieffer and Wolff [56], who projected the Anderson model onto the Kondo model [57]. The unitary transformation yields the effective Hamiltonian [11]

$$\hat{H}_{\text{eff}} = \sum_{k\sigma} \varepsilon_k \hat{c}_{k\sigma}^\dagger \hat{c}_{k\sigma} + \sum_{kk'} [2J_{kk'} \hat{\mathbf{s}}_{kk'} \cdot \hat{\mathbf{S}}_d + \hat{c}_{k\sigma}^\dagger K_{kk'} \hat{c}_{k'\sigma}] \quad (2.29)$$

where $\hat{\mathbf{s}}_{kk'} = \frac{1}{2} \sum_{\mu\nu} \hat{c}_{k\mu}^\dagger \boldsymbol{\sigma}_{\mu\nu} \hat{c}_{k'\nu}$ is the bath spin and $\hat{\mathbf{S}}_d = \frac{1}{2} \sum_{\mu\nu} \hat{d}_\mu^\dagger \boldsymbol{\sigma}_{\mu\nu} \hat{d}_\nu$ is the spin of the impurity. The exchange interaction $J_{kk'}$ and scattering term $K_{kk'}$ read

$$J_{kk'} = V_k^* V_{k'} \left[\frac{1}{U + \epsilon - \varepsilon_{k'}} + \frac{1}{\varepsilon_k - \epsilon} \right], \quad (2.30)$$

$$K_{kk'} = -\frac{1}{2} V_k^* V_{k'} \left[\frac{1}{U + \epsilon - \varepsilon_{k'}} - \frac{1}{\varepsilon_k - \epsilon} \right]. \quad (2.31)$$

Neglecting the k -dependence of $J_{kk'}$ and $K_{kk'}$, the effective Hamiltonian can be approximated as

$$\hat{H}_{\text{eff}} \approx \sum_{k\sigma} \tilde{\varepsilon}_k \hat{c}_{k\sigma}^\dagger \hat{c}_{k\sigma} + 2J \hat{\mathbf{S}}_d \cdot \hat{\mathbf{s}}, \quad (2.32)$$

where $\hat{\mathbf{s}} = \frac{1}{2} \sum_{kk'} \sum_{\nu\mu} \hat{c}_{k\nu}^\dagger \boldsymbol{\sigma}_{\nu\mu} \hat{c}_{k'\mu}$ represents the bath spin at the impurity site. The scattering term K as been absorbed in the bath, yielding different bath parameters. This effective Hamiltonian is known as the Kondo [57] or sd -Hamiltonian.

3. Local electronic interaction

As discussed in the previous chapter, the Hubbard model eq. (2.1) is a minimal model for electronic correlation. In this chapter, we will discuss the non-perturbative treatment of this Hamiltonian using the DMFT, which maps the Hubbard model to an effective SIAM. For the SIAM numerically exact methods are available; we discuss the continuous-time quantum Monte Carlo (CT-QMC) algorithm and the complementary tensor network approach.

3.1. Dynamical mean-field theory

The typical starting point to treat interacting systems are mean-field theories. A static mean-field theory replaces the lattice problem by an effective single-site problem. A site couples only to an effective parameter, which has to be determined self-consistently. The typical example is the Weiss mean field for the Ising model [58], which we won't elaborate here; we stick to the Hubbard model. The quartic interaction term can be decoupled by neglecting terms quadratic in the fluctuations $\delta\hat{n}_{i\sigma} = \hat{n}_{i\sigma} - \langle\hat{n}_{i\sigma}\rangle$ around the expectation value, that is $\delta\hat{n}_{i\uparrow}\delta\hat{n}_{i\downarrow} \stackrel{!}{=} 0$. This approximation replaces the quartic interaction term by an effective quadratic term containing the averages

$$U_i\hat{n}_{i\uparrow}\hat{n}_{i\downarrow} \approx U_i[\hat{n}_{i\uparrow}\langle\hat{n}_{i\downarrow}\rangle + \langle\hat{n}_{i\uparrow}\rangle\hat{n}_{i\downarrow} - \langle\hat{n}_{i\uparrow}\rangle\langle\hat{n}_{i\downarrow}\rangle]; \quad (3.1)$$

the expectation values are evaluated using the decoupled quadratic interaction term. This is the Hartree approximation, in which sites couple to the effective parameter $U_i\langle\hat{n}_{i\sigma}\rangle$, that is determined self-consistently. Electrons feel the repulsion of the average density of the opposite spin.

DMFT [59–63], on the other hand, self-consistently maps the lattice problem onto an impurity problem. An impurity model couples, in our case, a single site to a reservoir of non-interacting electrons. Thus, it couples a site to a time or frequency dependent *effective bath*, instead of a static parameter. This allows for local but time-dependent fluctuations. In the limit of infinite coordination number the mapping is exact; it yields valuable insight into the Mott transition of the Hubbard model [62].

The DMFT self-consistency equations can be derived employing the so-called *cavity method* [62], an alternative approach is based on the exact grand potential for infinite coordination number [64, 65]. Here, we employ the cavity method following [62, 66]; this is the same derivation I presented in an extended version in my Master thesis [67] with slight variations. The general idea of the cavity method is the following: One interacting lattice site, $i = \circ$, is selected, the remaining sites are integrated out determining a non-interacting bath. The selected site, $i = \circ$, is thus mapped onto an interacting impurity embedded in this bath. We solve the impurity problem and use its self-energy for the lattice site. This mapping procedure is repeated until self-consistency of the one-particle Green's function

is achieved, that is the local lattice Green's function and the impurity Green's function agree.

The cavity method is conveniently expressed using the field integral representation [10, 11]. The grand canonical partition function of the lattice Hamiltonian eq. (2.1) reads

$$\mathcal{Z} = \int \prod_{i,\sigma} \mathcal{D}[c_{i\sigma}^+(\tau), c_{i\sigma}(\tau)] e^{-S_{\text{lat}}[\mathbf{c}^+(\tau), \mathbf{c}(\tau)]}, \quad (3.2)$$

with the lattice action

$$S_{\text{lat}}[\mathbf{c}^+(\tau), \mathbf{c}(\tau)] = \int_0^\beta d\tau \left(\sum_{ij\sigma} c_{i\sigma}^+(\tau) [(\partial_\tau + \epsilon_i - \mu)\delta_{ij} + t_{ij}] c_{j\sigma}(\tau) + \sum_i U_i n_{i\uparrow}(\tau) n_{i\downarrow}(\tau) \right), \quad (3.3)$$

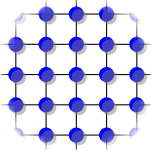
where $c_{i\sigma}(\tau)$ and $c_{i\sigma}^+(\tau)$ are Grassmann fields, and $n_{i\sigma}(\tau) := c_{i\sigma}^+(\tau)c_{i\sigma}(\tau)$. The vectorial notation $\mathbf{c}(\tau)$ and $\mathbf{c}^+(\tau)$ denotes the set of all Grassmann fields $\mathbf{c}(\tau) = \{c_{i\sigma}(\tau)\}$ and $\mathbf{c}^+(\tau) = \{c_{i\sigma}^+(\tau)\}$. The Grassmann fields are always functions of the imaginary time τ , unless frequencies are specified. If all fields depend on the same τ ,¹ we omit it to shorten the notation.

We select a specific site $i = \circ$ and single it out by tracing out all other sites

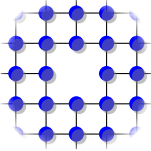
$$\frac{1}{\mathcal{Z}_{\text{eff}}} e^{-S_{\text{eff}}[\mathbf{c}_\circ^+, \mathbf{c}_\circ]} := \frac{1}{\mathcal{Z}} \int \prod_{i \neq \circ, \sigma} \mathcal{D}[c_{i\sigma}^+, c_{i\sigma}] e^{-S_{\text{lat}}[\mathbf{c}^+, \mathbf{c}]}. \quad (3.4)$$

The action $S_{\text{eff}}[\mathbf{c}_\circ^+, \mathbf{c}_\circ]$ defines the effective single-site problem, which needs to be solved. By definition (3.4), the expectation value with respect to the effective action of *local* quantities $\mathcal{O}[\mathbf{c}_\circ^+, \mathbf{c}_\circ]$ is the same as the expectation value in the lattice system $\langle \mathcal{O} \rangle_{S_{\text{eff}}} \equiv \langle \mathcal{O} \rangle_{S_{\text{lat}}}$. Thus, within DMFT we can calculate all local quantities of the lattice system, by solving the impurity system.

Effective action. To derive an explicit expression for the effective action eq. (3.4), we split the lattice action eq. (3.3) into three parts:



$$S_{\text{lat}} = S^{(\circ)} + S_\circ + \Delta S \quad (3.5)$$



$$S^{(\circ)} = \int_0^\beta d\tau \left(\sum_{ij \neq \circ, \sigma} c_{i\sigma}^+ [(\partial_\tau + \epsilon_i - \mu)\delta_{ij} + t_{ij}] c_{j\sigma} + \sum_{i \neq \circ} U_i n_{i\uparrow} n_{i\downarrow} \right) \quad (3.6)$$



$$S_\circ = \int_0^\beta d\tau \left(\sum_\sigma c_{\circ\sigma}^+ (\partial_\tau + \epsilon_\circ - \mu) c_{\circ\sigma} + U_\circ n_{\circ\uparrow} n_{\circ\downarrow} \right) \quad (3.7)$$

¹In fact, there is an infinitesimal time difference to correctly order the fields. This is, however, not of relevance for the derivation, and will therefore be omitted.

$$-\Big|_{-} \quad \Delta S = \int_0^\beta d\tau \sum_{i \neq \circ, \sigma} (c_{i\sigma}^+ t_{i\circ} c_{\circ\sigma} + c_{\circ\sigma}^+ t_{\circ i} c_{i\sigma}), \quad (3.8)$$

where $S^{(\circ)}$ is the action of the lattice with a cavity at site $i = \circ$, S_\circ is the local action of the isolated site $i = \circ$, and ΔS is the action of the hopping between site $i = \circ$ and the cavity lattice. We call $S^{(\circ)}$ cavity action, and expectation values $\langle \cdot \rangle_{S^{(\circ)}}$ cavity quantities. The local action S_\circ is independent of all other sites, it can be pulled out of the integration for the effective action

$$\frac{1}{\mathcal{Z}_{\text{eff}}} e^{-S_{\text{eff}}[c_\circ^+, c_\circ]} = \frac{1}{\mathcal{Z}} e^{-S_\circ} \int \prod_{i \neq \circ, \sigma} \mathcal{D}[c_{i\sigma}^+, c_{i\sigma}] e^{-S^{(\circ)}} e^{-\Delta S} = \frac{\mathcal{Z}^{(\circ)}}{\mathcal{Z}} e^{-S_\circ} \langle e^{-\Delta S} \rangle_{S^{(\circ)}}, \quad (3.9)$$

we identify the integral as average over the cavity system. The cavity action $S^{(\circ)}$ is not quadratic in the Grassmann fields, therefore the cavity average cannot in general be evaluated.

The cavity average $\langle \exp(-\Delta S) \rangle_{S^{(\circ)}}$ is the generating functional [10, 68] of the cavity Green's functions, allowing us to express the average in terms of the interacting cavity Green's functions. We identify the source terms $\eta_{i\sigma}(\tau) := t_{i\circ} c_{\circ\sigma}(\tau)$ and $\eta_{i\sigma}^+(\tau) := c_{\circ\sigma}^+(\tau) t_{\circ i}$ for the generating functional

$$e^{-S_{\text{eff}}[\boldsymbol{\eta}, \boldsymbol{\eta}^+]} = \frac{\mathcal{Z}_{\text{eff}} \mathcal{Z}^{(\circ)}}{\mathcal{Z}} e^{-S_\circ} \left\langle \exp \left(- \int_0^\beta d\tau \sum_{i \neq \circ, \sigma} [c_{i\sigma}^+ \eta_{i\sigma} + \eta_{i\sigma}^+ c_{i\sigma}] \right) \right\rangle_{S^{(\circ)}}. \quad (3.10)$$

For a more compact notation, we introduce the multi-indices $1 = (i, \sigma, \tau)$; overlined indices $\bar{1}$ are summed over, where the site $i = \circ$ is excluded, that is $\sum_{i \neq \circ, \sigma} \int d\tau$. In this compact notation, the generating functional reads

$$e^{-S_{\text{eff}}[\boldsymbol{\eta}, \boldsymbol{\eta}^+]} = \frac{\mathcal{Z}_{\text{eff}} \mathcal{Z}^{(\circ)}}{\mathcal{Z}} e^{-S_\circ} \left\langle \exp \left(c^+(\bar{1}) \eta(\bar{1}) + \eta^+(\bar{1}) c(\bar{1}) \right) \right\rangle. \quad (3.11)$$

Differentiation with respect to the sources $\eta(1')$ and $\eta^+(1)$ generates the Grassmann fields $c^+(1')$ and $c(1)$ inside the cavity average $\langle \cdot \rangle_{S^{(\circ)}}$. Consequently, the n -particle cavity Green's functions is proportional to the derivative [10]

$$(-1)^{n+1} G^{(\circ)}(1 \dots n; 1' \dots n') \propto \frac{\delta^{2n}}{\delta \eta^+(1) \dots \delta \eta^+(n) \delta \eta(1') \dots \delta \eta(n')} e^{-S_{\text{eff}}[\boldsymbol{\eta}, \boldsymbol{\eta}^+]} \Big|_{\boldsymbol{\eta}, \boldsymbol{\eta}^+ = 0}, \quad (3.12)$$

where $G^{(\circ)}(1 \dots n; 1' \dots n') = -\langle c(1) \dots c(n) c^+(1') \dots c^+(n') \rangle_{S^{(\circ)}}$ denotes the n -particle cavity Green's function, and the upright \mathbf{n} is the n th multi-index $\mathbf{n} = (i, \sigma, \tau)$. Grassmann numbers and derivatives anticommute, thus the factor $(-1)^n$ arises as we need to move the derivative $\frac{\delta}{\delta \eta}$ past c^+ to act on the source η . We can eliminate the sign by changing the order of the derivatives, first differentiating with respect to η^+ and then with respect to η . The effective action S_{eff} is the logarithm of the generating functional eq. (3.10). Thus, we identify

$$-S_{\text{eff}}[\boldsymbol{\eta}, \boldsymbol{\eta}^+] \propto \ln \left(\langle e^{-\Delta S} \rangle_{S^{(\circ)}} \right) \quad (3.13)$$

as the generating functional for *connected* Green's functions [10]

$$G_c^{(\circ)}(1 \dots n; 1' \dots n') = \frac{\delta^{2n}}{\delta\eta(1) \dots \delta\eta(n) \delta\eta^+(1') \dots \delta\eta^+(n')} S_{\text{eff}}[\boldsymbol{\eta}, \boldsymbol{\eta}^+] \Big|_{\eta, \eta^+ = 0}. \quad (3.14)$$

Averages with an unbalanced number of c and c^+ vanish for the action eq. (3.3), thus we can expand the effective action in terms of connected Green's functions

$$S_{\text{eff}} = -\ln\left(\frac{\mathcal{Z}_{\text{eff}} \mathcal{Z}^{(\circ)}}{\mathcal{Z}}\right) + S_{\circ} + \sum_{n=1}^{\infty} \frac{1}{(n!)^2} \eta^+(\bar{1}) \dots \eta^+(\bar{n}) \eta(\bar{1}') \dots \eta(\bar{n}') G_c^{(\circ)}(\bar{1} \dots \bar{n}; \bar{1}' \dots \bar{n}'), \quad (3.15)$$

where the factor $1/(n!)^2$ accounts for permutations of the operators. The formula can be verified by comparing the derivatives of both sides. In the non-interacting case, $U = 0$, all but the $n = 1$ particle connected Green's function vanish, as non-interacting Green's functions factorize for a quadratic action.

In the limit of infinite coordination number $Z \rightarrow \infty$ this expression simplifies considerably. To arrive at a non-trivial limit the hopping elements t_{ij} need to be scaled $t_{ij} \rightarrow t_{ij}/Z^{\|i-j\|/2}$ [59], where $\|i-j\|$ is the 1-norm or Manhattan distance. Only the one-particle connected Green's $G_c^{(\circ)}(1, 1')$ function survives, which is identical to the one-particle Green's function $G^{(\circ)}(1, 1')$, all connected Green's functions for $n > 1$ particles vanish in the limit $Z \rightarrow \infty$ [62, 69]. Using the separate indices (i, σ, τ) again, the effective action reads in imaginary time

$$S_{\text{eff}}[\mathbf{c}_{\circ}, \mathbf{c}_{\circ}^+] = \int_0^{\beta} d\tau \left(\sum_{\sigma} c_{\circ\sigma}^+(\tau) (\partial_{\tau} + \epsilon_{\circ} - \mu) c_{\circ\sigma}(\tau) + U_{\circ} n_{\circ\uparrow}(\tau) n_{\circ\downarrow}(\tau) \right) + \int_0^{\beta} d\tau \int_0^{\beta} d\tau' \sum_{ij \neq \circ\sigma} t_{\circ i} c_{\circ\sigma}^+(\tau) G_{\sigma ij}^{(\circ)}(\tau - \tau') t_{i\circ} c_{\circ\sigma}(\tau'). \quad (3.16)$$

In the following, we omit the spin index σ of the Green's functions for a more concise notation.

Equivalence with the action of an interacting SIAM. We compare the effective action eq. (3.16) with the action of the SIAM, eq. (2.26), which we treat as a functional of the hybridization function $S_{\text{imp}}[\mathbf{d}^+, \mathbf{d}; \Delta]$. For a bath chosen such that

$$\Delta(i\omega_n) = \sum_{ij} t_{\circ i} G_{ij}^{(\circ)}(i\omega_n) t_{j\circ} \quad (3.17)$$

and matching on-site energies, we identify that the effective action and the impurity action are identical $S_{\text{eff}}[\mathbf{c}_{\circ}^+, \mathbf{c}_{\circ}] \hat{=} S_{\text{imp}}[\mathbf{d}^+, \mathbf{d}; \Delta]$. In the literature, often the non-interacting impurity Green's function is compared instead, yielding the condition

$$G_{0\text{imp}}^{-1}(i\omega_n) = i\omega_n + \mu - \epsilon_{\circ} - \sum_{ij} t_{\circ i} G_{ij}^{(\circ)}(i\omega_n) t_{j\circ} =: \mathcal{G}_0^{-1}(i\omega_n). \quad (3.18)$$

Here, we stick to the formulation of the impurity action $S_{\text{imp}}[\mathbf{d}^+, \mathbf{d}; \Delta]$ in terms of the hybridization function $\Delta(i\omega_n)$.

The next step is to establish a connection between the cavity Green's $G_{ij}^{(\circ)}$ function and the Green's function of the full lattice G_{ij} . In the limit of infinite coordination number, the self-energy is local $\Sigma_{ij}(i\omega_n) = \Sigma_i(i\omega_n)\delta_{ij}$ [70], the relation

$$G_{ij}^{(\circ)}(i\omega_n) = G_{ij}(i\omega_n) - \frac{G_{i\circ}(i\omega_n)G_{\circ j}(i\omega_n)}{G_{\circ\circ}(i\omega_n)}, \quad (3.19)$$

is obtained. This relation can be motivated using the interpretation of the Green's function as a propagator: The lattice Green's functions G_{ij} contains all possible paths going through the site \circ in addition to the paths contained in the cavity Green's function $G_{ij}^{(\circ)}$. For the non-interacting case, a derivation is provided in my master thesis [67]. We substitute this relation into the effective bath and the hybridization function eqs. (3.17) and (3.18). For a *homogeneous* system all lattice sites are equivalent and thus $\Sigma_i(i\omega_n) = \Sigma(i\omega_n)$. After further simplifications [67], the hybridization function reads

$$\Delta(i\omega_n) = i\omega_n + \mu - \epsilon_\circ - \Sigma(i\omega_n) - G_{\circ\circ}^{-1}(i\omega_n). \quad (3.20)$$

We note, that the hybridization function should not have any constant contributions and asymptotically decay like $\Delta(i\omega_n) \sim c/i\omega_n$. If the DOS $\rho(\varepsilon) := \frac{1}{N} \sum_k \delta(\varepsilon - \varepsilon_k)$ has a finite first moment

$$\varepsilon^{(1)} := \int d\varepsilon \rho(\varepsilon) \varepsilon = \frac{1}{N} \sum_k \varepsilon_k, \quad (3.21)$$

it has to be absorbed into the on-site energy. In the limit of infinite coordination number the self-energy is k -independent, and the k -dependency is absorbed into the DOS; the local lattice Green's function writes

$$G_{\circ\circ}(i\omega_n) = \int d\varepsilon \frac{\rho(\varepsilon)}{i\omega_n + \mu - \epsilon_\circ - \Sigma(i\omega_n) - \varepsilon} = G_{0\circ\circ}(i\omega_n - \Sigma(i\omega_n)), \quad (3.22)$$

where $G_{0\circ\circ}$ is the non-interacting Green's function.

Equation (3.20) provides a way to self-consistently calculate the local Green's function $G_{\circ\circ} = G_{\text{imp}}[\Delta]$ by solving the SIAM $S_{\text{imp}}[\mathbf{d}^+, \mathbf{d}; \Delta]$. In this case solving means to obtain the self-energy $\Sigma_{\text{imp}}[\Delta]$ of the impurity model. The DMFT self-consistency equations read:

Provide initial self-energy $\Sigma(i\omega_n)$;

repeat

local Green's function $G_{\circ\circ}(i\omega_n) := \int d\varepsilon \frac{\rho(\varepsilon)}{i\omega_n + \mu - \epsilon_\circ - \Sigma(i\omega_n) - \varepsilon}$;

hybridization function $\Delta(i\omega_n) := i\omega_n + \mu - \epsilon_\circ - \Sigma(i\omega_n) - G_{\circ\circ}^{-1}(i\omega_n)$;

solve impurity problem $\Sigma_{\text{imp}}[\Delta]$;

set lattice self-energy to impurity self-energy $\Sigma(i\omega_n) = \Sigma_{\text{imp}}(i\omega_n)$;

until *self-consistency* $G_{\circ\circ}(i\omega_n) = G_{\text{imp}}(i\omega_n)$;

Exact non-interacting and atomic limits. We discuss two special cases for *finite* coordination number. DMFT also yields the exact result for the non-interacting limit $U = 0$ and the atomic limit $t_{ij} = 0$. For $U = 0$, the self-energy of the impurity model vanishes $\Sigma_{\text{imp}}[\Delta] = 0$, and we correctly recover $G_{\text{imp}}^{-1}(i\omega_n) = [i\omega_n - \epsilon - \Delta(i\omega_n)]^{-1} = G_{\circ\circ}(i\omega_n)$.

From the cavity construction it is apparent, that the non-interacting limit is exact. The simplification in the limit of infinite coordination is that connected n -particle Green's functions in eq. (3.15) vanish for $n > 1$, this is also the case for non-interacting systems. For $t_{ij} = 0$ the DOS reduces to a delta function $\rho(\varepsilon) = \delta(\varepsilon)$. Thus, the hybridization function vanishes $\Delta(i\omega_n) = 0$, the effective action is the action of a single site of the atomic Hubbard model. The problem is no longer k -dependent, the impurity model yields the exact local Green's function $G_{\text{oo}}(i\omega_n) = [i\omega_n + \mu - \epsilon_{\text{o}} - \Sigma(i\omega_n)]^{-1} = G_{\text{oo}}(i\omega_n)$ [60].

3.1.1. Self-energy of the impurity model

The standard approach to get the self-energy of the impurity model is calculating the Green's function $G_{\sigma}(z)$, and using the Dyson equations

$$\Sigma_{\sigma}(z) = G_{\sigma}^{-1}(z) - G_{\sigma}^{-1}(z). \quad (3.23)$$

Bulla et al. [71] found this approach not to be particularly accurate for the numerical renormalization group. They proposed to use the equation of motion instead. The equation of motion for the one-particle Green's $G_{\alpha\beta}(z) = \langle\langle \hat{c}_{\alpha} | \hat{c}_{\beta}^{\dagger} \rangle\rangle(z)$ function reads

$$z \langle\langle \hat{c}_{\alpha} | \hat{c}_{\beta}^{\dagger} \rangle\rangle(z) - \langle\{\hat{c}_{\alpha}, \hat{c}_{\beta}^{\dagger}\}\rangle = \langle\langle [\hat{c}_{\alpha}, \hat{H}] | \hat{c}_{\beta}^{\dagger} \rangle\rangle(z) = \langle\langle \hat{c}_{\alpha} | [\hat{H}, \hat{c}_{\beta}^{\dagger}] \rangle\rangle(z). \quad (3.24)$$

For the SIAM eq. (2.15) the commutators read

$$[\hat{d}_{\sigma}, \hat{H}] = \sum_k V_k^* \hat{c}_{k\sigma} + \epsilon_{\sigma} \hat{d}_{\sigma} + U \hat{d}_{\sigma} \hat{d}_{-\sigma}^{\dagger} \hat{d}_{-\sigma} \quad (3.25)$$

$$[\hat{c}_{k\sigma}, \hat{H}] = \sum_k V_k \hat{d}_{k\sigma} + \epsilon_{k\sigma} \hat{c}_{k\sigma}. \quad (3.26)$$

Thus, the equation of motion for the off-diagonal Green's function yields

$$\langle\langle \hat{c}_{k\sigma} | \hat{d}_{\sigma}^{\dagger} \rangle\rangle(z) = \frac{V_k}{z - \epsilon_k} \langle\langle \hat{d}_{\sigma} | \hat{d}_{\sigma}^{\dagger} \rangle\rangle(z). \quad (3.27)$$

Inserting this equation into the equation of motion for the diagonal impurity Green's function yields

$$\langle\langle \hat{d}_{\sigma} | \hat{d}_{\sigma}^{\dagger} \rangle\rangle_{U=0}^{-1}(z) \langle\langle \hat{d}_{\sigma} | \hat{d}_{\sigma}^{\dagger} \rangle\rangle(z) - 1 = U \langle\langle \hat{d}_{\sigma} \hat{d}_{-\sigma}^{\dagger} \hat{d}_{-\sigma} | \hat{d}_{\sigma}^{\dagger} \rangle\rangle(z), \quad (3.28)$$

where the subscript $U = 0$ indicates the non-interacting Green's function. Naming the Green's functions $G_{\sigma}(z) = \langle\langle \hat{d}_{\sigma} | \hat{d}_{\sigma}^{\dagger} \rangle\rangle(z)$ and $F_{\sigma}(z) = \langle\langle \hat{d}_{\sigma} \hat{d}_{-\sigma}^{\dagger} \hat{d}_{-\sigma} | \hat{d}_{\sigma}^{\dagger} \rangle\rangle(z)$, and eliminating the non-interacting Green's function using the Dyson equation (3.23), we get the self-energy

$$\Sigma_{\sigma}(z) = U F_{\sigma}(z) G_{\sigma}^{-1}(z). \quad (3.29)$$

Hafermann et al. [72] found that this formula significantly reduces the high-frequency noise for the continuous-time quantum Monte Carlo in hybridization expansion (CT-HYB) algorithm; they labeled this formula as improved estimate. For calculations using time-dependent variational principle (TDVP), we found the improved estimate to be less significant, though in some cases the accuracy could be improved.

3.1.2. Beyond the single-site approximation

Several approaches exist to extend DMFT to include correlation effects beyond the single-site approximation. They can be roughly grouped into two categories: cluster and field-theoretical extensions. Cluster extensions [73] embed a cluster of sites instead of a single site into the bath, thereby including short-ranged nonlocal correlations contained within the cluster. The dynamical cluster approximation [74] does this in k -space, while cellular DMFT [75, 76] works in Wannier space. In principle, the exact result is recovered in the limit of infinite cluster size. The other approach, is to consider field-theoretical extensions [77]. The dynamical vertex approximation (D Γ A) [78] generates nonlocal correlation by considering the local two-particle vertex instead of a local self-energy. The dual fermion [79] approach performs the perturbation theory around the local reference system in terms of a Hubbard–Stratonovich transformation.

4. Continuous-time quantum Monte Carlo

CT-QMC algorithms are a suitable tool to solve impurity models with correlated electrons [13]. As an action-based method, CT-QMC allows simulating effective models. Therefore, it can treat an infinite number of bath sites by integrating them out, whereas Hamiltonian-based methods are limited by the exponential growth of the Hilbert space with the number of bath sites. Further applications of the CT-QMC include, e.g., the cluster extensions of DMFT to incorporate spatial fluctuations [73], the dual fermion approach [79], or the dynamical vertex approximation [78]. Versions of CT-QMC along the Keldysh contour [14, 80] also exist. There are three main formulations of the CT-QMC algorithm: the interaction expansion CT-INT [81], the hybridization expansion CT-HYB [82, 83], and the auxiliary-field formulation CT-AUX [84].

In this chapter, we explain the basics of the CT-HYB. We restrict the discussion to density-density interactions (as is the case with single-band problems), which can be efficiently treated using the segment picture [13]. Generalizations to generic interactions are rather straightforward, though implementation details might be more complex. Implementations of the CT-HYB are available, e.g. [C1, C8]. The review [13] provides detailed information. We follow the more accessible references [85–87], and give a rather schematic outline of the algorithm.

The basic idea for CT-QMC algorithm is to divide the action S into a solvable S_0 part and the rest ΔS :

$$\mathcal{Z}_{\text{imp}} = \int \prod_{\sigma} \mathcal{D}[\hat{d}_{\sigma}^{\dagger}(\tau), \hat{d}_{\sigma}(\tau)] e^{-S_0 - \Delta S} = \mathcal{Z}_0 \langle e^{-\Delta S} \rangle_{S_0}, \quad (4.1)$$

where the field integral is rewritten as an average with respect to the solvable action S_0 . Constant factors like \mathcal{Z}_0 do not affect observables and accordingly drop out of the Monte Carlo algorithm. The exponential in eq. (4.1) is expanded into its series representation

$$\mathcal{Z}_{\text{imp}} = \mathcal{Z}_0 \sum_{k=0}^{\infty} \frac{(-1)^k}{k!} \langle (\Delta S)^k \rangle_{S_0}. \quad (4.2)$$

The Monte Carlo algorithm samples over different contributions of any order k , the weight is determined by evaluating the field integral. The average expansion order $\langle k \rangle$ of such an expansion reads

$$\langle k \rangle = \frac{1}{\mathcal{Z}_{\text{imp}}} \mathcal{Z}_0 \sum_k \frac{(-1)^k}{k!} \langle (\Delta S)^k \rangle_{S_0} \quad k = -\langle \Delta S \rangle_S, \quad (4.3)$$

where we shifted the summation variable k to obtain the second equality. The CT-HYB algorithm expands the partition function in the hybridization, as the name indicates.

4.1. Hybridization expansion of the partition function

Using the effective action eq. (2.26) with the hybridization function $\Delta_\sigma(\tau)$, we write the partition function

$$\begin{aligned} \mathcal{Z}_{\text{imp}}/\mathcal{Z}_{\text{bath}} = & \int \prod_\sigma \mathcal{D}[d_\sigma^+(\tau), d_\sigma^-(\tau)] \exp \left(- \int_0^\beta d\tau \left[\sum_\sigma d_\sigma^+(\tau) (\partial_\tau + \epsilon_\sigma) d_\sigma(\tau) + U d_\uparrow^+(\tau) d_\uparrow(\tau) d_\downarrow^+(\tau) d_\downarrow(\tau) \right] \right. \\ & \left. - \int_0^\beta d\tau \int_0^\beta d\tau' \sum_\sigma d_\sigma^+(\tau) \Delta_\sigma(\tau - \tau') d_\sigma(\tau') \right). \end{aligned} \quad (4.4)$$

For the hybridization function, we use the local action $S_{\text{loc}} = S_0$ eq. (2.17) as solvable part

$$\mathcal{Z}_{\text{imp}} = \mathcal{Z}_{\text{bath}} \mathcal{Z}_{\text{loc}} \left\langle \exp \left(- \int_0^\beta d\tau \int_0^\beta d\tau' \sum_\sigma d_\sigma^+(\tau) \Delta_\sigma(\tau - \tau') d_\sigma(\tau') \right) \right\rangle_{S_{\text{loc}}}, \quad (4.5)$$

and expand in the hybridization function. The average expansion order eq. (4.3) reads

$$\langle k \rangle = \int_0^\beta d\tau \int_0^\beta d\tau' \sum_\sigma \Delta_\sigma(\tau - \tau') \langle d_\sigma(\tau') d_\sigma^+(\tau) \rangle_S = \sum_{\sigma n} \Delta_\sigma(i\omega_n) G_\sigma(i\omega_n); \quad (4.6)$$

this is the kinetic energy $\langle k \rangle = \beta E_{\text{kin}}$ [13, 88]. We note that the partition function eq. (4.5) is a generating function for n -particle Green's functions, functional derivatives with respect to the hybridization function $\Delta_\sigma(\tau - \tau')$ generate Green's functions up to the normalization by the partition function. Thus, the Green's function is the functional derivative of the logarithm

$$\mathcal{G}_\sigma(\tau' - \tau) = - \frac{\delta \log \mathcal{Z}_{\text{imp}}}{\delta \Delta_\sigma(\tau - \tau')}. \quad (4.7)$$

We abbreviate the notation by introducing compound indices $1 = (\sigma, \tau)$, e.g. $\Delta(1, 2) = \Delta_\sigma(\tau - \tau') \delta_{\sigma\sigma'}$, overlined indices are summed over σ and integrated over τ , that is $\sum_\sigma \int d\tau$. Using this abbreviated form, we express the exponential function by its series representation

$$\begin{aligned} \mathcal{Z}_{\text{imp}} &= \mathcal{Z}_{\text{bath}} \mathcal{Z}_{\text{loc}} \left\langle \exp \left[- d^+(\bar{1}) \Delta(\bar{1}, \bar{2}) d(\bar{2}) \right] \right\rangle_{S_{\text{loc}}} \\ &= \mathcal{Z}_{\text{bath}} \mathcal{Z}_{\text{loc}} \sum_k \frac{(-1)^k}{k!} \left\langle d^+(\bar{1}) d(\bar{1}') \dots d^+(\bar{k}) d(\bar{k}') \right\rangle_{S_{\text{loc}}} \Delta(\bar{1}, \bar{1}') \dots \Delta(\bar{k}, \bar{k}'). \end{aligned} \quad (4.8)$$

Note that k is a number denoting the expansion order, the upright \mathbf{k} , on the other hand, is the k th multi-index $\mathbf{k} = (\sigma, \tau)$.

This expansion is not yet suitable for sampling via a Monte Carlo algorithm, due to the anti-commutativity of the Grassmann algebra. The second order term $k = 2$ contains, e.g., the two terms [87]

$$\left\langle d^+(1) d(1') d^+(2) d(2') \right\rangle_{S_{\text{loc}}} \Delta(1, 1') \Delta(2, 2') \quad (4.9a)$$

$$\left\langle d^+(1) d(2') d^+(2) d(1') \right\rangle_{S_{\text{loc}}} \Delta(1, 2') \Delta(2, 1') = - \left\langle d^+(1) d(1') d^+(2) d(2') \right\rangle_{S_{\text{loc}}} \Delta(1, 2') \Delta(2, 1'). \quad (4.9b)$$

These two terms involve the same operators and therefore the same local Green's function, but it is weighted by different hybridization functions, and more importantly, with a different sign. The hybridization function is antisymmetric with $\Delta_\sigma(\tau) < 0$ for $\tau \in (0, \beta)$, see eq. (2.24). The permutation does not change the sign of the product of hybridization functions $\text{sign}[\Delta(1, 1')\Delta(2, 2')] = \text{sign}[\Delta(1, 2')\Delta(2, 1')]$. Monte Carlo sampling of sums with terms of different signs is inaccurate. Werner et al. [82] found that it is essential to collect all such combinations, and sample them simultaneously. We permute all primed indices, obtaining a minus sign for odd permutations due to the Grassmann algebra. This is the definition of the determinant

$$\det(\mathbf{A}) = \sum_{\sigma \in S_k} \text{sign}(\sigma) \prod_{i=1}^k a_{i\sigma_i} \quad \text{with} \quad (\mathbf{A})_{ij} = a_{ij}, \quad (4.10)$$

where S_k is the symmetric group with permutations σ . The sign is $\text{sign}(\sigma) = +1$ for a permutation achieved by an even number of exchanges of two entries, and $\text{sign}(\sigma) = -1$ for an odd number. The Grassmann algebra yields the identical sign, as between two operators $d(1')$ and $d(2')$, there is always an odd number of d^+ and an even number of d . There are $|S_k| = k!$ permutations for the order k , thus we can rewrite the expanded partition function

$$\mathcal{Z}_{\text{imp}} = \mathcal{Z}_{\text{bath}} \mathcal{Z}_{\text{loc}} \sum_k \frac{(-1)^k}{(k!)^2} \left\langle d^+(\bar{1})d(\bar{1}') \dots d^+(\bar{k})d(\bar{k}') \right\rangle_{S_{\text{loc}}} \det \Delta^k \quad (4.11)$$

with the matrix elements $(\Delta^k)_{ij} = \Delta(i, j)$; the matrix is of size $k \times k$ and implicitly carries the same indices as the Grassmann fields in the average. The prefactor $1/(k!)^2$ can be compensated by restricting sums to ordered sums.

It remains to calculate the local expectation values. The local Hilbert space is of size 4^m , where m is the number of orbitals (or impurity sites). One option is to diagonalize the local Hamiltonian and evaluate the expectation value in its eigenbasis. To treat large numbers of local degrees of freedom, that is large numbers of orbitals or cluster sites, it is essential to exploit symmetries of the local Hamiltonian [88, 89]. Alternatives are Krylov-based methods in the particle-number basis [90], or more recently tensor-network-based methods [91]. Here, we only discuss the simplest case: density-density type interaction. For this case, the interaction is diagonal in the particle number basis; the so-called segment picture can be employed.

4.1.1. Segment picture of the local Hamiltonian

While the segment picture is valid for multiple local degrees of freedom (as long as the interaction is approximated by density-density interaction), we restrict the discussion to the single-band model for clarity. A term of order k consists of $k_\uparrow \leq k$ pairs of creation and annihilation operators for spin $\sigma = \uparrow$ and $k_\downarrow = k - k_\uparrow$ pairs for spin $\sigma = \downarrow$. The segment picture is a mean to visualize such a configuration. We draw the impurity time axis on the interval $\tau \in [0, \beta]$, plotting the time from right to left to match the chronology of the time ordering. From a creation $d_\sigma^+(\tau)$ at time τ to the next annihilation $d_\sigma(\tau')$ at a later time τ' a spin- σ electron occupies the impurity. This time interval is denoted a segment; we represent it by a line. The impurity can be already occupied at time $\tau = 0$,

which can be annihilated by $d_\sigma(\tau)$ and created again $d_\sigma^\dagger(\tau')$ at a later time τ' , resulting in an open line wrapping around the boundaries. Figure 4.1 shows an example of order $k = 3$ for the spin-up channel only.

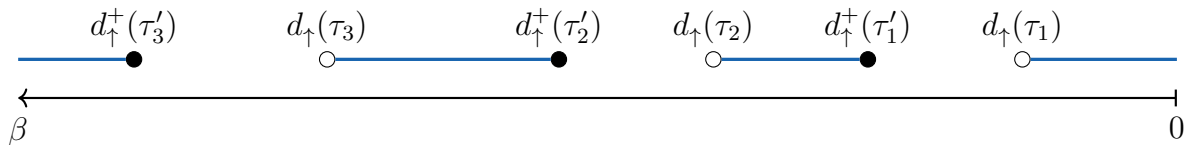


Figure 4.1.: Example of a segment picture of order $k_\uparrow = 3$ for the $\sigma = \uparrow$ channel.

To calculate the contribution of the local action S_{loc} , it is suitable to change to the Hamiltonian formalism. The expectation value is the trace over the local basis states; a single one-band impurity has the four basis states $|0\rangle$, $|\uparrow\rangle$, $|\downarrow\rangle$, and $|\uparrow\downarrow\rangle$. For $k_\downarrow > 0$ and $k_\uparrow > 0$, only a single state of the trace contributes, determined by the first segment. For density-density interaction, the Hamiltonian is diagonal in the occupation number basis with the elements

$$\langle 0|\hat{H}_{\text{loc}}|0\rangle = 0, \quad \langle \uparrow|\hat{H}_{\text{loc}}|\uparrow\rangle = \epsilon_\uparrow, \quad \langle \downarrow|\hat{H}_{\text{loc}}|\downarrow\rangle = \epsilon_\downarrow, \quad \langle \uparrow\downarrow|\hat{H}_{\text{loc}}|\uparrow\downarrow\rangle = \epsilon_\uparrow + \epsilon_\downarrow + U. \quad (4.12)$$

Segments only contribute if there is an equal number of creation and annihilation operators for each spin; we only need to consider contributions where the spin indices of the annihilation operators are a permutation of the spin indices of the creation operators. Thus, the local weight

$$W_{\text{loc}}^k := \text{Tr}_{\text{loc}} \left[e^{-\beta \hat{H}_{\text{loc}}} \mathcal{T} \hat{d}_{\sigma_1}^\dagger(\tau_1) \hat{d}_{\sigma_1}(\tau_1') \dots \hat{d}_{\sigma_k}^\dagger(\tau_k) \hat{d}_{\sigma_k'}(\tau_k') \right], \quad (4.13)$$

can be read directly from the segment picture; here \mathcal{T} is the time ordering symbol necessary in the Hamiltonian formalism. If there are operators for all spin channels, only a single state contributes to the trace. The total lengths of the segments of spin σ , L_σ , determine the contribution of the on-site energy ϵ_σ , and the overlap $O_{\uparrow\downarrow}$ determines the contribution of the interaction; the weight reads

$$W_{\text{loc}}^k = s \exp(-\epsilon_\uparrow L_\uparrow - \epsilon_\downarrow L_\downarrow - U O_{\uparrow\downarrow}), \quad (4.14)$$

where s is the sign from time ordering. The weights agree with the physical intuition, U suppresses the double occupation related to $O_{\uparrow\downarrow}$, $\epsilon_\sigma > 0$ suppresses occupation related to L_σ , while $\epsilon_\sigma < 0$ increases it. Figure 4.2 shows such an example segment. After explaining how to calculate all terms, it remains to sample the configurations using a Monte Carlo algorithm.

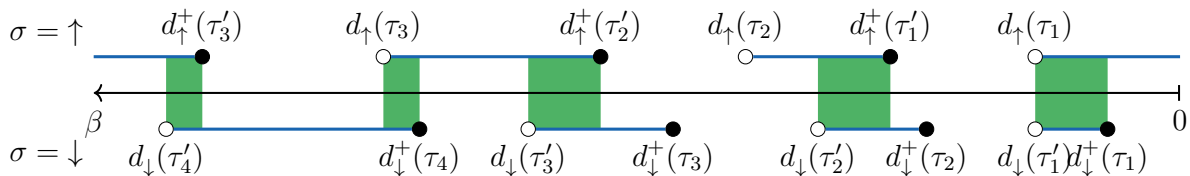


Figure 4.2.: Segment picture of order $k_\uparrow = 3$, $k_\downarrow = 4$ for the impurity state. L_\uparrow is the total length of the segments with $\sigma = \uparrow$ and L_\downarrow of those with $\sigma = \downarrow$. $O_{\uparrow\downarrow}$ is the length of the overlap which is colored green.

4.1.2. Monte Carlo sampling of segment configurations

Assuming the local weights and determinants are positive we can perform the regular Monte Carlo sampling. The partition function is the high-dimensional sum-integral

$$\begin{aligned} \mathcal{Z}_{\text{loc}} &= \mathcal{Z}_{\text{bath}} \mathcal{Z}_{\text{imp}} \sum_k \sum_{\sigma_1 \sigma_{1'}} \cdots \sum_{\sigma_k \sigma_{k'}} \int_0^\beta d\tau_1 \int_0^\beta d\tau_{1'} \cdots \int_0^\beta d\tau_k \int_0^\beta d\tau_{k'} \frac{1}{(k!)^2} W_{\text{loc}}^{(k)} \det \Delta^k \\ &=: \mathcal{Z}_{\text{bath}} \mathcal{Z}_{\text{imp}} \sum_k \int d\zeta_k \frac{1}{(k!)^2} W_{\text{loc}}^{\zeta_k} \det \Delta^{\zeta_k} =: \sum_k \int d\zeta_k W_{\text{MC}}^{\zeta_k}; \end{aligned} \quad (4.15)$$

we write it as sum over all possible configurations ζ_k , where one configuration is represented by the segment picture introduced previously. Mathematically, every configuration ζ_k is a tuple

$$\zeta_k = ([\sigma_1 \tau_1, \sigma_{1'} \tau_{1'}], \dots, [\sigma_k \tau_k, \sigma_{k'} \tau_{k'}]). \quad (4.16)$$

The weight $W_{\text{loc}}^{\zeta_k}$, the matrix Δ^{ζ_k} , and $W_{\text{MC}}^{\zeta_k}$ depend on all indices of the corresponding configuration. Monte Carlo is the method of choice for such high-dimensional integrals, as its rate of convergence is independent of the dimension. We employ a standard Markov chain Monte Carlo with importance sampling. The importance sampling is constructed from a set of updates.

These updates have to fulfill *ergodicity*, that is any configuration ζ_k can be generated from any other configuration $\zeta_{k'}$ by a finite number of updates. To fulfill ergodicity, it is sufficient to define an insertion update and a removal update. The insertion update adds a pair of creation and annihilation operators, that is a segment, to the configurations, thereby increasing the expansion order k by one. The removal update removes such a pair, thereby decreasing the expansion order k by one. Evidently, starting from a configuration $\zeta_{k'}$, any configuration ζ_k can be reached by first removing all $2k'$ operators of $\zeta_{k'}$, and then inserting the $2k$ desired operators of ζ_k . In practice, additional updates are necessary depending on the physical problem, as such transitions might be very unlikely, which can trap the algorithm in certain regions of the phase space.

The second property that has to be fulfilled is that the generated distribution is *stationary*. As usual, we demand *detailed balance*

$$p(\zeta_k) T_{\zeta_k \rightarrow \zeta_{k'}} = p(\zeta_{k'}) T_{\zeta_{k'} \rightarrow \zeta_k}, \quad (4.17)$$

where $p(\zeta_k)$ is the probability of a configuration ζ_k , and $T_{\zeta_k \rightarrow \zeta_{k'}}$ is the transition probability. Detailed balance is a sufficient condition to guarantee a stationary distribution

$$\int d\zeta_k p(\zeta_{k'}) T_{\zeta_{k'} \rightarrow \zeta_k} = p(\zeta_k) \int d\zeta_k T_{\zeta_k \rightarrow \zeta_{k'}} = p(\zeta_k); \quad (4.18)$$

it reflects reversibility. We use the Metropolis choice [92, 93] to determine the transition probabilities. The transition probabilities are split into a proposal probability P and an acceptance probability A :

$$T_{\zeta_k \rightarrow \zeta_{k'}} = P_{\zeta_k \rightarrow \zeta_{k'}} A_{\zeta_k \rightarrow \zeta_{k'}} \quad (4.19)$$

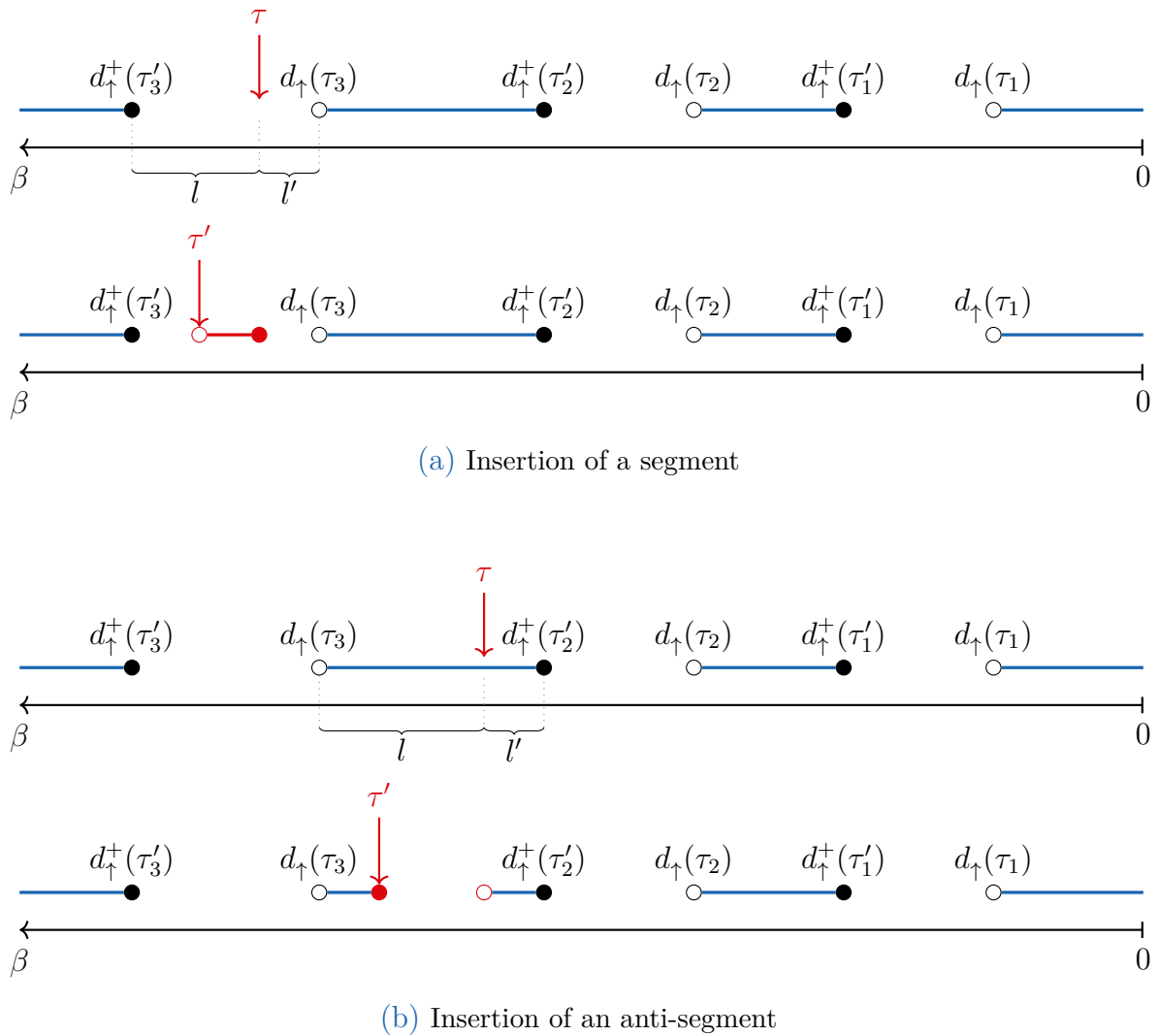


Figure 4.3.: Example of insertion update for the $\sigma = \uparrow$ channel, the inserted operators are drawn in red. A configuration of order $k_{\uparrow} = 3$ is shown. (a) Insertion of a segment $d_{\uparrow}(\tau')d_{\uparrow}^+(\tau)$ if at time τ the $\sigma = \uparrow$ channel is empty; (b) insertion of an anti-segment $d_{\uparrow}^+(\tau')d_{\uparrow}(\tau)$ if at time τ the $\sigma = \uparrow$ channel is occupied.

The Metropolis choice for an acceptance probability A , to fulfill the detailed balance condition, is

$$A_{\zeta_k \rightarrow \zeta'_{k'}} = \min \left(1, \frac{p(\zeta'_{k'})P_{\zeta'_{k'} \rightarrow \zeta_k}}{p(\zeta_k)P_{\zeta_k \rightarrow \zeta'_{k'}}} \right). \quad (4.20)$$

Let's consider the basic updates. First we consider the probability of inserting an (anti-)segment, i.e., a pair of operators $\hat{d}_{\sigma}^{\dagger}(\tau)$ and $\hat{d}_{\sigma}(\tau')$, increasing the expansion order by one, $k \rightarrow k + 1$. The insertion probability decomposes into choosing the quantum number, here the spin σ , yielding a factor $1/2$, and choosing the two times τ and τ' . Figure 4.3 shows an example for an insertion in the $\sigma = \uparrow$ spin channel. First, we choose a time τ with the probability $d\tau/\beta$. If the impurity is empty for spin σ at that time, an electron is added $\hat{d}_{\sigma}^{\dagger}(\tau)$ (segment); if it is filled, an electron is removed $\hat{d}_{\sigma}(\tau)$ (anti-segment). Next,

we choose a time τ' between τ and the next operator (wrapping around the time β in the absence of operators in the interval $(\tau, \beta]$). We call the length of this interval l , the probability is $d\tau'/l$. Thus, the proposal probability of an insertion is

$$P_{\zeta_k \rightarrow \zeta_{k+1}} = \frac{d\tau d\tau'}{2\beta l}. \quad (4.21)$$

An alternative choice for the update is

$$P'_{\zeta_k \rightarrow \zeta_{k+1}} = \frac{d\tau d\tau'}{2\beta^2}, \quad (4.22)$$

choosing two arbitrary times. Proposals with times $\tau' > \tau + l$ are always rejected, because such a configuration is invalid, i.e., it has probability $p(\zeta_{k+1}) = 0$, as the local expectation value $W_{\text{loc}}^{\zeta_k}$ vanishes. A third choice would be $\tau' \in (\tau - l', \tau + l)$, where l' is the time distance to the previous operator. The probability of removing a segment, i.e. a pair of operators, is simply

$$P_{\zeta_k \rightarrow \zeta_{k-1}} = \frac{1}{2k}. \quad (4.23)$$

The probability of the configuration ζ_k can be read off the partition function eq. (4.15):

$$p(\zeta_k) \propto d\tau_1 d\tau_{1'} \dots d\tau_k d\tau_{k'} \frac{1}{(k!)^2} W_{\text{loc}}^{\zeta_k} \det \Delta^{\zeta_k}. \quad (4.24)$$

Thus, the acceptance ratio according to the Metropolis choice eq. (4.20) for an insertion is

$$A_{\zeta_k \rightarrow \zeta_{k+1}} = \min \left(1, \frac{p(\zeta_{k+1}) P_{\zeta_{k+1} \rightarrow \zeta_k}}{p(\zeta_k) P'_{\zeta_k \rightarrow \zeta_{k+1}}} \right) = \min \left(1, \frac{W_{\text{loc}}^{\zeta_{k+1}} \det \Delta^{\zeta_{k+1}} \beta^2}{(k+1)^2 W_{\text{loc}}^{\zeta_k} \det \Delta^{\zeta_k} k+1} \right), \quad (4.25)$$

for a removal it is

$$A_{\zeta_{k+1} \rightarrow \zeta_k} = \min \left(1, \frac{p(\zeta_k) P'_{\zeta_k \rightarrow \zeta_{k+1}}}{p(\zeta_{k+1}) P_{\zeta_{k+1} \rightarrow \zeta_k}} \right) = \min \left(1, \frac{(k+1)^2 W_{\text{loc}}^{\zeta_k} \det \Delta^{\zeta_k} k+1}{W_{\text{loc}}^{\zeta_{k+1}} \det \Delta^{\zeta_{k+1}} \beta^2} \right). \quad (4.26)$$

Only the ratios of weights are relevant, constants in the partition function correctly drop out. It is essential to efficiently calculate the ratio of the determinants.

4.1.3. Evaluation of determinants

We consider an insertion increasing the order from $k-1$ to k . The matrices $\Delta^{\zeta_{k-1}}$ and Δ^{ζ_k} are closely related, as the insertion is a local update. We simplify the notation by omitting the specific configuration ζ_k and write Δ^k instead; its matrix elements read $(\Delta^k)_{ij} = \Delta(i, j)$. If the order k of the matrix Δ is clear from its elements, we omit the superscript k . The matrix after an insertion can be expressed as the block matrix

$$\Delta^k = \begin{pmatrix} \Delta^{k-1} & \Delta_{[:,k]}^k \\ \Delta_{[k,:]}^k & \Delta(k, k) \end{pmatrix} = \begin{pmatrix} \Delta^{k-1} & \Delta_{[:,k]} \\ \Delta_{[k,:]} & \Delta(k, k) \end{pmatrix}; \quad (4.27)$$

appending a row and column to the matrix Δ^{k-1} yields the matrix Δ^k after the insertion. The ratio of determinants can be efficiently calculated using the determinant formula for partitioned matrices [94]

$$\det \begin{pmatrix} \mathbf{T} & \mathbf{U} \\ \mathbf{V} & \mathbf{W} \end{pmatrix} = \det(\mathbf{T}) \det(\mathbf{W} - \mathbf{V}\mathbf{T}^{-1}\mathbf{U}), \quad (4.28)$$

thus, we can replace the ratio of determinants by

$$\frac{\det(\Delta^k)}{\det(\Delta^{k-1})} = \Delta(\mathbf{k}, \mathbf{k}) - \Delta_{[k,:]}(\Delta^{k-1})^{-1} \Delta_{[:,k]}, \quad (4.29)$$

expressing the ratio in terms of the matrix inverse $(\Delta^{k-1})^{-1} =: \mathbf{M}^{k-1}$. Likewise, we can keep track of the inverse \mathbf{M}^k , using the Woodbury matrix identity [95]

$$(\mathbf{A} + \mathbf{UCV})^{-1} = \mathbf{A}^{-1} - \mathbf{A}^{-1}\mathbf{U}(\mathbf{C}^{-1} + \mathbf{VA}^{-1}\mathbf{U})^{-1}\mathbf{VA}^{-1}. \quad (4.30)$$

The matrix after an insertion Δ^k can be expressed in terms of the previous matrix Δ^{k-1} by adding a column and a row

$$\begin{aligned} \Delta^k &= \begin{pmatrix} \Delta^{k-1} & \mathbf{0} \\ \mathbf{0}^\top & 1 \end{pmatrix} + \begin{pmatrix} \Delta_{[:,k]} \\ \Delta(\mathbf{k}, \mathbf{k}) - 1 \end{pmatrix} \hat{\mathbf{e}}_k^\top + \hat{\mathbf{e}}_k \begin{pmatrix} \Delta_{[k,:]} & 0 \end{pmatrix} \\ &= \underbrace{\begin{pmatrix} \Delta^{k-1} & \mathbf{0} \\ \mathbf{0}^\top & 1 \end{pmatrix}}_{\mathbf{A}} + \underbrace{\begin{pmatrix} \Delta_{[:,k]} & \mathbf{0} \\ \Delta(\mathbf{k}, \mathbf{k}) - 1 & 1 \end{pmatrix}}_{\mathbf{U}} \underbrace{\begin{pmatrix} \mathbf{0}^\top & 1 \\ \Delta_{[k,:]} & 0 \end{pmatrix}}_{\mathbf{V}}, \end{aligned} \quad (4.31)$$

where $\mathbf{0}$ is the (column) vector of zeros $(\mathbf{0})_i = 0$, $\hat{\mathbf{e}}_k$ is the unit vector $(\hat{\mathbf{e}}_k)_i = \delta_{ik}$. The reader might wonder about the 1 in the bottom right element of the first summand, which is subtracted by the second summand. This one is needed, for the first summand to be invertible. Thus, Δ^k can be calculated as a rank-two update of the block-structure of Δ^{k-1} . Evaluating the matrix-products and the 2×2 matrix inverse, we get the formula for the inverse

$$\begin{aligned} \mathbf{M}^k &= \begin{pmatrix} \mathbf{M} & \mathbf{0} \\ \mathbf{0}^\top & 1 \end{pmatrix} - \frac{1}{\Delta(\mathbf{k}, \mathbf{k}) - \Delta_{[k,:]} \mathbf{M} \Delta_{[:,k]}} \begin{pmatrix} -\mathbf{M} \Delta_{[:,k]} \Delta_{[k,:]} \mathbf{M} & \mathbf{M} \Delta_{[:,k]} \\ \Delta_{[k,:]} \mathbf{M} & \Delta(\mathbf{k}, \mathbf{k}) - \Delta_{[k,:]} \mathbf{M} \Delta_{[:,k]} - 1 \end{pmatrix} \\ &= \begin{pmatrix} \mathbf{M} & \mathbf{0} \\ \mathbf{0}^\top & 0 \end{pmatrix} - \frac{1}{\Delta(\mathbf{k}, \mathbf{k}) - \Delta_{[k,:]} \mathbf{M} \Delta_{[:,k]}} \begin{pmatrix} -\mathbf{M} \Delta_{[:,k]} \Delta_{[k,:]} \mathbf{M} & \mathbf{M} \Delta_{[:,k]} \\ \Delta_{[k,:]} \mathbf{M} & -1 \end{pmatrix}, \end{aligned} \quad (4.32)$$

where we dropped the superscript $k-1$ of the matrix $\mathbf{M}^{k-1} =: \mathbf{M}$; in the second line we canceled the factor 1 in the lower right element, which was introduced to make the summand invertible. The second addend is a rank-1 matrix, evidently it is separable

$$\mathbf{M}^k = \begin{pmatrix} \mathbf{M}^{k-1} & \mathbf{0} \\ \mathbf{0}^\top & 0 \end{pmatrix} + \frac{1}{\Delta(\mathbf{k}, \mathbf{k}) - \Delta_{[k,:]} \mathbf{M}^{k-1} \Delta_{[:,k]}} \begin{pmatrix} \mathbf{M}^{k-1} \Delta_{[:,k]} \\ -1 \end{pmatrix} \begin{pmatrix} \Delta_{[k,:]} \mathbf{M}^{k-1} & -1 \end{pmatrix}, \quad (4.33)$$

which allows to efficiently update the matrix $\mathbf{M}^k = (\Delta^k)^{-1}$. Moreover, we need the inverse operation for the removal. The calculation for the update of the matrix inverse is

analogue to the relation of the cavity Green's function to the lattice Green's function eq. (3.19). It can easily be shown using the matrix inverse for partitioned matrices [96]. We partition the matrix $\mathbf{M}^k = (\Delta^k)^{-1}$

$$\mathbf{M}^k = \begin{pmatrix} \mathbf{M}_{[k,:k]}^k & \mathbf{M}_{[:k,k]}^k \\ \mathbf{M}_{[k,:k]}^k & M_{kk}^k \end{pmatrix}. \quad (4.34)$$

Then the block in first row and column of its inverse yields the matrix Δ^{k-1} :

$$\Delta^{k-1} = \left[\mathbf{M}_{[k,:k]}^k - \mathbf{M}_{[k,:k]}^k (M_{kk}^k)^{-1} \mathbf{M}_{[:k,k]}^k \right]^{-1}. \quad (4.35)$$

The new matrix $\mathbf{M}^{k-1} = (\Delta^{k-1})^{-1}$ is readily obtained by inverting this equation. Blocking the matrix Δ^k instead

$$\Delta^k = \begin{pmatrix} \Delta_{[:k,:k]} & \Delta_{[:k,k]} \\ \Delta_{[k,:k]} & \Delta(\mathbf{k}, \mathbf{k}) \end{pmatrix}, \quad (4.36)$$

we analogously obtain the equation

$$\mathbf{M}_{kk}^k = \left[\Delta(\mathbf{k}, \mathbf{k}) - \Delta_{[k,:k]} (\Delta_{[:k,:k]})^{-1} \Delta_{[:k,k]} \right]^{-1}, \quad (4.37)$$

which is exactly the determinant ratio eq. (4.29), thus

$$\frac{\det(\Delta^{k-1})}{\det(\Delta^k)} = M_{kk}^k. \quad (4.38)$$

4.1.4. Sampling of Green's function

Partition function sampling. The quantity we are actually interested in is not the partition function but the Green's function (and other observables). One way to obtain the one-particle Green's function is the logarithmic derivative

$$\mathcal{G}(1, 2) = -\frac{\delta \ln \mathcal{Z}_{\text{imp}}}{\delta \Delta(2, 1)} = -\frac{1}{\mathcal{Z}_{\text{imp}}} \frac{\delta \mathcal{Z}_{\text{imp}}}{\delta \Delta(2, 1)} = \frac{\mathcal{Z}_{\text{bath}} \mathcal{Z}_{\text{loc}}}{\mathcal{Z}_{\text{imp}}} \sum_k \frac{(-1)^k}{(k!)^2} W_{\text{loc}}^{\zeta_k} \frac{\delta \det \Delta^k}{\delta \Delta(2, 1)}. \quad (4.39)$$

The derivative of the determinant amounts to removing the row and column containing $\Delta(2, 1)$, if no such element exists the derivative is zero. This can be seen from the definition of the determinant eq. (4.10), or even simpler by remembering the definition eq. (4.8). This also coincides with the definition of the Green's function

$$\begin{aligned} \mathcal{G}(1^*, 2^*) &= -\left\langle d(1^*) d^+(2^*) \right\rangle_{S_{\text{imp}}} = -\frac{1}{\mathcal{Z}_{\text{imp}}} \mathcal{Z}_{\text{bath}} \mathcal{Z}_{\text{loc}} \sum_k \frac{(-1)^k}{k!} \left\langle d(1^*) d^+(2^*) (\Delta S)^k \right\rangle_{S_{\text{loc}}} \\ &= -\frac{\mathcal{Z}_{\text{bath}} \mathcal{Z}_{\text{loc}}}{\mathcal{Z}_{\text{imp}}} \sum_k \frac{(-1)^k}{k!} \left\langle d(1^*) d^+(2^*) d^+(\bar{1}) d(\bar{1}') \dots d(\bar{k}) d^+(\bar{k}') \right\rangle_{S_{\text{loc}}} \Delta(\bar{1}, \bar{1}') \dots \Delta(\bar{k}, \bar{k}'), \end{aligned} \quad (4.40)$$

the average contains one ‘free’ pair of Grassmann fields $d(1^*)d^+(2^*)$, all others are connected by hybridization lines. Thus, we can write the Green’s function in the form

$$\mathcal{G}(1, 2) = -\frac{\mathcal{Z}_{\text{bath}}\mathcal{Z}_{\text{loc}}}{\mathcal{Z}_{\text{imp}}} \sum_k \int d\zeta_k \frac{(-1)^k}{(k!)^2} W_{\text{loc}}^{\zeta_k} \det \Delta^{\zeta_k} \frac{\det \Delta^{\zeta_{k-1}}}{\det \Delta^{\zeta_k}}, \quad (4.41)$$

where $\Delta^{\zeta_{k-1}}$ is the matrix with the column and row corresponding to the derivative $\delta\Delta(2, 1)$ removed. Such a ratio of determinants was calculated for the removal update eq. (4.26); it is simply the aforementioned matrix element $M(1, 2)$, see eq. (4.38). This result can be derived much more elegantly using Gaussian integration [97]. The determinant can be written as a Gaussian Berezin integral

$$\det(\Delta) = \int \prod \mathcal{D}[\boldsymbol{\eta}^+, \boldsymbol{\eta}] \exp(\boldsymbol{\eta}^+ \Delta \boldsymbol{\eta}) = \int \prod_1 \mathcal{D}[\eta^+(1), \eta(1)] \exp(\eta^+(\bar{1})\Delta(\bar{1}, \bar{2})\eta(\bar{2})). \quad (4.42)$$

This way derivatives are readily available, e.g. the first derivative

$$\frac{\delta \det(\Delta)}{\delta \Delta(2, 1)} = \det(\Delta) \Delta^{-1}(1, 2) = \det(\Delta) M(1, 2), \quad (4.43)$$

higher order derivatives for n -particle Green’s functions are straightforward [11]. The rest of the factors in eq. (4.41) is simple the Monte Carlo weight W_{MC} which appears in the calculation for the partition function \mathcal{Z}_{imp} . Therefore, the Green’s function is sampled as

$$\mathcal{G}(1, 2) = -\frac{1}{\mathcal{Z}_{\text{imp}}} \sum_k \int d\zeta_k W_{\text{MC}}^{\zeta_k} M(1, 2) =: -\mathbb{E}(M(1, 2)), \quad (4.44)$$

where we introduce the symbol \mathbb{E} for the Monte Carlo average. While sampling the partition function, we remove the hybridization line connecting a pair of operators for a given configuration to obtain a Green’s function sample. To save the Green’s function in imaginary time, it has to be binned in time. Alternatively, it can be Fourier transformed to Matsubara frequencies using a nonuniform fast Fourier transform (NUFFT) to avoid the binning error, see [87, 98]. In practice, the binning error of Green’s functions depending only on one time difference is not problematic. A sufficient fine time-mesh can be chosen to keep it small; the error is dominated by the stochastic Monte Carlo error.

The static quantity occupation $\hat{n}_\sigma = \hat{d}_\sigma^\dagger \hat{d}_\sigma$ and double occupations $\hat{n}_\uparrow \hat{n}_\downarrow$ can be accurately measured in the segment picture. They commute with the local Hamiltonian $[\hat{n}_\sigma, \hat{H}_{\text{loc}}]$ and can be directly evaluated from the lengths of the segments

$$\langle \hat{n}_\sigma \rangle = \mathbb{E}(L_\sigma) \quad \langle \hat{n}_\uparrow \hat{n}_\downarrow \rangle = \mathbb{E}(O_{\uparrow\downarrow}). \quad (4.45)$$

Likewise, the two particle Green’s function

$$\mathcal{F}_\sigma(\tau - \tau') = \left\langle d_{-\sigma}^+(\tau) d_{-\sigma}(\tau) d_\sigma(\tau) d_\sigma^+(\tau') \right\rangle_S \quad (4.46)$$

which is needed for the improved estimate of the self-energy $\Sigma_\sigma(i\omega_n) = UF_\sigma(i\omega_n)/G_\sigma(i\omega_n)$, can be sampled just as the Green’s function $G_\sigma(\tau)$ of spin σ with hardly any additional effort. It is enough to check whether the segment of the opposite spin is occupied $[d_{-\sigma}^+(\tau) d_{-\sigma}(\tau)]$.

General two particle Green's functions can be calculated analogously as the second derivative. However, to sample the Green's function this way requires suitable hybridization lines to appear in the expansion of the partition function \mathcal{Z}_{imp} . The partition function sampling fails, e.g., in the atomic case $\Delta = 0$. The number of Green's function samples strongly depends on the expansion order. In general this technique fails to sample off-diagonal observables like the spin-flip susceptibility

$$\chi^{+-}(\tau - \tau') = \left\langle d_{\uparrow}^{+}(\tau) d_{\downarrow}(\tau) d_{\downarrow}^{+}(\tau') d_{\uparrow}(\tau') \right\rangle_S. \quad (4.47)$$

In this case, samples would only be obtained for configurations with segments where operators of opposite spin coincide in time. Statistically, such configurations appear almost never.

Worm sampling. The aforementioned problems can be amended using worm sampling [99]; we give a short summary of the algorithm as presented in [87, 99]. The worm algorithm extends the configuration space by not only expanding the partition function, but also the Green's function. We denote the corresponding parts of the extended configuration space as partition function space and Green's function space. Green's function configurations are generated by inserting a *worm*, that is the operators of the Green's function without attached hybridization lines. We define the phase-space volume in the n -particle Green's function space

$$\mathcal{Z}_{G^{(n)}} = G^{(n)}(\bar{1}, \dots, \bar{n}, \bar{1}', \dots, \bar{n}'), \quad (4.48)$$

where $G^{(n)}(1, \dots, n, 1', \dots, n') = -\langle d(1) \dots d(n) d^{+}(1') \dots d^{+}(n') \rangle_S$ denotes the n -particle Green's function, and we switch back to the multi-index notation $1 = (\sigma, \tau)$. The Green's function phase-space expands analogous to eq. (4.15)

$$\begin{aligned} \mathcal{Z}_{G^{(n)}} / \frac{\mathcal{Z}_{\text{bath}} \mathcal{Z}_{\text{loc}}}{\mathcal{Z}_{\text{imp}}} &= - \sum_k \frac{(-1)^k}{(k!)^2} \left\langle \underbrace{d(\bar{1}^*) \dots d(\bar{n}^*) d^{+}(\bar{1}'^*) \dots d^{+}(\bar{n}'^*)}_{\text{worm}} d^{+}(\bar{1}) d(\bar{1}') \dots d^{+}(\bar{k}) d(\bar{k}') \right\rangle_{S_{\text{loc}}} \det \mathbf{\Delta}^k \\ &= - \sum_k \int d\gamma_k \frac{1}{(k!)^2} W_{\text{loc}}^{\gamma_k} \det \mathbf{\Delta}^{\gamma_k}, \end{aligned} \quad (4.49)$$

where the starred numbers indicate the worm Grassmann fields without hybridization lines. The Green's function configuration is a tuple

$$\begin{aligned} \gamma_k &= ([\sigma_1^* \tau_1^*, \sigma_{1'}^* \tau_{1'}^*], \dots, [\sigma_n^* \tau_n^*, \sigma_{n'}^* \tau_{n'}^*], [\sigma_1 \tau_1 \sigma_{1'} \tau_{1'}], \dots, [\sigma_n \tau_n \sigma_{n'} \tau_{n'}]) \\ &= ([\sigma_1^* \tau_1^*, \sigma_{1'}^* \tau_{1'}^*], \dots, [\sigma_n^* \tau_n^*, \sigma_{n'}^* \tau_{n'}^*]) \oplus \zeta_k, \end{aligned} \quad (4.50)$$

it consists of the worm and a partition function configuration. The determinant $\det \mathbf{\Delta}^{\gamma_k}$ is the same as for the corresponding partition function configuration ζ_k with the worm removed. A combined 'partition function' is introduced

$$W = \mathcal{Z} + \eta^{(n)} \mathcal{Z}_{G^{(n)}}, \quad (4.51)$$

where $\eta^{(n)}$ takes the role of a weight factor to balance the time spent in partition function space and Green's function space. To change a partition function configuration ζ_k into a Green's function configuration γ_k a worm has to be inserted; the proposal probability is analogous to the segment insertion

$$P_{\zeta_k \rightarrow \gamma_k} = \frac{(\mathrm{d}\tau^*)^{2n}}{\beta^{2n}}, \quad (4.52)$$

as for an n -particle Green's function $2n$ operators have to be inserted. Note that the configuration γ_k contains $2(k+n)$ operators, $2k$ connected by hybridization lines and the worm of $2n$ free operators. The proposal probability for the removal of the worm is simply

$$P_{\gamma_k \rightarrow \zeta_k} = 1. \quad (4.53)$$

The probabilities of Green's function configurations γ_k are scaled by the weight factor $\eta^{(n)}$ and can be read from the expansion of the Green's function phase-space volume eq. (4.49)

$$p(\gamma_k) \propto \eta^{(n)} (\mathrm{d}\tau^*)^{2n} \mathrm{d}\tau_1 \mathrm{d}\tau_{1'} \dots \mathrm{d}\tau_k \mathrm{d}\tau_{k'} \frac{1}{(k!)^2} W_{\mathrm{loc}}^{\gamma_k} \det \Delta^{\gamma_k}. \quad (4.54)$$

Thus, the acceptance ratio according to the Metropolis choice eq. (4.20) for an insertion of a worm is

$$\begin{aligned} A_{\zeta_k \rightarrow \gamma_k} &= \min \left(1, \frac{p(\gamma_k) P_{\gamma_k \rightarrow \zeta_k}}{p(\zeta_k) P_{\zeta_k \rightarrow \gamma_k}} \right) = \min \left(1, \frac{\eta^{(n)} (\mathrm{d}\tau^*)^n W_{\mathrm{loc}}^{\gamma_k} \beta^{2n}}{W_{\mathrm{loc}}^{\zeta_k} (\mathrm{d}\tau^*)^{2n}} \right), \\ &= \min \left(1, \eta^{(n)} \frac{W_{\mathrm{loc}}^{\gamma_k}}{W_{\mathrm{loc}}^{\zeta_k}} \beta^{2n} \right), \end{aligned} \quad (4.55)$$

where $p(\zeta_k)$ is given in eq. (4.24). The contribution by the hybridization function cancels as the worm contains no hybridization lines. Analogously, the acceptance ratio for a removal of a worm is

$$A_{\gamma_k \rightarrow \zeta_k} = \min \left(1, \frac{p(\zeta_k) P_{\zeta_k \rightarrow \gamma_k}}{p(\gamma_k) P_{\gamma_k \rightarrow \zeta_k}} \right) = \min \left(1, \frac{1}{\eta^{(n)}} \frac{W_{\mathrm{loc}}^{\zeta_k}}{W_{\mathrm{loc}}^{\gamma_k}} \frac{1}{\beta^{2n}} \right). \quad (4.56)$$

The insertion and removal updates are not enough to satisfy ergodicity, as shown by the example in fig. 4.4. Removing the worm yields an invalid configuration, therefore such a configuration can never be generated from a partition function configuration by a worm insertion. We further need to define (anti-) segment insertions $\gamma_k \rightarrow \gamma_{k+1}$ and removals $\gamma_{k+1} \rightarrow \gamma_k$ in the Green's function space. Their probabilities are analogous to the corresponding updates in partition function space. To obtain reasonable autocorrelation times an additional updated, the worm replacement update, is necessary [99]. The worm replacement $\gamma_k \rightarrow \gamma'_k$ exchanges a free worm operator with an operator connected by hybridization lines. This update only modifies hybridization lines, therefore the acceptance ratio of the worm replacement update depends only on the determinant ratio of the hybridization function

$$A_{\gamma_k \rightarrow \gamma'_k} = \min \left(1, \frac{\det \Delta^{\gamma'_k}}{\det \Delta^{\gamma_k}} \right). \quad (4.57)$$

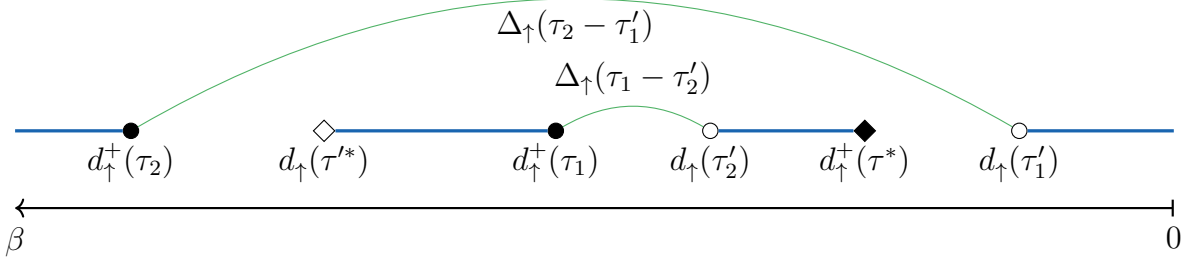


Figure 4.4.: Example of a segment for the $\sigma = \uparrow$ channel of order $k_\uparrow = 3$ with a worm of two $\sigma = \uparrow$ operators, e.g. $G_\uparrow(\tau^* - \tau'^*)$. Worm operators are indicated by the diamonds, the green edges show hybridization lines.

The Green's function $G^{(n)}$ can readily be measured in Green's function space; only the normalization has to be taken care of, as the Monte Carlo measurement normalizes to the phase-space volume $\mathcal{Z}_{G^{(n)}}$ and not the physical partition function \mathcal{Z} . This is amended by rescaling the Green's function by the factor $N_{G^{(n)}}/N_{\mathcal{Z}}\eta^{(n)}$, where $N_{G^{(n)}}$ are the steps taken in Green's function space and $N_{\mathcal{Z}}$ the steps taken in partition function space [99].

4.1.5. Negative sign and error estimate

So far, we always assumed the weights to be positive, such that they can be interpreted as probabilities for the Monte Carlo sampling. For fermions, this is not necessarily the case, as minus signs are generated by exchanging operators. To use Monte Carlo, we have to consider the absolute of the weights instead. We define the average sign, where the average \mathbb{E}' is calculated from the absolute weights:

$$\mathbb{E}'(\text{sign}) = \frac{\sum_k \int d\zeta_k |W_{\text{MC}}^{\zeta_k}| \text{sign}(W_{\text{MC}}^{\zeta_k})}{\sum_k \int d\zeta_k |W_{\text{MC}}^{\zeta_k}|}. \quad (4.58)$$

We expand the estimate of an observable by the sum-integral over the absolute weight:

$$\begin{aligned} \langle \hat{\mathcal{O}} \rangle &\simeq \mathbb{E}(\hat{\mathcal{O}}) = \frac{\sum_k \int d\zeta_k W_{\text{MC}}^{\zeta_k} \langle \hat{\mathcal{O}} \rangle_{\zeta_k}}{\sum_k \int d\zeta_k W_{\text{MC}}^{\zeta_k}} \\ &= \frac{\sum_k \int d\zeta_k |W_{\text{MC}}^{\zeta_k}| \text{sign}(W_{\text{MC}}^{\zeta_k}) \langle \hat{\mathcal{O}} \rangle_{\zeta_k}}{\sum_k \int d\zeta_k |W_{\text{MC}}^{\zeta_k}|} \frac{\sum_k \int d\zeta_k |W_{\text{MC}}^{\zeta_k}|}{\sum_k \int d\zeta_k W_{\text{MC}}^{\zeta_k}} = \mathbb{E}'(\hat{\mathcal{O}}) / \mathbb{E}'(\text{sign}), \end{aligned} \quad (4.59)$$

that is we sample according to the absolute weight and divide the result by the average sign. For small values of the average sign, this estimate becomes very inaccurate; a sum of almost compensating terms is sampled and divided by a tiny number. This is known as the sign problem [100].

As Monte Carlo is a stochastic estimate, it is important to provide an error estimate. Sampling the variance of observables is prone to underestimating the error, as we employ a Markov chain: our samples are not independent but correlated. Standard algorithms,

so-called resampling techniques, like Jackknife and bootstrap exist to give reliable error estimates [101]. A simple technique is to run many independent Monte Carlo simulations averaging over the runs. The error can then be estimated from the variance of the different runs. Care has to be taken in seeding the pseudo random number generators to ensure that the runs are indeed independent. Note that it is important that the Markov chain has reached stationarity to obtain reliable results. For this purpose, it is common to perform a large amount of Monte Carlo iterations before starting to measure, this is called burn-in or warm-up.

4.2. Analytic continuation

The CT-QMC algorithm yields Green's function in imaginary time or Matsubara frequencies. Typically, we are interested in Green's functions on the real-frequency axis. Analytic continuation is a technique to recover these results, it is however an ill-conditioned procedure to recover the Green's function from limited information on the imaginary axis.

By considering the Lehmann representation of the commutator Green's function $G(z)$ and the Matsubara Green's function $G^{(n)}$ and comparing them, we find

$$G(i\omega_n) = G^{(n)} \quad \forall n \in \mathbb{Z} \quad (4.60)$$

for fermionic Green's function with the Matsubara frequencies $i\omega_n = (2n + 1)\pi/\beta$ and

$$G(i\nu_n) = G^{(n)} \quad \forall n \in \mathbb{Z}/\{0\} \quad (4.61)$$

for bosonic Green's functions with the Matsubara frequencies $i\nu_n = 2n\pi/\beta$. The Padé analytic continuation interpolates $G^{(n)}$ by a rational polynomial, the Padé approximant [102–104]. It is discussed in detail in sections 4.2.1 and 4.2.2. Recently Fei et al. [105] proposed the use of Nevanlinna functions to interpolate $G^{(n)}$, to ensure non-negative spectra.

Alternatively, the analytic continuation can be performed by inverting the integral equation obtained from Cauchy's integral formula. For imaginary times $\tau \in (0, \beta)$, the Green's function can be expressed as the contour integral

$$\mathcal{G}(\tau) = \frac{1}{\beta} \sum_{n=-\infty}^{\infty} G^{(n)} e^{-i\omega_n \tau} = \frac{1}{2\pi i} \oint_{\mathcal{L}} dz G(z) [1 - f(z)] e^{-z\tau} \quad (4.62)$$

for fermionic Green's functions with the Fermi function $f(z) = 1/[\exp(\beta z) - 1]$ which has poles at the Matsubara frequencies $i\omega_n$, cf. eq. (A.37), and

$$\mathcal{G}(\tau) = \frac{1}{\beta} \sum_{n=-\infty}^{\infty} G^{(n)} e^{-i\nu_n \tau} = \frac{1}{\beta} G^{(0)} + \frac{1}{2\pi i} \oint_{\mathcal{L}} dz G(z) [1 - b(z)] e^{-z\tau} \quad (4.63)$$

for bosonic Green's functions with the Bose function $b(z) = 1/[\exp(\beta z) + 1]$. In the following, we consider the fermionic Green's function, the bosonic Green's function can be treated analogously. Choosing the contour \mathcal{L} parallel to the real axis

$$(4.64)$$

yields the integral over the real frequency axis

$$\mathcal{G}(\tau) = \int_{-\infty}^{\infty} d\omega \left([1 - f(\omega)] e^{-\omega\tau} \right) \frac{G(\omega + i0^+) - G(\omega - i0^+)}{2\pi i} =: - \int_{-\infty}^{\infty} d\omega K(\tau, \omega) A(\omega) \quad (4.65)$$

with $A(\omega) = [G(\omega - i0^+) - G(\omega + i0^+)]/2\pi i$. The kernel $K(\tau, \omega)$ exponentially decreases in ω , therefore the spectrum $A(\omega)$ at large frequencies contributes little to the imaginary time Green's function $\mathcal{G}(\tau)$. Similar integral equations can be formulated in terms of the Matsubara Green's function:

$$\begin{aligned} G(i\omega_n) &= \frac{1}{2\pi i} \oint_{\mathcal{L}} dz \frac{G(z)}{z - i\omega_n} = - \int_{-\infty}^{\infty} d\omega \frac{1}{\omega - i\omega_n} A(\omega) \\ &=: - \int_{-\infty}^{\infty} d\omega K(i\omega_n, \omega) A(\omega); \end{aligned} \quad (4.66)$$

for the second equality the contour \mathcal{L} is chosen along the real axis analogous to eq. (4.64). The kernel $K(i\omega_n, \omega)$ decays algebraically in ω . In the following, we outline three common approaches to solve integral equations like eqs. (4.62), (4.63) and (4.66) for the spectral function $A(\omega)$: the maximum entropy (MaxEnt) method, the stochastic optimization method (SOM), and the sparse modeling (SpM) approach.

Maximum entropy method. The MaxEnt method [106, 107] (sometimes also abbreviated MEM) employs Bayesian methods to tackle the inversion of the integral equation. A pedagogical introduction is given by Jarrell [108] which also includes a step-by-step instruction; we summarize the essence of the algorithm. The expectation values of the Green's function sampled by QMC are denoted

$$\mathbb{E}(\mathcal{G}_l) = \frac{1}{N} \sum_{j=1}^N \mathcal{G}_l^j, \quad (4.67)$$

where j enumerates the samples or bins; here \mathcal{G}_l denotes either the Green's function evaluated at time point $\mathcal{G}_l = \mathcal{G}(\tau_l)$ or a frequency point $\mathcal{G}_l = G(i\omega_l)$. The 'exact value' $\mathcal{G}_l[A]$ for a given spectrum A is obtained from one of the integral equations eqs. (4.62), (4.63) and (4.66). The MaxEnt method assumes the conditional probability for the sampled Green's function $\mathbb{E}(\mathcal{G}_l)$ for a given the spectrum A to be Gaussian distributed

$$P(\mathbb{E}(\mathcal{G})|A) \propto \exp(-\chi^2/2) \quad \text{with} \quad \chi^2 = \sum_l \frac{[\mathcal{G}_l[A] - \mathbb{E}(\mathcal{G}_l)]^2}{\sigma_l^2}, \quad (4.68)$$

where σ_l is the variance, which is chosen as the square root of the diagonal elements of the estimate of the covariance matrix

$$C_{ll'} = \frac{1}{N-1} \sum_{j=1}^N [\mathcal{G}_l^j - \mathbb{E}(\mathcal{G}_l)][\mathcal{G}_{l'}^j - \mathbb{E}(\mathcal{G}_{l'})] = \frac{N}{N-1} [\mathbb{E}(\mathcal{G}_l \mathcal{G}_{l'}) - \mathbb{E}(\mathcal{G}_l) \mathbb{E}(\mathcal{G}_{l'})]. \quad (4.69)$$

The conditional probability $P(\mathbb{E}(\mathcal{G}_l)|A)$ is referred to as likelihood function. Using the definition of conditional probability

$$P(A|B) = \frac{P(A \cap B)}{P(B)}, \quad (4.70)$$

we can reverse eq. (4.68) to get the conditional probability of the spectral function given the measured data $\mathbb{E}(\mathcal{G}_l)$:

$$P(A|\mathbb{E}(\mathcal{G})) = \frac{P(\mathbb{E}(\mathcal{G})|A)P(A)}{P(\mathbb{E}(\mathcal{G}))}, \quad (4.71)$$

this equation is known as Bayes' theorem. The sampled QMC data $\mathbb{E}(\mathcal{G})$ is fixed, therefore its probability is not relevant; we choose $P(\mathbb{E}(\mathcal{G})) = 1$. The probability of a spectrum $P(A)$ is assumed to be the exponential of an entropy term

$$P(A|\alpha, m) \propto \exp(\alpha S[A, m]) \quad (4.72)$$

$$S[A, m] = \int d\omega \left[A(\omega) - m(\omega) - A(\omega) \ln \left(\frac{A(\omega)}{m(\omega)} \right) \right], \quad (4.73)$$

where $m > 0$ is a default model and α is a numerical parameter weighting the entropy term. The probability $P(A)$ is referred to as prior. The factor α and the default model m still have to be determined, this is not discussed here; we refer to ref. [108] and the references mentioned therein.

In practice, there are a few issues to be taken into consideration. The assumption of a Gaussian distribution is an approximation. The error at adjacent or close time points τ_l is correlated. Thus, if the off-diagonal elements of the auto-covariance matrix $C_{ll'}$ are relevant,

$$\chi^2 = \sum_{ll'} [\mathcal{G}_l - \mathbb{E}(\mathcal{G}_l)] (C^{-1})_{ll'} [\mathcal{G}_{l'} - \mathbb{E}(\mathcal{G}_{l'})] \quad (4.74)$$

should be used. This equation can be evaluated using the singular value decomposition (SVD); we write the covariance matrix as

$$\mathbf{C} = \mathbf{X} \mathbf{X}^\dagger \quad \text{with} \quad X_{lj} = \frac{\mathcal{G}_l^j - \mathbb{E}(\mathcal{G}_l)}{\sqrt{N-1}}, \quad (4.75)$$

and use the SVD $\mathbf{X} = \mathbf{U} \mathbf{\Sigma} \mathbf{V}^\dagger$. We define $x_l = \mathcal{G}_l[A] - \mathbb{E}(\mathcal{G}_l)$, and write χ^2 in the form

$$\chi^2 = \mathbf{x}^\dagger (\mathbf{X} \mathbf{X}^\dagger)^{-1} \mathbf{x} = \mathbf{x}^\dagger \mathbf{U} \mathbf{\Sigma}^{-2} \mathbf{U}^\dagger \mathbf{x} = \sum_j \frac{1}{\sigma_j^2} \left| \sum_l U_{jl}^* [\mathcal{G}_l[A] - \mathbb{E}(\mathcal{G}_l)] \right|^2, \quad (4.76)$$

the last equation writes the matrix and vector products out as the corresponding sums. Furthermore, a Gaussian distribution is not appropriate for the imaginary time Green's function $\mathcal{G}(\tau)$ as $\mathcal{G} \leq 0$ for $\tau \in (0, \beta)$; this is mostly relevant for small absolute values of \mathcal{G} as is the case close to $\tau = \beta/2$ for gapped spectral functions. Various implementations of MaxEnt are available, one example is the code [C4].

Stochastic optimization method. The main advantage of SOM [109] is to overcome the dependence on a default model m that is present in MaxEnt. We summarize the description given by Mishchenko [110]. The basic idea is to average over numerous possible spectral functions

$$A = \int dA' P(A' | \mathbb{E}(\mathcal{G})) A'. \quad (4.77)$$

In SOM, the trail spectral functions A' are parametrized as a sum of boxes, i.e., piecewise constant functions with finite support. The spectral functions are written

$$A'(\omega) = \sum_{t=1}^K \eta_{h_t, \omega_t, c_t}(\omega) = \sum_{t=1}^K h_t 1_{[-\omega_t/2, +\omega_t/2]}(\omega - c_t), \quad (4.78)$$

where h_t is the height, ω_t the width, c_t the center of the boxes, and $1_{[-\omega_t/2, +\omega_t/2]}(\omega)$ the indicator function which equals 1 for $\omega \in [-\omega_t/2, +\omega_t/2]$ and 0 else. The simple form of the spectral function A' allows for an efficient calculation of the Green's function

$$\mathcal{G}_l[A'] = \int d\omega K(l, \omega) A'(\omega). \quad (4.79)$$

The quality of a particular spectral function A' is assessed by the deviation measure

$$D[A'] = \sum_l \left| \frac{\mathcal{G}_l - \mathbb{E}(\mathcal{G}_l)}{S_l} \right|, \quad (4.80)$$

where S_l can be chosen as variance $S_l = \sigma_l$ to respect error bars of the data $\mathbb{E}(\mathcal{G}_l)$, or $S_l = |\mathbb{E}(\mathcal{G}_l)|^d$ with $0 \leq d \leq 1$ to weight data points of different magnitude equally for $d \rightarrow 1$ [110]. In essence, SOM generates different spectral functions A'_j parametrized as eq. (4.78) using a Monte Carlo procedure. Good enough spectra A'_j , that is spectra with $D[A'_j]$ below a certain threshold δ , are kept. The resulting spectrum is the average

$$A(\omega) = \frac{\sum_j \Theta(\delta - D[A'_j]) A'_j(\omega)}{\sum_j \Theta(\delta - D[A'_j])}, \quad (4.81)$$

where Θ is the Heaviside step function. The procedure is computationally demanding, but efficient GPU implementations exist, e.g. [C5].

Sparse modeling approach. The SpM approach [111] starts from the discretization of one of the integral equations eqs. (4.62), (4.63) and (4.66). Applying a quadrature rule, we can rewrite the integral equation as matrix equation

$$\mathcal{G} = -\mathbf{K} \mathbf{A} \quad \text{with elements} \quad \mathcal{G}_l = - \sum_j K(l, \omega_j) A(\omega_j); \quad (4.82)$$

we assume possible integration weights to be incorporated in $A(\omega_j)$. The goal is to minimize the square error

$$\chi^2(\mathbf{A}) = \frac{1}{2} \|\mathcal{G} - \mathbf{K} \mathbf{A}\|_2^2, \quad (4.83)$$

the result can be additionally constrained to ensure non-negativity and normalization

$$(\mathbf{A})_j \geq 0, \quad \sum_j (\mathbf{A})_j = 1. \quad (4.84)$$

The ill-condition of the matrix equation eq. (4.82) is revealed by the SVD of the kernel matrix \mathbf{K}

$$\mathbf{K} = \mathbf{U}\mathbf{\Sigma}\mathbf{V}^\dagger, \quad (4.85)$$

the singular values decay exponentially. A common approach to invert such matrix equations is to truncate small singular values, as they enhance errors. The SpM approach suggest using an L_1 regularization instead. This is known as *least absolute shrinkage and selection operator (LASSO)*; it favors coefficients to be exactly zero therefore reducing overfitting [112]. The regularization is performed in the SVD basis of the kernel matrix

$$\mathbf{A}' = \mathbf{V}^\dagger \mathbf{A} \quad \mathbf{G}' = \mathbf{U}^\dagger \mathbf{G}; \quad (4.86)$$

the regularized cost function reads

$$F(\mathbf{A}') = \frac{1}{2} \|\mathbf{G}' - \mathbf{\Sigma}\mathbf{A}'\|_2^2 + \lambda \|\mathbf{A}'\|_1. \quad (4.87)$$

This is a quadratic programming problem [112], for the selection of the optimal regularization parameter λ and concrete implementation we refer to Otsuki et al. [111], an implementation is available [C3]. Motoyama et al. [113] recently combined the SpM approach with the Padé approximation, to improve the accuracy of the robust SpM around the Fermi level.

4.2.1. Padé approximants

We focus on probably the simplest method: the Padé approximants. An advantage of Padé is that its simplicity allows for a large amount of insight. Furthermore, it provides an analytic (or more precisely meromorphic) function, which can be evaluated anywhere in the upper complex half-plane.

The Padé approximant is a rational polynomial $p(z)/q(z)$, with polynomials p of degree N and q of degree M , approximating a function $f(z)$. The Padé approximant writes

$$[N/M](z) = \frac{p(z)}{q(z)} \approx f(z). \quad (4.88)$$

For Green's functions with the asymptote $G(z) \sim 1/z$ for $|z| \rightarrow \infty$, an approximant $[N/N+1](z)$ with $M = N+1$ is appropriate, for self-energies the approximant $[N/N](z)$ with $M = N$ can be used. Thiele's reciprocal difference method [102, 104] provides a recursive algorithm to calculate the polynomials of these particular degrees.

Thiele's reciprocal difference. The reciprocal difference method calculates an approximant of degrees $[\frac{L}{2}/\frac{L+1}{2}]$ interpolating the function $G(z)$ exactly at L sample points z_n :

$$\left[\frac{L}{2} / \frac{L+1}{2} \right] (z_n) = G(z_n); \quad (4.89)$$

the division is an integer division. Such a rational fit of given function values is called a *multipoint* or *N-point* Padé approximant. From the samples $G(z_n)$ we calculate the coefficients

$$a_n = g_n(z_n) \quad \text{with} \quad g_n(z) = \frac{g_{n-1}(z_{n-1}) - g_{n-1}(z)}{(z - z_{n-1})g_{n-1}(z)} \quad g_0(z) = G(z) \quad (4.90)$$

The fit $f_n(z)$ for n points can be recursively calculated

$$f_n(z) = \frac{A_n(z)}{B_n(z)} \quad (4.91)$$

$$\frac{A_{n+1}(z)}{B_{n+1}(z)} = \frac{A_n + (z - z_n)a_{n+1}A_{n-1}}{B_n + (z - z_n)a_{n+1}B_{n-1}} \quad (4.92)$$

with the starting values

$$A_{-1} = 0, \quad A_0 = a_0, \quad B_{-1} = 1, \quad B_0 = 1. \quad (4.93)$$

The function f_{2n+1} using an odd number of sample points is of degree $N = n$, $M = n + 1$; the function f_{2n} using an even number of sample points is of degree $N = n$, $M = n$. This algorithm can be used to evaluate the analytic continuation at any point z , or to directly calculate the rational polynomial $p(z)/q(z)$.

Two issues of this approach for analytic continuation of Monte Carlo data are: (i) the number of poles is fixed by the number of sample points taken into account; (ii) it is an exact interpolation, the Monte Carlo data, on the other hand, is subject to noise. In practice these problems are not as large as they might seem, as the spurious poles appear along the imaginary axis to compensate noise. Such poles have little impact on the real axis.

4.2.2. Pole-based Padé approximants

Recently, a Padé algorithm based on the direct calculation of the poles was developed by Ito and Nakatsukasa [114]. This algorithm is formulated in a least-squares sense in contrast to the interpolation used in Thiele's algorithm. First, the optimal number of poles is determined; in a second step, their optimal position is determined taking all data points into consideration. We give a summary of this algorithm applied to the physical problem of continuing Green's functions.

Matrix formulation. As before, we look for a rational polynomial approximating our function

$$f(z) \approx p(z)/q(z), \quad (4.94)$$

where $f(z)$ is known only at L sample points z_l , and polynomials $p(z)$ and $q(z)$ with degrees N and M respectively. The degree M is the number of poles. For physical Green's functions we know the relation between the degrees N and M , for Green's functions with the asymptote $G(z) \sim 1/z$ as $|z| \rightarrow \infty$, we require $M = N + 1$. We linearize the rational polynomial approximation

$$f(z)q(z) \approx p(z). \quad (4.95)$$

The $L \times (M + 1)$ Vandermonde matrix \mathbf{V}_q for the polynomial $q(z)$ of degree M reads $(\mathbf{V}_q)_{lm} = z_l^m$, accordingly \mathbf{V}_p denotes the $L \times (N + 1)$ Vandermonde matrix for the polynomial $p(z)$ of degree N . In terms of these Vandermonde matrices, we can express the equation at sample points z_l as the matrix equation

$$\mathbf{F}\mathbf{V}_q\mathbf{q} = \mathbf{V}_p\mathbf{p} \quad (4.96)$$

where the matrix \mathbf{F} is the diagonal matrix containing the function values $(\mathbf{F})_{ll} = f(z_l)\delta_{ll}$, and \mathbf{q} and \mathbf{p} are the vectors of polynomial coefficients. This equation shows the reason why naive matrix-based algorithms are unstable: The Vandermonde matrices for equidistant sample points, the Matsubara frequencies $i\omega_n$, are ill-conditioned [95]. We rewrite the linearized eq. (4.96) as the homogeneous matrix equation

$$0 = \begin{pmatrix} \mathbf{F}\mathbf{V}_q & \mathbf{V}_p \end{pmatrix} \begin{pmatrix} \mathbf{q} & -\mathbf{p} \end{pmatrix}^\top =: \mathbf{C}\mathbf{x}. \quad (4.97)$$

Theoretically, this equation gives us a clear recipe: We search the right-singular vectors corresponding to vanishing singular values of \mathbf{C} . These vectors span the null space of \mathbf{C} . To obtain a unique solution $\mathbf{x}^\top = (\mathbf{q} \ -\mathbf{p})$, we determine the number of poles M such that the numerical null dimension of the matrix \mathbf{C} is $\dim(\text{null}(\mathbf{C})) = 1$. In practice, the huge condition number for Vandermonde matrices on an equidistant grid prohibits naive numerical treatment. For M poles and L Matsubara frequencies, the ratio between the largest and the smallest element of the Vandermonde matrix $\mathbf{V}_q^{L \times (M+1)}$ is $(i\omega_L/i\omega_0)^M = (2L + 1)^M$; for example for $M = 100$, $L = 500$ they span 300 orders of magnitude. The top left of fig. 4.5 shows the singular values, normalized to the biggest singular value σ_0 for $\beta = 100$, $M = 100$, $L = 500$. The singular values span 150 orders of magnitude, the smallest singular value is 77 orders of magnitude smaller than the second-smallest. We recognize this as an intrinsic problem of analytic continuation: The Matsubara frequency mesh is not suitable to obtain information on the real axis. A preconditioning of the matrix \mathbf{C} is necessary.

Conditioning. We define the diagonal matrix \mathbf{D} , with the inverse row norm of the concatenated Vandermonde matrices as diagonal elements

$$\mathbf{D} := \text{diag} \left(1 / \left\| \begin{pmatrix} \mathbf{V}_q^{L \times (M+1)} \\ \mathbf{V}_p^{L \times (N+1)} \end{pmatrix}_{[l,:]} \right\| \right) \quad (4.98)$$

and scale eq. (4.97) by left-multiplying \mathbf{D} to get row norms of the same magnitude

$$0 = \begin{pmatrix} \mathbf{D}\mathbf{F}\mathbf{V}_q & \mathbf{D}\mathbf{V}_p \end{pmatrix} \begin{pmatrix} \mathbf{q} & -\mathbf{p} \end{pmatrix}^\top. \quad (4.99)$$

Figure 4.5(a) shows how this scaling affects the singular values. The condition number of \mathbf{V}_q significantly improves, however it is still quite large with a magnitude of order 25.

Furthermore, we choose a suitable polynomial basis instead of monomials. Instead of searching for suitable orthogonal polynomials, we independently transform the basis of $q(z)$ and $p(z)$, using the QR-decomposition:

$$\mathbf{D}\mathbf{F}\mathbf{V}_q = \mathbf{Q}_{Df_q}\mathbf{R}_{Df_q}, \quad \mathbf{D}\mathbf{V}_p = \mathbf{Q}_{Dp}\mathbf{R}_{Dp}. \quad (4.100)$$

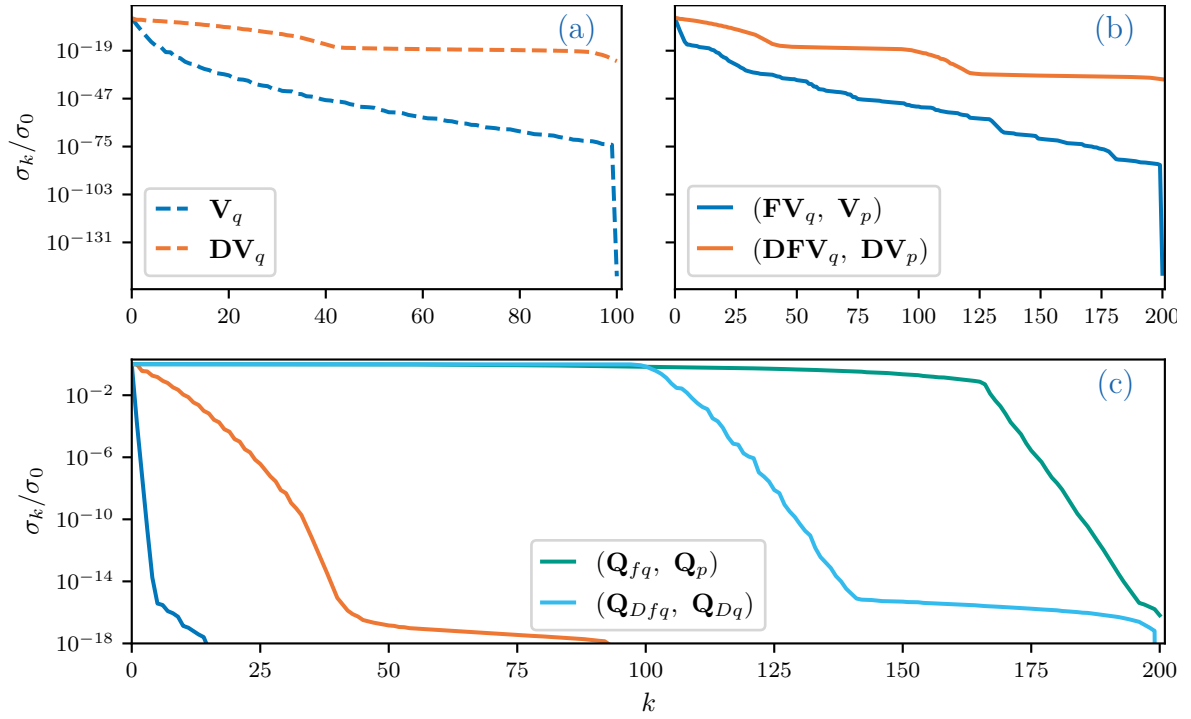


Figure 4.5.: Singular values of the Vandermonde matrix \mathbf{V}_q (top left) and the matrix $\mathbf{C} = (\mathbf{F}\mathbf{V}_q, \mathbf{V}_p)$ for the Green's function of a half-filled Bethe lattice (top right and bottom). Roughly the first $k = 100$ singular values of $(\mathbf{Q}_{Dfq}, \mathbf{Q}_{Dq})$ are nearly constant; the smallest singular value (not shown) is 46 orders of magnitudes smaller than the second smallest.

This gives an optimal basis; the matrices \mathbf{Q} are unitary and thus optimally conditioned. In the new basis given by \mathbf{R}_{Dfq} and \mathbf{R}_{Dp} , the homogeneous equation reads

$$0 = \begin{pmatrix} \mathbf{Q}_{Dfq} & \mathbf{Q}_{Dp} \end{pmatrix} \begin{pmatrix} \mathbf{R}_{Dfq}\mathbf{q} & \mathbf{R}_{Dp}\mathbf{p} \end{pmatrix}^\top =: \tilde{\mathbf{C}}\tilde{\mathbf{x}}. \quad (4.101)$$

The optimal number of poles M can now be determined from the null-dimension of $\tilde{\mathbf{C}}$; we vary M until numerically the null-dimension equals one. Figure 4.5(c) shows the singular values of the conditioned matrix \mathbf{C} . For the scaled and transformed matrix, a plateau of roughly 100 singular values becomes visible, and there is a clear separation from the smallest singular value (not shown).

Calculating the poles. After finding the optimal number M of poles, we directly calculate these poles. The poles of $f(z)$ are the roots of the denominator polynomial $q(z)$. We factorize a pole ϵ_m from the polynomial $q(z)$ of degree M

$$q(z) = \theta(z)(z - \epsilon_m) \quad (4.102)$$

with the remainder polynomial $\theta(z)$ of degree $M - 1$. Substituting this into the linearized eq. (4.95) yields

$$zf(z)\theta(z) - p(z) = \epsilon_m f(z)\theta(z). \quad (4.103)$$

For the L sample points z_j , this yields the matrix equation

$$\mathbf{Z}\mathbf{F}\mathbf{V}_\theta\boldsymbol{\theta} - \mathbf{V}_p\mathbf{p} = \begin{pmatrix} \mathbf{Z}\mathbf{F}\mathbf{V}_\theta & \mathbf{V}_p \end{pmatrix} \begin{pmatrix} \boldsymbol{\theta} & -\mathbf{p} \end{pmatrix}^\top = \epsilon_m \mathbf{F}\mathbf{V}_\theta\boldsymbol{\theta}, \quad (4.104)$$

where \mathbf{Z} is the diagonal matrix of sample points $\mathbf{Z} = \text{diag}(z_l)$. This equation can be written as the generalized eigenvalue problem

$$\begin{pmatrix} \mathbf{Z}\mathbf{F}\mathbf{V}_\theta & \mathbf{V}_p \end{pmatrix} \begin{pmatrix} \boldsymbol{\theta} & -\mathbf{p} \end{pmatrix}^\top = \epsilon_m \begin{pmatrix} \mathbf{F}\mathbf{V}_\theta & \mathbf{0} \end{pmatrix} \begin{pmatrix} \boldsymbol{\theta} & -\mathbf{p} \end{pmatrix}^\top \quad (4.105)$$

by expanding the right-hand side with a zero-matrix. Ito and Nakatsukasa [114] also detail how to solve this equation.

In the following, we summarize the essence of this algorithm. We realize that eq. (4.105) is of dimension $M + (N + 1)$, thus it produces $N + 1$ spurious poles ϵ_m . These additional eigenvalues correspond to poles at infinity [114]. They can be removed by eliminating the polynomial $p(z)$, which is not related to the poles but the zeros, from the equation. The QR-decomposition of the Vandermonde matrix \mathbf{V}_p is

$$\mathbf{V}_p = \begin{pmatrix} \mathbf{Q}_p & \mathbf{V}_{p\perp} \end{pmatrix} \begin{pmatrix} \mathbf{R}_p & \mathbf{0} \end{pmatrix}^\top \quad \text{with } \mathbf{V}_{p\perp}^\dagger \mathbf{V}_p = \mathbf{0}, \quad (4.106)$$

$\mathbf{V}_{p\perp}$ is the orthogonal complement of \mathbf{V}_p [115]. Multiplying eq. (4.105) by $\begin{pmatrix} \mathbf{Q}_p & \mathbf{V}_{p\perp} \end{pmatrix}^\dagger$ from the left yields

$$\begin{pmatrix} \mathbf{Q}_p^\dagger \mathbf{Z}\mathbf{F}\mathbf{V}_\theta & \mathbf{R}_p \\ \mathbf{V}_{p\perp}^\dagger \mathbf{Z}\mathbf{F}\mathbf{V}_\theta & \mathbf{0} \end{pmatrix} \begin{pmatrix} \boldsymbol{\theta} & -\mathbf{p} \end{pmatrix}^\top = \epsilon_m \begin{pmatrix} \mathbf{Q}_p^\dagger \mathbf{F}\mathbf{V}_\theta & \mathbf{0} \\ \mathbf{V}_{p\perp}^\dagger \mathbf{F}\mathbf{V}_\theta & \mathbf{0} \end{pmatrix} \begin{pmatrix} \boldsymbol{\theta} & -\mathbf{p} \end{pmatrix}^\top. \quad (4.107)$$

The second line of this equation is the eigenvalue equation orthogonal to $p(z)$:

$$\mathbf{V}_{p\perp}^\dagger \mathbf{Z}\mathbf{F}\mathbf{V}_\theta\boldsymbol{\theta} = \epsilon_m \mathbf{V}_{p\perp}^\dagger \mathbf{F}\mathbf{V}_\theta\boldsymbol{\theta}. \quad (4.108)$$

Again, we transform the polynomial basis of $\theta(z)$ to $\tilde{\theta} = \mathbf{R}_{f\theta}\theta$ using the QR-decomposition $\mathbf{FV}_\theta = \mathbf{Q}_{f\theta}\mathbf{R}_{f\theta}$ to improve the condition:

$$\mathbf{V}_{p\perp}^\dagger \mathbf{ZQ}_{f\theta}\tilde{\theta} = \epsilon_m \mathbf{V}_{p\perp}^\dagger \mathbf{Q}_{f\theta}\tilde{\theta}. \quad (4.109)$$

This eigenvalue equation provides the M poles ϵ_m of $f(z)$.

Calculating the roots. In principle, the roots could be calculated just as the poles of $1/f(z) = q(z)/p(z)$. However, it is important to use the position of the poles to determine the roots. Knowing all M roots ϵ_m , we can represent the polynomial $q(z)$ by its factorized form

$$q(z) = \prod_{m=1}^M (z - \epsilon_m), \quad (4.110)$$

where we choose the constant prefactor to be one without loss of generality. The roots of $f(z)$ are the roots of the numerator polynomial $p(z)$. We factorize a root z_n from the polynomial $p(z)$ of degree N

$$p(z) = \pi(z)(z - z_n) \quad (4.111)$$

with the reminder polynomial $\pi(z)$ of degree $N - 1$. Substituting this into the linearized eq. (4.95) yields

$$f(z)q(z) - z\pi(z) = -z_n\pi(z). \quad (4.112)$$

For the L sample points z_j , this yields the matrix equation

$$\mathbf{FQ} - \mathbf{ZV}_\pi\pi = \begin{pmatrix} \mathbf{FQ} & \mathbf{ZV}_\pi \end{pmatrix} \begin{pmatrix} 1 & -\pi \end{pmatrix}^\top = -z_n \mathbf{V}_\pi\pi \quad (4.113)$$

where \mathbf{Q} is the $L \times 1$ matrix of the denominator polynomial values at the sample points $(\mathbf{Q})_{i0} = q(z_i)$. Again, we expand this equation to the generalized eigenvalue problem

$$\begin{pmatrix} \mathbf{FQ} & \mathbf{ZV}_\pi \end{pmatrix} \begin{pmatrix} 1 & -\pi \end{pmatrix}^\top = z_n \begin{pmatrix} 0 & \mathbf{V}_\pi \end{pmatrix} \begin{pmatrix} 1 & -\pi \end{pmatrix}^\top. \quad (4.114)$$

As previously, we project out the spurious eigenvalue, which, in this case, is associated with the denominator polynomial. We calculate the orthogonal complement of \mathbf{FQ} :

$$\mathbf{FQ} = \begin{pmatrix} \mathbf{Q}_{FQ} & (\mathbf{FQ})_\perp \end{pmatrix} \begin{pmatrix} R_{FQ} & \mathbf{0} \end{pmatrix}^\top \quad \text{with } (\mathbf{FQ})_\perp^\dagger \mathbf{FQ} = 0. \quad (4.115)$$

Multiplying eq. (4.114) by $\begin{pmatrix} \mathbf{Q}_{FQ} & (\mathbf{FQ})_\perp \end{pmatrix}^\dagger$ from the left yields

$$\begin{pmatrix} R_{FQ} & \mathbf{Q}_{FQ}^\dagger \mathbf{ZV}_\pi \end{pmatrix} \begin{pmatrix} 1 & -\pi \end{pmatrix}^\top = z_n \begin{pmatrix} 0 & \mathbf{Q}_{FQ}^\dagger \mathbf{V}_\pi \end{pmatrix} \begin{pmatrix} 1 & -\pi \end{pmatrix}^\top. \quad (4.116)$$

The second line of this equation is the eigenvalue equation for the roots

$$(\mathbf{FQ})_\perp^\dagger \mathbf{ZV}_\pi\pi = z_n (\mathbf{FQ})_\perp^\dagger \mathbf{V}_\pi\pi. \quad (4.117)$$

We transform the polynomial basis of $\pi(z)$ to $\tilde{\pi} = \mathbf{R}_\pi\pi$ using the QR-decomposition $\mathbf{V}_\pi = \mathbf{Q}_\pi\mathbf{R}_\pi$ to improve the condition:

$$(\mathbf{FQ})_\perp^\dagger \mathbf{ZQ}_\pi\tilde{\pi} = z_n (\mathbf{FQ})_\perp^\dagger \mathbf{Q}_\pi\tilde{\pi}. \quad (4.118)$$

This eigenvalue equation provides the N roots z_n of $f(z)$.

Padé approximant as rational polynomial. Having determined all poles ϵ_m and roots z_n , we write the Padé approximant as the rational polynomial

$$f(z) = \frac{p(z)}{q(z)} = \frac{c \prod_{n=1}^N (z - z_n)}{\prod_{m=1}^M (z - \epsilon_m)}. \quad (4.119)$$

What is left to determine is the constant factor c . It can be calculated as the mean of

$$c_l = f(z_l) \frac{\prod_{n=1}^N (z_l - z_n)}{\prod_{m=1}^M (z_l - \epsilon_m)} = f(z_l) \frac{\prod_{m=1}^M (z_l - \epsilon_m)}{\prod_{n=1}^N (z_l - z_n)}. \quad (4.120)$$

This constant is the high-frequency asymptote $f(z) \sim cz^{N-M}$ for $|z| \rightarrow \infty$, which is typically known exactly, e.g. $c = 1 = \langle \{\hat{c}, \hat{c}^\dagger\} \rangle$ for the diagonal one-particle Green's function.

Determining the residues. Physical Green's functions decay with large frequencies, thus they have more poles than roots $N < M$. Self-energies can have an additional constant and thus $N = M$; the constant is the high-frequency asymptote c in eq. (4.119). Therefore, we can write the rational polynomial as the sum over the residues

$$f(z) = c\delta_{NM} + \sum_{m=1}^M \frac{r_m}{z - \epsilon_m}, \quad (4.121)$$

where r_m is the residue of the simple pole ϵ_m . Knowing the poles ϵ_m , for $N < M$ eq. (4.121) yields the matrix equation at the sample points

$$\mathbf{f} = \mathbf{E}\mathbf{r} \quad (4.122)$$

where \mathbf{f} is the vector of sample points $(\mathbf{f})_l = f(z_l)$ and \mathbf{E} is the matrix of poles $(\mathbf{E})_{lm} = 1/(z_l - \epsilon_m)$. This linear equation can be solved for the residues \mathbf{r} using standard techniques. For $N = M$, the constant c can either be calculated from the roots z_n using eq. (4.120) or from analytic knowledge of the asymptote $f(z) \sim c$ for $|z| \rightarrow \infty$, and subtracted from the function values $f(z_j)$. Alternative, we can include c in the linear equation

$$\begin{pmatrix} \mathbf{1} & \mathbf{E} \end{pmatrix} \begin{pmatrix} c & \mathbf{r} \end{pmatrix}^\top = \mathbf{f}. \quad (4.123)$$

If additional high-frequency moments are known, they can be included as equality constrains to the least-squares problem [115].

It is also possible to determine the residues from the imaginary time Green's function. The imaginary time Green's function corresponding to eq. (4.121) with $N \neq M$ writes

$$\mathcal{G}(\tau) = \sum_{m=1}^M -r_m [\Theta(\tau) - sn_s(\epsilon_m)] e^{-\epsilon_m \tau} =: \sum_{m=1}^M g(\tau, \epsilon_m) \quad (4.124)$$

where the sign is $s = +1$ ($s = -1$) for Fermions (Bosons) and $n_{+1}(z) = f(z)$ is the Fermi function ($n_{-1}(z) = b(z)$ the Bose function); $\Theta(\tau)$ is the Heaviside step function. Again, this yields a matrix equation at the sample points

$$\mathcal{G}\mathbf{r} = \mathbf{g}, \quad (4.125)$$

where $(\mathcal{G})_{lm} = g(\tau_l, \epsilon_m)$ is the matrix of single-pole Green's functions, and $(\mathbf{g})_l = \mathcal{G}(\tau_l)$ is the vector of sample points. The formulas in frequency eq. (4.122) and imaginary-time space eq. (4.125) can be combined

$$\begin{pmatrix} \mathbf{E} & \mathcal{G} \end{pmatrix}^\top \mathbf{r} = \begin{pmatrix} \mathbf{f} & \mathbf{g} \end{pmatrix}^\top. \quad (4.126)$$

Algorithm. The full algorithm consists of three basic parts:

1. Determine the number of poles M .
2. Calculate the position of the poles ϵ_m .
3. Calculate one of the following:
 - a) the roots z_n from the poles ϵ_m ,
 - b) the residues r_m corresponding to the poles ϵ_m .

The algorithm yields an analytic formula of the Padé approximant which can be evaluated for any frequency point z . In contrast to Thiele's reciprocal difference method which interpolates the data, the pole-based Padé approximant performs a least-squares fit. This readily allows for the incorporation of uncertainties of the data: The weighted least-squares solution is obtained by left-multiplying the diagonal matrix of the variances $\text{diag}(1/\sigma_l)$. Including information of the covariance matrix \mathbf{C} is more complicated if \mathbf{C} is ill-conditioned, a generalized least-squares algorithm should be employed instead [115]. An implementation of this algorithm is provided in ref. [C2].

4.2.3. Numerical example: Bethe Green's function

We consider the analytic continuation of the Bethe Green's function to illustrate the pole-based Padé algorithm. The energy scale is fixed by setting the half-bandwidth of the Bethe DOS to $D = 1$. First, we discuss the Padé approximant not for the Matsubara frequencies but for a suitable contour for analytic continuation. This demonstrates the properties of the Padé approximant. Next, we discuss realistic test cases for Matsubara frequencies to discuss some problems one encounters in practice.

We consider the analytic continuation for the Green's function $G(z_l)$ given at frequency points on the unit half-circle in the upper complex half-plane:

$$z_l = \exp\left(\pi i \frac{l}{L+1}\right), \quad l \in \{1, \dots, L\}. \quad (4.127)$$

As all frequencies are of the magnitude $|z_l| = 1$, all elements of the Vandermonde matrices are of the same magnitude. Figure 4.6 shows that in this case the Padé approximant closely reproduces the retarded Green's function also on the real axis where the spectrum shows sharp edges. The pole-based Padé algorithm yields a [14/15] approximant without any spurious poles. Even though a slight asymmetry of the poles is visible, the resulting spectral function is highly accurate. The spectral function becomes slightly negative ($\approx 2 \times 10^{-3}$) around the band edge. It is evident that a sharp band-edge is a very challenging feature to reproduce with a Padé algorithm. The band-edge is related to a branch cut in the Green's function, which Padé approximates by a finite number of poles; this requires close zero-pole pairs. It is necessary to approximate only the retarded Green's function which is defined in the upper complex half-plane and not the Green's function which is defined for all complex frequencies. This allows to approximate branch cuts on the real axis by complex poles in the lower complex half-plane. If we use complex frequencies $z_l = \exp(2\pi il/L)$ on the full unit-circle instead of eq. (4.127) only in the upper half-plane, the poles ϵ_m of the Padé approximant are forced to the real axis. This

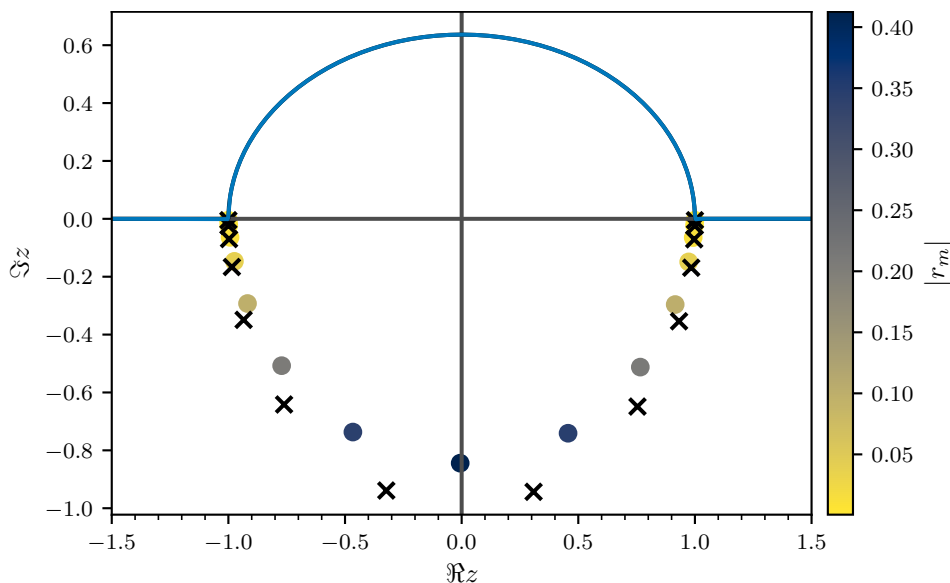


Figure 4.6.: Padé approximant of the retarded Bethe Green's function. The $[14/15]$ Padé approximant was generated from $L = 256$ frequencies on the unit circle eq. (4.127). The circles indicate the positions of the poles ϵ_m in the lower complex half-plane, their color indicates the absolute values of the corresponding residues $|r_m|$; the crosses indicate the position of the zeros z_n . The blue line shows the spectral function corresponding to the Padé approximant.

results in a Padé spectrum consisting of few sharp delta-like peaks, whose sign depends on whether the poles are slightly above or below the real axis. Thus, only positive Matsubara frequencies should be used for the analytic continuation; fig. 4.6 shows a dominant pole on the lower half of the imaginary axis which would conflict with negative Matsubara frequencies.

Next, we consider the case of Green's function values on Matsubara frequencies $i\omega_n$, which we are mainly interested in. Before considering realistic noisy data, we emphasize that the quality of the Padé approximants is temperature dependent as this modifies the mesh of input points $i\omega_n = i(2n + 1)\pi/\beta$. For bigger values of β the frequencies are closer to the real axis, therefore more of the structure of the Green's function is revealed. Figure 4.7 shows the Padé approximants obtained for $\beta = 100$ and $\beta = 10$ for exact input data $G^{(n)}$. The pole-based Padé algorithm underfits the data compared to fig. 4.6. While for $\beta = 100$ the algorithm produces a reasonable analytic continuation away from the band-edges, for $\beta = 10$ a spiky spectral function is produced. The reason for the spurious peaks is the too small number of poles, which is unable to reproduce the spectrum of the continuous branch cut. Thiele's reciprocal difference method suffers from the same problem, in spite of producing a $[\frac{L}{2}/\frac{L+1}{2}]$ approximant with much more poles.

We generate the data by running the CT-HYB code for a non-interacting impurity $U = 0$, which reproduces the non-interacting input Green's function up to noise. This approach produces realistic noise compared to putting artificial Gaussian noise on the test data. We consider $\beta = 100$ and use 64 bins for a long run with 5×10^7 measurements and a short one with 5×10^5 . Figure 4.8 shows the corresponding approximants, both are $[25/26]$ approximants; several spurious zero-pole pairs with small residue are generated in the upper complex half-plane. These spurious poles are placed along the imaginary axis,

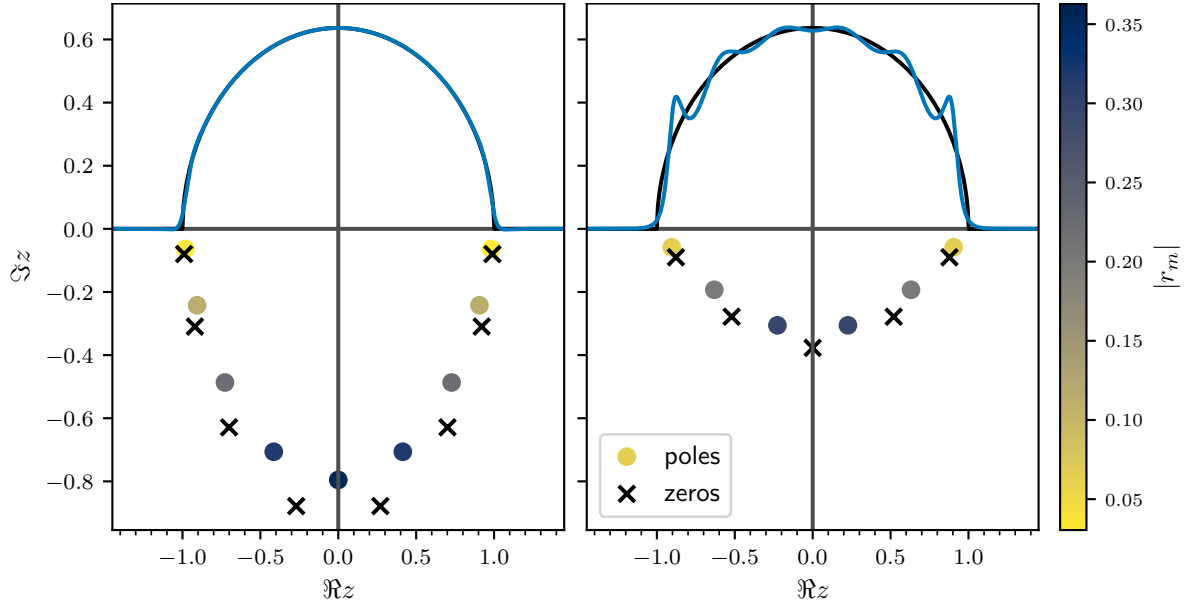


Figure 4.7.: Padé approximant of the retarded Bethe Green's function at $L = 1024$ Matsubara frequencies. Left shows the $[8/9]$ Padé approximant for $\beta = 100$, right shows the $[5/6]$ approximant for $\beta = 10$. The blue line shows the spectral function corresponding to the Padé approximant, the black line indicates the exact spectral function.

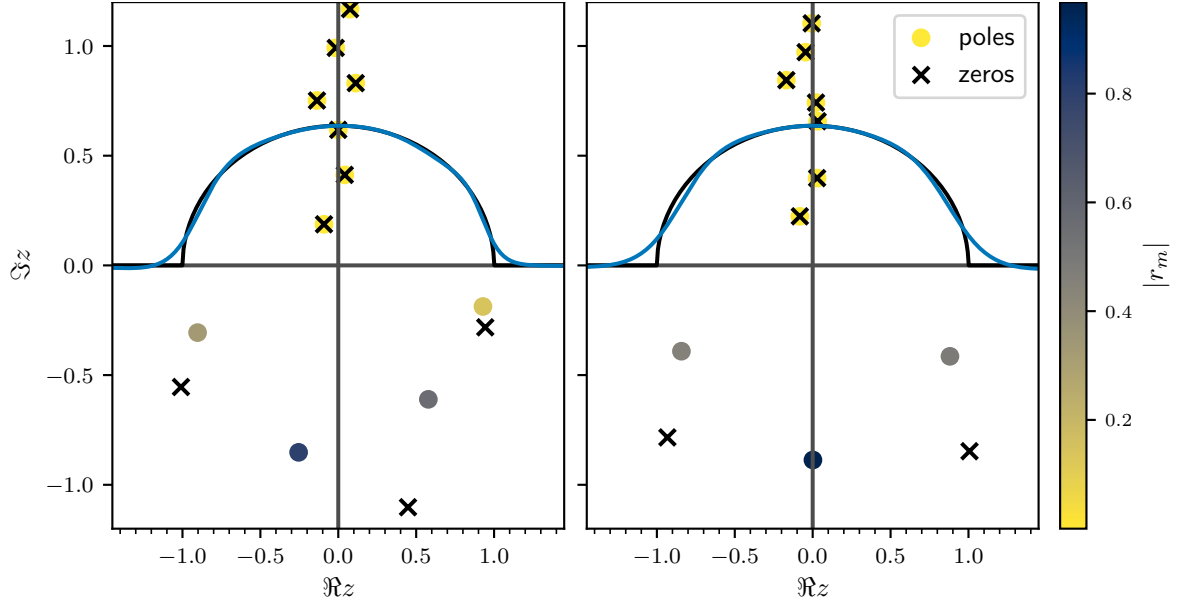


Figure 4.8.: Padé approximant of the retarded Bethe Green's function for $\beta = 100$ at $L = 1024$ Matsubara frequencies obtained from QMC data. Left shows the approximant for an error of order 10^{-5} and $\mathcal{G}(\tau)$, right shows the approximant for an error of order 10^{-4} ; both use a $[25/26]$ approximant. Not all poles and zeros in the upper complex half-plane are shown.

they are added to fit the noise in the data; they hardly affect the analytic continuation on the real axis as they have a small residue and are reasonably far from the real axis. More problematic is that in the presence of noise Padé can resolve less physical poles in the lower complex half-plane, therefore the approximation is worse, especially around the band-edge. Around the Fermi level the approximation is in general good, as we have a close-by data point at the zeroth Matsubara frequency $i\omega_0$. Again, Thiele's reciprocal difference method yields similar results.

5. Tensor network methods

Tensor-network-based impurity solvers [116–121] are complementary to the quantum Monte Carlo approach. They are Hamiltonian-based methods, which solve the SIAM for a finite number of bath sites. While finite temperature extensions exist, see e.g. Feiguin and White [122], most methods target the ground state. So in contrast to quantum Monte Carlo, tensor network methods work at zero-temperature and can calculate quantities for real times and frequencies. To solve the impurity problem, we consider a two-step procedure: First, the ground state is calculated, and subsequently a (real-) time evolution is performed to obtain the Green’s functions. Although methods calculating the Green’s function directly on frequencies exist [123], like the correction vector technique [124], or the dynamical density matrix renormalization group (DMRG) by Jeckelmann [125], we do not consider them in this work. Roughly speaking, whereas frequency methods are well suited for a precise frequency resolution, time evolution is suitable to provide a wide frequency window.

First, we explain how to express quantum states and operators in terms of tensor networks. At the heart of the tensor network algorithm lies the singular value decomposition (SVD), which allows for a controlled compression of the tensors representation of the states in the exponentially large Hilbert space. Next, we give a short, rather mathematical, introduction into DMRG, originally developed by White [21, 22], to calculate the ground state. This chapter will introduce the basic concepts and provide the steps to write a (rather naive) DMRG algorithm without going into rigorous proofs. At the end, we explain the time evolution using the time-dependent variational principle (TDVP) to obtain the zero temperature Green’s functions from the ground state. The code [C9] can be used as a supplement to this chapter, it provides a basic explanatory implementation.

In this chapter, we mainly employ tensor network diagrams. A nice introduction into the notation is given by Bridgeman and Chubb [126]; most of the notation is, nonetheless, quite self-explanatory. A tensor of order n is represented by a box with n legs. If one connects two legs of different tensors the corresponding index is summed over, that is the tensors are contracted. The connected legs are also referred to as bond. Likewise, connecting two legs of the same order- n tensor corresponds to a trace over the corresponding indices reducing the order to $n - 2$. We can group or split legs, to reshape the order- n tensor $T_{i_1 \dots i_n} \in \mathbb{C}^{d_1 \times \dots \times d_n}$ to an equivalent order- m tensor $\tilde{T}_{j_1 \dots j_m} \in \mathbb{C}^{\tilde{d}_1 \times \dots \times \tilde{d}_m}$, for matching sizes $\prod_{i=1}^n d_i = \prod_{j=1}^m \tilde{d}_j$, as the vector spaces are isomorphic. This allows us to apply the toolbox of linear algebra not only to order-2 tensors, but also to higher order tensors by defining a bipartition to reshape them into a matrix. Consider for example an order-5 tensor T_{ijklm} with a bipartition between the indices ij and klm :

$$\begin{array}{c} j \quad k \\ | \quad | \\ \boxed{T} \\ | \quad | \\ i \quad l \\ | \quad | \\ m \end{array} = \begin{array}{c} j \quad k \\ | \quad | \\ \boxed{T} \\ | \quad | \\ i \quad l \\ | \quad | \\ m \end{array} \sim \alpha \text{---} \boxed{\tilde{T}} \text{---} \beta. \quad (5.1)$$

We group the indices ij to the multi-index $\alpha = (i, j)$ and the indices klm to the multi-index $\beta = (k, l, m)$ to write the tensor T_{ijklm} as the equivalent matrix $\tilde{T}_{\alpha\beta}$; the particular order of indices is not relevant in this example. The central algorithms employed from linear algebra are the SVD and the QR-decomposition [95, 115]; we assume the reader to be familiar with them. In the following, we omit the indices as well as the symbols for the tensor in the diagrammatic notation.

5.1. Tensor representation of quantum states

Consider a given local basis of states $|\alpha_i\rangle$, e.g., the occupation of a spin-orbital of a given site. In terms of this basis, a quantum state can be written as the vector

$$|\psi\rangle = \sum_{\{\alpha_i\}} M_{\alpha_1 \dots \alpha_N} |\alpha_1\rangle \otimes \dots \otimes |\alpha_N\rangle = \sum_{\{\alpha_i\}} M_{\alpha_1 \dots \alpha_N} |\alpha_1 \dots \alpha_N\rangle. \quad (5.2)$$

For the given basis, the state is fully characterized by the tensor $M_{\alpha_1 \dots \alpha_N}$. Hence, the state $|\psi\rangle$ is equivalent to the tensor M , which we depict graphically as

$$|\psi\rangle \sim \begin{array}{c} | \\ | \\ \dots \\ | \\ \hline M \\ \hline | \\ | \\ \dots \\ | \end{array}, \quad \langle\psi| \sim \begin{array}{c} \hline M^* \\ \hline | \\ | \\ \dots \\ | \end{array}. \quad (5.3)$$

We draw the legs upwards for kets and downwards for bras. The complex conjugation of the tensor will often be omitted, it is clear from the orientation of the legs. Thus, an overlap between two states $|\psi\rangle$ and $|\phi\rangle$, represented by the tensors M and N , is calculated by contracting the corresponding legs:

$$\langle\phi|\psi\rangle = \begin{array}{c} \hline N^* \\ \hline | \\ | \\ \dots \\ | \\ \hline M \\ \hline \end{array}. \quad (5.4)$$

The overlap is a scalar equal to the contracted tensor, it is basis independent and therefore an equality not just an equivalence.

The size of such a tensor M , eq. (5.2), representing a quantum states grows exponentially with the system size N . For local basis states $|\alpha_i\rangle$ with dimension d , the size of the tensor is d^N . Direct numerical treatment is therefore restricted to small system sizes N ; even for moderate system sizes it is impossible to naively store or process states on a computer. Tensor network methods substitute the order- N tensor $M_{\alpha_1 \dots \alpha_N}$ by a network of tensors of low order. Depending on the problem, this can significantly compress the amount of computer memory required to store the tensor elements.

Consider a given state $|\psi\rangle$. While in practice we can neither fit $M_{\alpha_1 \dots \alpha_N}$ into memory, nor process it in any reasonable time, for now we assume exact knowledge of the quantum state. By defining a bipartition of the tensor (red dashed line), it can be decomposed

using the *thin* SVD¹

$$\text{---} \boxed{\text{---}} \text{---} = \text{---} \begin{array}{c} \text{---} \\ \text{---} \end{array} U \begin{array}{c} \text{---} \\ \text{---} \end{array} \Sigma \begin{array}{c} \text{---} \\ \text{---} \end{array} V^\dagger \text{---} . \quad (5.5)$$

Trapezoidal wedges, $\begin{array}{c} \text{---} \\ \text{---} \end{array}$, indicate isometric maps: Contracting all legs on the long side with its conjugate yields the identity

$$\text{---} \begin{array}{c} \text{---} \\ \text{---} \end{array} U^* \begin{array}{c} \text{---} \\ \text{---} \end{array} U \text{---} = \text{---} . \quad (5.6)$$

The short side indicates that the dimension of its legs is smaller (or equal) than the dimension of the legs at the long side. Diamonds, \diamond , represent diagonal tensors. The repeated application of thin SVDs allows to decompose the tensor into a network of tensors. Performing a single SVD yields

$$\text{---} \boxed{M} \text{---} = \begin{array}{c} \text{---} \\ \text{---} \end{array} U_1 \begin{array}{c} \text{---} \\ \text{---} \end{array} \Sigma_2 \begin{array}{c} \text{---} \\ \text{---} \end{array} V_2^\dagger \text{---} = \begin{array}{c} \text{---} \\ \text{---} \end{array} U_1 \boxed{M_2} \text{---} , \quad (5.7)$$

where the dashed box indicates the contraction of Σ_2 and V_2^\dagger yielding the node M_2 . The cheaper QR-decomposition could be employed instead to split the tensor, later, however, we will make explicit use of the properties of the SVD. Iterating through the whole tensor, we generate the tensor train

$$\text{---} \boxed{M} \text{---} = \begin{array}{c} \text{---} \\ \text{---} \end{array} U_1 \begin{array}{c} \text{---} \\ \text{---} \end{array} U_2 \begin{array}{c} \text{---} \\ \text{---} \end{array} U_3 \text{---} \dots \text{---} \boxed{M_N} \text{---} . \quad (5.8)$$

This procedure is known as tensor-train decomposition [127]. In physics, the tensor train (as well as a tensor ring [128]) is often referred to as matrix product state (in spite of all inner nodes being order-3 tensors). There is a geometric and a gauge freedom in decomposing a high-order tensor into a tensor network. Choosing different bipartitions, the tensor M can also be decomposed into other geometries than this train, e.g., the fork geometry [120]. Depending on the system that is studied, different geometries might be suitable. For simplicity, we concentrate in the following on the tensor-train geometry, however, any loop-free tree could be also considered. Even for a fixed geometry, the tensor network is not unique; the tensor-train representation still has a gauge freedom. Doing the tensor-train decomposition from right to left, yields e.g. the different representation:

$$\text{---} \boxed{M} \text{---} = \boxed{M_1} \begin{array}{c} \text{---} \\ \text{---} \end{array} V_2^\dagger \begin{array}{c} \text{---} \\ \text{---} \end{array} V_3^\dagger \text{---} \dots \text{---} \begin{array}{c} \text{---} \\ \text{---} \end{array} V_N^\dagger \text{---} . \quad (5.9)$$

¹The *full* SVD yields unitary matrices \mathbf{U} and \mathbf{V} and the rectangular diagonal matrix $\mathbf{\Sigma}$. As we are not interested in the null-space, it is sufficient to perform the more economic *thin* SVD which yields only the relevant rectangular part of \mathbf{U}/\mathbf{V} which is isometric and the square diagonal matrix $\mathbf{\Sigma}$. See standard linear algebra books, e.g., Golub and Van Loan [115].

In principle, identities like eq. (5.6) can be inserted in any bond, modifying the neighboring bonds upon contraction. This freedom is useful to bring the tensor train into a form suitable for numerical algorithms.

So far, we have not addressed the problem that the space required to store the state grows exponentially with the system size N . The *thin* SVD of an $M \times N$ matrix $\mathbf{M}^{M \times N}$ is

$$\mathbf{M}^{M \times N} = \mathbf{U}^{M \times K} \boldsymbol{\Sigma}^{K \times K} (\mathbf{V}^\dagger)^{K \times N} = \mathbf{U}^{M \times K} \mathbf{R}^{K \times M}, \quad (5.10)$$

where $K = \min(M, N)$. Thus, starting from U_1 at the left margin of eq. (5.8), the bond dimension, that is the dimension of the connection between two tensors, grows exponentially till the middle and decays again towards the boundary:

$$M^{d^{\otimes N}} = U_1^{d \times d} U_2^{d \times d \times d^2} U_3^{d^2 \times d \times d^3} \dots U_{N-1}^{d^2 \times d \times d} M_N^{d \times d}. \quad (5.11)$$

We indicate this in eq. (5.8), by increasing the thickness of the bonds. Thus, the central tensor $U_{N/2}$ is of the same size as the original tensor M . At this point, the tensor network requires more computer memory than the initial tensor. For an efficient representation, it is necessary to compress the network.

5.1.1. Low rank approximation of a tensor network

We can use the properties of the SVD to compress the tensor train, eq. (5.8). Not all the K singular values (*thin* SVD) have to be taken into account, only nonzero singular values (*compact* SVD) contribute. Numerically, it is not possible to distinguish tiny singular values from those that are exactly zero. In fact, it is numerically favorable to discard small singular values, to improve the condition number, which (for the spectral norm) is given by the ratio of the largest and the smallest singular value. Thus, depending on the state under consideration, it might be sufficient to keep only a small enough number of singular values, instead of the exponentially growing number, making the state traceable.

For matrices, the *truncated* SVD, which keeps only the $T < K$ largest singular values, is known to be the best rank- T approximation as proven by the Eckart–Young–Mirsky theorem [129, 130]. The SVD decomposition of a matrix \mathbf{A} has the form

$$\mathbf{A} = \mathbf{U} \boldsymbol{\Sigma} \mathbf{V}^\dagger = \sum_{k=1}^K \sigma_k \mathbf{u}_k \mathbf{v}_k^\dagger, \quad (5.12)$$

where \mathbf{u}_k is the k -th column vector of \mathbf{U} , that is $\mathbf{u}_k = \mathbf{U}_{[:,k]}$, likewise $\mathbf{v}_k = \mathbf{V}_{[:,k]}$, and σ_k are the corresponding singular values $\sigma_k = (\boldsymbol{\Sigma})_{k,k}$. The singular values are sorted in descending order $\sigma_1 \geq \sigma_2 \geq \dots \geq \sigma_K$. The optimal rank- T approximation of \mathbf{A} is then a matrix

$$\mathbf{A}_T = \sum_{k=1}^T \sigma_k \mathbf{u}_k \mathbf{v}_k^\dagger. \quad (5.13)$$

This is a controlled approximation: The error is readily available in the spectral norm as the largest truncated singular value

$$\|\mathbf{A} - \mathbf{A}_T\|_2 = \sigma_{T+1}, \quad (5.14)$$

or in the Frobenius norm as the square root of the sum of the squared truncated singular values

$$\|\mathbf{A} - \mathbf{A}_T\|_F = \sqrt{\sum_{k=T+1}^K \sigma_k^2}. \quad (5.15)$$

The well known low-rank approximation of matrices, eqs. (5.13) to (5.15), needs to be generalized to nodes of a tensor network; while we know that the truncation is optimal locally for a single tensor, it might not be optimal globally for the network. It is possible that the network scales the singular values of the node. The Frobenius norm of a matrix is the trace

$$\|\mathbf{A}\|_F = \sqrt{\text{tr } \mathbf{A}^\dagger \mathbf{A}}. \quad (5.16)$$

This norm readily generalizes from matrices to tensors by contracting all legs of a tensor M with the equivalent legs of its conjugate

$$\left\| \begin{array}{c} \text{---} \\ \square \\ \text{---} \end{array} M \begin{array}{c} \text{---} \\ \square \\ \text{---} \end{array} \right\|^2 = \begin{array}{c} \square \\ \text{---} \\ \square \\ \text{---} \end{array} M \begin{array}{c} \square \\ \text{---} \\ \square \\ \text{---} \end{array} M^*. \quad (5.17)$$

The Frobenius norm of a tensor M is also the norm of the corresponding state $|\psi\rangle \sim M$:

$$\| |\psi\rangle \| = \sqrt{\langle \psi | \psi \rangle} = \|M\|, \quad (5.18)$$

cf. eq. (5.4).

It is useful to introduce the concept of a *center of orthogonality*. We call a tensor C the center of orthogonality of a tensor network M if all legs connected to C are isometric towards C , e.g.:

$$\begin{array}{c} \text{---} \\ \square \\ \text{---} \end{array} M \begin{array}{c} \text{---} \\ \square \\ \text{---} \end{array} = \begin{array}{c} \text{---} \\ \text{---} \\ \text{---} \end{array} \begin{array}{c} \text{---} \\ \square \\ \text{---} \end{array} C \begin{array}{c} \text{---} \\ \text{---} \\ \text{---} \end{array}. \quad (5.19)$$

Due to the isometry $\begin{array}{c} \text{---} \\ \text{---} \\ \text{---} \end{array} \begin{array}{c} \text{---} \\ \square \\ \text{---} \end{array} \begin{array}{c} \text{---} \\ \text{---} \\ \text{---} \end{array} = \text{---}$, the norm of the tensor network M reduces to the norm of the center of orthogonality C :

$$\begin{aligned} \left\| \begin{array}{c} \text{---} \\ \square \\ \text{---} \end{array} M \begin{array}{c} \text{---} \\ \square \\ \text{---} \end{array} \right\|^2 &= \begin{array}{c} \text{---} \\ \text{---} \\ \text{---} \end{array} \begin{array}{c} \text{---} \\ \square \\ \text{---} \end{array} C \begin{array}{c} \text{---} \\ \text{---} \\ \text{---} \end{array} \begin{array}{c} \text{---} \\ \text{---} \\ \text{---} \end{array} \begin{array}{c} \text{---} \\ \square \\ \text{---} \end{array} C^* \begin{array}{c} \text{---} \\ \text{---} \\ \text{---} \end{array} \\ &= \begin{array}{c} \text{---} \\ \text{---} \\ \text{---} \end{array} \begin{array}{c} \text{---} \\ \square \\ \text{---} \end{array} C \begin{array}{c} \text{---} \\ \text{---} \\ \text{---} \end{array} \begin{array}{c} \text{---} \\ \square \\ \text{---} \end{array} C^* \begin{array}{c} \text{---} \\ \text{---} \\ \text{---} \end{array} = \left\| \begin{array}{c} \text{---} \\ \square \\ \text{---} \end{array} C \begin{array}{c} \text{---} \\ \square \\ \text{---} \end{array} \right\|^2. \end{aligned} \quad (5.20)$$

If we replace this tensor C by its low rank approximation C_T , we obtain the new tensor network M_T

$$\begin{array}{c} \text{---} \\ \square \\ \text{---} \end{array} M_T \begin{array}{c} \text{---} \\ \square \\ \text{---} \end{array} = \begin{array}{c} \text{---} \\ \text{---} \\ \text{---} \end{array} \begin{array}{c} \text{---} \\ \square \\ \text{---} \end{array} C_T \begin{array}{c} \text{---} \\ \text{---} \\ \text{---} \end{array}. \quad (5.21)$$

The error of approximation of the network M equals that of the low-rank approximation of the center of orthogonality C :

$$\|M - M_T\| = \left\| \begin{array}{c} \text{---} \\ \text{---} \\ \text{---} \end{array} \begin{array}{c} \text{---} \\ \square \\ \text{---} \end{array} C - C_T \begin{array}{c} \text{---} \\ \text{---} \\ \text{---} \end{array} \right\| = \|C - C_T\|. \quad (5.22)$$

As the error $\|C - C_T\|$ is minimal for the optimal low-rank approximation of C given by the truncated SVD, this also minimizes the error for the whole tensor network $\|M - M_T\|$. Thus, if the tensor node we approximate is the center of orthogonality, the SVD provides globally the best low-rank approximation for the tensor network M .

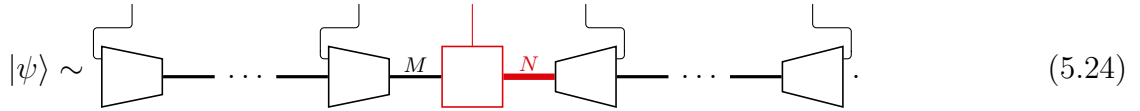
Furthermore, we note that the norm of network M is given by the singular values σ_k of the center of orthogonality C :

$$\| \text{---} \boxed{M} \text{---} \| = \| \text{---} \boxed{C} \text{---} \| = \sqrt{\sum_k \sigma_k^2}. \quad (5.23)$$

Thus, we can normalize the vector $|\psi\rangle$ represented by a tensor network M by normalizing the singular values of the center of orthogonality $\sum_k \sigma_k^2 \stackrel{!}{=} 1$. After truncating the singular values, it is necessary to re-normalize the network.

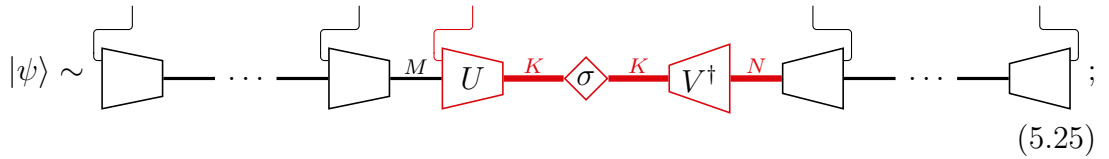
5.1.2. Iterative compression of tensor trains

To compress the tensor representing a state $|\psi\rangle$, we require it to have a center of orthogonality. If this is not already the case, we can iteratively apply QR decompositions (or SVDs) starting from the nodes the furthest away from the desired center and contract the non-isometric part towards the center. This procedure works for all *loop-free* tensor networks; the distance between two nodes can be defined as the number of nodes on the unique path between them. Consider the state

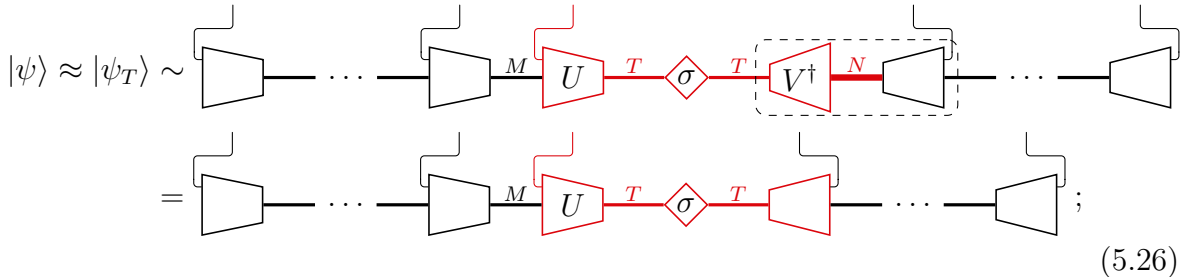


The tensor train is compressed to a given accuracy by iterating through the train starting from the center of orthogonality throwing away small singular values and normalizing the network. In the following, we explicitly iterate the steps, to compress the bond of dimension N to the right of the center of orthogonality highlighted in red:

1. Perform the thin SVD of center of orthogonality:



2. Discard singular values smaller than a threshold ϵ , thus limiting the bond dimension to $T_\epsilon := \max\{T \leq K \mid \sum_{k=T+1}^K \sigma_k^2 < \epsilon^2\}$, or impose a hard limit T_{\max} that is computational feasible $T := \min(T_\epsilon, T_{\max})$:



3. Normalize the singular values $\tilde{\sigma}_k := \sigma_k / \sqrt{\sum_{k=1}^T \sigma_k^2}$, and therefore the state $|\psi_T\rangle$:

$$|\psi\rangle \approx |\tilde{\psi}_T\rangle \sim \text{[Diagram]}; \quad (5.27)$$

4. Contract the nodes moving the center of orthogonality right if desired:

$$|\psi\rangle \approx |\tilde{\psi}_T\rangle \sim \text{[Diagram]} \quad (5.28)$$

$$= \text{[Diagram]}$$

Note that truncating the bond dimension to T_ϵ guarantees the error to be smaller than ϵ . In practice, however, it might be necessary to truncate the bond dimension to a smaller value $T_{\max} < T_\epsilon$, with the value of T_{\max} limited by computer resources. Such a truncation is not controlled anymore since the truncation errors can grow arbitrarily large. In this case, we have to be careful.

The same procedure can be also applied for the bond left of the center of orthogonality of size M , allowing to move the center of orthogonality to the left. To compress the complete tensor train, we can start with the center of orthogonality at one end iterating to the other end, as we can automatically move the center at each truncation step. In the DMRG algorithm, which will be introduced in section 5.3, the truncation step is explicitly integrated into the sweeping procedure.

5.2. Tensor representation of operators

Before we discuss algorithms, we still have to represent operators, most importantly the Hamiltonian operator, in the language of tensor networks. Given the basis $|\alpha_i\rangle$ used for the state eq. (5.2), an operator can be written as

$$\begin{aligned} \hat{\mathcal{O}} &= \sum_{\{\alpha_i\}} \sum_{\{\alpha'_i\}} |\alpha_1 \dots \alpha_N\rangle \langle \alpha_1 \dots \alpha_N| \hat{\mathcal{O}} |\alpha'_1 \dots \alpha'_N\rangle \langle \alpha'_1 \dots \alpha'_N| \\ &= \sum_{\{\alpha_i\}} \sum_{\{\alpha'_i\}} |\alpha_1 \dots \alpha_N\rangle \mathcal{O}_{\alpha_1 \dots \alpha_N}^{\alpha'_1 \dots \alpha'_N} \langle \alpha'_1 \dots \alpha'_N|. \end{aligned} \quad (5.29)$$

The operator \mathcal{O} is fully characterized by the tensor $\mathcal{O}_{\alpha_1 \dots \alpha_N}^{\alpha'_1 \dots \alpha'_N}$. Graphically, we depict the operator $\hat{\mathcal{O}}$ by the equivalent tensor

$$\hat{\mathcal{O}} \sim \text{[Diagram]}, \quad (5.30)$$

where the upwards pointing legs connect with bra states and the downwards pointing legs with ket states. Thus, a matrix element between two states $|\psi\rangle$ and $|\phi\rangle$, represented by the tensors M and N , is calculated by simply connecting the corresponding legs:

$$\langle\phi|\hat{O}|\psi\rangle = \begin{array}{c} \boxed{N^*} \\ \vdots \\ \boxed{O} \\ \vdots \\ \boxed{M} \end{array}. \quad (5.31)$$

Most operators of interest are already sparse, and a small-sized representation in terms of a tensor network can be found.

We consider the Hamiltonian of the one-band SIAM, eq. (2.15), for a finite number L of bath sites. It is convenient to rename $\hat{c}_{0\sigma}^\dagger := \hat{d}_\sigma^\dagger$, and write the Hamiltonian as

$$\hat{H} = \sum_{\sigma} \epsilon_{0\sigma} \hat{c}_{0\sigma}^\dagger \hat{c}_{0\sigma} + U \hat{n}_{0\uparrow} \hat{n}_{0\downarrow} + \sum_{\sigma} \sum_{l=1}^L \epsilon_{l\sigma} \hat{c}_{l\sigma}^\dagger \hat{c}_{l\sigma} + \sum_{\sigma} \sum_{l=1}^L (V_{l\sigma} \hat{c}_{l\sigma}^\dagger \hat{c}_{0\sigma} + V_{l\sigma}^* \hat{c}_{0\sigma}^\dagger \hat{c}_{l\sigma}). \quad (5.32)$$

The tensor-train representation of this Hamiltonian is given by Bauernfeind [131]; instead of providing a general algorithm, we state the result and verify its correctness.

We start with spin-less fermions and build the elementary operators in Fock space. The local basis $|\alpha_i\rangle$ consists of two states: The site i can either be empty, $|0_i\rangle = (0, 1)^\top$, or occupied, $|1_i\rangle = (1, 0)^\top$. The raising and lowering operators with the matrix representation

$$\sigma_+ = \begin{pmatrix} 0 & 1 \\ 0 & 0 \end{pmatrix}, \quad \sigma_- = (\sigma_+)^\dagger = \begin{pmatrix} 0 & 0 \\ 1 & 0 \end{pmatrix} \quad (5.33)$$

map these two states onto each other, $\sigma_+ |0_i\rangle = |1_i\rangle$, $\sigma_- |1_i\rangle = |0_i\rangle$. The Fock states for many particles, however, have to be properly anti-symmetrized. Thus, the creation and annihilation operators have to additionally keep track of the fermionic signs for commuting electrons. For the Fock states, we choose the sign convention, that the operators are ordered with increasing (bath) site index, e.g. for $L = 4$ bath sites

$$|10110\rangle = |1_0\rangle \otimes |0_1\rangle \otimes |1_2\rangle \otimes |1_3\rangle \otimes |0_4\rangle = \hat{c}_0^\dagger \hat{c}_2^\dagger \hat{c}_3^\dagger |0\rangle. \quad (5.34)$$

With this convention, the creation/annihilation operator are represented by

$$\left. \begin{array}{l} \hat{c}_i^\dagger \\ \hat{c}_i \end{array} \right\} = \underbrace{\sigma_z \otimes \cdots \otimes \sigma_z}_{i\text{-times}} \otimes \sigma_\pm \otimes \underbrace{\mathbf{1} \otimes \cdots \otimes \mathbf{1}}_{(L-i)\text{-times}} = \boxed{\sigma_z} \cdots \boxed{\sigma_z} \boxed{\sigma_\pm} \left| \cdots \right|, \quad (5.35)$$

where σ_z is the parity matrix

$$\sigma_z = \begin{pmatrix} +1 & 0 \\ 0 & -1 \end{pmatrix}, \quad (5.36)$$

which flips the sign, whenever we have to permute the operator past a creation operator. The occupation number operator \hat{n}_i consists of a pair of a creation and an annihilation operator, no additional signs are necessary:

$$\hat{n}_i = \underbrace{\mathbb{1} \otimes \cdots \otimes \mathbb{1}}_{i\text{-times}} \otimes \mathbf{n} \otimes \underbrace{\mathbb{1} \otimes \cdots \otimes \mathbb{1}}_{(L-i)\text{-times}} = \left| \begin{array}{c} \dots \\ \boxed{\mathbf{n}} \\ \dots \end{array} \right|, \quad (5.37)$$

where \mathbf{n} is the number matrix

$$\mathbf{n} = \sigma_+ \sigma_- = \begin{pmatrix} 0 & 0 \\ 0 & 1 \end{pmatrix}. \quad (5.38)$$

For a hopping from site i to j , only the signs for the occupied sites in between of i and j have to be considered. For example for $j < i$, we write

$$\hat{c}_j^\dagger \hat{c}_i = \underbrace{\mathbb{1} \otimes \cdots \otimes \mathbb{1}}_{j\text{-times}} \otimes \sigma_+ \otimes \underbrace{\sigma_z \otimes \cdots \otimes \sigma_z}_{(i-j-1)\text{-times}} \otimes \sigma_- \otimes \underbrace{\mathbb{1} \otimes \cdots \otimes \mathbb{1}}_{(L-i)\text{-times}}. \quad (5.39)$$

With the representation of the basic operators, we can start building the Hamiltonian.

For spin-less fermions, we do not have an interaction term. Thus, for the impurity site, we have four possible operations: creating a fermion \hat{c}_0^\dagger , annihilating a fermion \hat{c}_0 , counting the fermions \hat{n}_0 , and the identity $\hat{1}$. For the impurity site, we choose the tensor node as the row vector, containing these four operations:

$$\mathbf{W}_0 = (\mathbb{1} \quad \epsilon_0 \mathbf{n} \quad \sigma_+ \quad \sigma_-). \quad (5.40)$$

For the bath sites, the tensor node needs an equivalent column generating the on-site terms and the hopping (with the amplitude V_j). Additionally, we need to propagate the hopping terms to/from the impurity multiplied by the correct sign. Bauernfeind [131] proposes

$$\mathbf{W}_i = \begin{pmatrix} \mathbb{1} & \epsilon_i \mathbf{n} & 0 & 0 \\ 0 & \mathbb{1} & 0 & 0 \\ 0 & V_i^* \sigma_- & \sigma_z & 0 \\ 0 & V_i \sigma_+ & 0 & \sigma_z \end{pmatrix}. \quad (5.41)$$

Performing the symbolic matrix multiplication, we correctly start accumulating the Hamiltonian in the second column of the row-matrix

$$\mathbf{W}_0 \mathbf{W}_1 = (\mathbb{1} \otimes \mathbb{1}, \quad [\epsilon_0 \mathbf{n} \otimes \mathbb{1} + \epsilon_1 \mathbb{1} \otimes \mathbf{n} + V_1^* \sigma_+ \otimes \sigma_- + V_1 \sigma_- \otimes \sigma_+], \quad \sigma_+ \otimes \sigma_z, \quad \sigma_- \otimes \sigma_z), \quad (5.42)$$

commata are added to make the columns more visible. The third and fourth column of $\mathbf{W}_0 \mathbf{W}_1$ accumulate the fermionic signs necessary for hopping terms eq. (5.39). Filling up the remaining sites with the tensor identity further clarifies this structure, as the fermionic operators in Fock space are recovered in the second column:

$$\mathbf{W}_0 \mathbf{W}_1 \bigotimes_{l=2}^L \mathbb{1} = \left(\hat{\mathbf{1}}, \left[\sum_{i=0}^1 \epsilon_i \hat{n}_i + V_1^* \hat{c}_0^\dagger \hat{c}_1 + V_1 \hat{c}_1^\dagger \hat{c}_0 \right], \sigma_+ \otimes \sigma_z \otimes \bigotimes_{l=2}^L \mathbb{1}, \sigma_- \otimes \sigma_z \otimes \bigotimes_{l=2}^L \mathbb{1} \right). \quad (5.43)$$

Evidently, the ordered matrix product writes

$$\prod_{i=0}^L \mathbf{W}_i = \left(\hat{\mathbf{1}}, \left[\sum_{i=0}^L \epsilon_i \hat{n}_i + \sum_{l=1}^L (V_l \hat{c}_l^\dagger \hat{c}_0 + \text{H.c.}) \right], \sigma_+ \otimes \bigotimes_{l=1}^L \sigma_z, \sigma_- \otimes \bigotimes_{l=1}^L \sigma_z \right). \quad (5.44)$$

Thus, replacing the last matrix \mathbf{W}_L in the product by its second column $\tilde{\mathbf{W}}_L = (\mathbf{W}_L)_{[:,2]}$, the matrix product is a tensor train representing the spin-less SIAM Hamiltonian. The in- and outgoing legs of the nodes have the local physical dimensions $d = 2$; inner nodes have the bond dimensions $\chi = 4$ to the two neighboring sites:

$$\hat{H} \sim \begin{array}{c} \begin{array}{cccc} & 2 & & 2 \\ & | & & | \\ \hat{H} \sim & \boxed{\mathbf{W}_0} & \boxed{\mathbf{W}_1} & \dots & \boxed{\mathbf{W}_{L-1}} & \boxed{\tilde{\mathbf{W}}_L} \\ & | & | & & | & | \\ & 2 & 2 & & 2 & 2 \end{array} \end{array}. \quad (5.45)$$

Thus, the Hamiltonian of the size $2^N \times 2^N$ is equivalent to the tensor train, eq. (5.45), with size of the order of $(2^2 \times 4^2)N = 64N$, where $N = L + 1$ is the number of bath plus impurity sites. The tensor-train representation exploits the sparsity of the Hamiltonian.

Next, we include the spin degree of freedom. The only term in the Hamiltonian eq. (5.32) coupling the spins is the on-site interaction $U \hat{n}_{0\uparrow} \hat{n}_{0\downarrow}$ at the impurity site. Thus, the natural choice is to duplicate our spinless tensor train and couple the trains at the impurity site $i = 0$. To fix the geometry of our tensor network, we arrange the up-spins in descending order, followed by the down-spins in ascending order. The total Hamiltonian consists of the three parts

$$\hat{H} = \hat{H}_\uparrow + U \hat{n}_{0\uparrow} \hat{n}_{0\downarrow} + \hat{H}_\downarrow. \quad (5.46)$$

We already gave the tensor representation eq. (5.45) for \hat{H}_\uparrow and \hat{H}_\downarrow . The interaction term requires only terms at the impurity site, thus it suffices to introduce a bond of dimension 3 connecting the up- and down-spin nodes at the impurity site to accommodate the three terms. We extend the row-matrix \mathbf{W}_0 eq. (5.40) by two rows

$$\mathbf{W}_{\downarrow 0} = \begin{pmatrix} \mathbb{1} & \epsilon_{\downarrow 0} \mathbf{n} & \sigma_+ & \sigma_- \\ 0 & \mathbb{1} & 0 & 0 \\ 0 & U \mathbf{n} & 0 & 0 \end{pmatrix}, \quad (5.47)$$

such that the second column accumulates the three Hamiltonian parts. Similarly, $\mathbf{W}_{\uparrow 0}$ is

$$\mathbf{W}_{\uparrow 0} = \begin{pmatrix} 0 & \mathbb{1} & 0 \\ \mathbb{1} & \epsilon_{\uparrow 0} \mathbf{n} & \mathbf{n} \\ 0 & \sigma_+ & 0 \\ 0 & \sigma_- & 0 \end{pmatrix}. \quad (5.48)$$

The total Hamiltonian of size $4^N \times 4^N$ can thus be written as the tensor train

$$\hat{H} \sim \begin{array}{c} 2 \\ | \\ \tilde{\mathbf{W}}_{\uparrow L} \\ | \\ 2 \end{array} \begin{array}{c} 4 \\ \text{---} \\ \dots \\ \text{---} \\ 4 \end{array} \begin{array}{c} 2 \\ | \\ \mathbf{W}_{\uparrow 1} \\ | \\ 2 \end{array} \begin{array}{c} 4 \\ \text{---} \\ \dots \\ \text{---} \\ 4 \end{array} \begin{array}{c} 2 \\ | \\ \mathbf{W}_{\uparrow 0} \\ | \\ 2 \end{array} \begin{array}{c} 3 \\ \text{---} \\ \dots \\ \text{---} \\ 3 \end{array} \begin{array}{c} 2 \\ | \\ \mathbf{W}_{\downarrow 0} \\ | \\ 2 \end{array} \begin{array}{c} 4 \\ \text{---} \\ \dots \\ \text{---} \\ 4 \end{array} \begin{array}{c} 2 \\ | \\ \mathbf{W}_{\downarrow 1} \\ | \\ 2 \end{array} \begin{array}{c} 4 \\ \text{---} \\ \dots \\ \text{---} \\ 4 \end{array} \begin{array}{c} 2 \\ | \\ \tilde{\mathbf{W}}_{\downarrow L} \\ | \\ 2 \end{array} \quad (5.49)$$

with size of the order $64 \times 2N = 128N$. Thus, the tensor network representation of our Hamiltonian grows only linearly in the system size N . Applying this Hamiltonian to a tensor-train state of bond dimension χ costs of the order of $128N\chi^2$ operations. The bond dimension of the new state $\hat{H}|\psi\rangle$, however, might be up to 4χ , depending on how much it can be compressed again using truncated SVD.

Instead of writing down an explicit tensor-train representation of the Hamiltonian, one could just numerically sum up the tensor trains of the individual operators eqs. (5.37) and (5.39) and compress the result [132]. In contrast to states, operators are not normalized, thus the compression has to be done more carefully. The Hamiltonian operator, for example, is extensive, thus a center of orthogonality would accumulate the macroscopic norm in a single node, potentially leading to large numerical errors. We use the explicit form given in eq. (5.49), and do not discuss the compression of operators further.

5.3. Two-site density matrix renormalization group

Using conventional matrix-based methods such as exact diagonalization, Lanczos [9, 133], or Davidson [134], the ground state can only be obtained for very small system sizes as the Hilbert space grows exponentially in system size. The DMRG algorithm [21, 22] allows for treating considerably larger systems. It can be naturally formulated in terms of tensor networks [19]. The energy is iteratively lowered by a local optimization of nodes in a sweeping procedure.

Using the tensor network representation of the previous sections 5.1 and 5.2, we can write the energy of a state $|\psi\rangle$ as the network

$$E_\psi = \langle \psi | \hat{H} | \psi \rangle = \begin{array}{c} \square \text{---} \dots \text{---} \square \text{---} \square \text{---} \square \text{---} \square \text{---} \dots \text{---} \square \\ | \\ \tilde{\mathbf{W}}_{\uparrow N} \text{---} \dots \text{---} \mathbf{W}_{\uparrow 1} \text{---} \mathbf{W}_{\uparrow 0} \text{---} \mathbf{W}_{\downarrow 0} \text{---} \mathbf{W}_{\downarrow 1} \text{---} \dots \text{---} \tilde{\mathbf{W}}_{\downarrow N} \\ | \\ \square \text{---} \dots \text{---} \square \text{---} \square \text{---} \square \text{---} \square \text{---} \dots \text{---} \square \end{array} \quad (5.50)$$

Finding the ground state is then equivalent to minimizing the energy for a normalized state

$$\min_{\langle \phi | \phi \rangle = 1} \langle \phi | \hat{H} | \phi \rangle. \quad (5.51)$$

Although the minimization with respect to the full state $|\phi\rangle$ is not in general possible, given a trial state $|\psi\rangle$, we can locally optimize nodes of eq. (5.50). For a fixed tensor

geometry, the DMRG is independent of the particular Hamiltonian under consideration, thus we omit its details in the following.

We consider a trial state $|\phi\rangle$ in form of a tensor train with a center of orthogonality at position i . The energy is given by the network

$$E_\phi = \text{[Diagram showing tensor network contraction]} \quad (5.52)$$

We select the center of orthogonality and one adjacent node, in this case the *right* one, and contract the rest indicated by the dashed rectangles. Next, we locally minimize the energy, keeping all other nodes fixed. This corresponds to finding the eigenstate with the lowest energy of the matrix represented by the tensor

$$\mathbf{H}_{[i:i+2]}^\phi := \text{[Diagram of effective two-site Hamiltonian]} \quad (5.53)$$

where the red dashed line indicates the bipartition. The matrix $\mathbf{H}_{[i:i+2]}^\phi$ is called the effective two-site Hamiltonian. A dense matrix-vector product costs only of the order of $\mathcal{O}(d^4\chi^4)$ operations, where χ is the bond dimension of the state and d the local physical dimension. Using the tensor network structure this can be reduced to $\mathcal{O}(2hd^2\chi^3)$, where h is the dimension of the bonds of the Hamiltonian. The size of this problem is manageable, i.e., standard sparse diagonalization algorithms like e.g. Lanczos [9, 133] or Davidson [134] can be employed. The tensor-train representation of the state $|\phi\rangle$ provides a starting point that can be used in iterative diagonalization methods. Furthermore, since we only perform a local optimization, a lower accuracy result is sufficient; we can increase the accuracy in later iterations.

The sparse diagonalization yields the new node for the two sites i and $i+1$, which we split via SVD

$$|\phi_{[i:i+2]}^{\text{new}}\rangle := \text{[Diagram of SVD decomposition]} \quad (5.54)$$

The internal bond dimensions grow by the physical dimension d , compared to the outer bond dimensions. Thus, the local optimization can automatically increase the bond dimension. The full new state is the old state $|\phi\rangle$, where the two nodes $|\phi_{[i:i+2]}\rangle$ are replaced by $|\phi_{[i:i+2]}^{\text{new}}\rangle$. The new nodes are the center of orthogonality of the state, thus we can truncate (and re-normalize) the smallest singular values to compress the tensor, reducing the bond dimension $d\chi \rightarrow \tilde{\chi}$. We can contract the node of singular values either with the left neighboring node, keeping the center of orthogonality at the same site, or contract it with the right node, moving the center from site i to the right to $i + 1$:

$$|\phi_{[i:i+2]}^{\text{new}}\rangle \approx \begin{array}{c} x \\ \text{---} \end{array} \begin{array}{c} d \\ \text{---} \end{array} U \begin{array}{c} \tilde{\chi} \\ \text{---} \end{array} \begin{array}{c} d \\ \text{---} \end{array} \sigma \begin{array}{c} \tilde{\chi} \\ \text{---} \end{array} \begin{array}{c} d \\ \text{---} \end{array} V^\dagger \begin{array}{c} x \\ \text{---} \end{array} = \begin{array}{c} x \\ \text{---} \end{array} \begin{array}{c} d \\ \text{---} \end{array} U \begin{array}{c} \tilde{\chi} \\ \text{---} \end{array} \begin{array}{c} d \\ \text{---} \end{array} \square \begin{array}{c} x \\ \text{---} \end{array}. \quad (5.55)$$

Having moved the center of orthogonality one site to the right, we can repeat the procedure optimizing the next two nodes $i + 1$ and $i + 2$. This is the essence of the two-site DMRG: We sweep the tensor state from left to right and back, always optimizing two nodes at a time using an iterative diagonalization method. After the local optimization, we split the new node and truncate the smallest singular values. Thus, the bond dimensions are automatically adjusted. The contractions of the energy eq. (5.52) for the two-site Hamiltonian eq. (5.53) can be reused for efficiency, as we always move only by a single site. We calculate all partial contractions and save them; in every step we only have to update a single contraction, where the nodes changed.

DMRG is a variational method, minimizing the energy by locally optimizing nodes in a sweeping procedure, left to right and back. The energy monotonously decreases with every DMRG step. However, the method can get stuck in local energy minima. This can be amended by combining the DMRG method with, e.g., an imaginary time evolution [135]. Another option is to consider more than two sites at once [136]. The DMRG method described here readily generalizes from tensor trains to loop-free tensor trees, e.g. to the fork tensor-product states [120] for the multi-orbital SIAM.

5.4. Subspace expansion for single-site methods

It can be preferable to optimize only a single site at a time instead of two, as this is computationally cheaper. Naively, this can be done by simply replacing the two-site Hamiltonian eq. (5.53) by an effective one-site Hamiltonian $\mathbf{H}_{[i:i+1]}^\phi$. This naive single-site algorithm, however, would be prone to getting stuck in local minima. Furthermore, it lacks the automatic adjustment of the bond dimensions, which is naturally present in the two-site algorithm, where the bond dimension between the updated nodes increases eq. (5.54). White [137] proposed a correction term for the density matrix to amend these problems. For the tensor-train formulation, a subspace expansion [138] can be used to increase the bond dimension by hand.

We consider the left-to-right sweep. After optimizing the center of orthogonality at site i , the subspace expansion is used to enlarge the bond χ_i between site i and $i + 1$. We introduce the following graphical notation for the expansion:

$$\begin{array}{c} i \\ \text{---} \end{array} M \begin{array}{c} x_i \\ \text{---} \end{array} \begin{array}{c} i+1 \\ \text{---} \end{array} B = \begin{array}{c} i \\ \text{---} \end{array} \begin{array}{c} M \\ P \end{array} \begin{array}{c} x_i \\ \text{---} \end{array} \begin{array}{c} B \\ 0 \end{array} \begin{array}{c} i+1 \\ \text{---} \end{array}, \quad (5.56)$$

where M and P denote the nodes at sites i and $i + 1$, the blue-shaded parts indicate the expansion terms. Formally, we concatenate the node $M \in \mathbb{C}^{\chi_{i-1} \times d_i \times \chi_i}$ at site i with an expansion term $P \in \mathbb{C}^{\chi_{i-1} \times d_i \times \chi_P}$:

$$\tilde{M}_{l\sigma r} = \begin{cases} M_{l\sigma r} & \text{if } r \leq \chi_i, \\ P_{l\sigma r'} \text{ with } r' = r - \chi_i & \text{else,} \end{cases} \quad (5.57)$$

or in short $\tilde{M} = \begin{pmatrix} M & P \end{pmatrix}$. We have to expand the node $B \in \mathbb{C}^{\chi_i \times d_{i+1} \times \chi_{i+1}}$ at site $i + 1$ accordingly by padding it with zeros

$$\tilde{B}_{l\sigma r} = \begin{cases} B_{l\sigma r} & \text{if } l \leq \chi_i, \\ 0 & \text{else,} \end{cases} \quad (5.58)$$

or in short $\tilde{B} = \begin{pmatrix} B & 0 \end{pmatrix}$. This expansion amounts to adding a zero, written in matrix notation

$$\begin{pmatrix} M \\ P \end{pmatrix} \begin{pmatrix} B & 0 \end{pmatrix} = MB + P0 = MB. \quad (5.59)$$

After the artificial expansion, eq. (5.56), a truncated SVD of the node \tilde{M} with subsequent normalization is performed and the center of orthogonality is moved to the right:

The diagrammatic equation (5.60) illustrates the decomposition of a tensor product. On the left, a horizontal line represents a tensor network. It consists of a box labeled M with a vertical line on top and a horizontal line on the bottom. Below the M box is a blue-shaded box labeled P with a vertical line on top and a horizontal line on the bottom. A horizontal line labeled χ_i connects the right side of the M box to the left side of a trapezoidal box labeled B . Below the B box is a blue-shaded box labeled 0 with a vertical line on top and a horizontal line on the bottom. A horizontal line labeled χ_P connects the right side of the B box to the left side of the 0 box. This is followed by an approximation symbol \approx . The middle part shows a trapezoidal box on the left, a diamond-shaped box labeled $\tilde{\chi}_i$ in the center, and another trapezoidal box on the right. A dashed box encloses the diamond and the right trapezoid. A horizontal line labeled $\tilde{\chi}_i$ connects the left trapezoid to the diamond. A horizontal line labeled χ_i connects the diamond to the right trapezoid. Below the right trapezoid is a blue-shaded box labeled B with a vertical line on top and a horizontal line on the bottom. Below the B box is a blue-shaded box labeled 0 with a vertical line on top and a horizontal line on the bottom. A horizontal line labeled χ_P connects the right side of the B box to the left side of the 0 box. This is followed by an equals sign $=$. The final part shows a trapezoidal box on the left, a square box labeled $\tilde{\chi}_i$ in the center, and a vertical line on the right. A horizontal line labeled $\tilde{\chi}_i$ connects the left trapezoid to the square box.

Equations (5.56) and (5.60) allow to dynamically adjust the bond dimension, just like in the two-site DMRG eqs. (5.54) and (5.55). Suitable terms for the subspace expansion P are given by Hubig et al. [138] based on Dolgov and Savostyanov [139]. We conclude that the use of the subspace expansion allows for efficient single-site versions of the DMRG [138], which automatically adjusts the size of bond dimensions by introducing additional degrees of freedom.

5.5. Density matrix in tensor trains

At this point, the reader might wonder why the algorithm is named density matrix renormalization group, as the density matrix has not been mentioned yet. In his seminal work [21], White introduced the density matrix to decide which states to keep in the truncation scheme. In the tensor formulation, this corresponds to the compression of tensor trains discussed in section 5.1 and using eq. (5.54) in the DMRG algorithm. White [22] established the connection between the density matrix and the SVD; we introduce the density matrix ρ to show that the SVD used in the two-site DMRG corresponds to the diagonalization of ρ .

The density matrix is usually introduced by a bipartition of the universe into the system and its environment [140]. A general state then reads

$$|\Psi\rangle = \sum_{ij} C_{ij} |\phi_i\rangle \otimes |\theta_j\rangle, \quad (5.61)$$

where $|\phi_i\rangle$ is a complete basis of the system, and $|\theta_j\rangle$ a complete basis of the environment. The density matrix is then defined as

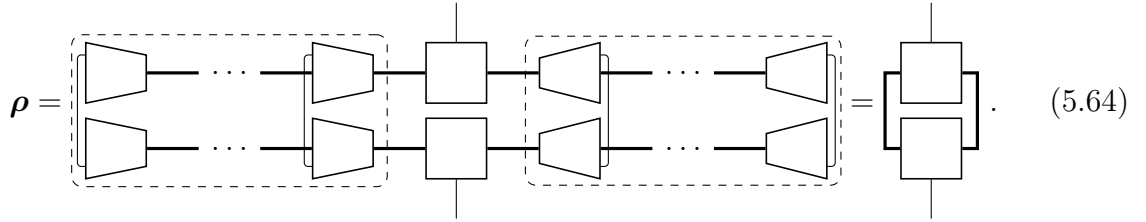
$$\rho := \mathbf{C}\mathbf{C}^\dagger \quad \rho_{ii'} = C_{ij}C_{ji'}^*, \quad (5.62)$$

such that the expectation value of an operator \hat{O} , acting only on the system, can be written as the trace over the system

$$\langle\Psi|\hat{O}|\Psi\rangle = \sum_{ii'} \langle\phi_i|\hat{O}|\phi_{i'}\rangle \rho_{i'i} = \text{Tr } \mathbf{O}\rho \quad (5.63)$$

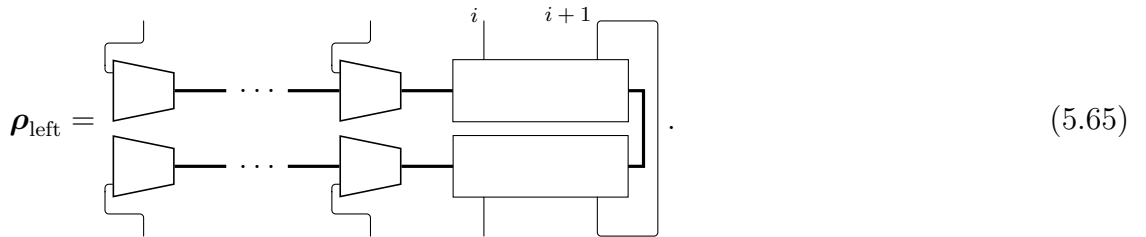
with $(\mathbf{O})_{ii'} = \langle\phi_i|\hat{O}|\phi_{i'}\rangle$.

We consider a state $|\psi\rangle$ represented by a tensor train, eq. (5.24). If the center of orthogonality of the state is considered as ‘system’ and the other sites as ‘environment’, the density matrix takes a very simple form:



$$\rho = \text{[Diagram]} = \text{[Simplified Diagram]}. \quad (5.64)$$

Tracing out the isometric tensors yields only identities, thus the density matrix is fully described by the center of orthogonality. In the DMRG algorithm discussed in the previous section, we partition the state in ‘left’ (system) and ‘right’ (environment), where the middle is between the sites i and $i+1$ which have been optimized, eq. (5.54). The density matrix of the left half, where the right half (environment) was traced out, reads



$$\rho_{\text{left}} = \text{[Diagram]} = \text{[Simplified Diagram]}. \quad (5.65)$$

It is well known that the SVD of a matrix \mathbf{C} diagonalizes the matrix product $\mathbf{C}\mathbf{C}^\dagger$:

$$\mathbf{C} = \mathbf{U}\mathbf{\Sigma}\mathbf{V}^\dagger \Rightarrow \rho = \mathbf{C}\mathbf{C}^\dagger = \mathbf{U}\mathbf{\Sigma}^2\mathbf{U}^\dagger. \quad (5.66)$$

Apparently, splitting the double-node using SVD, eq. (5.54), corresponds to a truncated diagonalization of the density matrix, where the eigenvalues correspond to the squared

the singular values:

Thus, the truncation of the density matrix in the original algorithm is encoded in the SVD [22].

5.6. Time-dependent variational principle

There is a variety of methods available to time-evolve tensor trains, Paeckel et al. [20] gave a recent overview and comparison of the methods. A typical approach to time evolution is a Trotter-Suzuki [141, 142] decomposition. It is the basis of the so-called time-evolving block decimation (TEBD) by Vidal [143, 144]. We focus on a different approach, the TDVP by Haegeman et al. [145, 146] and Lubich et al. [147].

5.6.1. Dirac-Frenkel time-dependent variational principle

First we provide the abstract formulation of the TDVP following ref. [148]. The first usage is attributed to Dirac [149] deriving the equation of motion of the time-dependent Hartree-Fock method.

We start by defining the Lagrange density² [150, 151]

$$\mathcal{L}'[\psi^*(t), \psi(t)] = \langle \psi(t) | i\hbar\partial_t - \hat{H} | \psi(t) \rangle \quad (5.68)$$

and the action

$$\mathcal{A}' = \int_{t_1}^{t_2} dt \mathcal{L}'[\psi^*(t), \psi(t)]. \quad (5.69)$$

Variation of the action \mathcal{A}' with respect to $\psi^*(t)$ generates the time-dependent Schrödinger equation

$$\frac{\delta \mathcal{A}'}{\delta \langle \psi(t) |} = [i\hbar\partial_t - \hat{H}] |\psi(t)\rangle. \quad (5.70)$$

Fixing the endpoints $\delta\psi(t_1) = \delta\psi(t_2) = 0$, and doing a partial integration, the variation with respect to $\psi(t)$ generates the adjoint equation

$$\frac{\delta \mathcal{A}'}{\delta |\psi(t)\rangle} = \langle \psi(t) | [-i\hbar\overleftarrow{\partial}_t - \hat{H}]; \quad (5.71)$$

²The prime is used here as the Lagrange density is not symmetrized and appropriate for normalized states. These subtleties are not relevant for this section and thus are not elaborated further, see ref. [150] for more details.

were the arrow indicates that the derivative acts on the left. Demanding that the variation of the action \mathcal{A}' vanishes

$$0 \stackrel{!}{=} \delta\mathcal{A}' = \langle \delta\psi(t) | i\hbar\partial_t - \hat{H} | \psi(t) \rangle + \langle \psi(t) | -i\hbar\overleftarrow{\partial}_t - \hat{H} | \delta\psi(t) \rangle \quad (5.72)$$

and is thus equivalent to the time-dependent Schrödinger equation, as the variations $\delta\psi$ and $\delta\psi^*$ are independent. A common approach is to approximate the solution, e.g. using a Trotter decomposition. The variational principle, on the other hand, enables us to approximate the Schrödinger equation by restricting solutions to a submanifold of the Hilbert space.

We restrict the variations to a smooth submanifold \mathcal{M} of the full Hilbert space \mathcal{H} , which contains the initial vector $|\psi(0)\rangle \in \mathcal{M}$. For every $|u\rangle \in \mathcal{M}$, $\mathcal{T}_u\mathcal{M}$ denotes the tangent space at u , which consists of all derivatives of differential paths on \mathcal{M} passing through $|u\rangle \in \mathcal{M}$ [148]. That is, for $|u(t)\rangle \in \mathcal{M}$, $\frac{\partial}{\partial t}|u(t)\rangle \in \mathcal{T}_{u(t)}\mathcal{M}$. According to the variational principle, the approximate solution $\frac{\partial}{\partial t}|u(t)\rangle \in \mathcal{T}_{u(t)}\mathcal{M}$ has to fulfill the condition

$$\langle v(t) | i\hbar\partial_t - \hat{H} | u(t) \rangle = 0 \quad \forall |v(t)\rangle \in \mathcal{T}_{u(t)}\mathcal{M}, \quad (5.73)$$

i.e., the residual is orthogonal to the tangent space. The orthogonality guarantees that the variational approximation $\frac{\partial}{\partial t}|u(t)\rangle \approx |\hat{v}(t)\rangle \in \mathcal{T}_{u(t)}\mathcal{M}$ minimizes the error

$$\left\| |\hat{v}(t)\rangle - \frac{1}{i\hbar}\hat{H}|u(t)\rangle \right\|. \quad (5.74)$$

Consider a different approximation $|\tilde{v}(t)\rangle \in \mathcal{T}_{u(t)}\mathcal{M}$. We write it in terms of the variational approximation as $|\tilde{v}(t)\rangle = |\hat{v}(t)\rangle + |v(t)\rangle$ with $|v(t)\rangle \in \mathcal{T}_{u(t)}\mathcal{M}$. Therefore, the error of the approximation $|\tilde{v}(t)\rangle$ is

$$\left\| |\tilde{v}(t)\rangle - \frac{1}{i\hbar}\hat{H}|u(t)\rangle \right\| = \left\| |\hat{v}(t)\rangle - \frac{1}{i\hbar}\hat{H}|u(t)\rangle \right\| + 2\Re \left\langle v(t) \left| \hat{v}(t) - \frac{1}{i\hbar}\hat{H}|u(t)\rangle \right. \right\rangle + \|v(t)\|. \quad (5.75)$$

The second summand vanishes as the approximate solution $|\hat{v}(t)\rangle$ is chosen such that it fulfills the variational principle, eq. (5.73), proving that $|\hat{v}(t)\rangle \in \mathcal{T}_{u(t)}\mathcal{M}$ indeed minimizes the error. The difference between $|\hat{v}(t)\rangle$ and the exact time evolution is orthogonal to the tangent space $\mathcal{T}_{u(t)}\mathcal{M}$; therefore, we can rewrite eq. (5.73) as a differential equation on the manifold \mathcal{M} [148]:

$$\frac{\partial}{\partial t}|u(t)\rangle = \hat{P}_u \frac{1}{i\hbar}\hat{H}|u(t)\rangle, \quad (5.76)$$

where \hat{P}_u is the projector onto the tangent space $\mathcal{T}_{u(t)}\mathcal{M}$. In the following, we set $\hbar = 1$ as usual.

5.6.2. Projection onto tangent space of tensor trains

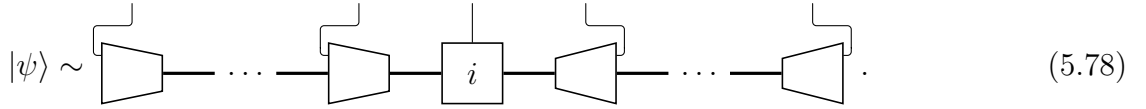
The applications of the TDVP to tensor trains is given by Haegeman et al. [146] and Lubich et al. [147]; for the overview of the time-evolution algorithms see Paeckel et al. [20].

We choose the submanifold of tensor trains \mathcal{M}_{TT} and solve the Schrödinger equations projected to the tangent space $\mathcal{T}_{\psi[\mathbf{A}(t)]}\mathcal{M}_{TT}$:

$$\frac{\partial}{\partial t} |\psi[\mathbf{A}(t)]\rangle = -i\hat{P}_{\psi}\hat{H} |\psi[\mathbf{A}(t)]\rangle, \quad (5.77)$$

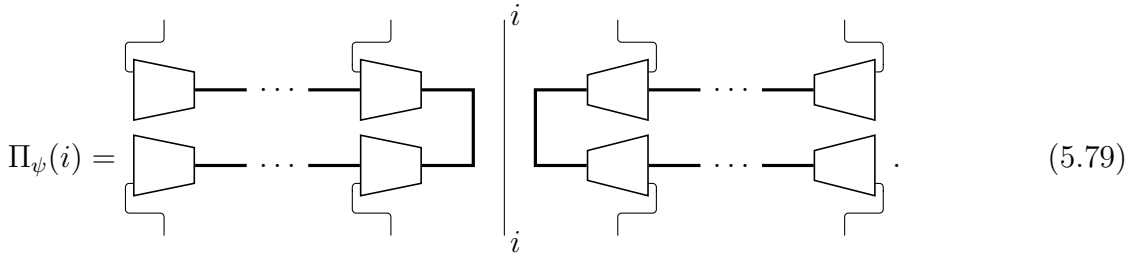
where \hat{P}_{ψ} is the projector on the tangent space $\mathcal{T}_{\psi[\mathbf{A}(t)]}\mathcal{M}_{TT}$ [152]. In this notation, the elements of $\mathbf{A}(t)$ represent the nodes of the tensor train representing the state ψ .

First, we discuss the explicit form of the projector \hat{P}_{ψ} . The detailed derivation of the projector is given in the references [146, 147]. We first define the site projector $\Pi_{\psi}(i)$, which projects onto the space of tensor-train states which only differ from $|\psi\rangle$ in the node at site i . Using the gauge freedom of the tensor train, we write the state $|\psi\rangle$ as tensor train with a center of orthogonality at site i :



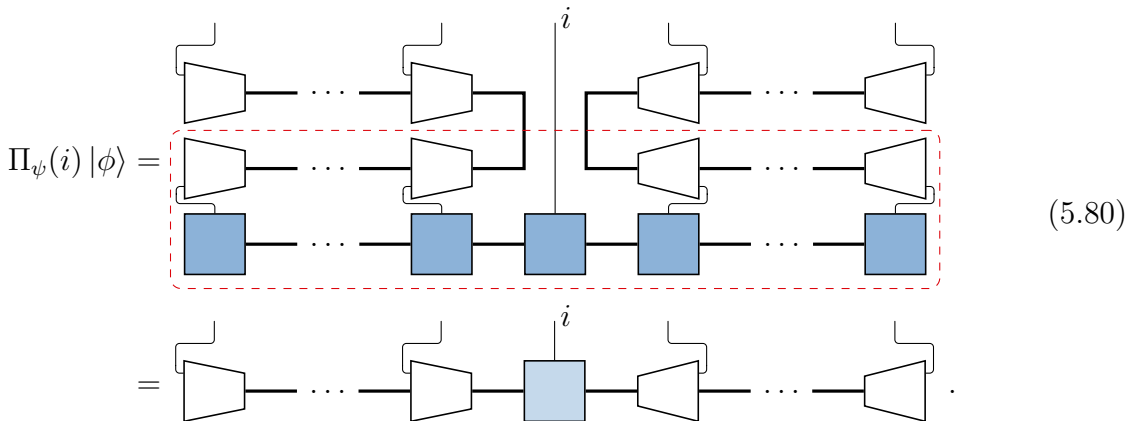
The diagram shows a horizontal chain of trapezoidal tensors connected by horizontal lines. The central tensor is labeled 'i'. The chain is symmetric around this central tensor, with ellipses indicating continuation on both sides. Each tensor has two legs extending upwards and two extending downwards.

For this state, we define the projector $\Pi_{\psi}(i)$ as



The diagram shows two identical tensor train structures side-by-side, separated by a vertical line labeled 'i'. Each structure consists of two rows of trapezoidal tensors. The top row tensors are connected to the bottom row tensors at site 'i' by a vertical line. Ellipses indicate continuation of the chains on both sides.

From the isometry, it is clear that this is indeed a projector $\Pi_{\psi}^2(i) = \Pi_{\psi}(i)$. Applying the projector $\Pi_{\psi}(i)$ to the state $|\psi\rangle$ fixes the gauge such that the center of orthogonality is at site i . Applying $\Pi_{\psi}(i)$ to a different state $|\phi\rangle$ (shaded in blue), likewise fixes the center of orthogonality to the site i , furthermore the state $\Pi_{\psi}(i)|\phi\rangle$ can differ from $|\psi\rangle$ only in the node at site i :



The diagram shows the application of the projector $\Pi_{\psi}(i)$ to a state $|\phi\rangle$. The top part shows the projector (two rows of tensors) applied to the state $|\phi\rangle$ (a single row of blue-shaded tensors). A red dashed rectangle encloses the tensors at site 'i' from both the projector and the state. The bottom part shows the result: a single row of tensors where the central tensor at site 'i' is blue, while all other tensors are white. The vertical line 'i' is present in both parts.

Contracting the nodes in the red rectangle yields the center of orthogonality node at site i . All other nodes are identical to those of $|\psi\rangle$. As we want to project to the tangent space, we still need to remove states parallel to $|\psi\rangle$. Again using the gauge freedom of

identities effectively replaces the identity at site i in $\Pi_\psi(i)$ by isometric nodes analogous to $\Pi_\psi(\bar{i})$ such that the difference of the two terms vanishes, resulting in the orthogonality eq. (5.85). Analogously, we can show that for any $i \geq j$ the bond and site projectors are orthogonal to the difference in the brackets:

$$\Pi_\psi(j)[\Pi_\psi(i+1) - \Pi_\psi(\bar{i})] = 0, \quad \Pi_\psi(\bar{j})[\Pi_\psi(i+1) - \Pi_\psi(\bar{i})] = 0. \quad (5.87)$$

Using the orthogonality relations eqs. (5.85) and (5.87), we find

$$\Pi_\psi(j)\hat{P}_\psi = \Pi_\psi(j)\left(\sum_{i=1}^{j-1}[\Pi_\psi(i) - \Pi_\psi(\bar{i})] + \sum_{i=j}^{N-1}[\Pi_\psi(i+1) - \Pi_\psi(\bar{i})] + \Pi_\psi(j)\right) = \Pi_\psi(j), \quad (5.88)$$

$$\Pi_\psi(\bar{j})\hat{P}_\psi = \Pi_\psi(\bar{j})\left(\sum_{i=1}^j[\Pi_\psi(i) - \Pi_\psi(\bar{i})] + \sum_{i=j}^{N-1}[\Pi_\psi(i+1) - \Pi_\psi(\bar{i})] + \Pi_\psi(\bar{j})\right) = \Pi_\psi(\bar{j}). \quad (5.89)$$

Thus, the tangent-space projector \hat{P}_ψ eq. (5.83) is indeed a projector $\hat{P}_\psi^2 = \hat{P}_\psi$.

Substituting the explicit form of the tangent-space projector eq. (5.83) into the time-dependent Schrödinger equation eq. (5.77), we obtain the system of coupled differential equations

$$\frac{\partial}{\partial t} |\psi\rangle = -i\hat{P}_\psi\hat{H}|\psi\rangle = \sum_{i=1}^{N-1} [-i\Pi_\psi(i)\hat{H} + i\Pi_\psi(\bar{i})\hat{H}]|\psi\rangle - i\Pi_\psi(N)\hat{H}|\psi\rangle. \quad (5.90)$$

The projection on the sites $\Pi_\psi(i)$ can be interpreted as forward time evolution, and the projection on the bonds $\Pi_\psi(\bar{i})$ as backward time evolution. The equation can be decoupled using eqs. (5.88) and (5.89), projecting the Schrödinger equation to sites and bonds:

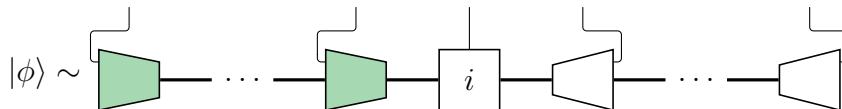
$$\begin{aligned} \Pi_\psi(i)\frac{\partial}{\partial t} |\psi\rangle &= -i\Pi_\psi(i)\hat{H}|\psi\rangle \quad \forall i \in \{1, \dots, N\} \\ \Pi_\psi(\bar{i})\frac{\partial}{\partial t} |\psi\rangle &= +i\Pi_\psi(\bar{i})\hat{H}|\psi\rangle \quad \forall i \in \{1, \dots, N-1\}. \end{aligned} \quad (5.91)$$

These locally projected Schrödinger equations each evolve a single site or bond node and can be integrated in closed form. This is the essential idea of the TDVP, the algorithm will be stated in the next section.

5.6.3. Single-site time-dependent variational principle

The TDVP can be implemented analogous to the DMRG as a sweeping algorithm going back and forth, locally updating the nodes at a site [146, 147]. In this case, instead of minimizing the energy, the nodes are time evolved.

We consider a state with center of orthogonality i ,



$$|\phi\rangle \sim \text{---} \left[\text{Green Node} \right] \text{---} \dots \text{---} \left[\text{Green Node} \right] \text{---} \left[\text{Square Node } i \right] \text{---} \dots \text{---} \left[\text{White Node} \right] \text{---} \dots \text{---} \left[\text{White Node} \right] \text{---} \quad (5.92)$$

and explicitly show a single update for the left-to-right sweep. The green-shaded nodes left to the center indicate sites that have already been transformed by the update described in the following. Analogous to the two-site effective Hamiltonian eq. (5.53) for DMRG, (1) we define the effective one-site Hamiltonian for TDVP as

$$\begin{aligned}
 H_{[i:i+1]}^\phi &:= \text{Diagram with green and white tensors} \\
 &= \text{Diagram with green and white blocks and a red dashed line}
 \end{aligned}
 \tag{5.93}$$

Again, the red dashed line indicates the bipartition. (2) We evolve the center of orthogonality by half a step $\delta/2$ forward in time, exactly integrating the node

$$\begin{aligned}
 |\phi_{[i:i+1]}(t + \delta/2)\rangle &:= \text{Diagram with green node } i \\
 &:= \exp\left(-i\frac{\delta}{2}\right) \cdot \text{Diagram with green and white blocks}
 \end{aligned}
 \tag{5.94}$$

Applying the (matrix) exponential of the one-site Hamiltonian to the original node (white) yields the new time-evolved node (green) at site i . The action of the matrix exponential [153] on the vector can be accurately evaluated using only matrix-vector products [154], allowing to use the tensor structure instead of explicitly constructing a dense matrix, just like for the energy minimization in DMRG. (3) We split the new node using the QR-algorithm

$$|\phi_{[i:i+1]}(t + \delta/2)\rangle = \text{Diagram with green node } i = \text{Diagram with green trapezoid and green square}
 \tag{5.95}$$

The node $|\phi_{[i:i+1]}\rangle$ is replaced by the new time evolved node $|\phi'_{[i:i+1]}\rangle = |\phi_{[i:i+1]}(t + \delta/2)\rangle$,

from which we construct the effective zero-site Hamiltonian

$$\begin{aligned}
 \mathbf{K}_i^{\phi'} &:= \text{[Diagram showing a sequence of tensors for sites } i \text{ and } i+1 \text{, with a dashed box around the } i \text{ site part.]} \\
 &= \text{[Diagram showing a contraction of the } i \text{ site part with a vertical bar, resulting in a simplified tensor structure.]}
 \end{aligned} \tag{5.96}$$

(4) We evolve the new center of orthogonality between sites i and $i + 1$ by half a step backward in time

$$\text{[Diagram showing a contraction of a tensor with a vertical bar, resulting in an exponential expression involving a tensor and a vertical bar.]} \tag{5.97}$$

(5) Finally, we contract the bond node eq. (5.97) with the node at site $i + 1$, moving the center of orthogonality one site to the right

$$|\phi_{[i+1:i+2]}^{\text{new}}(t)\rangle := \text{[Diagram showing the contraction of the bond node with a tensor at site } i+1 \text{, resulting in a new tensor structure.]} \tag{5.98}$$

Repeating steps (1) – (5) starting from the left $i = 1$, we iteratively change all nodes left of the center of orthogonality to a basis representing the state at $t + \delta/2$. When we reach the right end $i = N$, only steps (1) and (2) are applied; we do not need to split the node anymore, no backward time evolution, eqs. (5.96) to (5.98), is performed. At this point, the complete state was evolved by half a time step $\delta/2$. The algorithm is then applied again sweeping from right to left, to evolve the state by a full time step δ . The one-site algorithm conserves the normalization of states as well as energy, as only unitary time-evolutions eqs. (5.94) and (5.97) are applied, which can be performed numerically exact.

For an imaginary time evolution, the single-site TDVP is equivalent to the single-site DMRG algorithm in the limit $i\delta = \tau \rightarrow \infty$ [146]. In this case, the forward time evolution eq. (5.94) yields the ground state of the one-site Hamiltonian, eq. (5.93); contributions of states with larger eigenvalues are suppressed. As the zero-site Hamiltonian, eq. (5.96), is built from the resulting node eq. (5.95) and the one-site Hamiltonian, the backward time evolution eq. (5.97) is applied to its eigenstate. Therefore, it yields only a factor $\exp(\tau E_0)$, where E_0 is the eigenvalue, which cancels the factor $\exp(-\tau E_0)$ from the forward time evolution. Just like DMRG, the TDVP can be formulated as a two-site algorithm [146], allowing to adjust bond dimensions. In this case, however, the truncation can break the energy conservation present in the one-site algorithm. Instead of the two-site algorithm, a subspace-expansion can be employed to adjust the bond dimension in the one-site algorithm, retaining the unitarity of the time-evolution [135].

6. Multicomponent alloys: substitutional disorder [W3]

In this chapter, we consider an alloy consisting of M types of atoms ('alloy components') denoted by the index α . We model the alloy by a lattice Hamiltonian with substitutional disorder. Substitutional disorder means that every lattice site i is occupied by a certain type of component α ; the lattice structure itself is not affected by the disorder. Every lattice site i is uniquely mapped to a particular component α as expressed by

$$i \mapsto \alpha \equiv \text{site } i \text{ is occupied by component } \alpha. \quad (6.1)$$

This is the physical situation in multicomponent alloys. To address multiple sites, we use the notation

$$i, j \mapsto \alpha, \beta := (i \mapsto \alpha) \wedge (j \mapsto \beta). \quad (6.2)$$

We refer to a specific mapping of the N lattice sites to the M components as a *configuration* (conf) or *disorder realization*. A certain disorder configuration, conf, maps every site to one specific component

$$\text{conf} : \{i\} \rightarrow \{\alpha\}. \quad (6.3)$$

Mathematically, a configuration is therefore a function

$$i \mapsto \text{conf}(i). \quad (6.4)$$

We denote the set of all possible configurations by

$$\mathbb{C} = \{\text{conf}\}. \quad (6.5)$$

As the specific configuration of a sample measured in an experiment is unknown, the common procedure is to average over all possible configurations. Typically, the concentrations c^α of the different components α are assumed to be known, thus we restrict the average to configurations compatible with these concentrations. For a given configuration, conf, we denote the set of lattice sites i occupied by component α as

$$\mathbb{S}^\alpha := \{i | i \mapsto \alpha\}. \quad (6.6)$$

For a given set of concentrations $\{c^\alpha\}$, a physical configuration must fulfill the conditions that the size (cardinality) of \mathbb{S}^α matches the concentrations:

$$|\mathbb{S}^\alpha| \stackrel{!}{=} Nc^\alpha \quad \text{with} \quad \sum_{\alpha} |\mathbb{S}^\alpha| = N = \sum_i 1. \quad (6.7)$$

The set of configurations restricted to the given concentrations $\{c^\alpha\}$ is denoted

$$\mathbb{C}_{\{c^\alpha\}} := \left\{ \text{conf} \mid \bigwedge_{\alpha} (|\mathbb{S}^\alpha| = Nc^\alpha) \right\}. \quad (6.8)$$

In the absence of additional information, we assume the probability of each physical configuration to be identical:

$$\forall \text{conf} \in \mathbb{C}_{\{c^\alpha\}} : \quad P(\text{conf}) = \frac{1}{|\mathbb{C}_{\{c^\alpha\}}|}. \quad (6.9)$$

Let X be a random variable, its possible realizations are denoted x_{conf} ; they depend on the configuration. The stochastic average of X is the weighted sum over all physical configurations

$$\mathbb{E}(X) = \sum_{\text{conf} \in \mathbb{C}_{\{c^\alpha\}}} P(\text{conf}) x_{\text{conf}} = \frac{1}{|\mathbb{C}_{\{c^\alpha\}}|} \sum_{\text{conf} \in \mathbb{C}_{\{c^\alpha\}}} x_{\text{conf}}. \quad (6.10)$$

The probability for a specific lattice site i to be occupied by the component α is the concentration of that component $P(i \mapsto \alpha) = c^\alpha$.

6.1. Tight-binding Hamiltonian [W3]

For a specific configuration, we consider the tight-binding (Anderson) model

$$\hat{H} = \sum_i v_i \hat{n}_i - \sum_{ij} t_{ij} \hat{c}_i^\dagger \hat{c}_j, \quad (6.11)$$

with configuration dependent on-site energies v_i and hopping elements t_{ij} . The hopping elements are Hermitian $t_{ij} = t_{ji}^*$ and off-diagonal, that is $t_{ii} = 0$. In this section, we omit the explicit spin-dependency. While this model is non-interacting, we can include effective local interactions by replacing $v_i \rightarrow v_i + \Sigma_i(z)$. The 1-particle Hamiltonian can be written in the compact matrix form

$$\hat{H} =: \hat{\mathbf{c}}^\dagger \mathbf{H} \hat{\mathbf{c}}, \quad \mathbf{H} = \mathbf{v} + \mathbf{T}, \quad H_{ij} = v_{ij} + T_{ij} = \delta_{ij} v_i + t_{ij}, \quad (6.12)$$

where we introduced $N \times 1$ column matrices to represent the operators. The rows of the matrix $\hat{\mathbf{c}}$ are the annihilation operators, $(\hat{\mathbf{c}})_{[i,:]} = \hat{c}_i$. We call \mathbf{H} the (1-particle) Hamiltonian matrix.

The magnitude of the hopping parameters t_{ij} depends on the alloy components located on sites i and j , respectively, which are referred to as *terminal points*. In the following we employ the *terminal-point approximation* [155, 156] which assumes the parameters with terminal points i, j, k, \dots depend only on the components occupying sites i, j, k, \dots and not on the components surrounding these sites. Thus, for a specific configuration (disorder realization) the parameters v_i and t_{ij} take a value depending on the component occupying the respective site or sites. We denote these configuration-specific values with Fraktur letters with a superscript indicating the component. If site i is occupied by component α , i.e., $i \mapsto \alpha$, the parameter v_i takes the value \mathfrak{v}^α . If sites i and j are occupied by components α and β respectively, i.e., $i, j \mapsto \alpha, \beta$, the parameter t_{ij} takes the value $\mathfrak{t}^{\alpha\beta}(|\mathbf{r}_i - \mathbf{r}_j|)$.

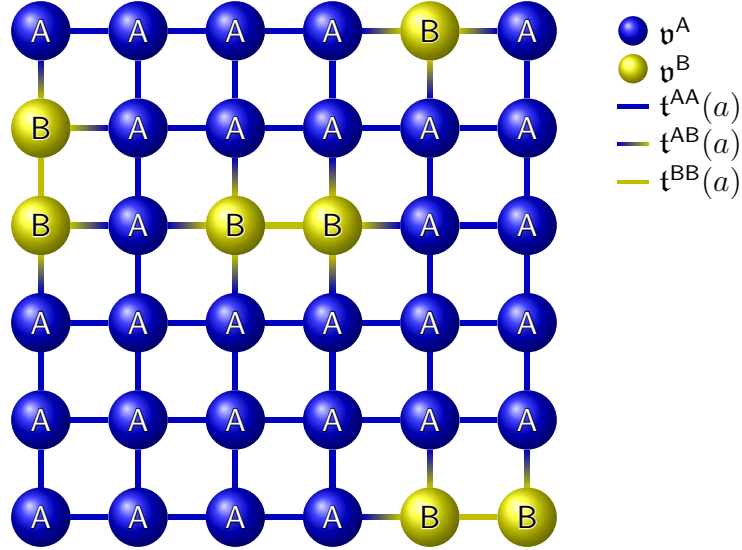


Figure 6.1.: Sketch of a configuration for a disordered binary alloy with two components A and B. The parameters in eq. (6.14) are determined by the components occupying the sites as indicated by the legend; the lattice constant is denoted a .

This will be formalized in the following. The terminal point approximation can be expressed conveniently using the indicator function

$$1_{\mathbb{S}^\alpha}(i) := \begin{cases} 1 & \text{if } i \in \mathbb{S}^\alpha, \\ 0 & \text{if } i \notin \mathbb{S}^\alpha. \end{cases} \quad (6.13)$$

Since every site must be occupied by exactly one component, the sum over components is one: $\sum_\alpha 1_{\mathbb{S}^\alpha}(i) = 1$. Thus, the parameters of the Hamiltonian eq. (6.11) read

$$v_i = \sum_\alpha 1_{\mathbb{S}^\alpha}(i) \mathbf{v}^\alpha, \quad t_{ij} = \sum_{\alpha\beta} 1_{\mathbb{S}^\alpha}(i) \mathbf{t}^{\alpha\beta}(|\mathbf{r}_i - \mathbf{r}_j|) 1_{\mathbb{S}^\beta}(j), \quad (6.14)$$

$$H_{ij} = \sum_{\alpha\beta} 1_{\mathbb{S}^\alpha}(i) \mathfrak{H}_{ij}^{\alpha\beta} 1_{\mathbb{S}^\beta}(j), \quad \text{with } \mathfrak{H}_{ij}^{\alpha\beta} = \delta_{ij} \delta^{\alpha\beta} \mathbf{v}^\alpha - \mathbf{t}^{\alpha\beta}(|\mathbf{r}_i - \mathbf{r}_j|). \quad (6.15)$$

This means, we have a finite set of different values $v_i \in \{\mathbf{v}^\alpha\}$, $t_{ij} \in \{\mathbf{t}^{\alpha\beta}(|\mathbf{r}_i - \mathbf{r}_j|)\}$, where the size of the sets is determined by the number of components $|\{\mathbf{v}^\alpha\}| = M$, $|\{\mathbf{t}^{\alpha\beta}(|\mathbf{r}_i - \mathbf{r}_j|)\}| = M^2$. We further note, that the conditional expectation value of parameters equals component variables written in Fraktur

$$\mathbb{E}(v_i | i \mapsto \alpha) = \mathbf{v}^\alpha, \quad \mathbb{E}(t_{ij} | i, j \mapsto \alpha, \beta) = \mathbf{t}^{\alpha\beta}(|\mathbf{r}_i - \mathbf{r}_j|), \quad \mathbb{E}(H_{ij} | i, j \mapsto \alpha, \beta) = \mathfrak{H}_{ij}^{\alpha\beta}. \quad (6.16)$$

The Hamiltonian eq. (6.11) is quadratic; it contains only terms with pairs of creation/annihilation operators. Thus, the Green's function $\mathbf{G}(z)$ is given by the resolvent of the Hamiltonian matrix \mathbf{H} :

$$\mathbf{G}(z) = [\mathbb{1}z - \mathbf{H}]^{-1}. \quad (6.17)$$

The central task for disordered systems is to calculate the average Green's function $\mathbb{E}(\mathbf{G}(z))$. We are mostly interested in the average of the local Green's function $\mathbb{E}(G_{ii}(z))$,

as it determines the average spectral function. Furthermore, we investigate the conditional average $\mathbb{E}(G_{ii}(z)|i \mapsto \alpha)$. According to the law of total probability [157] the expectation value is

$$\mathbb{E}(G_{ii}(z)) = \sum_{\alpha} \mathbb{E}(G_{ii}(z)|i \mapsto \alpha)P(i \mapsto \alpha) = \sum_{\alpha} \mathbb{E}(G_{ii}(z)|i \mapsto \alpha)c^{\alpha}; \quad (6.18)$$

the conditional averages fully determine the average.

Notation convention. Lowercase boldface symbols, e.g. \mathbf{v} , indicate diagonal matrices; uppercase boldface symbols, e.g. \mathbf{T} , indicate matrices which contain off-diagonal elements. Indices indicating components are denoted by Greek superscripts (α, β); indices indicating lattice sites are denoted by roman subscripts (i, j). Fraktur, e.g. \mathfrak{v}^{α} , is used for component dependent quantities. In particular, it is used for matrices in *component* space, e.g. \mathfrak{S} , which we introduce in detail in section 6.4.1.

6.2. Propagator expansion and the \mathcal{T} -matrix

We choose the propagator expansion to derive approximate methods to treat disorder, compare e.g. Gonis [158]. Therefore, we give a short definition of the propagator expansion and the \mathcal{T} -matrix. We consider a non-interacting Hamiltonian \mathbf{H} , then the Green's function is given by the resolvent eq. (6.17) and the propagator expansion is expressed in terms of simple linear algebra. All equations in this section 6.2 are exact, no approximations are applied. We partition the Hamiltonian matrix

$$\mathbf{H} = \mathbf{H}_0 + \mathbf{V} \quad (6.19)$$

where \mathbf{V} is considered as a perturbation. In this section, \mathbf{V} can be any matrix; for the application to disorder, \mathbf{V} describes the random, or rather component dependent quantities, while \mathbf{H}_0 describes the homogeneous nonrandom contribution. The Green's function corresponding to the nonrandom part \mathbf{H}_0 is the resolvent

$$\mathbf{G}_0(z) := [\mathbf{1}z - \mathbf{H}_0]^{-1}. \quad (6.20)$$

This Green's function is called propagator as \mathbf{H}_0 typically contains the hopping processes. We write the full Green's function $\mathbf{G}(z)$ in terms of the propagator

$$\mathbf{G}(z) = [\mathbf{1}z - \mathbf{H}]^{-1} = \mathbf{G}_0(z)[\mathbf{1} - \mathbf{V}\mathbf{G}_0(z)]^{-1}. \quad (6.21)$$

We rewrite the matrix inverse on the right-hand side of eq. (6.21):

$$\begin{aligned} [\mathbf{1} - \mathbf{V}\mathbf{G}_0(z)]^{-1} &= \mathbf{1} + [\mathbf{1} - \mathbf{V}\mathbf{G}_0(z)]^{-1}\{\mathbf{1} - [\mathbf{1} - \mathbf{V}\mathbf{G}_0(z)]\} \\ &= \mathbf{1} + [\mathbf{1} - \mathbf{V}\mathbf{G}_0(z)]^{-1}\mathbf{V}\mathbf{G}_0(z), \end{aligned} \quad (6.22)$$

where we added and subtracted the identity matrix $\mathbf{1}$. Substituting this expression back into eq. (6.21), we obtain the equation

$$\begin{aligned} \mathbf{G}(z) &= \mathbf{G}_0(z) + \mathbf{G}_0(z)[\mathbf{1} - \mathbf{V}\mathbf{G}_0(z)]^{-1}\mathbf{V}\mathbf{G}_0(z) \\ &=: \mathbf{G}_0(z) + \mathbf{G}_0(z)\mathcal{T}(z)\mathbf{G}_0(z); \end{aligned} \quad (6.23)$$

this is sometimes referred to as Schwinger equation. It defines the \mathcal{T} -matrix:

$$\mathcal{T}(z) := [\mathbf{1} - \mathbf{V}\mathbf{G}_0(z)]^{-1}\mathbf{V} = \mathbf{V} + \mathbf{V}\mathbf{G}_0(z)\mathcal{T}(z). \quad (6.24)$$

The average Green's function reads in terms of the average \mathcal{T} -matrix:

$$\mathbb{E}(\mathbf{G}(z)) = \mathbf{G}_0(z) + \mathbf{G}_0(z)\mathbb{E}(\mathcal{T}(z))\mathbf{G}_0(z). \quad (6.25)$$

Employing the Neumann series in eq. (6.21), the Green's function is expanded into a series with respect to the perturbation \mathbf{V} :

$$\mathbf{G}(z) = \mathbf{G}_0(z) \sum_{k=0}^{\infty} [\mathbf{V}\mathbf{G}_0(z)]^k = \mathbf{G}_0(z) + \mathbf{G}_0(z) \sum_{k=0}^{\infty} [\mathbf{V}\mathbf{G}_0(z)]^k \mathbf{V}\mathbf{G}_0(z). \quad (6.26)$$

Instead of the Green's function, we can also expand the \mathcal{T} -matrix:

$$\mathcal{T}(z) := [\mathbf{1} - \mathbf{V}\mathbf{G}_0(z)]^{-1}\mathbf{V} = \sum_{k=0}^{\infty} [\mathbf{V}\mathbf{G}_0]^k \mathbf{V} = \mathbf{V} \sum_{k=0}^{\infty} [\mathbf{V}\mathbf{G}_0]^k \quad (6.27)$$

In case the perturbation \mathbf{V} is small, a naive approach would be to calculate the sum up to a certain order and truncate terms of higher order in \mathbf{V} . However, this leads to large errors; at least some terms need to be treated to infinite order. A partial series of eq. (6.27) is not suitable for approximating the average Green's function $\mathbb{E}(\mathbf{G}(z))$. The reason is, that the series contains terms like

$$V_{ii}G_{0ii}(z)V_{ii}G_{0ii}(z)\dots V_{ii}, \quad (6.28)$$

where i is the lattice site; other indices are suppressed. Such terms describe multiple scattering from the same site. This term is highly correlated, as all random terms V_{ii} are at the same site and therefore identical. The expectation value of such a term is

$$\mathbb{E}(V_{ii}^n G_{0ii}^{n-1}(z)), \quad (6.29)$$

it contains the n -th moment of the random variable V_{ii} . These terms need to be treated to infinite order. This can be illustrated by the following minimal example: We consider a single site, where the on-site potential can take the two values 0 and Δ . This corresponds to the probability distribution $p(v) = c\delta(v) + (1-c)\delta(v-\Delta)$, where c is the probability¹ of the on-site energy $v = 0$. The average Green's function is the two-pole function

$$\mathbb{E}(G(z)) = \frac{c}{z} + \frac{1-c}{z-\Delta}. \quad (6.30)$$

Taking the average of every term of the series representation eq. (6.27) of the \mathcal{T} -matrix, on the other hand, yields

$$\mathbb{E}(\mathcal{T}(z)) = c\Delta \sum_{k=0}^{\infty} \Delta^k G_0^k(z) = c\Delta \sum_{k=0}^{\infty} \left(\frac{\Delta}{z}\right)^k. \quad (6.31)$$

This series diverges for all $|z| < \Delta$ independent of c .

¹For large systems the probability c is just the concentration.

In the following sections 6.3 and 6.4, we consider a diagonal perturbation $\mathbf{V} \rightarrow \mathbf{v}$ with $(\mathbf{v})_{ij} = \delta_{ij}v_i$. We separate the propagator $\mathbf{G}_0(z)$ into its local part $[\mathbf{g}_{\text{loc}}(z)]_{ij} = \delta_{ij}G_{0ii}(z)$ and its off-diagonal part $\mathbf{G}'(z)$:

$$\mathbf{G}_0(z) = \mathbf{g}_{\text{loc}}(z) + \mathbf{G}'(z). \quad (6.32)$$

Accordingly, we rewrite the \mathcal{T} -matrix eq. (6.24), separating the parts containing the local propagator $\mathbf{g}_{\text{loc}}(z)$ and the off-diagonal propagator $\mathbf{G}'(z)$:

$$\begin{aligned} \mathcal{T}(z) &= \mathbf{v}\mathbf{g}_{\text{loc}}(z)\mathcal{T}(z) + \mathbf{v}[\mathbf{1} + \mathbf{G}'(z)\mathcal{T}(z)] \\ &= [\mathbf{1} - \mathbf{v}\mathbf{g}_{\text{loc}}(z)]^{-1}\mathbf{v}[\mathbf{1} + \mathbf{G}'(z)\mathcal{T}(z)]. \end{aligned} \quad (6.33)$$

This equation defines the local or atomic \mathbf{t} -matrix:

$$\mathbf{t}(z) := [\mathbf{1} - \mathbf{v}\mathbf{g}_{\text{loc}}(z)]^{-1}\mathbf{v}. \quad (6.34)$$

In terms of the local \mathbf{t} -matrix, the \mathcal{T} -matrix reads:

$$\mathcal{T}(z) = \mathbf{t}(z) + \mathbf{t}(z)\mathbf{G}'(z)\mathcal{T}(z). \quad (6.35)$$

The local \mathbf{t} -matrix contains the repeated scattering of the same site, which we have to treat to infinite order.

Comparing the Schwinger equation eq. (6.25) to the Dyson equation $\mathbb{E}(\mathbf{G}(z)) = \mathbf{G}_0(z) + \mathbf{G}_0(z)\mathbf{\Sigma}(z)\mathbb{E}(\mathbf{G}(z))$, we can express the self-energy of the averaged system in terms of the averaged \mathcal{T} -matrix:

$$\mathbf{\Sigma}(z) = \mathbb{E}(\mathcal{T}(z))[\mathbf{1} + \mathbf{G}_0(z)\mathbb{E}(\mathcal{T}(z))]^{-1}. \quad (6.36)$$

To this point, all expressions are exact, we have not applied any approximations yet.

6.3. Diagonal disorder: coherent potential approximation

In this section, we consider only the problem of diagonal substitutional disorder [159]. This means the parameter t_{ij} is independent of the terminal point components $\mathbf{t}^{\alpha\beta} = \mathbf{t}$ and therefore nonrandom. The disorder acts only in form of the random local on-site potentials \mathbf{v}^α .

The coherent potential approximation (CPA) [158–164] provides a local approximation for the average Green's function $\mathbb{E}(\mathbf{G}(z))$. Let's consider a binary alloy with components A and B, i.e., lattice sites are randomly occupied either by component A or B. The idea of CPA is to replace all random components by 'average' components thereby restoring periodicity. Substituting the average component by A or B on a single site gives rise to scattering off this site. CPA chooses the average components such that this scattering vanishes on average.

Section 6.3.1 gives an ad-hoc definition of the CPA as a local effective medium. Section 6.3.2 provides a systematic derivation of CPA as a controlled expansion.

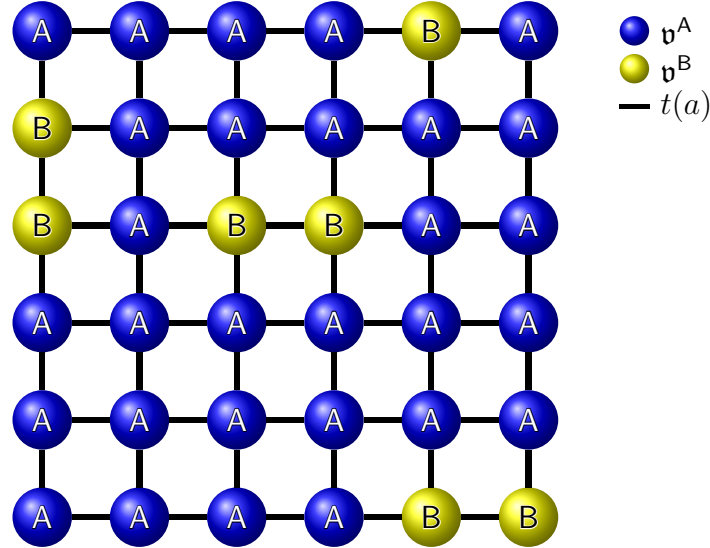


Figure 6.2.: Sketch of a configuration for a disordered binary alloy with two component A and B, considering only diagonal disorder. In contrast to fig. 6.1, the hopping amplitudes are assumed to be independent of the components $t^{AA}(a) = t^{AB}(a) = t^{BB}(a) = t(a)$, this is indicated by the black lines.

6.3.1. Local effective medium

The goal is to find an effective Hamiltonian $\mathbf{H}_{\text{eff}}(z)$ describing the average Green's function

$$\mathbb{E}(\mathbf{G}(z)) = [\mathbf{1}z - \mathbf{H}_{\text{eff}}(z)]^{-1}. \quad (6.37)$$

Formally, this equation defines the exact effective Hamiltonian. Assuming the average Green's function has the same symmetry as the lattice, we also require the effective Hamiltonian \mathbf{H}_{eff} to have of the same symmetry. Thus, it is diagonal in k -space; the lattice Fourier transform yields

$$\mathbb{E}(G(z, k)) = [z - H_{\text{eff}}(z, k)]^{-1}. \quad (6.38)$$

We decompose the effective Hamiltonian into the lattice dispersion ε_k , encoding the lattice symmetry, and the rest which we call coherent potential σ :

$$H_{\text{eff}}(z, k) = \varepsilon_k + \sigma(z, k). \quad (6.39)$$

Of course, we still need a strategy to determine the $\sigma(z, k)$.

CPA is the self-consistent local approximation to the exact coherent potential; in k -space this corresponds to omitting the k -dependence $\sigma(z, k) \approx \sigma(z)$. Thus, the CPA is a single-site approximation. We focus on the average local Green's function. The average restores the lattice symmetry and is a linear operation, therefore all the following expressions are equal:

$$\mathbb{E}(G_{ii}(z)) = \mathbb{E}(G_{00}(z)) = \frac{1}{N} \sum_i \mathbb{E}(G_{ii}(z)) = \frac{1}{N} \text{Tr}(\mathbf{G}(z)) := g_{\text{loc}}(z). \quad (6.40)$$

In terms of the effective Hamiltonian, the local Green's function writes

$$g_{\text{loc}}(z) = \frac{1}{N} \sum_k \frac{1}{z - H_{\text{eff}}(z, k)} = \frac{1}{N} \text{Tr} [\mathbb{1} - \mathbf{H}_{\text{eff}}(z)]^{-1}. \quad (6.41)$$

We can also express this average in terms of the conditional average if we apply the law of total probability or the law of total expectation [157]

$$g_{\text{loc}}(z) \stackrel{!}{=} \mathbb{E}(G_{ii}(z)) = \sum_{\alpha} \mathbb{E}(G_{ii}(z) | i \mapsto \alpha) P(i \mapsto \alpha) = \sum_{\alpha} c^{\alpha} \mathbb{E}(G_{ii}(z) | i \mapsto \alpha). \quad (6.42)$$

We define the component Green's function as the conditional average of the local Green's function

$$g_{\text{loc}}^{\alpha} := \mathbb{E}(G_{ii}(z) | i \mapsto \alpha). \quad (6.43)$$

Within the local approximation of CPA, we can calculate g_{loc}^{α} from the effective Hamiltonian $\mathbf{H}_{\text{eff}}(z)$ by replacing $\sigma(z)$ at a specific site $i = 0$ by the on-site energy \mathbf{v}^{α} :

$$(\mathbf{H}_{\text{eff}}^{\alpha})_{ij} = \begin{cases} \mathbf{v}^{\alpha} & \text{if } i = j = 0, \\ (H_{\text{eff}})_{ij} & \text{else,} \end{cases} \quad (6.44)$$

or in matrix form

$$\mathbf{H}_{\text{eff}}^{\alpha}(z) = \mathbf{H}_{\text{eff}} - \mathbb{1}_{[:,0]} [\sigma(z) - \mathbf{v}^{\alpha}] \mathbb{1}_{[0,:]}. \quad (6.45)$$

This is a rank-1 update of the effective Hamiltonian, therefore we can relate the component Green's function $g_{\text{loc}}^{\alpha}(z)$ to the effective local Green's function $g_{\text{loc}}(z)$ using the Woodbury matrix identity [95]:

$$g_{\text{loc}}^{\alpha}(z) = \frac{g_{\text{loc}}(z)}{1 - [\mathbf{v}^{\alpha} - \sigma(z)]g_{\text{loc}}(z)}. \quad (6.46)$$

According to the law of total probability eq. (6.42), we get the self-consistency equation for the local Green's function

$$g_{\text{loc}}(z) = \sum_{\alpha} c^{\alpha} \frac{g_{\text{loc}}(z)}{1 - [\mathbf{v}^{\alpha} - \sigma(z)]g_{\text{loc}}(z)}, \quad (6.47)$$

or equivalently

$$0 = \mathbb{E} \left(\frac{\mathbf{v}^{\alpha} - \sigma(z)}{1 - [\mathbf{v}^{\alpha} - \sigma(z)]g_{\text{loc}}(z)} \right). \quad (6.48)$$

This is the CPA self-consistency condition for the effective medium $\sigma(z)$, which is sketched in fig. 6.3. The approximation is to demand the effective medium to be local $\sigma(z, k) \approx \sigma(z)$. Furthermore, the introduction of the conditional effective Hamiltonian $\mathbf{H}_{\text{eff}}^{\alpha}$ was ad-hoc. In the thermodynamic limit, however, this step is unproblematic, as fixing one site does not affect the probabilities of the other sites.

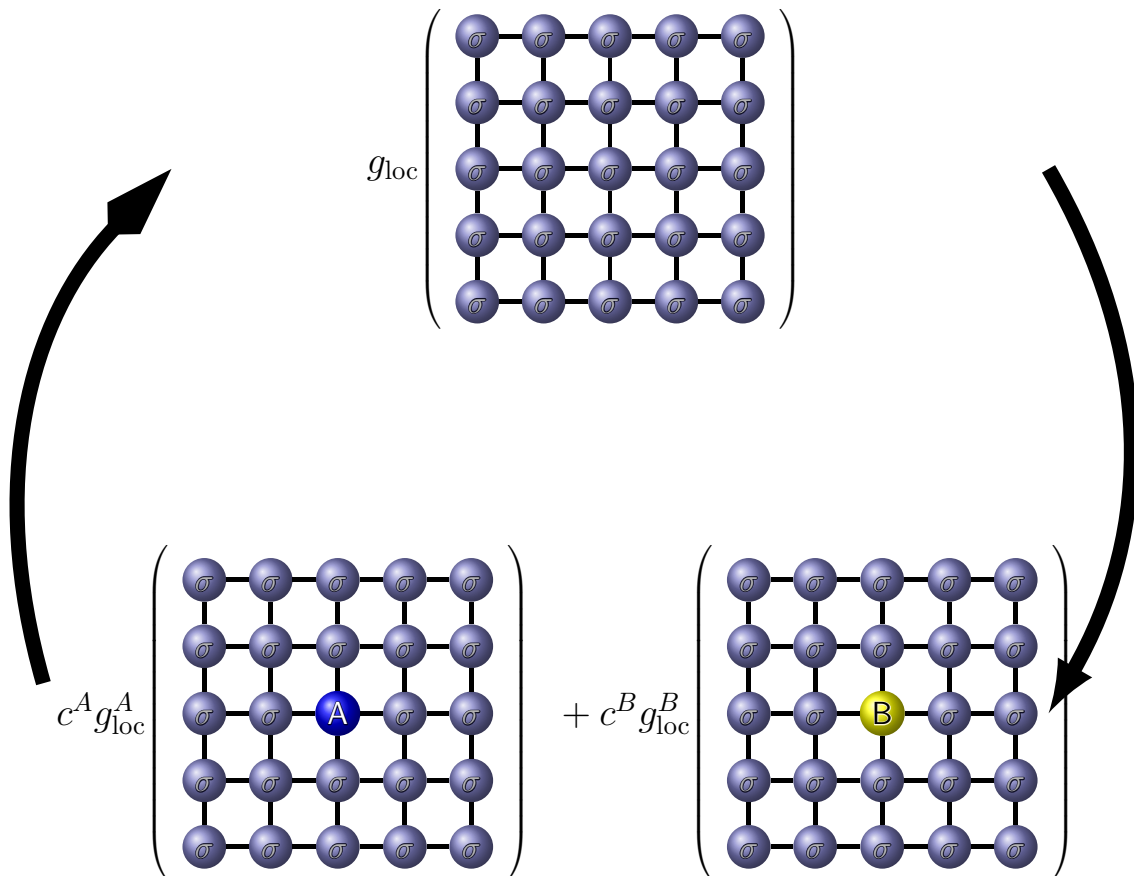


Figure 6.3.: Sketch of the CPA self-consistency. The average Green's function is calculated from a homogeneous effective lattice. The component Green's functions $g_{\text{loc}}^\alpha(z)$ are obtained by replacing the effective site by a site occupied by component α . At self-consistency the local Green's function of the effective lattice is equal to the average of component Green's functions.

6.3.2. Derivation of the coherent potential approximation

In this section, we rederive the CPA theory as a controlled expansion. We define the effective Hamiltonian

$$\mathbf{H}_{\text{eff}}(z) = \boldsymbol{\sigma}(z) + \mathbf{T}, \quad (6.49)$$

where \mathbf{T} is the exact hopping matrix. The corresponding effective Green's function is the resolvent

$$\mathbf{G}_{\text{eff}}(z) = [\mathbb{1}z - \mathbf{H}_{\text{eff}}(z)]^{-1}. \quad (6.50)$$

We treat the difference between the exact and the effective Hamiltonian as perturbation and write the Dyson equation

$$\mathbf{G}(z) = \mathbf{G}_{\text{eff}}(z) + \mathbf{G}_{\text{eff}}(z)[\mathbf{H} - \mathbf{H}_{\text{eff}}(z)]\mathbf{G}(z). \quad (6.51)$$

The corresponding Schwinger equation reads

$$\mathbf{G}(z) = \mathbf{G}_{\text{eff}}(z) + \mathbf{G}_{\text{eff}}(z)\mathcal{T}(z)\mathbf{G}_{\text{eff}}(z) \quad (6.52)$$

with the \mathcal{T} -matrix

$$\mathcal{T}(z) = [\mathbb{1} - [\mathbf{v} - \boldsymbol{\sigma}(z)]\mathbf{G}_{\text{eff}}(z)]^{-1}[\mathbf{v} - \boldsymbol{\sigma}(z)] = [\mathbf{v} - \boldsymbol{\sigma}(z)] + [\mathbf{v} - \boldsymbol{\sigma}(z)]\mathbf{G}_{\text{eff}}(z)\mathcal{T}(z); \quad (6.53)$$

see section 6.2. The only configuration dependent quantity in the Schwinger equation is the \mathcal{T} -matrix, therefore, the average is

$$\mathbb{E}(\mathbf{G}(z)) = \mathbf{G}_{\text{eff}}(z) + \mathbf{G}_{\text{eff}}(z)\mathbb{E}(\mathcal{T}(z))\mathbf{G}_{\text{eff}}(z). \quad (6.54)$$

The desired effective medium yielding the average Green's function $\mathbf{G}_{\text{eff}}(z) = \mathbb{E}(\mathbf{G}(z))$ is the effective medium with a vanishing average \mathcal{T} -matrix

$$\mathbb{E}(\mathcal{T}(z)) \stackrel{!}{=} 0. \quad (6.55)$$

CPA is a local effective medium theory; the effective medium is local and homogeneous $\boldsymbol{\sigma}(z) = \mathbb{1}\sigma(z)$. In order to decompose the \mathcal{T} -matrix into its local contributions, we separate the effective Green's function $\mathbf{G}_{\text{eff}}(z)$ into its local part $\mathbf{g}_{\text{loc}}(z)$ and its off-diagonal part $\mathbf{G}'(z)$:

$$\mathbf{G}_{\text{eff}}(z) = \mathbf{g}_{\text{loc}}(z) + \mathbf{G}'(z). \quad (6.56)$$

Then we can express the \mathcal{T} -matrix

$$\mathcal{T}(z) = \mathbf{t}(z) + \mathbf{t}(z)\mathbf{G}'(z)\mathcal{T}(z) \quad (6.57)$$

in terms of the local \mathbf{t} -matrix

$$\mathbf{t}(z) = [\mathbb{1} - [\mathbf{v} - \boldsymbol{\sigma}(z)]\mathbf{g}_{\text{loc}}(z)]^{-1}[\mathbf{v} - \boldsymbol{\sigma}(z)]; \quad (6.58)$$

cf. section 6.2. The average \mathcal{T} -matrix writes

$$\mathbb{E}(\mathcal{T}(z)) = \mathbb{E}(\mathbf{t}(z)) + \mathbb{E}[\mathbf{t}(z)\mathbf{G}'(z)\mathcal{T}(z)], \quad (6.59)$$

we have to average terms of the form

$$\mathbb{E}[\mathbf{t}(z)\mathbf{G}'(z)\mathbf{t}(z)\dots\mathbf{G}'(z)\mathbf{t}(z)]. \quad (6.60)$$

The off-diagonal matrix \mathbf{G}' always couples local \mathbf{t} elements belonging to different sites. If no repeated elements of the same site would appear, the average would factorize, and it would be sufficient to calculate the average $\mathbb{E}(\mathbf{t}(z))$. In general, however, this is just an *approximation*. Within this approximation, we get

$$\mathbb{E}(\mathcal{T}(z)) \approx \mathbb{E}(\mathbf{t}(z)) + \mathbb{E}(\mathbf{t}(z))\mathbf{G}'(z)\mathbb{E}(\mathcal{T}(z)), \quad (6.61)$$

and therefore the average \mathcal{T} -matrix vanishes for

$$\mathbb{E}(\mathbf{t}(z)) \stackrel{!}{=} 0. \quad (6.62)$$

The average restores translation invariance for the diagonal \mathbf{t} -matrix, thus we get the scalar equation

$$\mathbb{E}(\mathbf{t}(z)) = \mathbb{E}\left(\frac{\mathbf{v}^\alpha - \sigma(z)}{1 - [\mathbf{v}^\alpha - \sigma(z)]g_{\text{loc}}(z)}\right) \stackrel{!}{=} 0. \quad (6.63)$$

This equation is the self-consistency condition for the CPA effective medium $\sigma(z)$. The approximation (6.61) yields the correct average Green's function eq. (6.54) up to $\mathcal{O}(\mathbf{t}^4(z))$

$$\mathbb{E}(\mathbf{G}(z)) - \mathbf{G}_{\text{eff}}(z) = \mathbf{G}_{\text{eff}}(z)\mathbb{E}(\mathcal{T}(z))\mathbf{G}_{\text{eff}}(z) = \mathcal{O}(\mathbf{t}^4(z)). \quad (6.64)$$

This can be verified expanding the \mathcal{T} -matrix eq. (6.57) into its Neumann series. As $\mathbf{G}'(z)$ in eq. (6.61) is off-diagonal, the order $\mathbf{t}^2(z)$ contains only terms on different sites, and the order $\mathbf{t}^3(z)$ contains at least one term on a different site; all terms up to $\mathcal{O}(\mathbf{t}^4(z))$ vanish due to $\mathbb{E}(\mathbf{t}(z)) \stackrel{!}{=} 0$, eq. (6.62).

For practical implementations, it is favorable to write the self-consistency equation in terms of the effective medium $\sigma(z)$. We consider a guess $\hat{\sigma}(z)$ for the effective medium and therefore the guess $\hat{\mathbf{H}}_{\text{eff}}(z) = \hat{\sigma}(z) + \mathbf{T}$ for the effective Hamiltonian. The *exact* effective Hamiltonian yields the average Green's function $\mathbb{E}(\mathbf{G}(z)) = \mathbf{G}_{\text{eff}}(z)$, therefore the propagator expansion can be formulated in the difference of the *exact* effective Hamiltonian $\mathbf{H}_{\text{eff}}(z)$ and our guess $\hat{\mathbf{H}}_{\text{eff}}(z)$, effectively replacing $[\mathbf{v} - \sigma(z)]$ by $[\sigma(z) - \hat{\sigma}(z)]$. From eq. (6.58), we get the relation

$$\sigma(z) = \hat{\sigma}(z) + \frac{\mathbb{E}(\mathbf{t}(z))}{1 + \mathbb{E}(\mathbf{t}(z))g_{\text{loc}}(z)}. \quad (6.65)$$

This equation allows us to iterate the self-consistency equation, by updating the guess $\hat{\sigma}(z)$ by the expectation value of the \mathbf{t} -matrix eq. (6.58) calculated from $\hat{\sigma}(z)$.

The CPA has many desirable properties for the treatment of disorder, see Velický et al. [162] and Gonis [158]. CPA is symmetric in the components, there is no artificial division into a host material and impurities. We consider a binary alloy with components **A** and **B**. CPA is exact in the dilute limit $c^{\text{A/B}} \ll 1$. We define the disorder strength as $\delta = \frac{v^{\text{B}} - v^{\text{A}}}{D}$, where D is the half-bandwidth. CPA is also exact in the limit of weak disorder $\delta \ll 1$, as well as the atomic limit $D \rightarrow 0$. Independent of the parameter regime, CPA yields the first eight moments of the spectral function correctly [158].

6.4. Generalization to off-diagonal disorder [W3]

The Blackman–Esterling–Berk (BEB) formalism for disorder is a natural generalization of the CPA to include also off-diagonal disorder, that is component dependent hopping matrix elements t_{ij} . In 1971 these authors introduced a generalization of the CPA, incorporating the off-diagonal disorder in the single-site approximation [165, 166]. An in-depth analysis of the BEB formalism was performed in a tight-binding formalism by Gonis and Garland [167], using locators, propagators, as well as a variational technique, proving the analyticity of the BEB Green’s function.

In the conventional approach to systems with random variables, the Green’s function is first expanded and then an average over an appropriate set of terms is performed. In contrast, the BEB formalism treats both diagonal- and off-diagonal disorder on equal footing by employing an extended representation. A systematic way to introduce BEB is using what we call *component space*. We have seen in eq. (6.14) that the random parameters can be expressed in terms of indicator functions $1_{\mathbb{S}^\alpha}(i)$, eq. (6.13). The dependence on the components is shifted from the parameters into these indicator functions. The following section will formalize this. The formalism introduced by Koepernik et al. [155, 156] is particularly suitable for the BEB formalism. For this reason, we adopt the notation introduced by these references.

We remind the reader that every site has to be occupied by exactly one component. This fact is reflected in the following two important identities for the indicator function. Indicator functions evaluated at the same site can only contribute if they involve the same component:

$$1_{\mathbb{S}^\alpha}(i)1_{\mathbb{S}^\beta}(i) = \delta^{\alpha\beta}1_{\mathbb{S}^\alpha}(i). \quad (6.66)$$

Summing over all components yields one:

$$\sum_{\alpha} 1_{\mathbb{S}^\alpha}(i) = 1. \quad (6.67)$$

6.4.1. Component space and extended space [W3]

For a specific disorder configuration, we introduce the indicator tensor

$$(\boldsymbol{\eta})_{ij}^{[\alpha, \cdot]} = 1_{\mathbb{S}^\alpha}(i)\delta_{ij} = \begin{array}{c} \alpha \\ \text{---} \\ \text{---} \\ i \end{array} \left[\boldsymbol{\eta} \right] \text{---} j. \quad (6.68)$$

The upper leg carries the alloy component indices α , and the lower legs correspond to the site indices i, j . This tensor is equivalent to an $MN \times N$ matrix. We group the left indices for sites i and components α , or in the graphical notation the legs above each other; thus the matrix is equivalent to the vertical bipartition of the tensor. In the following, we refer to the MN -dimensional vector space of grouped sites and components as *extended space*. Matrix products in the extended space sum over the grouped MN elements for components and site indices; they are equivalent to tensor contractions of two legs, one for the components and one for the sites. We denote the N -dimensional space of lattice sites as *lattice space*, and the M -dimensional space of components *component space*. The

indicator tensor eq. (6.68) maps a vector from the lattice to the extended space. Note that the sum over components

$$\sum_{\alpha} \eta^{\alpha} = \eta^{\top} \eta = \text{---} \left[\begin{array}{c} \eta^{\top} \\ \eta \end{array} \right] \text{---} = \mathbb{1}^{N \times N}, \quad (6.69)$$

is the $N \times N$ identity matrix in lattice space, following directly from eqs. (6.66) and (6.67). The transpose η^{\top} is the left inverse. Thus, mathematically speaking, η is an isometric (distance preserving) embedding of the lattice space in the extended space. Physically, η^{\top} selects one specific disorder configuration; it is a mapping from the extended space to the lattice space of this configuration. It is a configuration dependent quantity and therefore random. The expectation value of a certain component α of the indicator tensor eq. (6.68) is

$$\mathbb{E}(\eta_{ij}^{\alpha}) = \delta_{ij} c^{\alpha}, \quad (6.70)$$

it is proportional to the concentration c^{α} .

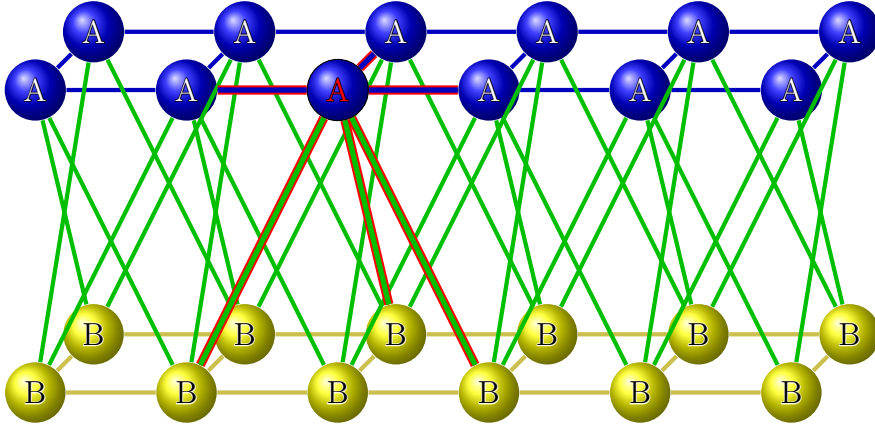


Figure 6.4.: Sketch of the extended space for a binary alloy with components A and B. In extended space, translational invariance is restored. We highlight the nearest neighbors of one site A in red.

We define the $MN \times MN$ extended Hamiltonian matrix \mathfrak{H} with the components

$$(\mathfrak{H})_{ij}^{\alpha\beta} = \delta_{ij} \mathbf{v}^{\alpha} \delta^{\alpha\beta} + \mathbf{t}^{\alpha\beta}(|\mathbf{r}_i - \mathbf{r}_j|). \quad (6.71)$$

The indicator tensor η transforms the extended Hamiltonian matrix \mathfrak{H} to the Hamiltonian matrix \mathbf{H} of one specific configuration:

$$\mathbf{H} = \eta^{\top} \mathfrak{H} \eta = \text{---} \left[\begin{array}{c} \eta^{\top} \\ \mathfrak{H} \\ \eta \end{array} \right] \text{---}. \quad (6.72)$$

The extended Hamiltonian matrix is independent of the particular disorder realization; it is nonrandom and independent of the concentrations. In the extended representation, for every lattice site the Hamiltonian matrix \mathfrak{H} is assigned a corresponding element for each component. In this way the Hamiltonian $\hat{H} = \hat{\mathbf{c}}^{\top} \mathbf{H} \hat{\mathbf{c}}$ can be generated by \mathfrak{H} for every disorder configuration.

It is important to note that the only configuration dependent parts of eq. (6.72) are the indicator tensors $\boldsymbol{\eta}^\top$ and $\boldsymbol{\eta}$; the rest is independent of the specific disorder realization. In other words, the configuration dependency is moved from the Hamiltonian matrix to the local indicator tensor eq. (6.68). This is the main idea of the BEB formalism: One can work with a nonrandom but extended Hamiltonian matrix $\boldsymbol{\mathfrak{H}}$, which contains the parameters for all possible configurations. A specific configuration is selected by applying indicator tensors $\boldsymbol{\eta}$. What remains to be averaged over are these local indicator tensors. Thus, we express the *nonlocal disorder* by *local random variables* in an *extended space*.

Using the indicator tensor $\boldsymbol{\eta}$, eq. (6.68), we define the projector onto a specific disorder configuration in extended space:

$$\boldsymbol{\chi} := \boldsymbol{\eta}\boldsymbol{\eta}^\top = \begin{array}{c} \text{---} \\ \text{---} \end{array} \left[\begin{array}{c} \text{---} \\ \boldsymbol{\eta} \\ \text{---} \end{array} \right] \left[\begin{array}{c} \boldsymbol{\eta}^\top \\ \text{---} \\ \text{---} \end{array} \right] \text{---}, \quad (6.73)$$

$$\boldsymbol{\chi}^2 = \begin{array}{c} \text{---} \\ \text{---} \end{array} \left[\begin{array}{c} \text{---} \\ \boldsymbol{\eta} \\ \text{---} \end{array} \right] \left[\begin{array}{c} \boldsymbol{\eta}^\top \\ \text{---} \\ \text{---} \end{array} \right] \left[\begin{array}{c} \text{---} \\ \boldsymbol{\eta} \\ \text{---} \end{array} \right] \left[\begin{array}{c} \boldsymbol{\eta}^\top \\ \text{---} \\ \text{---} \end{array} \right] \text{---} = \boldsymbol{\chi}. \quad (6.74)$$

It projects a vector in the extended space onto a single disorder configuration: It sets all elements corresponding to different disorder realizations to zero. The projector property, eq. (6.74), is a direct consequence of the identity eq. (6.69). Further, we define the component Green's function as

$$\boldsymbol{\mathfrak{G}}(z) := \boldsymbol{\eta}\boldsymbol{G}(z)\boldsymbol{\eta}^\top = \begin{array}{c} \text{---} \\ \text{---} \end{array} \left[\begin{array}{c} \text{---} \\ \boldsymbol{\eta} \\ \text{---} \end{array} \right] \left[\begin{array}{c} \boldsymbol{G}(z) \\ \text{---} \\ \text{---} \end{array} \right] \left[\begin{array}{c} \boldsymbol{\eta}^\top \\ \text{---} \\ \text{---} \end{array} \right] \text{---}. \quad (6.75)$$

The arrangement of indicator tensors $\boldsymbol{\eta}$ is reversed compared to eq. (6.72): Both the lattice Green's function $\boldsymbol{G}(z)$ and the component Green's function $\boldsymbol{\mathfrak{G}}(z)$ are configuration dependent. The sum over all components of $\boldsymbol{\mathfrak{G}}(z)$ recovers the physical lattice Green's function $\boldsymbol{G}(z)$:

$$\sum_{\alpha\beta} \boldsymbol{\mathfrak{G}}^{\alpha\beta}(z) = \boldsymbol{G}(z). \quad (6.76)$$

We note that local elements are diagonal in component space, i.e., $\boldsymbol{\mathfrak{G}}_{ii}^{\alpha\beta}(z) = \delta^{\alpha\beta}\boldsymbol{\mathfrak{G}}_{ii}^{\alpha\alpha}(z)$.

In the following, we derive the relation between the component Green's function $\boldsymbol{\mathfrak{G}}(z)$ and the extended Hamiltonian $\boldsymbol{\mathfrak{H}}$ by repeatedly applying the identity eq. (6.69). The starting point is the resolvent for the one-particle lattice Green's function

$$\mathbb{1} = [\mathbb{1}z - \boldsymbol{H}]\boldsymbol{G}(z). \quad (6.77)$$

We insert the extended Hamiltonian matrix $\boldsymbol{\mathfrak{H}}$ eq. (6.72) into the resolvent eq. (6.77) and insert the identity matrix eq. (6.69) between the bracket and the Green's function:

$$\mathbb{1} = [\mathbb{1}z - \boldsymbol{\eta}^\top\boldsymbol{\mathfrak{H}}\boldsymbol{\eta}]\boldsymbol{G}(z) = [z\boldsymbol{\eta}^\top - \boldsymbol{\eta}^\top\boldsymbol{\mathfrak{H}}\boldsymbol{\eta}\boldsymbol{\eta}^\top]\boldsymbol{\eta}\boldsymbol{G}(z). \quad (6.78)$$

We sandwich this equation from the left by the indicator tensor $\boldsymbol{\eta}$ and from the right by its transpose $\boldsymbol{\eta}^\top$:

$$\boldsymbol{\chi} = \boldsymbol{\eta}\boldsymbol{\eta}^\top = [\mathbb{1}z - \boldsymbol{\chi}\boldsymbol{\mathfrak{H}}\boldsymbol{\chi}]\boldsymbol{\eta}\boldsymbol{G}(z)\boldsymbol{\eta}^\top = [\mathbb{1}z - \boldsymbol{\chi}\boldsymbol{\mathfrak{H}}\boldsymbol{\chi}]\boldsymbol{\mathfrak{G}}(z). \quad (6.79)$$

This is the modified resolvent-like equation relating the extended Hamiltonian and the component Green's function in extended space.

Physical relevance of the component Green's function. To understand the physical relevance of the component Green's function, we need to relate its average

$$\mathbb{E}(\mathfrak{G}(z)) = \mathbb{E}(\boldsymbol{\eta}\mathbf{G}(z)\boldsymbol{\eta}^\top) \quad (6.80)$$

to the average of the lattice Green's function $\mathbb{E}(\mathbf{G}(z))$. The law of total probability [157] provides the relation between these two averages. The average is the weighted sum over all configurations satisfying the concentration restriction. For a given matrix element $\mathbb{E}(\mathfrak{G}_{ij}^{\alpha\beta}(z)) = \mathbb{E}(1_{\mathcal{S}^\alpha}(i)G_{ij}(z)1_{\mathcal{S}^\beta}(j))$, the indicator functions eliminates all configurations but the ones with $i \mapsto \alpha$ and $j \mapsto \beta$. We have to distinguish between (i) the diagonal case, $i = j$, and (ii) the off-diagonal case, $i \neq j$.

(i) For $i = j$, terms with $\alpha \neq \beta$ vanish. Only configurations where $i \mapsto \alpha = \beta$ contribute. We explicitly write out the expectation values:

$$\begin{aligned} \mathbb{E}(\mathfrak{G}_{ii}^{\alpha\alpha}) &= \sum_{\text{conf} \in \mathcal{C}_{\{c^\alpha\}}} P(\text{conf}) 1_{\mathcal{S}^\alpha}(i) G_{ii}(z) 1_{\mathcal{S}^\alpha}(i) = \sum_{\mathcal{C}_{\{c^\alpha\}}} P(\text{conf} \cap i \mapsto \alpha) G_{ii}(z) \\ &= \sum_{\mathcal{C}_{\{c^\alpha\}}} P(\text{conf} | i \mapsto \alpha) P(i \mapsto \alpha) G_{ii}(z) = c^\alpha \sum_{\mathcal{C}_{\{c^\alpha\}}} P(\text{conf} | i \mapsto \alpha) G_{ii}(z) \quad (6.81) \\ &= c^\alpha \mathbb{E}(G_{ii}(z) | i \mapsto \alpha). \end{aligned}$$

Thus, the expectation value of local elements of the component Green's function $\mathfrak{G}_{ii}^{\alpha\alpha}(z)$ is proportional to the conditional expectation value of the local one-particle Green's function $G_{ii}(z)$. The expectation value of the one-particle Green's function $G_{ii}(z)$ is given by

$$\begin{aligned} \mathbb{E}(G_{ii}(z)) &= \sum_{\alpha} \mathbb{E}(G_{ii}(z) | i \mapsto \alpha) P(i \mapsto \alpha) = \sum_{\alpha} \mathbb{E}(\mathfrak{G}_{ii}^{\alpha\alpha}) \\ &= \text{Tr}_{\alpha} \mathbb{E}(\mathfrak{G}_{ii}(z)) = \frac{1}{N} \text{Tr} \mathbb{E}(\mathfrak{G}(z)), \end{aligned} \quad (6.82)$$

where Tr_{α} is the trace in component space and Tr is the trace in extended space. Instead of using the law of total probability, eq. (6.82) can also be obtained from the indicator function identities eqs. (6.66) and (6.67), as we have already related the sum over the components of $\mathfrak{G}^{\alpha\beta}(z)$ to the lattice Green's function, see eq. (6.76).

(ii) For $i \neq j$, also the matrix elements with $\alpha \neq \beta$ that are off-diagonal in the components remain finite. Analogous to the previous case, the expectation value reads

$$\begin{aligned} \mathbb{E}(\mathfrak{G}_{ij}^{\alpha\beta}) &= \sum_{\text{conf}} P(\text{conf} | i, j \mapsto \alpha, \beta) P(i, j \mapsto \alpha, \beta) G_{ij}(z) \\ &= c^\alpha c^\beta \mathbb{E}(G_{ij}(z) | i, j \mapsto \alpha, \beta). \end{aligned} \quad (6.83)$$

The average of the matrix elements of the component Green's function $\mathfrak{G}_{ij}^{\alpha\beta}(z)$ is proportional to the conditional average of the lattice Green's function $G_{ij}(z)$. This time, however, the two components of two sites i and j are fixed, which results in the proportionality constant $c^\alpha c^\beta$ instead of c^α for $i = j$. Again, the average of the one-particle Green's function $G_{ij}(z)$ is given by

$$\mathbb{E}(G_{ij}(z)) = \sum_{\alpha\beta} \mathbb{E}(\mathfrak{G}_{ij}^{\alpha\beta}). \quad (6.84)$$

Thus, calculating the average $\mathbb{E}(\mathfrak{G}(z))$ yields not only the average $\mathbb{E}(\mathbf{G}(z))$, but also the conditional averages $\mathbb{E}(G_{ii}(z) | i \mapsto \alpha)$ and $\mathbb{E}(G_{ij}(z) | i, j \mapsto \alpha, \beta)$. Therefore, in the following we focus on calculating the average of the component Green's function, $\mathbb{E}(\mathfrak{G}(z))$.

6.4.2. Effective medium theory

Just like in section 6.3 for CPA, we define an effective medium $\mathfrak{G}(z)$. This time, however, we define the effective medium and effective Hamiltonian in the expanded space:

$$\mathfrak{H}_{\text{eff}}(z) := \mathfrak{G}(z) + \mathfrak{T} \quad \text{with} \quad (\mathfrak{T})_{ij}^{\alpha\beta} = t^{\alpha\beta}(|\mathbf{r}_i - \mathbf{r}_j|) \quad (6.85)$$

where we use the uppercase letter \mathfrak{T} for the matrix of hopping amplitudes as we use lowercase letters to indicate diagonal matrices. The corresponding effective Green's function is the resolvent

$$\mathfrak{G}_{\text{eff}}(z) = [\mathbb{1}z - \mathfrak{H}_{\text{eff}}(z)]^{-1}. \quad (6.86)$$

We relate the component Green's function $\mathfrak{G}(z)$ to the effective Green's function $\mathfrak{G}_{\text{eff}}(z)$, in order to find the condition for the effective potential $\mathfrak{G}(z)$. This is done by inserting the identity $\mathfrak{H} = \mathfrak{H} - \mathfrak{H}_{\text{eff}}(z) + \mathfrak{H}_{\text{eff}}(z)$. The component Green's function $\mathfrak{G}(z)$ eq. (6.75) is invariant under the projection χ ; eq. (6.79) reads in terms of the effective Green's function:

$$\begin{aligned} \mathfrak{G}(z) &= \chi \mathfrak{G}(z) = \chi \left[\mathbb{1}z - \chi \left(\mathbb{1}z - \mathfrak{H}_{\text{eff}}(z) + \mathfrak{H} \right) \chi + \chi \mathfrak{G}_{\text{eff}}^{-1}(z) \chi \right]^{-1} \chi \\ &=: \chi \left[-\mathfrak{A}(z) + \chi \mathfrak{G}_{\text{eff}}^{-1}(z) \chi \right]^{-1} \chi, \end{aligned} \quad (6.87)$$

where $\mathfrak{A}(z) = \chi \left(\mathbb{1}z - \mathfrak{H}_{\text{eff}}(z) + \mathfrak{H} \right) \chi - \mathbb{1}z$. We need to pay particular attention to the fact that the projector χ is a singular matrix. The newly defined matrix $\mathfrak{A}(z)$, on the other hand, is invertible for an appropriate $\mathfrak{H}_{\text{eff}}(z)$. There are exceptions for which $\mathfrak{A}(z)$ is singular, for example in the case $\mathfrak{H}_{\text{eff}}(z) \equiv \mathfrak{H}$. Here we assume that $\mathfrak{A}(z)$ is always invertible as the measure of the subspace of singular matrices is zero and singularity can be avoided by small perturbations of $\mathfrak{H}_{\text{eff}}$. We invert the bracket by applying the Woodbury matrix identity, avoiding the inversion of the singular projectors:

$$\begin{aligned} \mathfrak{G}(z) &= -\chi \mathfrak{A}^{-1}(z) \chi - \chi \mathfrak{A}^{-1}(z) \chi \left[\mathfrak{G}_{\text{eff}}(z) - \chi \mathfrak{A}^{-1}(z) \chi \right]^{-1} \chi \mathfrak{A}^{-1}(z) \chi \\ &=: -\mathfrak{B}(z) - \mathfrak{B}(z) \left[\mathfrak{G}_{\text{eff}}(z) - \mathfrak{B}(z) \right]^{-1} \mathfrak{B}(z), \end{aligned} \quad (6.88)$$

with the singular matrix $\mathfrak{B}(z) = \chi \mathfrak{A}^{-1}(z) \chi$. Next, we expand the remaining matrix inversion:

$$\begin{aligned} -\mathfrak{B}(z) \left[\mathfrak{G}_{\text{eff}}(z) - \mathfrak{B}(z) \right]^{-1} \mathfrak{B}(z) &= \mathfrak{B}(z) \left[\mathfrak{G}_{\text{eff}}(z) - \mathfrak{B}(z) \right]^{-1} \left[\mathfrak{G}_{\text{eff}}(z) - \mathfrak{B}(z) - \mathfrak{G}_{\text{eff}}(z) \right] \\ &= \mathfrak{B}(z) - \mathfrak{B}(z) \left[\mathfrak{G}_{\text{eff}}(z) - \mathfrak{B}(z) \right]^{-1} \mathfrak{G}_{\text{eff}}(z). \end{aligned} \quad (6.89)$$

Another application of an expansion like eq. (6.89) yields

$$\begin{aligned} \mathfrak{G}(z) &= \mathfrak{B}(z) \left[\mathfrak{B}(z) - \mathfrak{G}_{\text{eff}}(z) \right]^{-1} \mathfrak{G}_{\text{eff}}(z) \\ &= \mathfrak{G}_{\text{eff}}(z) + \mathfrak{G}_{\text{eff}}(z) \left[\mathfrak{B}(z) - \mathfrak{G}_{\text{eff}}(z) \right]^{-1} \mathfrak{G}_{\text{eff}}(z). \end{aligned} \quad (6.90)$$

Defining the \mathcal{T} -matrix in extended space $\mathcal{T}(z) := \left[\mathfrak{B}(z) - \mathfrak{G}_{\text{eff}}(z) \right]^{-1}$, we obtain the relation between component and effective Green's function

$$\mathfrak{G}(z) = \mathfrak{G}_{\text{eff}}(z) + \mathfrak{G}_{\text{eff}}(z) \mathcal{T}(z) \mathfrak{G}_{\text{eff}}(z). \quad (6.91)$$

The effective medium yielding the average component Green's function $\mathfrak{G}_{\text{eff}}(z) = \mathbb{E}(\mathfrak{G}(z))$, is the effective medium with a vanishing average \mathcal{T} -matrix

$$\mathbb{E}(\mathcal{T}(z)) = \mathbb{E}([\mathfrak{B}(z) - \mathfrak{G}_{\text{eff}}(z)]^{-1}) = 0. \quad (6.92)$$

As in CPA, this result is exact; however, we cannot in general find the appropriate medium without further simplifications.

6.4.3. Local approximation

As in CPA, we employ the local single-site approximate of the effective medium. We choose an effective medium local in lattice space $\mathfrak{G}_{ij}^{\alpha\beta}(z) = \delta_{ij}\mathfrak{G}_{ii}^{\alpha\beta}(z)$. A local matrix \mathbf{L} sandwiched between the projectors χ is also diagonal in component space; thus matrices of the type $\chi\mathbf{L}\chi$ are diagonal in extended space. Consequently, the matrix

$$\mathfrak{B}(z) = -\chi[\mathbb{1}z - \chi(\mathbb{1}z - \mathfrak{G}(z) + \mathbf{v})\chi]^{-1}\chi =: \mathbf{b}(z), \quad (6.93)$$

is diagonal in extended space; we change the notation to the lowercase letter \mathbf{b} to denote that it is a diagonal matrix. We split the effective Green's function $\mathfrak{G}_{\text{eff}}(z)$ into its local part $\mathfrak{g}_{\text{loc}}(z)$ and the off-diagonal part $\mathfrak{G}'_{\text{eff}}(z)$. The \mathcal{T} -matrix can be rewritten

$$\mathcal{T}(z) = [\mathbb{1} - \mathbf{t}(z)\mathfrak{G}'_{\text{eff}}(z)]^{-1}\mathbf{t}(z) = \mathbf{t}(z) + \mathbf{t}(z)\mathfrak{G}'_{\text{eff}}(z)\mathcal{T}(z) \quad (6.94)$$

in terms of the local \mathbf{t} -matrix

$$\mathbf{t}(z) = [\mathbf{b}(z) - \mathfrak{g}_{\text{loc}}(z)]^{-1}. \quad (6.95)$$

These equations are analogous to eqs. (6.57) and (6.58) in CPA, where in component space $\mathbf{b}(z)$ takes the role of $[\mathbf{v} - \sigma(z)]^{-1}$. As in CPA, we approximate the average by decoupling the terms

$$\begin{aligned} \mathbb{E}(\mathcal{T}(z)) &= \mathbb{E}(\mathbf{t}(z)) + \mathbb{E}\left(\mathbf{t}(z)\mathfrak{G}'_{\text{eff}}(z)\mathcal{T}(z)\right) \\ &\approx \mathbb{E}(\mathbf{t}(z)) + \mathbb{E}(\mathbf{t}(z))\mathfrak{G}'_{\text{eff}}(z)\mathbb{E}(\mathcal{T}(z)) \end{aligned} \quad (6.96)$$

and require

$$\mathbb{E}(\mathbf{t}(z)) \stackrel{!}{=} 0. \quad (6.97)$$

If we expand the local approximation to the \mathcal{T} -matrix eq. (6.94) into its Neumann series, we see from comparison with eq. (6.91) that

$$\mathbb{E}(\mathfrak{G}(z)) - \mathfrak{G}_{\text{eff}}(z) = \mathcal{O}\left(\mathbb{E}(\mathbf{t}^4)\right); \quad (6.98)$$

the approximation is accurate to fourth order, just like in the regular CPA.

6.4.4. Self-consistency equation

In this section, we present the self-consistency equation for the BEB formalism in terms of the local effective medium $\mathfrak{S}(z)$. We consider only substitutional without structural disorder; i.e., the lattice structure is assumed to be fixed. Thus, we assume that the lattice structure is the same for all components and the hopping tensor $\mathfrak{t}^{\alpha\beta}(|\mathbf{r}_i - \mathbf{r}_j|)$ can be decomposed into its component part, $\mathfrak{T}^{\alpha\beta}$, and its lattice part, $t(|\mathbf{r}_i - \mathbf{r}_j|)$:

$$(\mathfrak{T})_{ij}^{\alpha\beta} = \mathfrak{t}^{\alpha\beta}(|\mathbf{r}_i - \mathbf{r}_j|) =: \mathfrak{T}^{\alpha\beta} t(|\mathbf{r}_i - \mathbf{r}_j|), \quad (6.99)$$

or written in tensorial notation

$$\begin{array}{c} \text{---} \\ \text{---} \end{array} \boxed{\mathfrak{T}} \begin{array}{c} \text{---} \\ \text{---} \end{array} = \begin{array}{c} \text{---} \\ \text{---} \end{array} \boxed{\mathfrak{T}} \begin{array}{c} \text{---} \\ \text{---} \end{array} \cdot \begin{array}{c} \text{---} \\ \text{---} \end{array} \boxed{t} \begin{array}{c} \text{---} \\ \text{---} \end{array}. \quad (6.100)$$

Depending on the component of the endpoints, the matrix elements $\mathfrak{T}^{\alpha\beta}$ scale the hopping amplitudes on a given lattice structure by a dimensionless factor. In the following we refer to $\mathfrak{T}^{\alpha\beta}$ simply as a *dimensionless hopping parameter*. We perform the lattice Fourier transform of the hopping matrix elements as

$$\frac{1}{N} \sum_{ij} \mathfrak{T}^{\alpha\beta} t(|\mathbf{r}_i - \mathbf{r}_j|) e^{i\mathbf{k} \cdot (\mathbf{r}_i - \mathbf{r}_j)} = \mathfrak{T}^{\alpha\beta} \varepsilon_{\mathbf{k}}, \quad (6.101)$$

where $\varepsilon_{\mathbf{k}}$ is the lattice dispersion; in the following we omit the boldface notation for the vector \mathbf{k} .

With the lattice Fourier transform, the local effective Green's function $\mathfrak{g}_{\text{loc}}(z)$ for a given effective medium $\mathfrak{S}(z)$ is evaluated as the k -sum in component space

$$\text{---} \boxed{\mathfrak{g}_{\text{loc}}(z)} \text{---} = \mathfrak{g}_{\text{loc}}(z) = \frac{1}{N} \sum_{\mathbf{k}} [\mathbb{1}z - \mathfrak{S}(z) - \mathfrak{T}\varepsilon_{\mathbf{k}}]^{-1}. \quad (6.102)$$

These being local quantities, we omit the lattice indices. The effective medium as well as the effective local Green's function are represented by $M \times M$ matrices in the components. Next, we evaluate the \mathfrak{t} -matrix by using the Woodbury matrix identity:

$$\begin{aligned} \mathfrak{t}(z) &= [\mathfrak{b}(z) - \mathfrak{g}_{\text{loc}}(z)]^{-1} = [\boldsymbol{\chi} \mathfrak{a}^{-1}(z) \boldsymbol{\chi} - \mathfrak{g}_{\text{loc}}(z)]^{-1} \\ &= -\mathfrak{g}_{\text{loc}}^{-1}(z) - \mathfrak{g}_{\text{loc}}^{-1}(z) \boldsymbol{\chi} [\mathfrak{a}(z) - \boldsymbol{\chi} \mathfrak{g}_{\text{loc}}^{-1}(z) \boldsymbol{\chi}]^{-1} \boldsymbol{\chi} \mathfrak{g}_{\text{loc}}^{-1}(z), \end{aligned} \quad (6.103)$$

with the diagonal matrix $\mathfrak{a}(z) = -\mathbb{1}z + \boldsymbol{\chi}[\mathbb{1}z - \mathfrak{S}(z) + \mathfrak{v}]\boldsymbol{\chi}$. As $\mathfrak{g}_{\text{loc}}$ is local, $\boldsymbol{\chi} \mathfrak{g}_{\text{loc}}^{-1} \boldsymbol{\chi}$ is diagonal in extended space. The matrix inverse sandwiched by the projectors $\boldsymbol{\chi}$ in eq. (6.103) is therefore a diagonal matrix and can readily be evaluated as the reciprocal elements:

$$\left(\boldsymbol{\chi} [\boldsymbol{\chi} \mathfrak{g}_{\text{loc}}^{-1}(z) \boldsymbol{\chi} - \mathfrak{a}(z)]^{-1} \boldsymbol{\chi} \right)_{ii}^{\alpha\alpha} = \frac{1_{\mathbb{S}^{\alpha}}(i)}{[\mathfrak{g}_{\text{loc}}^{-1}(z)]^{\alpha\alpha} + \mathfrak{S}^{\alpha\alpha}(z) - \mathfrak{v}^{\alpha}} =: \tilde{\mathfrak{g}}_{ii}^{\alpha\alpha}(z); \quad (6.104)$$

the identity matrices $\mathbb{1}z$ in $\mathfrak{a}(z)$ cancel due to the surrounding projectors $\boldsymbol{\chi}$. The only random quantity is the indicator function, thus the expectation value reads

$$\bar{\mathfrak{g}}_{ii}^{\alpha\alpha}(z) := \mathbb{E}(\tilde{\mathfrak{g}}_{ii}^{\alpha\alpha}(z)) = \frac{c^{\alpha}}{[\mathfrak{g}_{\text{loc}}^{-1}(z)]^{\alpha\alpha} + \mathfrak{S}^{\alpha\alpha}(z) - \mathfrak{v}^{\alpha}}. \quad (6.105)$$

Therefore, the average of the \mathbf{t} -matrix eq. (6.103) is

$$\mathbb{E}(\mathbf{t}(z)) = -\mathbf{g}_{\text{loc}}^{-1}(z) + \mathbf{g}_{\text{loc}}^{-1}(z)\overline{\mathbf{g}}_{ii}(z)\mathbf{g}_{\text{loc}}^{-1}(z) \stackrel{!}{=} 0. \quad (6.106)$$

We multiply the matrix by $\mathbf{g}_{\text{loc}}(z)\overline{\mathbf{g}}_{ii}^{-1}(z)$ from the right to obtain the self-consistency equation

$$0 = \mathbf{g}_{\text{loc}}^{-1}(z) - \overline{\mathbf{g}}_{ii}^{-1}(z). \quad (6.107)$$

This equation can be solved numerically to obtain $\mathfrak{S}(z)$. Note that this self-consistency equation equals

$$\mathbf{g}_{\text{loc}}^{-1}(z) - \overline{\mathbf{g}}_{ii}^{-1}(z) = [\mathbb{1} + \mathbb{E}(\mathbf{t}(z))\mathbf{g}_{\text{loc}}(z)]^{-1} \mathbb{E}(\mathbf{t}(z)) \quad (6.108)$$

and is therefore of the same form as the CPA self-consistency equation eq. (6.65).

6.4.5. Efficient calculation: diagonal structure in k -points [W3]

To solve the BEB self-consistency eq. (6.107), we need to repeatedly evaluate the effective local Green's function

$$\mathbf{g}_{\text{loc}}(z) = \frac{1}{N} \sum_k [\xi(z) - \mathfrak{T}\varepsilon_k]^{-1}, \quad (6.109)$$

where $\xi(z) = \mathbb{1}z - \mathfrak{S}(z)$, or rather its inverse $\mathbf{g}_{\text{loc}}^{-1}(z)$. A naive evaluation is computationally involved, as we need to invert an $M \times M$ matrix for every k -point and every frequency point z . While this is feasible for small matrix sizes M , it also has the potential risk of inaccurate k -summations (or integrations), especially for DOSs with singularities (e.g. one-dimensional or square lattice).

We therefore propose an algorithm based on the *compact* SVD of the \mathfrak{T} -matrix:

$$\mathfrak{T} = U\sigma V^\dagger. \quad (6.110)$$

It is important to employ the *compact* SVD, keeping only non-zero singular values, as we explicitly use the inverse σ^{-1} . Due to finite precision in numerics, we need to introduce a cut-off value and consider all values that are smaller to be zero. Therefore, small singular values below this cut-off are truncated, this is referred to as *truncated* SVD. In case \mathfrak{T} is rank-deficient, the dimension of σ will be smaller than the component dimension. We note that for the binary alloy $M = 2$ the rank-1 case, where the SVD has only a single nonzero singular value, is given by a hopping parameter \mathfrak{T} of the type

$$\begin{pmatrix} \mathfrak{T}^{AA} & \sqrt{\mathfrak{T}^{AA}\mathfrak{T}^{BB}} \\ \sqrt{\mathfrak{T}^{AA}\mathfrak{T}^{BB}} & \mathfrak{T}^{BB} \end{pmatrix} = \begin{pmatrix} \sqrt{\mathfrak{T}^{AA}} \\ \sqrt{\mathfrak{T}^{BB}} \end{pmatrix} \begin{pmatrix} \sqrt{\mathfrak{T}^{AA}} & \sqrt{\mathfrak{T}^{BB}} \end{pmatrix}. \quad (6.111)$$

This is the structure of the hopping matrix discussed by Shiba [168]. Another prominent rank-1 example is the CPA limit with $\mathfrak{T}^{\alpha\beta} = 1$. As the \mathfrak{T} -matrix is Hermitian, we can use the unitary eigendecomposition instead of the SVD, to get slightly more symmetric equations:

$$\mathfrak{T} = U\lambda U^\dagger = U_L U_R^\dagger, \quad (6.112)$$

where $\boldsymbol{\lambda}$ is the diagonal matrix of real eigenvalues. We use the decomposition to split the matrix; here we partition the eigenvalues symmetrically as $\mathbf{U}_L = \mathbf{U}\sqrt{\boldsymbol{\lambda}}$, $\mathbf{U}_R^\dagger = \sqrt{\boldsymbol{\lambda}}\mathbf{U}^\dagger$.

The goal is to efficiently calculate the local component Green's function

$$\mathbf{g}_{\text{loc}}(z) = \frac{1}{N} \sum_k \mathfrak{G}(z, k) = \frac{1}{N} \sum_k [\boldsymbol{\xi}(z) - \mathbf{U}_L \varepsilon_k \mathbf{U}_R^\dagger]^{-1}. \quad (6.113)$$

We first consider $\mathfrak{G}(z, k)$ for $\varepsilon_k \neq 0$, employing the Woodbury matrix identity:

$$\mathfrak{G}(z, k) = \boldsymbol{\xi}^{-1}(z) - \boldsymbol{\xi}^{-1}(z) \mathbf{U}_L [\mathbf{U}_R^\dagger \boldsymbol{\xi}^{-1}(z) \mathbf{U}_L - \mathbb{1}/\varepsilon_k]^{-1} \mathbf{U}_R^\dagger \boldsymbol{\xi}^{-1}(z). \quad (6.114)$$

For each frequency z we calculate the eigendecomposition

$$\mathbf{U}_R^\dagger \boldsymbol{\xi}^{-1}(z) \mathbf{U}_L = \mathbf{P}(z) \mathbf{d}(z) \mathbf{P}^{-1}(z), \quad (6.115)$$

where $\mathbf{d}(z)$ is the diagonal matrix of eigenvalues. We note, that if \mathfrak{T} is real symmetric, we have $\mathbf{U}^\dagger = \mathbf{U}^\top$ and equation eq. (6.115) is complex symmetric as $\boldsymbol{\xi}(z)$ is complex symmetric. For a diagonalizable complex symmetric matrix, a complex orthogonal eigendecomposition exists [169].

Inserting this decomposition in the k -dependent Green's function, we get

$$\mathfrak{G}(z, k) = \boldsymbol{\xi}^{-1}(z) - \boldsymbol{\xi}^{-1}(z) \mathbf{U}_L \mathbf{P}(z) [\mathbf{d}(z) - \mathbb{1}/\varepsilon_k]^{-1} \mathbf{P}^{-1}(z) \mathbf{U}_R^\dagger \boldsymbol{\xi}^{-1}(z). \quad (6.116)$$

We note that only the term in the square brackets depends on k . It contains only diagonal matrices, therefore the matrix inverse only involves the reciprocal matrix elements. We focus on a particular diagonal element with the z -dependent eigenvalue $[\mathbf{d}(z)]_{ii} = d_i(z)$. We simplify the bracket

$$-\left[d_i(z) - \frac{1}{\varepsilon_k} \right]^{-1} = \frac{\varepsilon_k}{1 - \varepsilon_k d_i(z)} = \frac{1/d_i^2(z)}{1/d_i(z) - \varepsilon_k} - \frac{1}{d_i(z)}. \quad (6.117)$$

This result holds for the previously excluded case $\varepsilon_k = 0$. It is straightforward to carry out the k -summation:

$$\frac{1}{N} \sum_k \frac{1}{1/d_i(z) - \varepsilon_k} = g_0(1/d_i(z)); \quad (6.118)$$

it has the standard form of the lattice Hilbert transform. For many simple lattices, we know the analytic expression for g_0 (see e.g. [164, 170–174]); no numerical integration is necessary. For the local Green's function we obtain the lengthy expression

$$\mathbf{g}_{\text{loc}}(z) = \boldsymbol{\xi}^{-1}(z) + \boldsymbol{\xi}^{-1}(z) \mathbf{U}_L \mathbf{P}(z) \left[\mathbf{d}^{-1}(z) g_0(\mathbf{d}^{-1}(z)) - \mathbb{1} \right] \mathbf{d}^{-1}(z) \mathbf{P}^{-1}(z) \mathbf{U}_R^\dagger \boldsymbol{\xi}^{-1}(z). \quad (6.119)$$

Full-rank case. In the case of a full-rank matrix \mathfrak{T} , the Green's function simplifies as we can use $\mathbf{U}^\dagger = \mathbf{U}^{-1}$ in eq. (6.115), i.e., $\mathbf{U}_R^\dagger \boldsymbol{\xi}^{-1}(z) \mathbf{U}_L = \mathbf{P}(z) \mathbf{d}(z) \mathbf{P}^{-1}(z)$. Using $\mathbf{U}_L^{-1} = \boldsymbol{\lambda}^{-1/2} \mathbf{U}^\dagger$, we identify

$$\mathbf{d}^{-1}(z) \mathbf{P}^{-1}(z) \mathbf{U}_R^\dagger \boldsymbol{\xi}^{-1}(z) = \mathbf{P}^{-1}(z) \boldsymbol{\lambda}^{-1/2} \mathbf{U}^\dagger, \quad (6.120)$$

and with $(\mathbf{U}_R^\dagger)^{-1} = \mathbf{U}\boldsymbol{\lambda}^{-1/2}$, we identify

$$\boldsymbol{\xi}^{-1}(z)\mathbf{U}_L\mathbf{P}(z)\mathbf{d}^{-1}(z) = \mathbf{U}\boldsymbol{\lambda}^{-1/2}\mathbf{P}(z). \quad (6.121)$$

Using these two equations, eq. (6.119) simplifies to the expression

$$\mathbf{g}_{\text{loc}}(z) = \mathbf{U}\boldsymbol{\lambda}^{-1/2}\mathbf{P}(z)g_0(\mathbf{d}^{-1}(z))\mathbf{P}^{-1}(z)\boldsymbol{\lambda}^{-1/2}\mathbf{U}^\dagger \quad (6.122)$$

for the local Green's function. The inverse is also straightforward to calculate

$$\mathbf{g}_{\text{loc}}^{-1}(z) = \mathbf{U}_L\mathbf{P}(z)\frac{1}{g_0(\mathbf{d}^{-1}(z))}\mathbf{P}^{-1}(z)\mathbf{U}_R^\dagger. \quad (6.123)$$

We also note that in the full-rank problem, it is not necessary to invert $\boldsymbol{\xi}(z)$. Instead, we can also perform the eigendecomposition

$$\boldsymbol{\lambda}^{-1/2}\mathbf{U}^\dagger\boldsymbol{\xi}(z)\mathbf{U}\boldsymbol{\lambda}^{-1/2} = \mathbf{P}(z)\mathbf{d}^{-1}(z)\mathbf{P}^{-1}(z) \quad (6.124)$$

which immediately yields the desired inverse of the diagonal matrix $\mathbf{d}(z)$.

Rank-deficient case. In the rank-deficient case, we have to be more careful, the matrices \mathbf{U}_L and \mathbf{U}_R^\dagger are rectangular and cannot be inverted. Therefore, we cannot apply the simplifications and instead have to work with the form eq. (6.119) for the local Green's function. The matrix inversion can be carried out using the Woodbury matrix identity

$$\mathbf{g}_{\text{loc}}^{-1}(z) = \boldsymbol{\xi}(z) + \mathbf{U}_L\mathbf{P}(z)\left[\frac{1}{g_0(1/\mathbf{d}(z))} - 1/\mathbf{d}(z)\right]\mathbf{P}^{-1}(z)\mathbf{U}_R^\dagger. \quad (6.125)$$

If $\boldsymbol{\xi}(z) = \mathbf{U}_L\mathbf{P}(z)\mathbf{d}^{-1}(z)\mathbf{P}^{-1}(z)\mathbf{U}_R^\dagger$, then $\boldsymbol{\xi}(z)$ cancels the term $1/\mathbf{d}(z)$ in the bracket, and we verify that eq. (6.125) agrees with eq. (6.123)

Computational effort. Let's assume that the cost of matrix multiplications can be neglected compared to the cost of matrix inversion and diagonalization. The cost of directly evaluating $\mathbf{g}_{\text{loc}}^{-1}(z)$ using eq. (6.109) is $N_z(N_k + 1)$ matrix inversions, where N_z is the number of frequency points and N_k the number of k -points necessary to evaluate the k -summation. The computational effort using eq. (6.125), on the other hand, amounts to N_z matrix inversions to calculate $\boldsymbol{\xi}^{-1}(z)$, and N_z matrix diagonalizations [eq. (6.115)]. In the full-rank case, the matrix inversions can also be avoided; we only have to perform the N_z matrix diagonalizations. In the rank-deficient case, the matrix inversions are performed in the space of the compact SVD/eigendecomposition which is smaller than the full $M \times M$ component space. We conclude that eqs. (6.123) and (6.125) can be computed much more efficiently than the direct evaluation of $\mathbf{g}_{\text{loc}}^{-1}(z)$. Additionally, by isolating the k -summation, it is easier to control the accuracy of the k -summation, and analytically known lattice Hilbert transforms can be directly employed.

6.4.6. Self-consistency with renormalized indicator tensors [W3]

For alloy components $\alpha \neq \beta$, the self-consistency equation eq. (6.107) yields the high-frequency expansion of the effective medium

$$\mathfrak{S}^{\alpha\beta}(z) = -\varepsilon_{(1)}\mathfrak{T}^{\alpha\beta} + \mathcal{O}(z^{-1}), \quad (6.126)$$

$$\mathfrak{S}^{\alpha\alpha}(z) = -\frac{\bar{c}^\alpha}{c^\alpha}z + \frac{\mathbf{v}^\alpha - \mu + \bar{c}^\alpha\mathfrak{T}^{\alpha\alpha}\varepsilon_{(1)}}{c^\alpha} + \mathcal{O}(z^{-1}), \quad (6.127)$$

where $\bar{c}^\alpha = 1 - c^\alpha$ is the concentration complement; $\varepsilon_{(1)} = \int d\varepsilon \rho(\varepsilon)\varepsilon$ is the first moment of the DOS, which vanishes for standard definitions of the DOS of a lattice, as it is just a shift of the on-site energy.² Note that in case a local self-energy $\Sigma^\alpha(z)$ is included to describe interacting systems as in chapter 7, \mathbf{v} in eq. (6.127) has to incorporate the static part $\Sigma_{\text{HF}}^\alpha$. The diagonal matrix elements of the effective medium, $\mathfrak{S}^{\alpha\alpha}(z)$, contain a contribution which grows linearly in z , and the on-site energies in the static part are multiplied by the inverse of the concentration. The origin of this peculiar structure is evident from eqs. (6.81) and (6.83) and the definition eq. (6.102). Unlike the diagonal elements of a one-particle Green's function which are asymptotic equivalent to $G_{ii}(z) \sim 1/z$ for large z , the effective local Green's function $\mathbf{g}_{\text{loc}}(z)$ has the asymptote $\mathbf{g}_{\text{loc}}(z) \sim \mathbf{c}/z$. Its definition in terms of the effective medium, however, has the regular form of $[\mathbf{1}z - \mathfrak{S}(z) - \mathfrak{T}\varepsilon_k]^{-1}$, see eq. (6.102).

This strange behavior of the effective medium can be resolved by replacing the indicator tensor $\boldsymbol{\eta}$, eq. (6.68), with the concentration-scaled indicator tensor

$$\begin{array}{c} \alpha \\ \hline \boxed{\gamma} \\ \hline i \end{array} \begin{array}{c} \\ \hline \\ \hline j \end{array} = (\gamma)_{ij}^{[\alpha, \cdot]} := \sqrt{c^\alpha} \mathbb{1}_{\mathbb{S}^\alpha}(i) \delta_{ij} = \begin{array}{c} \alpha \\ \hline \boxed{\sqrt{c}} \diamond \boxed{\eta} \\ \hline i \end{array} \begin{array}{c} \\ \hline \\ \hline j \end{array} \quad (6.128)$$

and its Moore–Penrose inverse [175, 176] $\boldsymbol{\gamma}^+$ of its equivalent matrix representation. Here, the Moore–Penrose inverse is the left-inverse, i.e., $\boldsymbol{\gamma}^+\boldsymbol{\gamma} = \mathbb{1}$. The concentration-scaled indicator tensor $\boldsymbol{\gamma}$ is an embedding of the lattice space in the extended space but unlike $\boldsymbol{\eta}$ it is not isometric as $\boldsymbol{\gamma}^\top \neq \boldsymbol{\gamma}^+$. The components of the Moore–Penrose inverse read

$$(\boldsymbol{\gamma}^+)_{ij}^\alpha = \begin{cases} \frac{1}{\sqrt{c^\alpha}} \mathbb{1}_{\mathbb{S}^\alpha}(i) \delta_{ij} & \text{if } c^\alpha > 0, \\ 0 & \text{if } c^\alpha = 0. \end{cases} \quad (6.129)$$

We can express the projector eq. (6.73) in terms of the concentration-scaled $\boldsymbol{\gamma}$ -tensor:

$$\boldsymbol{\chi} = \boldsymbol{\eta}\boldsymbol{\eta}^\top = \boldsymbol{\gamma}\boldsymbol{\gamma}^+. \quad (6.130)$$

For the renormalized BEB formalism, we define the component Green's function and the Hamiltonian matrix in terms of $\boldsymbol{\gamma}$ and the inverse $\boldsymbol{\gamma}^+$ as

$$\begin{aligned} \widetilde{\mathfrak{S}}(z) &:= (\boldsymbol{\gamma}^+)^\top \mathbf{G}(z) \boldsymbol{\gamma}^+, \\ \mathbf{H} &:= \boldsymbol{\gamma} \widetilde{\mathfrak{S}} \boldsymbol{\gamma}^\top. \end{aligned} \quad (6.131)$$

²The DOS is defined as $\rho(\varepsilon) = \frac{1}{N} \sum_k \delta(\varepsilon - \varepsilon_k)$, where the dispersion ε_k are the eigenvalues of a matrix of hopping amplitudes \mathbf{T} . Therefore, the first moment is the normalized sum over eigenvalues $\varepsilon_{(1)} = \int d\varepsilon \rho(\varepsilon)\varepsilon = \frac{1}{N} \sum_k \varepsilon_k$, that is the trace $\varepsilon_{(1)} = \frac{1}{N} \text{Tr } \mathbf{T}$. Typically, the definition of the matrix of amplitudes \mathbf{T} contains only off-diagonal elements, consequently first moment vanished $\varepsilon_{(1)} = 0$.

Compared to the definitions in section 6.4.1, the Green's function and the Hamiltonian are scaled by the concentration.

The renormalized formalism can be conveniently demonstrated in the locator expansion

$$\mathbf{G}(z) = \mathbf{g}(z) + \mathbf{g}(z)\mathbf{T}\mathbf{G}(z), \quad (6.132)$$

where $\mathbf{g}(z) = [\mathbb{1}z - \mathbf{v}]^{-1}$ is the locator and $(\mathbf{T})_{ij} = t_{ij}$ the hopping matrix elements. Sandwiching this equation by $(\gamma^+)^T$ and γ^+ , we obtain

$$(\gamma^+)^T \mathbf{G}(z) \gamma^+ = (\gamma^+)^T \mathbf{g}(z) \gamma^+ + (\gamma^+)^T \mathbf{g}(z) \gamma^+ \gamma \mathbf{T} \gamma^T (\gamma^+)^T \mathbf{G}(z) \gamma^+, \quad (6.133)$$

where we inserted the identity $\gamma^+ \gamma = \mathbb{1} = (\gamma^+ \gamma)^T$. In terms of the renormalized component quantities, this equation writes

$$\tilde{\mathfrak{G}}(z) = \tilde{\mathfrak{g}}(z) + \tilde{\mathfrak{g}}(z) \tilde{\mathfrak{T}} \tilde{\mathfrak{G}}(z). \quad (6.134)$$

Compared to the regular BEB formalism the Green's functions are scaled with the reciprocal concentration, and the hopping matrix eq. (6.99) with the concentration

$$(\tilde{\mathfrak{T}})_{ij}^{\alpha\beta} = \sqrt{c^\alpha} t^{\alpha\beta} (|\mathbf{r}_i - \mathbf{r}_j|) \sqrt{c^\beta}. \quad (6.135)$$

The renormalized component Green's function $\tilde{\mathfrak{G}}(z)$ relates to the one-particle Green's $\mathbf{G}(z)$ function in the following way:

$$\mathbb{E} \left(\tilde{\mathfrak{G}}_{ij}^{\alpha\beta}(z) \right) = \begin{cases} \mathbb{E}(G_{ii}(z) | i \mapsto \alpha) \delta^{\alpha\beta} & \text{if } i = j, \\ \sqrt{c^\alpha c^\beta} \mathbb{E}(G_{ii}(z) | i, j \mapsto \alpha, \beta) & \text{if } i \neq j. \end{cases} \quad (6.136)$$

For the local Green's function $\mathbb{E}(\tilde{\mathfrak{G}}_{ii}^{\alpha\beta}(z))$ there is no concentration prefactor in the renormalized formulation; since the BEB formalism is a local theory, $\mathbb{E}(\tilde{\mathfrak{G}}_{ii}^{\alpha\beta}(z))$ is the central quantity. The renormalized version of the self-consistency equation eqs. (6.105) and (6.107) reads

$$0 = \tilde{\mathfrak{g}}_{\text{loc}}^{-1}(z) - \bar{\mathfrak{g}}^{-1}(z), \quad (6.137)$$

with the diagonal matrix in the components

$$\bar{\mathfrak{g}}^{\alpha\beta}(z) = \frac{c^\alpha \delta^{\alpha\beta}}{(\tilde{\mathfrak{g}}_{\text{loc}}^{-1})^{\alpha\alpha} + \tilde{\mathfrak{G}}^{\alpha\alpha} - \bar{c}^\alpha z + c^\alpha (\mu - \mathbf{v}^\alpha - \Sigma^\alpha)}. \quad (6.138)$$

With $\alpha \neq \beta$, the high-frequency expansion of the renormalized effective medium yields

$$\tilde{\mathfrak{G}}^{\alpha\beta}(z) = -\varepsilon_{(1)} \sqrt{c^\alpha} \mathfrak{T}^{\alpha\beta} \sqrt{c^\beta} + \mathcal{O}(z^{-1}) \quad (6.139)$$

$$\tilde{\mathfrak{G}}^{\alpha\alpha}(z) = \mathbf{v}^\alpha - \mu + \bar{c}^\alpha \mathfrak{T}^{\alpha\alpha} \varepsilon_{(1)} + \mathcal{O}(z^{-1}). \quad (6.140)$$

The renormalization removes the contribution proportional to z , and the static part is simply the on-site energy of the components for the typical case $\varepsilon_{(1)} = 0$. Furthermore, the static part remains finite for vanishing concentration $c^\alpha \rightarrow 0$.

6.4.7. Limit of independent components [W3]

We consider the limit of vanishing hopping between different components. If the hopping is diagonal in the components, $\mathfrak{T}^{\alpha\beta} \propto \delta^{\alpha\beta}$, the BEB effective medium $\mathfrak{S}(z)$ is also diagonal in the components, and the components decouple in the self-consistency equations eq. (6.107). In this case, the effective local Green's function eq. (6.102) can be readily calculated, since the matrix inverse is the reciprocal of the diagonal elements:

$$\mathbf{g}_{\text{loc}}^{\alpha\beta}(z) = \frac{1}{N} \sum_k \frac{\delta^{\alpha\beta}}{z - \mathfrak{S}^{\alpha\alpha}(z) - \mathfrak{T}^{\alpha\alpha}\varepsilon_k} = \delta^{\alpha\beta} g_0^\alpha(z - \mathfrak{S}^{\alpha\alpha}(z)). \quad (6.141)$$

Here, g_0^α is the lattice Hilbert transform $g_0(z) = \frac{1}{N} \sum_k \frac{1}{z - \varepsilon_k}$; its superscript α indicates that the bandwidth is scaled by $\mathfrak{T}^{\alpha\alpha}$:

$$g_0^\alpha(z) = \frac{1}{N} \sum_k \frac{1}{z - \mathfrak{T}^{\alpha\alpha}\varepsilon_k} = \frac{1}{\mathfrak{T}^{\alpha\alpha}} g_0(z/\mathfrak{T}^{\alpha\alpha}). \quad (6.142)$$

For the component α , the decoupled self-consistency eq. (6.107) reads

$$0 = \frac{\bar{c}^\alpha}{g_0^\alpha(z - \mathfrak{S}^{\alpha\alpha})} + \mathfrak{S}^{\alpha\alpha} - \mathbf{v}^\alpha, \quad (6.143)$$

with the concentration complement $\bar{c}^\alpha = 1 - c^\alpha \geq 0$.

For a Bethe lattice with coordination number Z with the lattice Hilbert transform [164]

$$g_0(z, Z) = 2(Z - 2) / \left[z \left(Z - 2 + Z \sqrt{1 - D^2/z^2} \right) \right], \quad (6.144)$$

where D is the half-bandwidth, the self-consistency condition is an algebraic equation and can be solved analytically. The BEB effective medium reads

$$\begin{aligned} \mathfrak{S}^{\alpha\alpha}(z, Z) \\ = \frac{(Z-2)\mathbf{v}^\alpha c^\alpha + Z\mathbf{v}^\alpha + (Z+2)c^\alpha z - Zz - 2(c^\alpha)^2 z - Z\bar{c}^\alpha s \sqrt{(z - \mathbf{v}^\alpha)^2 - c^\alpha (D^\alpha)^2 \frac{Z - c^\alpha}{Z - 1}}}{2c^\alpha (Z - c^\alpha)}, \end{aligned} \quad (6.145)$$

where s is the sign $s = \text{sign}(\Re(z - v^\alpha))$, and D^α is the half-bandwidth scaled by $\mathfrak{T}^{\alpha\alpha}$; this is the retarded solution. A conjugate solution exists with $-s$ and therefore with a plus sign in front of the square root.

We are interested in the bandwidth of the resulting component spectrum

$$A^\alpha(\omega) = -\frac{1}{c^\alpha \pi} \Im g_0^\alpha(\omega + i0^+ - \mathfrak{S}^{\alpha\alpha}(\omega + i0^+)). \quad (6.146)$$

For non-interacting systems, the Gershgorin circle theorem [177] gives the *maximal* spectral bounds

$$|\omega - \mathbf{v}^\alpha| \leq D^\alpha. \quad (6.147)$$

In the limit $\mathfrak{T}^{\alpha\beta} \propto \delta^{\alpha\beta}$, we can make a more precise statement and derive the exact spectral bounds of BEB as will be discussed below. The spectral function can only vanish where the imaginary part of the effective medium vanishes. Thus, for non-interacting

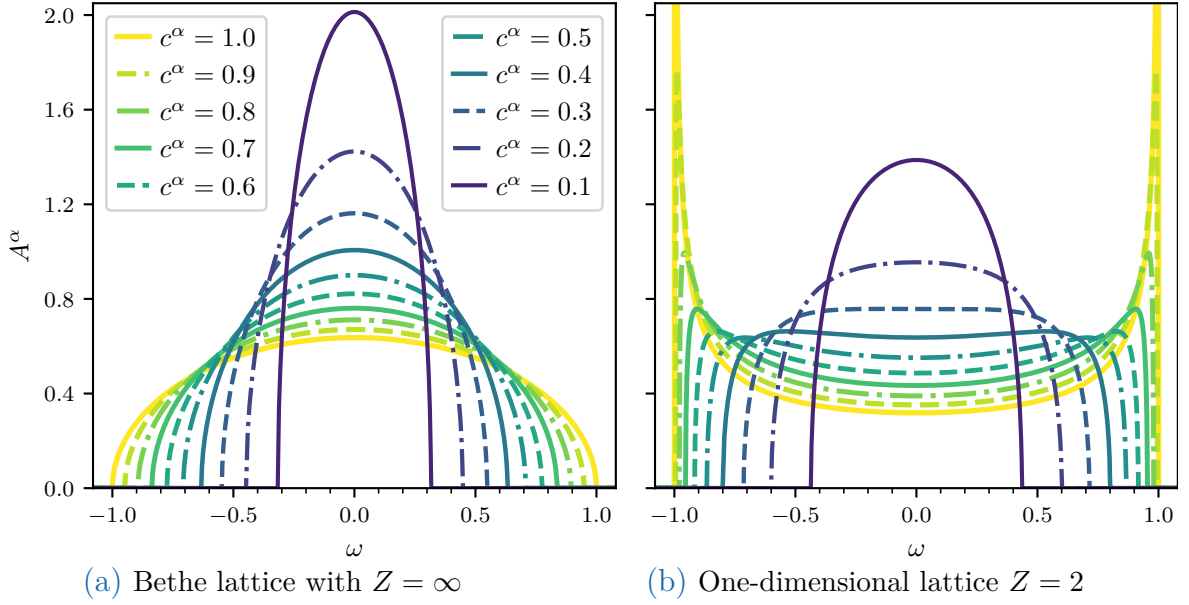


Figure 6.5.: Spectral function A^α for component α in the limit of independent components $\mathfrak{T}^{\alpha\beta} = \delta^{\alpha\beta}$ for different concentrations c^α . Only a single component α is shown as the components are independent. The on-site energy is $\mathbf{v}^\alpha = 0$, and half-bandwidth $D = 1$.

systems, we need to check where the argument of the square root is negative. One finds a finite imaginary part and therefore spectral weight for

$$|\omega - \mathbf{v}^\alpha| < \sqrt{c^\alpha \frac{Z - c^\alpha}{Z - 1}} D^\alpha. \quad (6.148)$$

Therefore, for the Bethe lattice with coordination number Z and $\mathfrak{T}^{\alpha\beta} \propto \delta^{\alpha\beta}$, the bandwidth is reduced due to concentration by a factor $\sqrt{c^\alpha(Z - c^\alpha)/(Z - 1)}$. We obtain the effective bandwidth

$$D_{\text{eff}}^\alpha = \sqrt{c^\alpha \frac{Z - c^\alpha}{Z - 1}} \mathfrak{T}^{\alpha\alpha} D. \quad (6.149)$$

Many of our numerical results were obtained for a semicircular DOS, i.e., the Bethe lattice with infinite coordination number $Z \rightarrow \infty$. In this limit one finds an effective bandwidth

$$D_{\text{eff}}^\alpha = \sqrt{c^\alpha} \mathfrak{T}^{\alpha\alpha} D. \quad (6.150)$$

The same factor \sqrt{c} was found by Byczuk et al. [178] in the CPA ($\mathfrak{T}^{\text{AA}} = \mathfrak{T}^{\text{AB}} = \mathfrak{T}^{\text{BB}} = 1$) in the limit of high disorder strength $(\mathbf{v}^{\text{B}} - \mathbf{v}^{\text{A}})/D = \delta \gg \max(1, U/D)$. In spite of the different parameter regimes, both limits, $\mathfrak{T}^{\alpha\beta} \propto \delta^{\alpha\beta}$ and $\delta \gg \max(1, U/D)$, describe the same physics, namely the decoupling of components. Indeed, the components decouple not only for vanishing hopping between the components $\mathfrak{T}^{\text{AB}} = 0$, but also in the case of a large separation in energy ($\delta \gg 1$). Figure 6.5(a) shows the component spectra of the Bethe lattice for different concentrations.

For coordination number $Z = 2$ another interesting limit of the Bethe lattice is obtained; this is the one-dimensional (1D) lattice [164], where

$$g_0^{1\text{D}}(z) = g_0(z, Z = 2) = 1 / \left[z \sqrt{1 - D^2/z^2} \right]. \quad (6.151)$$

The spectral bounds are given by

$$D_{\text{eff}}^{\alpha} = \sqrt{c^{\alpha}(2 - c^{\alpha})} \mathfrak{T}^{\alpha\alpha} D = \sqrt{1 - (\bar{c}^{\alpha})^2} \mathfrak{T}^{\alpha\alpha} D. \quad (6.152)$$

For the one-dimensional lattice and $\mathfrak{T}^{\alpha\beta} \propto \delta^{\alpha\beta}$ the bandwidth is reduced by the factor $\sqrt{c^{\alpha}(2 - c^{\alpha})}$. Figure 6.5(b) shows the corresponding component spectra for different concentrations.

7. Electronic correlation in alloys

7.1. The local CPA+DMFT approach for off-diagonal disorder [W3]

In this chapter, we combine chapters 3 and 6 to study disordered systems of interacting electrons; the notation of chapter 6, in particular section 6.4, is used. We treat the local Hubbard interaction within the DMFT [59, 62, 63], which assumes a local self-energy $\Sigma_{ij}(z) = \delta_{ij}\Sigma_{ii}(z)$; this property becomes exact in the limit of infinite coordination number.

The problem of interacting disordered electrons may hence equally be viewed as a system of non-interacting particles moving in an effective local, energy-dependent potential $\Sigma_{ii}(z)$ (for details see refs. [66, 179]). The DMFT self-consistency equations [62] are equivalent to a fixed-point problem which can be expressed by a functional $\hat{\Sigma}$: Given a self-energy Σ_{ii} and the resulting local Green's function $G_{ii}(\Sigma_{ii})$ this functional provides a new self-energy $\hat{\Sigma}[G_{ii}(\Sigma_{ii}), \Sigma_{ii}]$, such that the DMFT self-energy is determined self-consistently by the fixed-point

$$\Sigma_{ii} = \hat{\Sigma}[G_{ii}(\Sigma_{ii}), \Sigma_{ii}]. \quad (7.1)$$

Within the CPA, the local Green's function for a given self-energy $G_{ii}(\Sigma_{ii})$ is replaced by the conditional average $\mathbb{E}(G_{ii}(\Sigma_{ii})|i \mapsto \alpha) = \mathbf{g}_{\text{loc}}^{\alpha\alpha}(\Sigma_{ii})/c^\alpha$, see eqs. (6.81) and (6.102). Thus, the self-energy $\hat{\Sigma}[\mathbf{g}_{\text{loc}}^{\alpha\alpha}(\Sigma_{ii})/c^\alpha, \Sigma_{ii}]$ depends on the component α . Consequently, the self-energy at the fixed-point depends on the component α , but not on the explicit site i :

$$\Sigma^\alpha = \hat{\Sigma}[\mathbf{g}_{\text{loc}}^{\alpha\alpha}(\Sigma^\alpha)/c^\alpha, \Sigma^\alpha]. \quad (7.2)$$

This allows one to introduce the BEB+DMFT self-consistency which we will discuss next.

By merging the BEB formalism with DMFT a twofold self-consistency arises, one for the BEB and one for the DMFT corresponding to the fixed-point eq. (7.2). The self-consistency equation of the BEB formalism is pointwise in the frequencies and is therefore much simpler than the self-consistency condition of the DMFT, where frequencies mix due to the energy exchange caused by the interaction between the electrons. We view the BEB self-consistency as an inner part of the full self-consistency loop. In the BEB method we calculate an effective local Green's function matrix $\mathbf{g}_{\text{loc}}(z)$, eq. (6.102). The effective medium $\mathfrak{S}(z)$ and, therefore, the effective local Green's function have to be calculated self-consistently from eqs. (6.105) and (6.107). Including the DMFT self-energy $\Sigma^\alpha(z)$ for the component α in the on-site potential $\mathbf{v}^\alpha \rightarrow \mathbf{v}^\alpha + \Sigma^\alpha(z)$, the average eq. (6.105) reads

$$\bar{\mathbf{g}}^{\alpha\beta}(z) = \frac{c^\alpha \delta^{\alpha\beta}}{(\mathbf{g}_{\text{loc}}^{-1})^{\alpha\alpha}(z) + \mathfrak{S}^{\alpha\alpha}(z) + \mu - \mathbf{v}^\alpha - \Sigma^\alpha(z)}, \quad (7.3)$$

The self-consistent eq. (6.107) can be solved with standard root-search algorithms or by simple iteration. In practice, we use an implementation of the BEB formalism without interactions and merely shift the on-site energy $\mathbf{v}^\alpha \rightarrow \mathbf{v}^\alpha + \Sigma^\alpha(z)$. An efficient evaluation of the BEB self-consistency equation is discussed in section 6.4.5; an implementation is provided by the code [C2]. To emphasize the dependence on the self-energy, we denote the self-consistently determined effective local Green's function matrix for a given self-energy eq. (6.107) by $\mathbf{g}_{\text{loc}}(z, \Sigma(z))$.

With the BEB self-consistency condition eq. (6.107) for the local Green's function $\mathbf{g}_{\text{loc}}(z, \Sigma(z))$, the combined algorithm corresponds to the conventional DMFT self-consistency condition eq. (7.2), where the local Green's function, calculated from the lattice Hilbert transform, is replaced by the average

$$\mathbb{E}(G_{ii}|i \mapsto \alpha) = \mathbf{g}_{\text{loc}}^{\alpha\alpha}(z, \Sigma(z))/c^\alpha.$$

The multiplicative concentration factor $1/c^\alpha$ can be avoided by employing the concentration-scaled indicator tensor eq. (6.128), which leads to a slightly modified BEB self-consistency as elaborated in section 6.4.6. We have to solve a separate impurity problem for every component α . Starting from an initial guess for the DMFT self-energy $\Sigma^\alpha(z)$ for every component, the BEB+DMFT scheme is the following:

1. Calculate the effective local Green's function matrix eq. (6.102) using eqs. (6.107) and (7.3), which yields

$$\mathbf{g}_{\text{loc}}(z, \Sigma(z)). \quad (7.4a)$$

2. For every component α , calculate the hybridization function

$$\Delta^\alpha(z) = z + \mu - \mathbf{v}^\alpha - \Sigma^\alpha(z) - c^\alpha/\mathbf{g}_{\text{loc}}^{\alpha\alpha}(z, \Sigma(z)), \quad (7.4b)$$

3. For every component α , solve the impurity problem for the self-energy

$$\Sigma^\alpha(z) = \Sigma[\mathbf{v}^\alpha, \mathbf{u}^\alpha, \Delta^\alpha] \quad (7.4c)$$

4. Repeat from step 1 until self-consistency is reached.

The hybridization function can also be expressed in terms of BEB quantities using the self-consistency condition eq. (6.107):

$$\Delta^\alpha(z) = z - \mathfrak{S}^{\alpha\alpha}(z) - (\mathbf{g}_{\text{loc}}^{-1})^{\alpha\alpha}(z, \Sigma(z)). \quad (7.5)$$

This hybridization function differs from CPA+DMFT, where only one unique hybridization functions exists independent of the alloy components.

7.2. Numerical results [W3]

The above formalism is now used to study the effect of off-diagonal disorder in the Anderson–Hubbard model at zero temperature. We employ a Bethe lattice with infinite

coordination number, whose half-bandwidth D sets the energy scale. Furthermore, we consider a discrete binary random alloy distribution with components **A** and **B**.

In all applications we consider the case of half-filling on average $\mathbb{E}(n_i) = 1$; this leads to a fixed chemical potential which we choose as $\mu = 0$. In the following subsection we fix the alloy component concentration and study the change in the spectral function starting with the non-interacting case and equal atomic potentials. The alloy component spectral functions are the concentration-weighted conditional spectral functions

$$\mathfrak{A}^\alpha(\omega) := -\frac{1}{\pi} \Im \mathfrak{g}_{\text{loc}}^{\alpha\alpha}(\omega) = -\frac{c^\alpha}{\pi} \Im \mathbb{E}(G_{ii}(\omega) | i \mapsto \alpha). \quad (7.6)$$

The average spectral functions are given by the trace

$$\mathbb{E}(A(\omega)) = \sum_\alpha \mathfrak{A}^\alpha(\omega) = -\frac{1}{\pi} \Im \text{Tr} \mathfrak{g}_{\text{loc}}(\omega). \quad (7.7)$$

The central part of the DMFT problem is the impurity solver which provides the local dynamic self-energy eq. (7.4c). To this end, we employ a tensor-network-based zero-temperature solver, the fork tensor-product state solver [120]. We discretize the hybridization function eq. (7.4b) using 249 sites per spin resulting in a median energy distance of $0.03D$. We calculate the ground state $|GS\rangle$ of the finite size impurity problem using the DMRG [21, 22]. Subsequently, we perform the time evolution using the TDVP [145–147, 180]. To obtain the retarded time impurity Green's function $\mathcal{G}^r(t)$, the states $\hat{c}_\sigma |GS\rangle$, $\hat{c}_\sigma^\dagger |GS\rangle$, as well as their adjoint states are time-evolved, cf. Ganahl et al. [119], where \hat{c}_σ (\hat{c}_σ^\dagger) is the annihilation (creation) operator of the impurity site. For DMRG we chose a truncated weight of 10^{-15} and a maximal bond dimension of 100. We perform the TDVP using time steps of $0.1/D$ up to a maximal time $t_{\text{max}} = 150/D$ with a truncated weight of 10^{-9} and a maximal bond dimension of 150. The convergence with respect to these parameters is checked. For the Laplace transform, we use a shift $\eta = 0.08$ and calculate the first order correction

$$G(\omega + i0^+) = G(\omega + i\eta) + \eta F_\eta[t\mathcal{G}^r(t)](\omega) + \mathcal{O}(\eta^2) \quad (7.8)$$

see appendix B.4 eqs. (B.22) and (B.23). The self-energy is calculated from the equation of motion of the impurity model [71],

$$\Sigma_\sigma(z) = UF_\sigma(z)/G_\sigma(z), \quad (7.9)$$

$$\mathcal{F}^r(t) = \langle GS | \hat{c}_\sigma(t) \hat{n}_{-\sigma}(t) \hat{c}_\sigma^\dagger | GS \rangle, \quad (7.10)$$

where $F(z)$ is the Laplace transform of $\mathcal{F}^r(t)$, cf. section 3.1.1.

7.2.1. Non-interacting limit [W3]

We start with the non-interacting case by setting $\mathfrak{U}^A = \mathfrak{U}^B = 0$, which corresponds to the Anderson model with purely off-diagonal disorder. Since the non-interacting Green's function is independent of temperature the results presented in this section are valid not only for zero, but also for finite temperatures. We choose the parameters

$$\mathfrak{v}^A = \mathfrak{v}^B = -U/2 = 0; \quad c^A = 0.1 = 1 - c^B; \quad \mathfrak{T}^{AA} = \mathfrak{T}^{BB} = 1$$

and calculate the average and the alloy component spectral functions for several values of \mathfrak{T}^{AB} at half filling. The case $\mathfrak{T}^{\text{AB}} = 1$ is equivalent to the non-disordered case since $\mathbf{v}^{\text{A}} = \mathbf{v}^{\text{B}}$; in this case the components are indistinguishable. Thus, the average spectral function is just the spectral function of the non-disordered Bethe lattice, and the component Green's functions $\mathfrak{g}_{\text{loc}}^{\alpha\alpha}(\omega)$ are proportional to the Bethe Green's function with the concentration prefactor c^α .

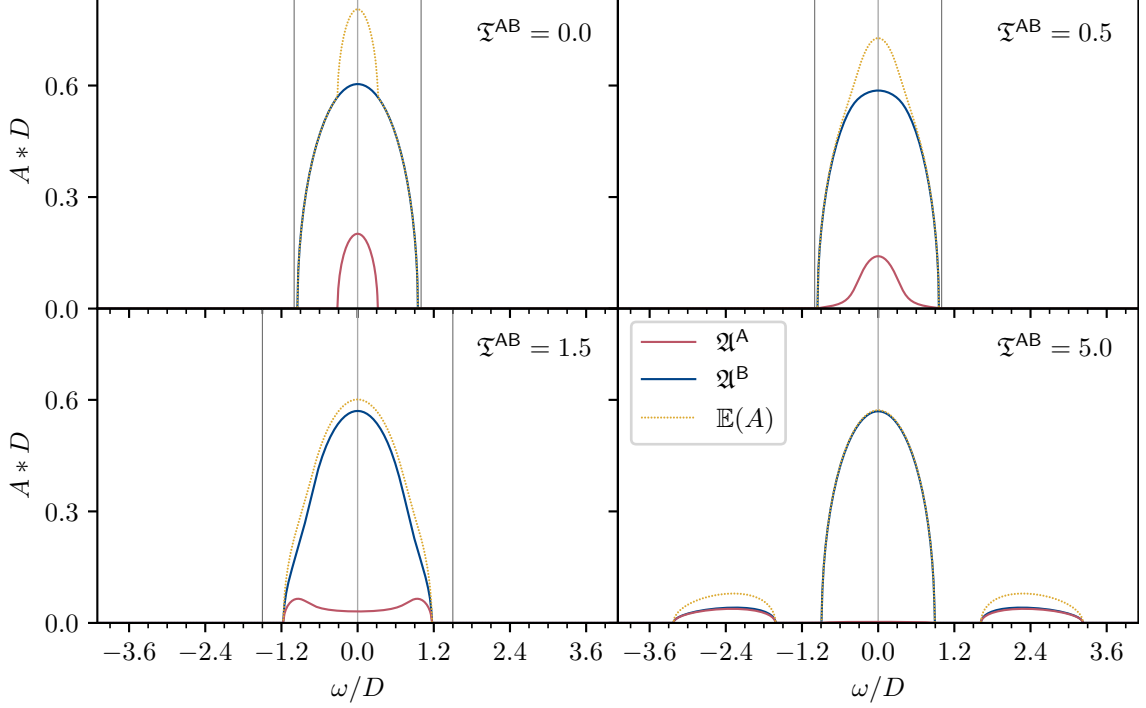


Figure 7.1: Non-interacting case: Comparison of spectral functions for different dimensionless hopping parameters \mathfrak{T}^{AB} . The parameters are $\mathfrak{U}^{\text{A}} = \mathfrak{U}^{\text{B}} = 0$, $\mathbf{v}^{\text{A}} = \mathbf{v}^{\text{B}} = 0$, $c^{\text{A}} = 0.1 = 1 - c^{\text{B}}$, and $\mathfrak{T}^{\text{AA}} = \mathfrak{T}^{\text{BB}} = 1$. The solid lines represent the component spectral functions $\mathfrak{A}^\alpha(z) = c^\alpha \mathbb{E}(A_i(z)|i \mapsto \alpha)$, where A is red and B is blue; the dotted yellow line shows the average spectral function $\mathbb{E}(A(z)) = \mathfrak{A}^{\text{A}}(z) + \mathfrak{A}^{\text{B}}(z)$. The thin vertical lines show the maximal spectral bounds given by the Gershgorin circle theorem [177]. Figure adapted from ref. [W3] (fig. 1).

Figure 7.1 shows the spectral function for off-diagonal disorder for the hopping parameters $\mathfrak{T}^{\text{AB}} = 0.0, 0.5, 1.5, 5.0$. The case $\mathfrak{T}^{\text{AB}} = 0$ was solved exactly in section 6.4.7. The panel $\mathfrak{T}^{\text{AB}} = 0$ in fig. 7.1 indicates that off-diagonal disorder reduces the bandwidths; according to eq. (6.149) the effective bandwidths are given by $D_{\text{eff}}^{\text{A}} = \sqrt{0.1}D \approx 0.32D$ and $D_{\text{eff}}^{\text{B}} = \sqrt{0.9}D \approx 0.95D$. For $\mathfrak{T}^{\text{AB}} < 1 = \mathfrak{T}^{\alpha\alpha}$ the probabilities for hopping between the alloy components A and B are less than those between the same component α . The spectral functions in the upper half of fig. 7.1 correspond to this situation. In spite of a similar support on the energy axis, the spectral function of the majority component B has a larger bandwidth, which encompasses the effective bandwidth of component A. By contrast, when $\mathfrak{T}^{\text{AB}} > 1 = \mathfrak{T}^{\alpha\alpha}$, A-B bonds are energetically favorable. The panel $\mathfrak{T}^{\text{AB}} = 1.5$ in fig. 7.1 shows that the spectral function of component A develops shoulders, although both components have similar effective bandwidths. When the value of \mathfrak{T}^{AB} is increased further the shoulders split off from the central band; for the parameters chosen the split-off is visible for $\mathfrak{T}^{\text{AB}} \geq 2.25$. According to Burdin and Fulde [181] the split-off

upper and lower bands correspond to bonding and antibonding states, respectively. In the particle-hole symmetric case, the bonding and antibonding bands in panel $\mathfrak{T}^{\text{AB}} = 5.0$ of fig. 7.1 have equal weights. Due to the large value $\mathfrak{T}^{\text{AB}} = 5.0$, the minority component **A** is completely suppressed in the central band. The components **A** and **B** contribute roughly equally to the bonding and antibonding subbands. Therefore, the central band of the average spectral function is depleted by an amount of $(1 - 2c^{\text{A}}) = 0.8$. The overall results and the spectral weight transfer from the central band are consistent with those reported by Burdin and Fulde [181].

7.2.2. Alloy components with equal interaction strengths [W3]

In the following, we will discuss the results for the interacting case using the setup described in section 7.2.1 at zero temperature ($T = 0$). The alloy components have identical on-site interaction parameters:

$$\mathfrak{U}^{\text{A}} = \mathfrak{U}^{\text{B}} = U = 3D.$$

At half-filling, the on-site energies are $\mathfrak{v}^{\text{A}} = \mathfrak{v}^{\text{B}} = -U/2 = -1.5D$.

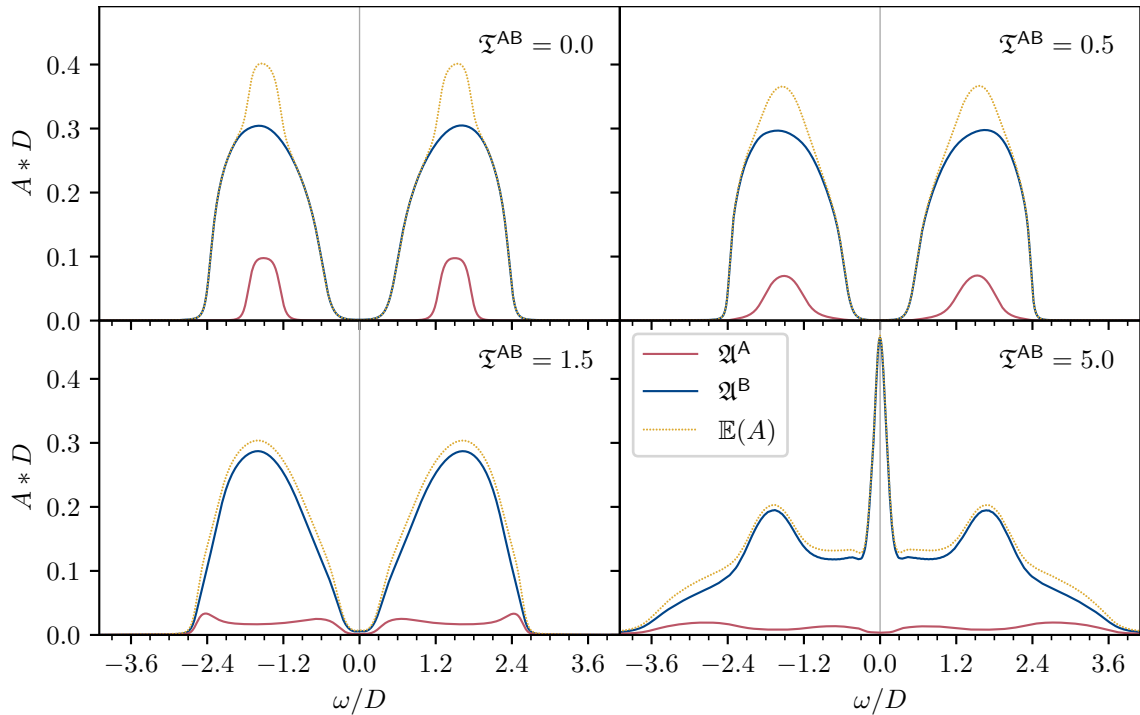


Figure 7.2.: Comparison of spectral functions for different values of the dimensionless hopping parameter \mathfrak{T}^{AB} with $\mathfrak{U}^{\text{A}} = \mathfrak{U}^{\text{B}} = 3D$, $\mathfrak{v}^{\text{A}} = \mathfrak{v}^{\text{B}} = -1.5D$, $c^{\text{A}} = 0.1 = 1 - c^{\text{B}}$, and $\mathfrak{T}^{\text{AA}} = \mathfrak{T}^{\text{BB}} = 1$ at $T = 0$. For $\mathfrak{T}^{\text{AB}} = 0$ a shift $\eta = 0.12$ had to be used; the other panels were calculated for $\eta = 0.08$. Figure adapted from ref. [W3] (fig. 2).

Figure 7.2 shows the spectral function for various values of \mathfrak{T}^{AB} . For $\mathfrak{T}^{\text{AB}} = 0$, when the self-consistency equations decouple, the spectral functions of both components imply insulating behavior due to the strong interaction $U = 3D$. The upper and lower Hubbard bands centered around $\pm U/2$ are visible. The bandwidth of the Hubbard bands is

effectively reduced according to eq. (6.149). Therefore, the gap is wider for component A. Finite values of \mathfrak{T}^{AB} lead to wider spectral functions, and the bandwidth of the minority component A broadens to the same bandwidth as for B. Although for $\mathfrak{T}^{\text{AB}} = 1.5$ the imaginary part of the self-energy shows a prominent peak at $\omega = 0$, the spectral function remains finite at the Fermi level. The convergence of the DMFT computations slows down for this value of $\mathfrak{T}^{\text{AB}} = 1.5$, hinting at the proximity of a transition. The minority component A exhibits shoulders at the band-edge. For $\mathfrak{T}^{\text{AB}} = 1.7$ (not shown) one observes a pronounced quasi-particle peak at the Fermi level of both components, indicating that the system is metallic. A further increase to $\mathfrak{T}^{\text{AB}} = 5.0$ leads to an increased spectral weight at the Fermi level for the majority component B, while the spectral function of A has a minimum at the Fermi level.

For small values of \mathfrak{T}^{AB} the spectral gap results from the local Hubbard physics. Disorder then plays a minor role and mostly modifies the bandwidth and therefore the gap size. An increase of \mathfrak{T}^{AB} leads to a larger bandwidth compared to that of the CPA+DMFT result for $\mathfrak{T}^{\text{AB}} = 1$. For larger values of \mathfrak{T}^{AB} the spectral function of the component A is seen to open a pseudogap around the Fermi level which is accompanied by an increase of spectral weight of the component B. For large \mathfrak{T}^{AB} , the pseudogap is a result of the off-diagonal disorder.

7.2.3. Alloy components with different interaction strengths [W3]

In a binary alloy the strength of the interaction between electrons may also depend on the alloy component. Therefore, we explore the effect of off-diagonal disorder in this case. We illustrate the results for an extreme case, namely for a strong repulsion $\mathfrak{U}^{\text{B}} = 3D$ of the majority component B only, while the minority component remains non-interacting ($\mathfrak{U}^{\text{A}} = 0$). We consider half-filling with $\mathfrak{v}^{\text{A}} = 0$, $\mathfrak{v}^{\text{B}} = -\mathfrak{U}^{\text{B}}/2 = -1.5D$ and note that, in spite of the different values $\mathfrak{v}^{\text{A}} \neq \mathfrak{v}^{\text{B}}$, the effective (diagonal) disorder strength is zero, since the Hartree self-energy compensates the difference.

Figure 7.3 shows the evolution of the spectral function for increasing \mathfrak{T}^{AB} . For $\mathfrak{T}^{\text{AB}} = 0$, the A alloy component is metallic, while due to the large \mathfrak{U}^{B} value the B component is insulating. We note that the two components have different effective bandwidths due to the different concentrations. The panel with $\mathfrak{T}^{\text{AB}} = 0.5$ shows a small peak for the B component, in spite of the large interaction strength. At $\mathfrak{T}^{\text{AB}} = 1$, the A-A, A-B, and B-B hopping probabilities are the same, which leads to the same effective bandwidths, and to the appearance of the metallic state for both alloy components.

In fig. 7.3 the panel with $\mathfrak{T}^{\text{AB}} = 1.5$ shows a distinct peak for the majority component B at the Fermi level, which reduces the spectral function for the A component at the Fermi level, leading to a local minimum. Increasing the inter-component hopping to $\mathfrak{T}^{\text{AB}} = 5.0$, the peak of B becomes even larger, and the spectral weight of A almost vanishes at the Fermi level. The panels with $\mathfrak{T}^{\text{AB}} = 5.0$ of figs. 7.2 and 7.3 are seen to be very similar; apparently the interaction of the minority component has little effect on the spectral function.

Figure 7.4 shows the quasi-particle weight

$$Z^{\alpha} = \left[1 - \frac{\partial \Re \Sigma^{\alpha}(\omega + i\eta)}{\partial \omega} \Big|_{\omega=0} \right]^{-1} \quad (7.11)$$

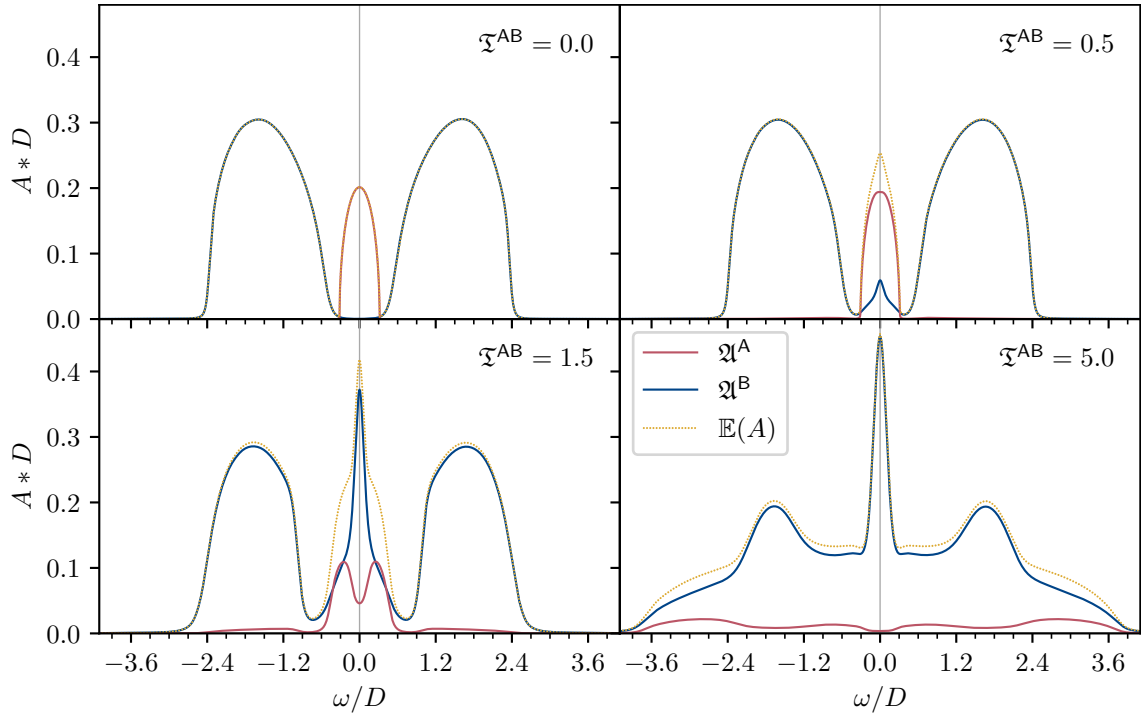


Figure 7.3.: Comparison of spectral functions for different values of the dimensionless hopping parameter \mathfrak{T}^{AB} with $\mathfrak{U}^A = 0$, $\mathfrak{U}^B = 3D$, $\mathfrak{v}^A = 0$, $\mathfrak{v}^B = -1.5D$, $c^A = 0.1 = 1 - c^B$, and $\mathfrak{T}^{AA} = \mathfrak{T}^{BB} = 1$ at $T = 0$. Figure adapted from ref. [W3] (fig. 3).

corresponding to the spectral functions of panel $\mathfrak{T}^{AB} = 5.0$ in the figs. 7.2 and 7.3. In spite of the large value of $\mathfrak{U}^A = 3D$, the quasiparticle weight Z^A is large, with a magnitude around 0.9. This gives an indication why the panels $\mathfrak{T}^{AB} = 5.0$ of figs. 7.2 and 7.3 are so similar; the large value of $\mathfrak{U}^A = 3D$ leads only to a small mass renormalization. Increasing the concentration of the weakly correlated component **A** leads to a significant increase of the quasiparticle weight Z^B for both setups. This can be explained by the increasing number of **A**-**B** bonds, which leads to an increased mobility of the electrons due to the large value of hopping parameter $\mathfrak{T}^{AB} = 5.0$ compared to the inter-component hopping parameters $\mathfrak{T}^{AA} = \mathfrak{T}^{BB} = 1$.

7.2.4. Combined effect of diagonal and off-diagonal disorder [W3]

In the following, we explore the combined effect of both diagonal and off-diagonal disorder, and their interplay with interaction. We choose a uniform interaction strength $\mathfrak{U}^A = \mathfrak{U}^B = U$ and introduce diagonal disorder with on-site potentials $\mathfrak{v}^A = -1.5D - U/2$, $\mathfrak{v}^B = +1.5D - U/2$. This means that the scattering strength is of the magnitude $\delta = (\mathfrak{v}^B - \mathfrak{v}^A)/D = 3$. We consider components with equal bandwidth $\mathfrak{T}^{AA} = \mathfrak{T}^{BB} = 1$ and equal concentration $c^A = c^B = 0.5$. Thus, the components are particle-hole conjugate and fulfill the relation

$$\mathfrak{g}_{\text{loc}}^{\text{AA}}(z) = -[\mathfrak{g}_{\text{loc}}^{\text{BB}}(z)]^*. \quad (7.12)$$

Figure 7.5 shows the average spectral function as well as that for the individual components for different values of the Hubbard parameter U and dimensionless inter-

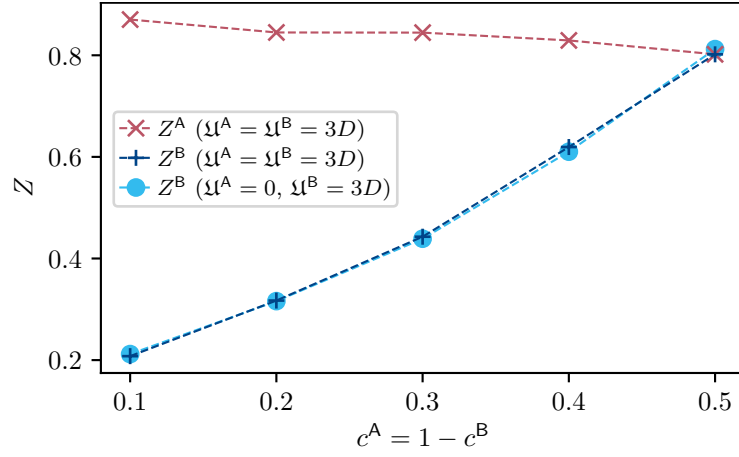


Figure 7.4.: Quasi-particle weight Z corresponding to $\mathfrak{T}^{AB} = 5.0$ in figs. 7.2 and 7.3 for the parameters $\mathbf{v}^A = -\varrho^A/2$, $\mathbf{v}^B = -\varrho^B/2$, $\mathfrak{T}^{AA} = \mathfrak{T}^{BB} = 1$, and $\mathfrak{T}^{AB} = 5.0$ at $T = 0$, calculated for a shift $\eta = 0.12$. Figure adapted from ref. [W3] (fig. 4).

component hopping amplitudes \mathfrak{T}^{AB} . In the non-interacting case $U = 0$ (first column of fig. 7.5) the split-band limit is apparent for all values of \mathfrak{T}^{AB} .

We first discuss the CPA limit $\mathfrak{T}^{AB} = 1$ (second row of fig. 7.5). In the split-band limit, there are no correlation effects: One component is basically filled $n_\sigma^A \approx 1$, and the other is depleted $n_\sigma^B \approx 0$. However, the Hartree energy, $\Sigma_\sigma^H = n_\sigma U$, decreases the effective disorder strength:

$$\begin{aligned} \delta_{\text{eff}} &= \frac{(\mathbf{v}^B + n_\sigma^B U) - (\mathbf{v}^A + n_\sigma^A U)}{D} \\ &\approx [\mathbf{v}^B - \mathbf{v}^A - U]/D = \delta - U/D. \end{aligned} \quad (7.13)$$

Switching on the interaction U effectively decreases the scattering strength δ . From $U \approx 2D$ on, the split-band limit at large scattering strength no longer applies, i.e., there is a combination of disorder and interaction effects. For $U = 4D$, we see the upper and lower Hubbard bands for each component, as well as a quasiparticle peak at the Fermi level. For even larger interaction strength ($U = 6D$) a Mott insulating phase is observed. Thus, by increasing U it is possible to tune the system from an alloy-band insulator, through a metallic phase, to a Mott insulating state. Similar results were reported by Lombardo *et al.* [182] for diagonal disorder using CPA+DMFT for somewhat different parameters and a finite-temperature impurity solver.

The behavior obtained in the CPA limit can now be modified by varying \mathfrak{T}^{AB} . At $U = 2D$ an off-diagonal hopping $\mathfrak{T}^{AB} < 1$ leads to metallic behavior, while $\mathfrak{T}^{AB} > 1$ favors a band gap. On the other hand, for $U = 6D$ a large \mathfrak{T}^{AB} favors metallicity. For $\mathfrak{T}^{AB} \leq 1$ the spectral function is gapped – similar to the result obtained in the Hubbard-I approximation [32].

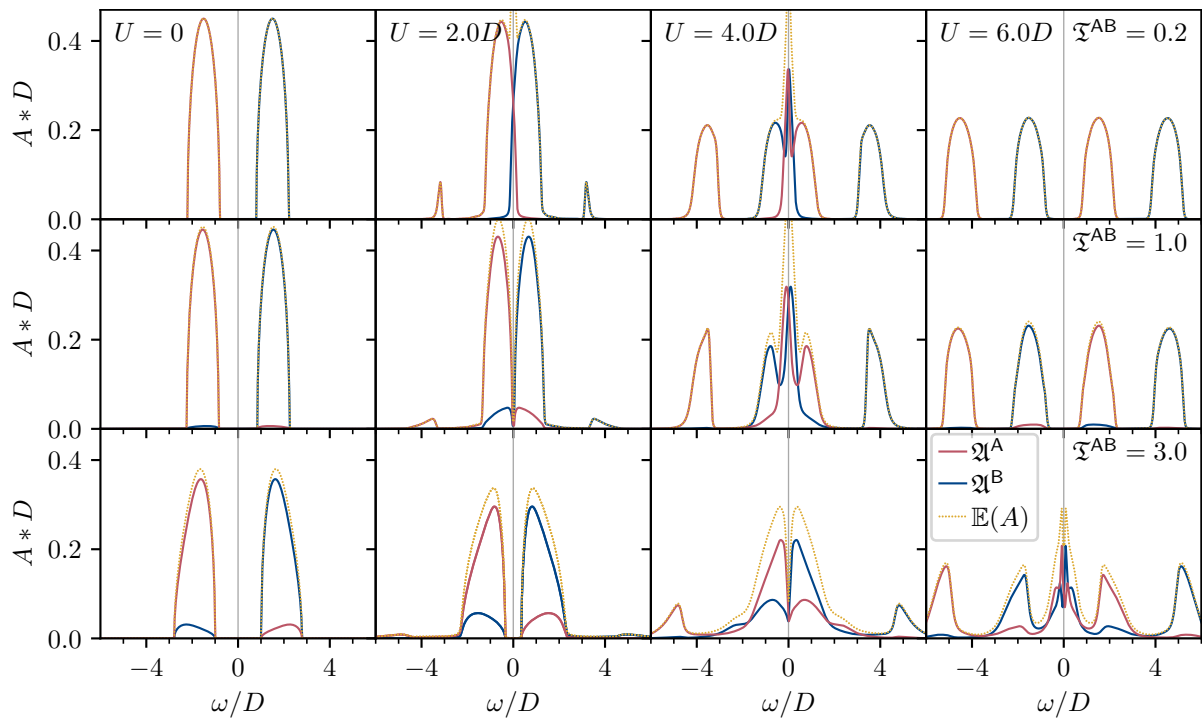


Figure 7.5.: Comparison of the spectral functions for $\mathfrak{U}^A = \mathfrak{U}^B = U$, $-(\mathfrak{v}^A + U/2) = \mathfrak{v}^B + U/2 = 1.5D$, $c^A = 0.5 = c^B$, $\mathfrak{T}^{AA} = \mathfrak{T}^{BB} = 1$, and $T = 0$ for different values of \mathfrak{T}^{AB} and U . Figure adapted from ref. [W3] (fig. 5).

8. Half-metals in layered systems [W2]

A half-metal is a material that has a metallic spectral function at the Fermi level for one spin channel and simultaneously a band gap for the other spin channel. This extreme asymmetry between the spin channels is the source of great promise for spintronic application [23, 24]. Half-metallic electrodes could provide fully spin-polarized currents and large magnetoresistance in giant magnetoresistance and tunnel magnetoresistance devices [23].

In this chapter, we investigate models for bulk and bilayers containing half-metallic ferromagnet (HMF), in order to elucidate the effects of strong electronic correlations on the spectral function. Our focus is on the evolution of the finite-temperature many-body induced tails in the half-metallic gap.

8.1. Revisiting the bulk [W2]

In the one-band model, eq. (2.1), a simple way to generate the half-metallic ferromagnetic state is to introduce a sufficiently strong spin splitting such that one spin subband is empty (or full) in the Hartree-Fock (Stoner) picture. This section discusses the results for a homogeneous Hubbard Hamiltonian eq. (2.1) of a Bethe lattice with infinite coordination number with half-bandwidth D (setting the energy scale), spin splitting $h = \tilde{\epsilon}_\downarrow - \tilde{\epsilon}_\uparrow = 0.5D$, on-site energy $\tilde{\epsilon} - \mu = (\tilde{\epsilon}_\downarrow + \tilde{\epsilon}_\uparrow)/2 - \mu = 1.5D$, and Hubbard interaction $U = 2D$. The on-site energies $\tilde{\epsilon}_\sigma$ are given with respect to the particle-hole symmetric case, that is $\tilde{\epsilon}_\sigma = \epsilon_\sigma - U/2$, cf. section 2.1.1. Difficulties in solving the Hubbard model for such a saturated ferromagnet are well known [27].

For the real-frequency results at zero temperature, the hybridization function of the Bethe lattice $\Delta_\sigma(\omega)$, eq. (3.20), is discretized using 251 bath sites per spin. We find the ground state $|GS\rangle$ ($T \equiv 0$) of the effective impurity model to be fully polarized ($n_\downarrow = 0$, $n_\uparrow = 0.341$). The interacting Green's function $\mathcal{G}^f(t)$ is calculated from the time-evolution of the states $\hat{c}_\sigma^\dagger |GS\rangle$ and $\hat{c}_\sigma |GS\rangle$, as well as of the adjoint states $\langle GS | \hat{c}_\sigma$ and $\langle GS | \hat{c}_\sigma^\dagger$, cf. Ganahl et al. [119], employing the TDVP described in section 5.6. This is done using time steps $\delta = 0.1/D$, up to a maximal time of $t_{\max} = 120/D$. For DMRG we chose a truncated weight of 10^{-15} and a maximal bond dimension of 100. For the TDVP, a truncated weight of 10^{-11} together with a maximal bond dimension of 500 is chosen. The Laplace transform is performed employing the quadratic Hermite-Padé algorithm, cf. appendix B.5 and evaluated for a shift $\eta = 10^{-3}$ into the imaginary plane.

For the QMC results at finite temperature, we compute the self-energy via the ratio of the two-particle Green's function $F_\sigma(z)$ and the one-particle Green's function $G_\sigma(z)$ [71, 72]:

$$\mathcal{F}_\sigma(\tau - \tau') = \left\langle c_\sigma(\tau) c_{-\sigma}^+(\tau) c_{-\sigma}(\tau) c_\sigma^+(\tau') \right\rangle_{S_{\text{eff}}}, \quad (8.1)$$

$$\Sigma_\sigma(i\omega_n) = U F_\sigma(i\omega_n) / G_\sigma(i\omega_n), \quad (8.2)$$

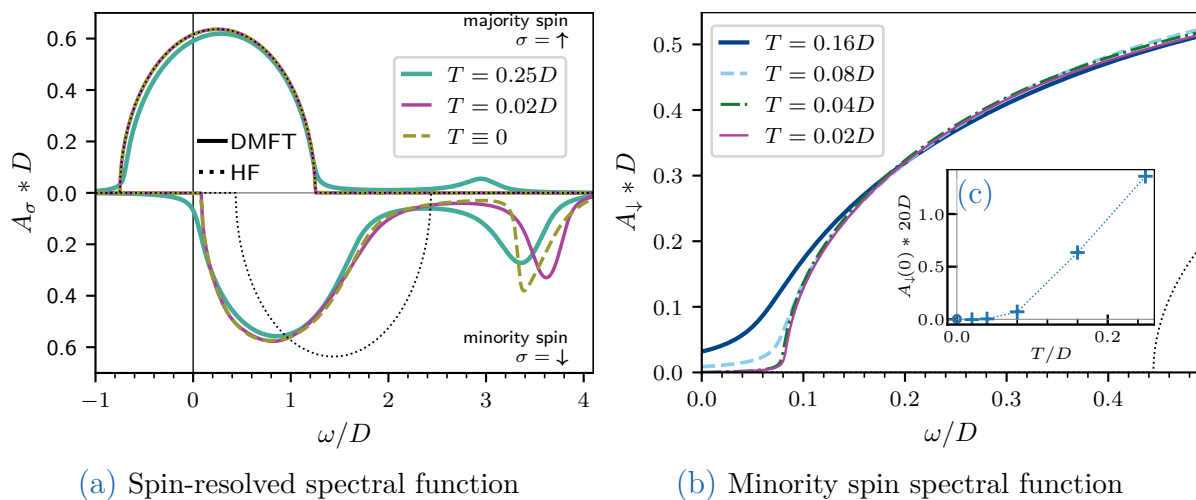


Figure 8.1.: (a) Spin-resolved spectral function $A_\sigma(\omega)$ for the bulk half-metal. Black dotted lines correspond to the Hartree-Fock (HF) approximation. At high temperatures ($T = 0.25D$), the tail of the spectral function $A_\downarrow(\omega)$ crosses the Fermi level, while for low enough temperatures ($T \leq 0.02D$) the half-metallic gap is preserved. (b) Evolution of the tail in the minority spin spectral function $A_\downarrow(\omega)$ with temperature, the lowest temperature corresponding to the low T result of the left panel. Again, the black dotted line shows the HF result. The inset (c) displays the T dependence of the spectral weight $A_\downarrow(\omega = 0)$. Crosses indicate finite temperatures shown in the left panel as well as $T = 0.25D$; the circle corresponds to $T \equiv 0$. Figure adapted from ref. [W2] (fig. 1).

as explained in section 3.1.1. The brackets $\langle \cdot \rangle_{S_{\text{eff}}}$ denote the average in the effective impurity model. This provides more accurate results than the Dyson equation, such that the Padé analytic continuation [102–104] of the self-energy is reasonably accurate. We calculate the spectral function from the analytically continued self-energy $\tilde{\Sigma}_\sigma(\omega)$:

$$A_\sigma(\omega) = -\frac{1}{\pi} \Im \int_{-D}^D d\varepsilon \frac{\rho(\varepsilon)}{\omega - \varepsilon - \tilde{\epsilon}_\sigma - \tilde{\Sigma}_\sigma(\omega)}, \quad (8.3)$$

where $\rho(\varepsilon)$ is the DOS of the lattice and $\tilde{\Sigma}(\omega)$ is the Padé analytic continuation of the self-energy, eq. (8.2). Note that the calculation of eq. (8.2) simplifies for the fully polarized ground state $|GS\rangle$, as $\hat{c}_\downarrow |GS\rangle = 0$ and $\hat{c}_\uparrow^\dagger \hat{n}_\downarrow |GS\rangle = 0$. Thus, at $T \equiv 0$ the two-particle Green's function for the \uparrow spin vanishes, i.e. $F_\uparrow \equiv 0$, and therefore also the self-energy $\Sigma_\uparrow \equiv 0$.

Figure 8.1(a) displays the results of the DMFT calculations for zero, low ($T = 0.02D$), and high ($T = 0.25D$) temperature. The dotted line shows the HF solution as a reference. We first discuss the $T \equiv 0$ spectrum. As the \downarrow spin is completely depleted, the result for the \uparrow spin are nearly identical to the HF result. The \uparrow -spin electrons are almost uncorrelated, and the magnitude of the self-energy $\Sigma_\uparrow(\omega)$ is negligibly small. For the \downarrow spin, we see two main effects of correlations. First, the size of the gap is reduced compared to the HF approximation. For low energies, there is a dynamical reduction of the (static) Hartree self-energy (cf. fig. 8.2). Additionally, a many-body satellite appears at $\omega \approx 3.5D$ in $A_\downarrow(\omega)$, as shown in fig. 8.1(a). At low temperature $T = 0.02D$, the QMC result for the spectral function eq. (8.3) is in good agreement with the real-frequency results for zero temperature. There is a deviation for the satellite; however, analytic continuation is

not expected to resolve features that far from the Fermi level well. At high temperature, $T = 0.25D$, we obtain a tail crossing the Fermi level $\omega = 0$ shown in fig. 8.1(a), which depolarizes the HMF. Because of the tail, the \downarrow spin is now partially filled, resulting in correlation effects also in the \uparrow spin. The many-body satellite is visible in both spin channels for the high temperature.

Previous calculations [183] used a simplified quantum Monte Carlo scheme within the so-called exact enumeration technique [62], and therefore results for high temperature ($T = 0.25D$) only were accessible. Our high- T results differ from the previous ones [183], which show additional peaks in the spectral function. In contrast to the previous calculations [183], we determine the spectra from the analytically continued self-energy using eq. (8.3). In fact, we demonstrated in the appendix of [W2] that a Padé analytic continuation of the Green's function – instead of the self-energy eq. (8.2) – causes the appearance of these spurious features in the spectral function. Compare also the examples in section 4.2.3 which show similar spurious features.

Figure 8.1(b) shows the temperature dependence of the spectral function for the minority spin, $A_{\downarrow}(\omega)$, in particular its tail crossing the Fermi level. The highest temperature is $T = 0.16D$, and subsequent lines correspond to always half the previous temperature. The disappearance of the spectral weight at the Fermi level with decreasing temperature is apparent. A specific many-body feature in HMFs is attributed to spin-polaron processes [28]: The down-spin electron excitations forbidden in the one-electron description of HMFs arise due to the superposition of up-spin electron excitations and virtual magnons. In model calculations, the existence of this feature has been shown by perturbation-theory arguments for the broad-band case [27] (cf. next paragraph), and in the opposite, infinite- U limit [23, 28]. An analytic approximation allows us to explore the shape of the temperature dependence of the spectral function for the minority spins considering a contact electron-magnon interaction described by the exchange parameter [23, 28, 184]. According to this theory, a nonlinear temperature dependence is obtained from the competing effects of the magnon contribution to the residue of the Green's function, $\sim T^{3/2}$, with the shift of the band edge states being proportional to $T^{5/2}$. By a direct fit $A_{\downarrow}(\omega = 0) \propto T^{\alpha}$ to the data in the inset of fig. 8.1(c), an exponent α in the range of 3/2 to 2 is obtained.

Considering the perturbation-theory arguments in more detail, we first note that for a completely depleted down-spin channel as depicted in fig. 8.1(a) for $T \equiv 0$ and $T = 0.02D$, it is evident that an added up-electron (or hole) is not subject to interactions. Therefore, the *up-spin* self-energy $\Sigma_{\uparrow}(\omega)$ vanishes. On the other hand, there is a significant contribution to the *down-spin* self-energy, $\Sigma_{\downarrow}(\omega)$, due to scattering at up-spin electron-hole pairs that arise because of electronic correlations [23, 27, 28, 184, 185] (while down-spin electron-hole pairs are not possible as the minority spin channel is depleted). The ferromagnetic instability is triggered by the scattering of the down electron and the up hole, and hence this electron-hole triplet ‘bound-state’ can be considered a magnon [23, 27]. In perturbation theory, the following expression for the imaginary part of the self-energy is found:

$$\Im\Sigma_{k,\downarrow}(\omega) = -\frac{\pi U^2 n_{\uparrow}}{N} \sum_q [1 - f(\varepsilon_{k+q,\uparrow}) + n(\omega_q)] \delta(\omega - \varepsilon_{k+q,\uparrow} - \hbar\omega_q), \quad (8.4)$$

where $\omega_q \propto q^2$ is the magnon dispersion, $f(\epsilon)$ denotes the Fermi-Dirac distribution, and $n(\omega)$ is the Bose-Einstein distribution. As a consequence of the local approximation of

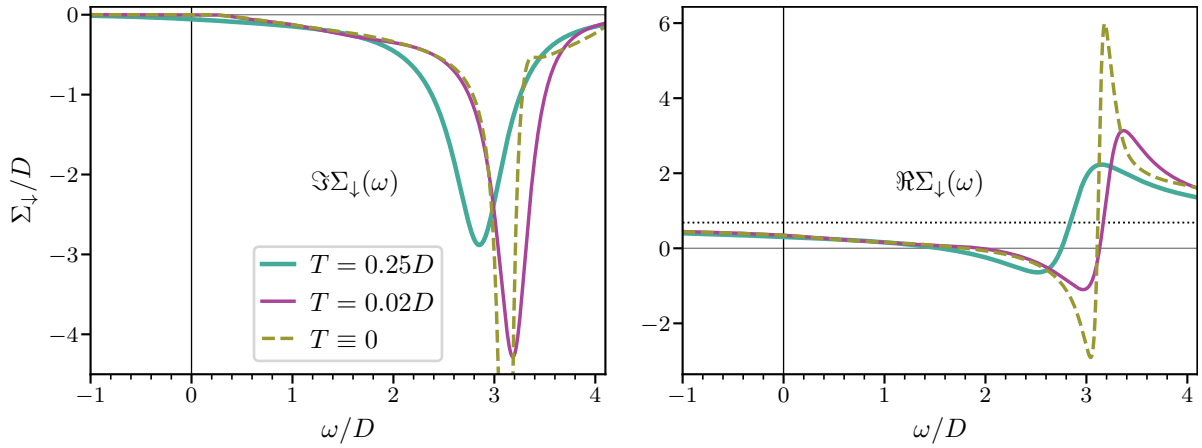


Figure 8.2.: Imaginary (left) and real (right) part of the down-spin self-energy $\Sigma_{\downarrow}(\omega)$ for the bulk half-metal. The dotted line for the real part indicates the HF result. The peak in $\Im\Sigma_{\downarrow}(\omega)$ for $T \equiv 0$ (truncated in the figure) extends downward to $-9.1D$. Figure adapted from ref. [W2] (fig. 2).

DMFT, the momentum dispersion of the magnons is lost; nevertheless, there is a pole in the magnetic susceptibility corresponding to a local spin flip. We thus conclude that the DMFT solver includes the scattering of electrons at virtual ‘magnons’ (of purely electronic origin), which can be described by diagrams constructed from the local Green’s function, and that the (numerical) local self-energy describes the same type of effective low-energy physics as discussed earlier [23, 27, 28, 184].

Figure 8.2 presents the self-energy for down-spin electrons corresponding to the spectral functions shown in fig. 8.1(a). At zero ($T \equiv 0$) and low ($T = 0.02D$) temperature, the imaginary part of the self-energy $\Im\Sigma_{\downarrow}$ vanishes at the Fermi level ($\omega = 0$); for high temperature ($T = 0.25D$), there is a finite tail, $-\Im\Sigma_{\downarrow} > 0$, crossing the Fermi level. The minimum of $\Im\Sigma(\omega)$ is located in the frequency range $3D$ to $3.5D$ for the temperatures considered, slightly below the energies where the satellite in the spectral function is visible in fig. 8.1(a). The satellite is located in the range $\omega - \Re\Sigma_{\downarrow}(\omega) \in (\tilde{\epsilon}_{\downarrow} - D, \tilde{\epsilon}_{\downarrow} + D)$; this range is reduced further due to the peak in the imaginary part of the self-energy. As a consequence, the satellites in the spectral functions are found at energies slightly above the peak of the imaginary part of the self-energy.

Furthermore, we investigate the *local* spin-flip susceptibility which we calculate from the effective impurity model:

$$\chi^{+-}(\tau - \tau') = \langle S^+(\tau)S^-(\tau') \rangle_{S_{\text{eff}}} = \langle c_{\uparrow}^+(\tau)c_{\downarrow}(\tau)c_{\downarrow}^+(\tau')c_{\uparrow}(\tau') \rangle_{S_{\text{eff}}}, \quad (8.5)$$

where S_{eff} is the same effective impurity model action from DMFT as in eq. (8.1). At zero temperature, the spin-flip susceptibility is obtained directly on the real axis by time-evolving the matrix-product state $|\psi\rangle = \hat{c}_{\downarrow}^{\dagger}\hat{c}_{\uparrow}|GS\rangle$ using TEBD and then calculating the overlap $\chi^{+-}(\tau - \tau') = \langle \psi(\tau)|\psi(\tau') \rangle$. Finite-temperature results are sampled with worm-sampling in CT-HYB [C1]; the analytic continuation to real frequencies is performed using a sparse modeling approach [C3, 111].

Figure 8.3 shows the imaginary part of the susceptibilities $\chi^{+-}(\omega)$ for different temperatures. For low and zero temperatures, the imaginary part is gapped; i.e., it vanishes for a finite region around $\omega = 0$, in correspondence with the gapped spectral function

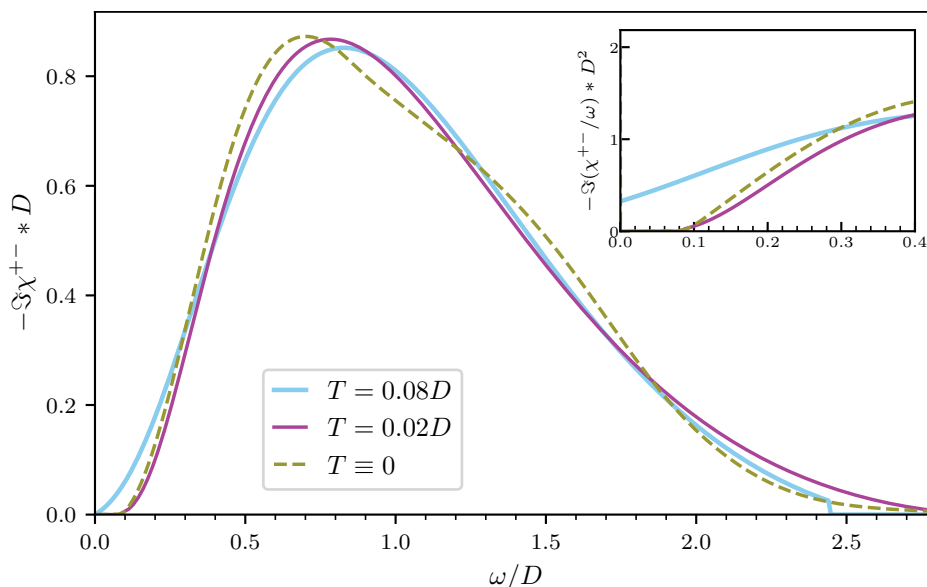


Figure 8.3.: Imaginary part of the local spin-flip susceptibility at zero temperature (dashed green line), and for a selection of finite temperatures ($T = 0.02D$ and $0.08D$: purple and blue solid lines). The inset shows the susceptibility divided by frequency: $-\Im\chi^{+-}(\omega)/\omega$. Figure adapted from ref. [W2] (fig. 3).

shown in fig. 8.1(b). For high temperatures, on the other hand, we obtain a power-law behavior, $\lim_{\omega \rightarrow 0}(-\Im\chi^{+-}(\omega)/\omega) > 0$, as visible in the inset of fig. 8.3; this is in agreement with the closing of the gap in fig. 8.1(b). All curves have one peak; the peak position (in frequency) seems to slightly increase with temperature. The real-frequency results show an additional shoulder around $\omega \approx 1.5D$. In addition, a small satellite is found near $\omega \approx 3.5D$, outside the area shown.

8.2. Half-metals in bilayers [W2]

The systems studied next consist of two coupled layers; one of the layers ($l = 1$) is half-metallic and the other ($l = 2$) is either a metal, a band insulator, or a Mott insulator. Within the layers, we consider two-dimensional square lattices as depicted in fig. 8.4. The DOS in a single layer has a half-bandwidth D , which corresponds to an in-plane hopping $t_{\alpha\beta}^l = D/4$ for nearest neighbors α and β within the layer l . The half-metallic layer has the same parameters as in section 8.1: $h_1 = 0.5D$, $\epsilon_1 = -1.5D$, and $U_1 = 2D$. We fix the filling of the bilayer to match the sum of the fillings of the isolated layers n_i^{iso} ; the HMF layer contributes a filling of $n_1^{\text{iso}} = 0.355$. The nearest-neighbor interlayer hopping $t_{12} = t_{21} = t = D/2$ couples the layers. For the remainder of section 8.2, we fix the temperature at $T = 0.16D$.

In the absence of interactions, $U_l = 0$ and $V_l = 0$, and in the presence of a splitting field h_1 acting only on the HMF layer $l = 1$, the energy spectrum shows bonding $[E_{\sigma}^-(k_{\parallel})]$

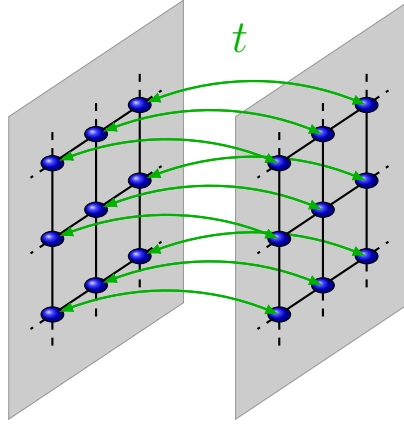


Figure 8.4.: Illustration of coupled monolayers of square lattices. The in- and interlayer hopping integrals are indicated. Figure adapted from ref. [W2] (fig. 4).

and anti-bonding $[E_{\sigma}^{+}(k_{\parallel})]$ subbands:

$$\begin{aligned}
 E_{\sigma}^{\pm}(k_{\parallel}) &= \varepsilon_{k_{\parallel}} + \bar{\epsilon}_{\sigma} \pm \sqrt{\bar{\epsilon}_{\sigma}^2 + \Delta_{\sigma}^2} =: \varepsilon_{k_{\parallel}} + \epsilon_{\sigma}^{\pm}, \\
 \varepsilon_{k_{\parallel}} &= -\frac{D}{2}(\cos k_x + \cos k_y), \\
 \bar{\epsilon}_{\sigma} &= (\tilde{\epsilon}_{1\sigma} + \tilde{\epsilon}_2)/2, \\
 \Delta_{\sigma}^2 &= t^2 - \tilde{\epsilon}_{1\sigma}\tilde{\epsilon}_2, \\
 \tilde{\epsilon}_{1\sigma} &= \tilde{\epsilon}_1 + \sigma h_1.
 \end{aligned} \tag{8.6}$$

For the Green's functions of the layers $l = 1, 2$, we get

$$G_{ll\sigma}^0(z, \varepsilon_{k_{\parallel}}) = \frac{1}{\epsilon_{\sigma}^{+} - \epsilon_{\sigma}^{-}} \left[\frac{\tilde{\epsilon}_{l\sigma} - \epsilon_{\sigma}^{-}}{(z - \varepsilon_{k_{\parallel}} - \epsilon_{\sigma}^{+})} - \frac{\tilde{\epsilon}_{l\sigma} - \epsilon_{\sigma}^{+}}{(z - \varepsilon_{k_{\parallel}} - \epsilon_{\sigma}^{-})} \right]. \tag{8.7}$$

The magnetic field (h_1) splits the two spin channels.

Figure 8.5 shows the spectral functions of the bilayer heterostructure with one HMF layer coupled to a metallic layer (M). The metallic layer $l = 2$ is non-interacting, $U_2 = 0$, nonmagnetic, $h_2 = 0$, and half-filled, $\epsilon_2 = 0$, $n_2^{\text{iso}} = 1$; these values imply a chemical potential of $\mu = -0.078D$. Both layer spectral functions $A_{l\sigma}(\omega)$, $l = 1, 2$ are metallic; the gap in the minority channel of the HMF layer $l = 1$ closes. The essential physics is the charge transfer between the half-metallic and the metallic layer, which increases the filling in the minority spin channel of the half-metal that closes the gap. This effect also occurs in the absence of interactions.

Figure 8.6 shows the spectral function of a bilayer structure of a HMF layer interfaced with a band-insulating (BI) layer. The band-insulating layer $l = 2$ is non-interacting, $U_2 = 0$, nonmagnetic, $h_2 = 0$, and completely empty, $\epsilon_2 = -2.25D$, $n_2^{\text{iso}} = 5 \times 10^{-5}$; these values imply a chemical potential of $\mu = -0.129D$. The layer-resolved spectral functions show that the disappearance of the minority spin half-metallic gap is due to the interactions in the half-metallic layer. According to the HF solution of the bilayer, both layers show a gap for down-spin electrons; cf. the dotted lines in figs. 8.6(a) and 8.6(b). The proximity to the correlated HMF layer causes the appearance of electronic states around the Fermi level of the band insulator. The many-body induced tail in the HMF is enhanced, decreasing the polarization of the HMF layer further.

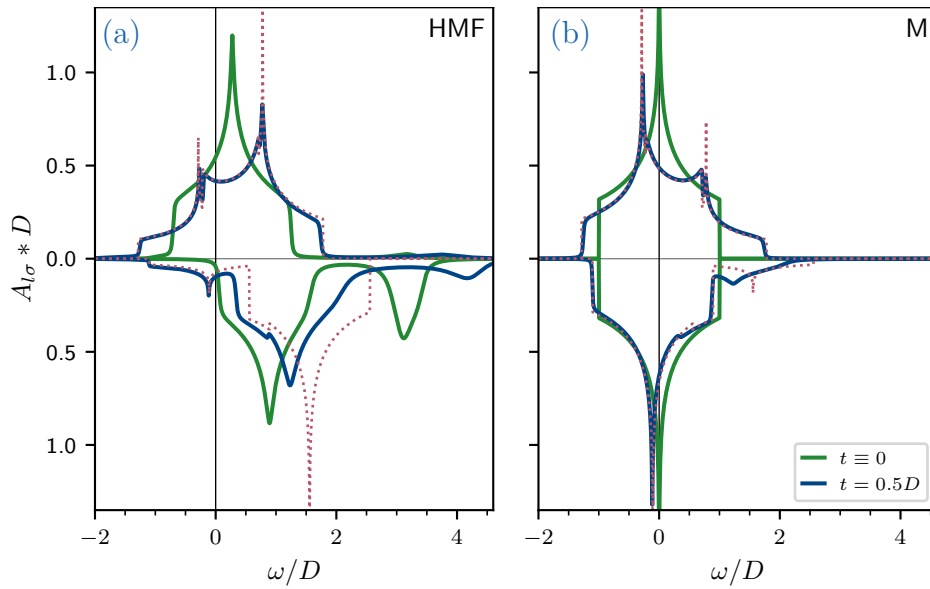


Figure 8.5.: Spin-resolved spectral function $A_{l\sigma}(\omega)$ for one HMF layer (a) interfaced with one metallic (M) layer (b). The solid lines are DMFT (CT-HYB), and the dotted lines the HF results ($t = 0.5D$). The green lines show the spectral function for isolated layers ($t \equiv 0$). Figure adapted from ref. [W2] (fig. 5).

Figure 8.7 shows the spectral functions of the bilayer formed by interfacing the HMF layer and a Mott insulating (MI) layer. Electrons in the MI layer are subject to a considerable interaction, $U_2 = 5D$, no magnetic splitting, $h_2 = 0$, and for the layer occupation the half-filled case ($\epsilon_2 = 0$, $n_2^{\text{iso}} = 1$) is considered; for these parameters, the chemical potential is $\mu = 0.013D$. At the level of HF, this corresponds to the interface between the half-metallic and the ordinary metallic layer as both spectral functions show states at and around the Fermi level. Within the insulating layer, fig. 8.7(b), the splitting into lower and upper Hubbard bands is visible (separated by $\approx U_2$). The proximity to the HMF layer induces a slightly spin-polarized quasiparticle (QP) peak located at the Fermi level of the MI layer. In contrast, the isolated Mott layer, $t_{ll} \equiv 0$, shows no QP peak for these parameters [186, 187]. In order to study the polarization of the QP peak, we perform calculations increasing the magnitude of U_2 starting from $U_2 = 1D$.

In fig. 8.8, we present the spectral function obtained for fixed parameters of the HMF layer ($U_1 = 2D$, $\epsilon_1 = -1.5D$, $h_1 = 0.5D$), while increasing the strength of the Hubbard parameter $U_2 = 1, 2, 3D$ toward a Mott insulator in the adjacent layer, $l = 2$ ($\epsilon_2 = 0$, $h_2 = 0$). The quasiparticle peak and the lower and upper Hubbard bands are already seen for $U_2 = 2D$ in fig. 8.8(b), and their separation increases with increasing U_2 . The spectral function of the HMF layer shows, besides the expected satellite at about $3.5D$, some additional spectral weight corresponding to the position of the lower Hubbard band of the Mott insulating layer. Likewise, at higher energies at the position of the upper Hubbard band a shoulder in the spectral function of the HMF layer is visible. Contrary to the homogeneous single layer, where increasing U_2 leads to a sharpening of the QP feature, the spectral weight induced by the charge transfer seems to overlay the QP. While the spectral weight around the Fermi level decreases with increasing U_2 , it persists even for values as large as $U_2 = 10D$. Accordingly, the double occupation of the MI layer is not

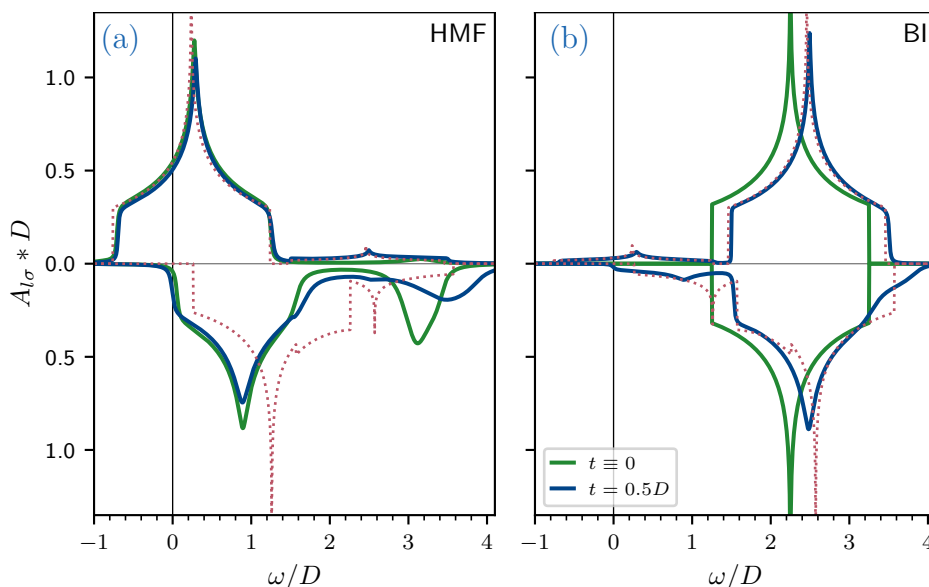


Figure 8.6.: Spin-resolved spectral function $A_{l\sigma}(\omega)$ for one HMF layer (a) interfaced with one band insulating (BI) layer (b). The solid lines are the DMFT (CT-HYB), and the dotted lines the HF results ($t = 0.5D$). The green lines show the spectral function for isolated layers ($t \equiv 0$). Figure adapted from ref. [W2] (fig. 6).

completely suppressed in the bilayer case: While increasing the interaction U_2 reduces it, the double occupation is larger than in the isolated MI layer case.

We point out that due to the proximity to the half-metallic layer, we do not expect a strict Mott transition in the sense of a vanishing quasiparticle weight, respectively of a divergent effective mass. Instead, the mutual doping of Mott and HMF layer leads to metallic behavior of the whole bilayer, similar to what was discussed previously [188, 189]. Thus, the system favors a certain amount of charge fluctuations, and the hopping between the layers is never renormalized to zero. Such a behavior has been coined ‘electronic reconstruction’ [190]. The common feature of these results indicates that the transfer of charge between the layers is a general phenomenon that produces metallic interfaces.

8.3. Summary [W2]

In summary, we have presented detailed model studies for the spectral properties of bulk HMFs as well as for bilayers containing HMFs. DMFT is employed to describe the local correlations between charge carriers. Our numerical results show that the correlation-induced tails in the vicinity of the Fermi level in bulk HMFs are significantly reduced at zero temperature, in agreement with analytical predictions [23]. On the other hand, for bilayers we find an enhancement of the tail contribution at the half-metallic side, as well as coherent quasiparticle states on the Mott insulating side. Furthermore, the Fermi liquid states at the interface reduce the full spin polarization characteristic for bulk HMFs.

For the bilayer setup, we consider a half-metallic monolayer in contact with either a metal, a band, or a Mott insulator; the layers are modeled as square lattices. We see that charge reconstruction at the interface causes the existence of metallicity, even in the

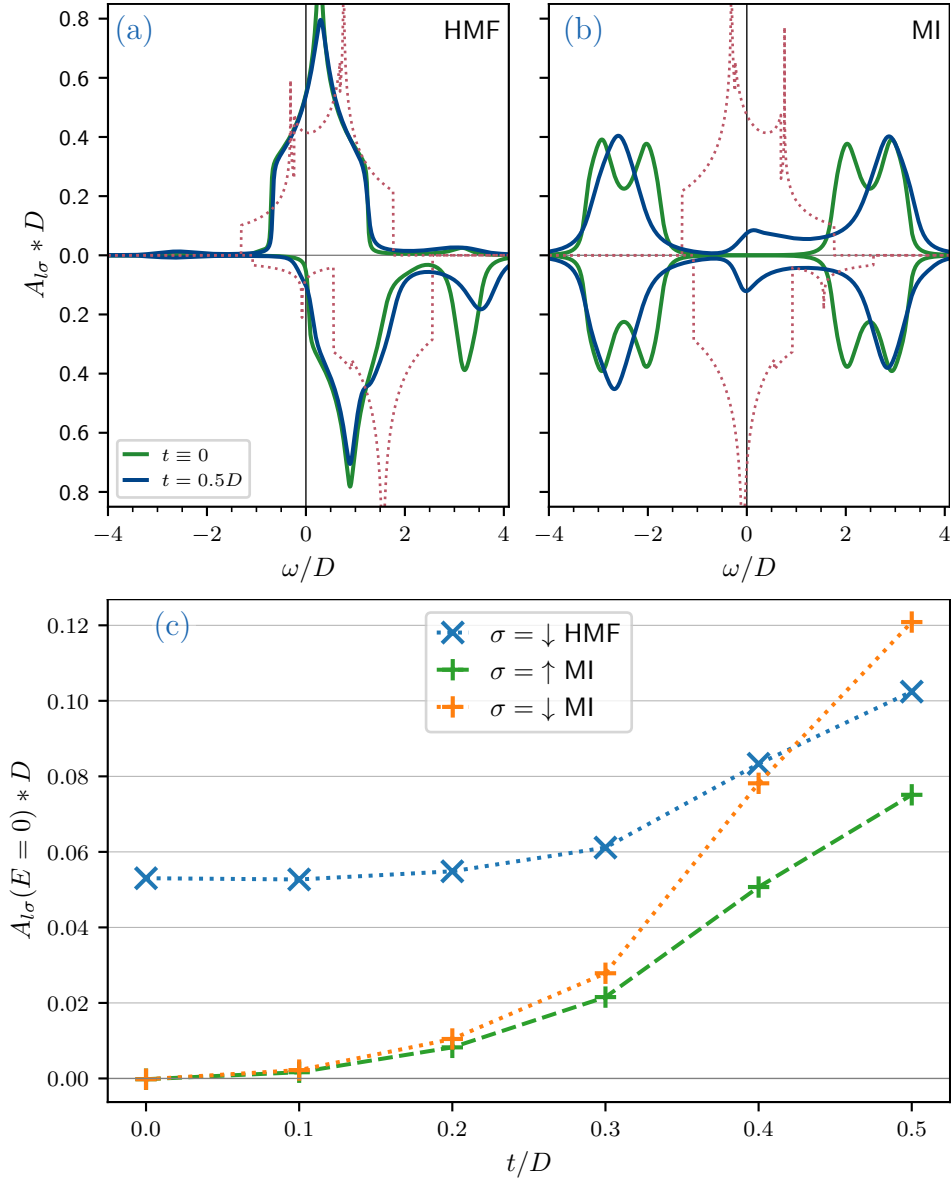


Figure 8.7.: Spin-resolved spectral function $A_{l\sigma}(\omega)$ for one HMF layer (a) interfaced with one Mott insulating (MI) layer (b). The solid lines are the DMFT (CT-HYB), and the dotted lines the HF results ($t = 0.5D$). The green lines show the spectral functions for isolated layers ($t = 0$).^{*} (c) Spectral weight at the Fermi level $A_{l\sigma}(\omega = 0)$ as function of the hopping t between the layers. Figure adapted from ref. [W2] (fig. 7).

^{*} Note that the analytic continuation for the MI layer at $t = 0$ is not reliable for the Hubbard bands; in this case Padé tends to overestimate features.

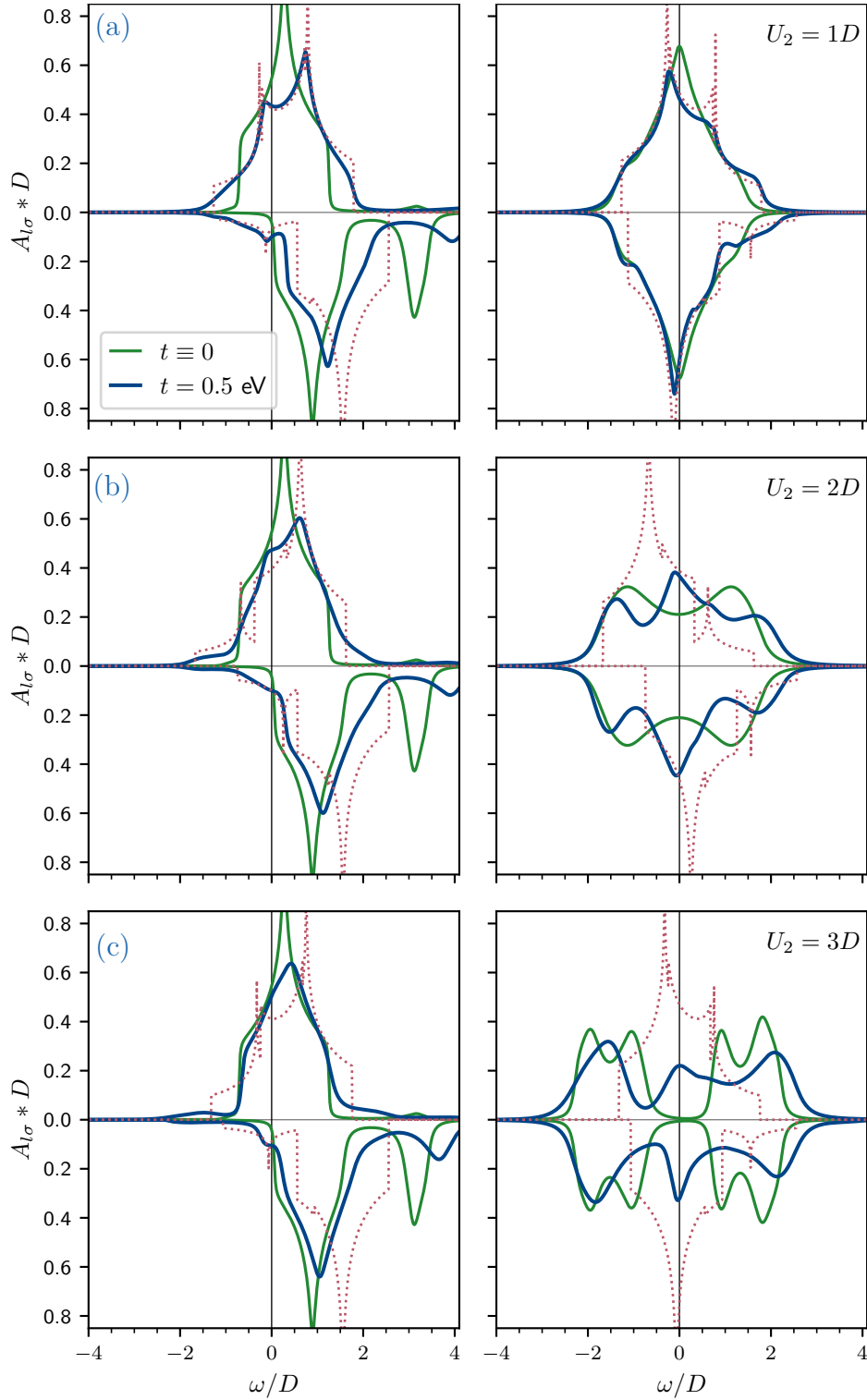


Figure 8.8.: Spin-resolved spectral function $A_{l\sigma}(\omega)$ for one HMF layer interfaced with one layer of different interacting strengths U_2 . The solid lines are the DMFT (CT-HYB), and the dotted lines the HF results ($t = 0.5D$). The green lines show the spectral function for isolated layers $t \equiv 0$. Figure adapted from ref. [W2] (fig. 8).

presence of large Hubbard U parameters at the Mott insulating layer. In the real-space DMFT analysis, the HMF/Mott insulator bilayers are Fermi liquids with well-defined quasiparticles, and thus the present approach offers a way to access Fermi liquid quantities on the basis of a microscopic model.

9. Electronic transport through a correlated magnetic layer [W4]

The electronic transport through a device can be conveniently addressed by applying scattering theory, which was pioneered by Landauer [191, 192] and Büttiker [193, 194], and worked out in detail by Meir and Wingreen [195]. This approach (see, e.g., Rammer and Smith [196]) typically considers a mesoscopic system, like a molecule or a quantum dot, coupled to ideal leads. These leads act as charge reservoirs which are so large that they can be described by equilibrium distributions. Hence, the corresponding left (L) and right (R) leads are characterized by the equilibrium Fermi distribution functions $f_{L/R}(\omega)$. The derivation assumes that the leads L and R are disconnected in the infinite past; the isolated leads and the central region are in equilibrium, albeit at their respective chemical potentials and temperatures. The couplings are then turned on adiabatically [197, 198]. In the following, we apply the Meir–Wingreen approach [195] to our heterostructure setup, in which electronic correlations are considered in the scattering region only, i.e., in the central layer. All layers are of macroscopic extent in the x - y -planes; we consider the transport direction along the z -axis, i.e., perpendicular to the layers.

Recently, Chioncel et al. [199] and Morari et al. [200] described how to take into account local interactions when computing the transmission of correlated heterostructures using density functional theory. Compared to the density functional theory + DMFT approach, the computation of the transmission becomes more apparent in the present tight-binding Hamiltonian. In particular, using the Meir–Wingreen formalism, we replace the scattering region Green’s function directly by its interacting counterpart, which takes electronic correlations into account through the local self-energy $\Sigma(\omega)$.

It is well known that the Meir–Wingreen approach [195] considerably simplifies for non-interacting systems, or when the two matrices, respectively describing the coupling to left and right lead, are proportional to each other. As long as the central region consists of just a single interacting layer, the proportionality is fulfilled for our setup. For two or more interacting layers, on the other hand, the lesser Green’s function will be needed.

9.1. Generic transport model [W4]

Figure 9.1 shows the geometry of the system: non-interacting leads, left (L) and right (R), separated by the central region (C). Both leads consist of a semi-infinite stack of square-lattice planes. The hopping amplitude between the layers in the left (right) lead is t_L (t_R), and the on-site energy is $\epsilon_{L\sigma}$ ($\epsilon_{R\sigma}$). The central region consists of a single square-lattice layer with the on-site energy $\epsilon_{0\sigma}$. Due to the two-dimensional translation invariance of the layers, the electrons are characterized by an in-plane dispersion.

For lattice sites i we introduce the multi-index $i = (l, \alpha)$, where l is the layer index and α denotes the site within the layer. The position vector \mathbf{r}_i of site i decomposes into the

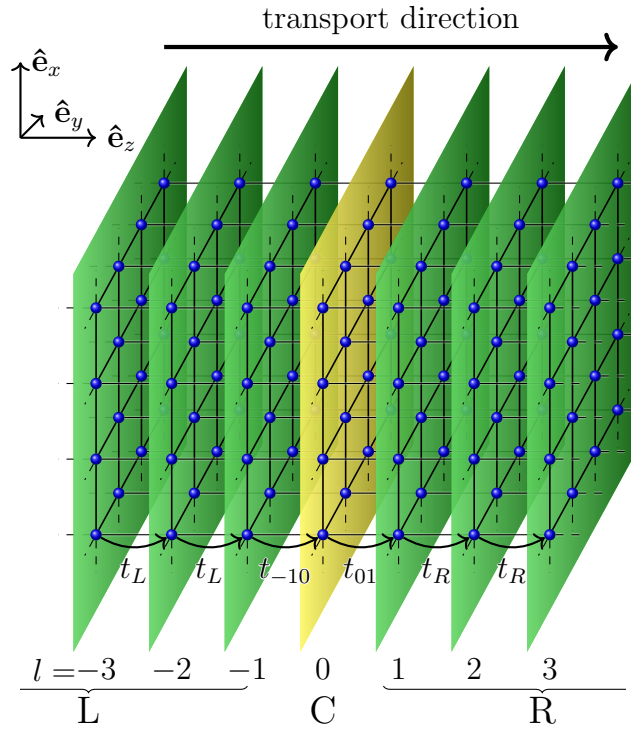


Figure 9.1.: Schematic graph of the model setup. The layers are labeled with l , such that $l < 0$ corresponds to the left, and $l > 0$ to the right lead. The central layer is $l = 0$. In the present setup, the z -direction, here labeled by l , is the direction of transport. The transverse (w.r.t. the transport direction) wave vector, \mathbf{k}_{\parallel} , is a good quantum number. Figure adapted from ref. [W4] (fig. 1).

parallel contribution $\mathbf{r}_l \parallel \hat{\mathbf{e}}_z$ of the layers and the perpendicular contribution $\mathbf{r}_\alpha \perp \hat{\mathbf{e}}_z$, i.e., $\mathbf{r}_i = \mathbf{r}_l + \mathbf{r}_\alpha$. We perform the two-dimensional in-plane Fourier transform:

$$\hat{c}_{i\sigma}^\dagger = \hat{c}_{l\alpha\sigma}^\dagger = \frac{1}{\sqrt{N_\parallel}} \sum_{k_x k_y} \hat{c}_{l\mathbf{k}_\parallel\sigma}^\dagger e^{-i(x_\alpha k_x + y_\alpha k_y)} = \frac{1}{\sqrt{N_\parallel}} \sum_{\mathbf{k}_\parallel} \hat{c}_{l\mathbf{k}_\parallel\sigma}^\dagger e^{-i\mathbf{r}_\alpha \cdot \mathbf{k}_\parallel}, \quad (9.1)$$

where $\mathbf{k}_\parallel = (k_x \ k_y)^\top \perp \hat{\mathbf{e}}_z$ and N_\parallel is the number of sites in a layer. The diagonal on-site terms $\hat{c}_{l\alpha\sigma}^\dagger \hat{c}_{l\alpha\sigma} = \hat{n}_{l\alpha\sigma}$ remain local after the Fourier transform. Likewise, the hopping between layers is not affected as we consider epitaxial layers with nearest-neighbor hopping only, where the position in the layer \mathbf{r}_α is independent of the layer l :

$$\sum_\alpha t_{ll'} \hat{c}_{l\alpha\sigma}^\dagger \hat{c}_{l'\alpha\sigma} = \frac{1}{N_\parallel} \sum_{\alpha \mathbf{k}_\parallel \mathbf{k}'_\parallel} t_{ll'} \hat{c}_{l\mathbf{k}_\parallel\sigma}^\dagger \hat{c}_{l'\mathbf{k}'_\parallel\sigma} e^{-i\mathbf{r}_\alpha \cdot (\mathbf{k}_\parallel - \mathbf{k}'_\parallel)} = \sum_{\mathbf{k}_\parallel} t_{ll'} \hat{c}_{l\mathbf{k}_\parallel\sigma}^\dagger \hat{c}_{l'\mathbf{k}_\parallel\sigma}. \quad (9.2)$$

Thus, the on-site energy terms, $\epsilon_{l\sigma} \hat{c}_{l\alpha\sigma}^\dagger \hat{c}_{l\alpha\sigma}$, as well as the hopping in transport direction $\hat{\mathbf{e}}_z$, $t_{l+1} \hat{c}_{l\alpha}^\dagger \hat{c}_{l+1\alpha}$, are diagonal in \mathbf{k}_\parallel -space and the coefficients are \mathbf{k}_\parallel -independent. For the two-dimensional square lattice, the Fourier transform yields the in-plane dispersion

$$\epsilon_{\mathbf{k}_\parallel} = 2t_\parallel [\cos(k_x) + \cos(k_y)] \quad (9.3)$$

where t_\parallel is the hopping within the layers. Thus, we identify the wave vector parallel to the layers, $\mathbf{k}_\parallel^\top = (k_x \ k_y)$, as a good quantum number of the model system.

In the mixed representation, treating the layers l in real-space and the in-layer degrees in \mathbf{k}_\parallel -space, the complete Hamiltonian can be partitioned as

$$\hat{H} = \hat{H}_L + \hat{H}_C + \hat{H}_R, \quad (9.4)$$

where \hat{H}_C contains the coupling between leads and central region. In particular, the Hamiltonians for the semi-infinite left and right leads read:

$$\hat{H}_L = \sum_{l < 0 \mathbf{k}_\parallel \sigma} (\epsilon_{L\sigma} + \epsilon_{\mathbf{k}_\parallel}) \hat{n}_{l\mathbf{k}_\parallel\sigma} - \sum_{l < 0 \mathbf{k}_\parallel \sigma} (t_L \hat{c}_{l-1\mathbf{k}_\parallel\sigma}^\dagger \hat{c}_{l\mathbf{k}_\parallel\sigma} + t_L^* \hat{c}_{l\mathbf{k}_\parallel\sigma}^\dagger \hat{c}_{l-1\mathbf{k}_\parallel\sigma}), \quad (9.5)$$

$$\hat{H}_R = \sum_{l > 0 \mathbf{k}_\parallel \sigma} (\epsilon_{R\sigma} + \epsilon_{\mathbf{k}_\parallel}) \hat{n}_{l\mathbf{k}_\parallel\sigma} - \sum_{l > 0 \mathbf{k}_\parallel \sigma} (t_R \hat{c}_{l\mathbf{k}_\parallel\sigma}^\dagger \hat{c}_{l+1\mathbf{k}_\parallel\sigma} + t_R^* \hat{c}_{l+1\mathbf{k}_\parallel\sigma}^\dagger \hat{c}_{l\mathbf{k}_\parallel\sigma}), \quad (9.6)$$

where $\sigma = \pm \frac{1}{2}$ labels the spin. For the central region containing just a single layer, the Hamiltonian reads:

$$\begin{aligned} \hat{H}_C = & - \sum_{\mathbf{k}_\parallel \sigma} (t_{-10} \hat{c}_{-1\mathbf{k}_\parallel\sigma}^\dagger \hat{c}_{0\mathbf{k}_\parallel\sigma} + \text{H.c.}) + \sum_{\mathbf{k}_\parallel \sigma} (\epsilon_{0\sigma} + \epsilon_{\mathbf{k}_\parallel}) \hat{n}_{0\mathbf{k}_\parallel\sigma} + U_0 \sum_i \hat{n}_{0i\downarrow} \hat{n}_{0i\uparrow} \\ & - \sum_{\mathbf{k}_\parallel \sigma} (t_{01} \hat{c}_{0\mathbf{k}_\parallel\sigma}^\dagger \hat{c}_{1\mathbf{k}_\parallel\sigma} + \text{H.c.}) \end{aligned} \quad (9.7)$$

The hopping amplitudes describing the hybridization between the central region and the leads, t_{-10} and t_{01} , are chosen to be real, positive, and equal $t_{-10} = t_{01}$. The hopping amplitudes in the transport direction are also assumed to be real, $t_{L/R} = t_{L/R}^*$, without loss of generality. Furthermore, $\epsilon_{0\sigma} = \epsilon_0 + \sigma h_0$ is the on-site energy, h_0 the magnetic splitting, and U_0 the on-site Hubbard interaction in the central layer.

The Meir–Wingreen formalism [195] is typically formulated for the case of lead Hamiltonians eqs. (9.5) and (9.6) that are diagonal, contrary to the layered structure, fig. 9.1, which we consider here. Therefore, we diagonalize the non-interacting leads, to obtain the same structure.

9.1.1. Diagonalizing the leads

To diagonalize the leads in the layers indices l , that is in transport direction perpendicular to the layers, we employ the discrete sine transform for the finite system. For $l < 0$, we define the unitary transformation (for real hopping it is orthogonal):

$$\hat{c}_{l\mathbf{k}_{\parallel}\sigma}^{\dagger} = \sqrt{\frac{2}{N_L + 1}} \sum_{n=1}^{N_L} \sin\left(\frac{\pi n l}{N_L + 1}\right) \hat{c}_{n\mathbf{k}_{\parallel}\sigma}^{\dagger} =: \sqrt{\frac{2}{N_L + 1}} \sum_{k_L} \sin(k_L l) \hat{c}_{k_L\mathbf{k}_{\parallel}\sigma}^{\dagger}, \quad (9.8)$$

where N_L is the number of left leads $l < 0$ (going to infinity). This defines the k -numbers $k_L \in \{\pi n / (N_L + 1)\}$ for the left lead. If the hopping amplitudes t_L were complex, we would have to modify the transformation by a factor $(t_L/t_L^*)^{n/2} =: e^{in\phi}$, where ϕ is the complex phase of t_L . The inverse transformation reads

$$\hat{c}_{k_L\mathbf{k}_{\parallel}\sigma}^{\dagger} = \sqrt{\frac{2}{N_L + 1}} \sum_{l=-1}^{-N_L} \sin(k_L l) \hat{c}_{l\mathbf{k}_{\parallel}\sigma}^{\dagger}. \quad (9.9)$$

This is a unitary transformation due to the orthogonality relation

$$\sum_{n=1}^N \sin\left(\frac{\pi n l}{N + 1}\right) \sin\left(\frac{\pi n l'}{N + 1}\right) = \frac{N + 1}{2} \delta_{ll'}. \quad (9.10)$$

By symmetry, the transformation for the right leads is analogous replacing L with R , and l by $-l$. Applying these transformations to the Hamiltonian yields for the leads:

$$\hat{H}_L = \sum_{k_L\mathbf{k}_{\parallel}\sigma} (\epsilon_{L\sigma} + \epsilon_{\mathbf{k}_{\parallel}} + \epsilon_{k_L}) \hat{n}_{k_L\mathbf{k}_{\parallel}\sigma} + \sqrt{\frac{2}{N_L + 1}} \sum_{k_L\mathbf{k}_{\parallel}\sigma} [\sin(-k_L) t_{-10} \hat{c}_{k_L\mathbf{k}_{\parallel}\sigma}^{\dagger} \hat{c}_{0\mathbf{k}_{\parallel}\sigma} + \text{H.c.}], \quad (9.11)$$

$$\hat{H}_R = \sum_{k_R\mathbf{k}_{\parallel}\sigma} (\epsilon_{R\sigma} + \epsilon_{\mathbf{k}_{\parallel}} + \epsilon_{k_R}) \hat{n}_{k_R\mathbf{k}_{\parallel}\sigma} + \sqrt{\frac{2}{N_R + 1}} \sum_{k_R\mathbf{k}_{\parallel}\sigma} [\sin(+k_R) t_{+10} \hat{c}_{k_R\mathbf{k}_{\parallel}\sigma}^{\dagger} \hat{c}_{0\mathbf{k}_{\parallel}\sigma} + \text{H.c.}], \quad (9.12)$$

with the left/right dispersion $\epsilon_{k_{L/R}} = 2t_{L/R} \cos(k_{L/R})$.

This can be conveniently expressed in matrix notation. Only the central region \hat{H}_C is subject to interaction; as it is invariant under the unitary transformation of the leads, it is sufficient to consider the non-interacting Hamiltonian \hat{H}_0 . The non-interacting Hamiltonian is diagonal in \mathbf{k}_{\parallel} and σ ; thus we suppress these indices for a more concise notation. The Hamiltonian can be written in the matrix form

$$\hat{H}_0 = \mathbf{c}^{\dagger} \mathbf{H}^0 \mathbf{c} = \begin{pmatrix} \mathbf{c}_L^{\dagger} & \mathbf{c}_C^{\dagger} & \mathbf{c}_R^{\dagger} \end{pmatrix} \begin{pmatrix} \mathbf{H}_L & \mathbf{t}_L & 0 \\ \mathbf{t}_L^{\dagger} & \mathbf{H}_C^0 & \mathbf{t}_R \\ 0 & \mathbf{t}_R^{\dagger} & \mathbf{H}_R \end{pmatrix} \begin{pmatrix} \mathbf{c}_L \\ \mathbf{c}_C \\ \mathbf{c}_R \end{pmatrix}, \quad (9.13)$$

the second equality is the block matrix form. The elements of the column vectors are the annihilation operators, i.e.,

$$\mathbf{c}_L^{\dagger} = (\hat{c}_{-N_L}^{\dagger} \quad \cdots \quad \hat{c}_{-1}^{\dagger}), \quad \mathbf{c}_C^{\dagger} = (\hat{c}_0^{\dagger}), \quad \text{and} \quad \mathbf{c}_R^{\dagger} = (\hat{c}_1^{\dagger} \quad \cdots \quad \hat{c}_{N_R}^{\dagger}). \quad (9.14)$$

In the setup we consider, the central block \mathbf{H}_C^0 of eq. (9.13) is of size 1×1 and can therefore be expressed as a scalar. Thus, the hopping to the central region takes a particular simple form, i.e. $\mathbf{t}_L^\dagger = \begin{pmatrix} 0 & \dots & 0 & t_{-10}^* \end{pmatrix}$ and an analogous expression for R . We consider the unitary transformation for the left block L . We define the unitary matrix for the left block

$$(\mathbf{U})_{nl} = \sqrt{\frac{2}{N_L + 1}} \sin\left(\frac{\pi nl}{N_L + 1}\right) \quad \text{with} \quad (\mathbf{U}^\dagger)_{ln} = \sqrt{\frac{2}{N_L + 1}} \sin\left(\frac{\pi ln}{N_L + 1}\right). \quad (9.15)$$

In the full matrix space, the matrix reads

$$\hat{\mathbf{U}} = \begin{pmatrix} \mathbf{U} & 0 & 0 \\ 0 & \mathbb{1}_C & 0 \\ 0 & 0 & \mathbb{1}_R \end{pmatrix} \quad (9.16)$$

with the identity matrices in the central block $\mathbb{1}_C$ and in the right block $\mathbb{1}_R$. Thus, by inserting the full identity $\mathbb{1} = \hat{\mathbf{U}}^\dagger \hat{\mathbf{U}}$, we diagonalize the left block

$$\hat{H}_0 = \mathbf{c}^\dagger \hat{\mathbf{U}}^\dagger \hat{\mathbf{U}} \mathbf{H}_0 \hat{\mathbf{U}} \hat{\mathbf{U}}^\dagger \hat{\mathbf{U}} \mathbf{c} = \begin{pmatrix} \mathbf{U} \mathbf{c}_L \\ \mathbf{c}_C \\ \mathbf{c}_R \end{pmatrix}^\dagger \begin{pmatrix} \mathbf{U} \mathbf{H}_L \mathbf{U}^\dagger & \mathbf{U} \mathbf{t}_L & 0 \\ \mathbf{t}_L^\dagger \mathbf{U}^\dagger & \mathbf{H}_C^0 & \mathbf{t}_R \\ 0 & \mathbf{t}_R^\dagger & \mathbf{H}_R \end{pmatrix} \begin{pmatrix} \mathbf{U} \mathbf{c}_L \\ \mathbf{c}_C \\ \mathbf{c}_R \end{pmatrix}. \quad (9.17)$$

This matrix defines the new vector of fermionic operators $\tilde{\mathbf{c}}_L = \mathbf{U} \mathbf{c}_L$; elements of the vector are the operators eq. (9.8) in \mathbf{k}_\parallel -space. While the left block has now a simpler diagonal form, the hopping between the left and central block is not sparse anymore. We obtain the hopping elements

$$(\mathbf{U} \mathbf{t}_L)_{n0} = \sqrt{\frac{2}{N_L + 1}} \sin\left(\frac{-\pi n}{N_L + 1}\right) t_{-10}. \quad (9.18)$$

The diagonalization of the right block is analogous. The unitary transformations commute:

$$\hat{\mathbf{U}} \hat{\mathbf{U}}_R = \begin{pmatrix} \mathbf{U} & 0 & 0 \\ 0 & \mathbb{1}_C & 0 \\ 0 & 0 & \mathbb{1}_R \end{pmatrix} \begin{pmatrix} \mathbb{1}_L & 0 & 0 \\ 0 & \mathbb{1}_C & 0 \\ 0 & 0 & \mathbf{U}_R \end{pmatrix} = \hat{\mathbf{U}}_R \hat{\mathbf{U}}, \quad (9.19)$$

as they act on different blocks of the Hamiltonian matrix, therefore the transformations can be applied independently.

Furthermore, we define the surface DOS for the leads. For the left lead, we write

$$\begin{aligned} \rho_L(\varepsilon) &:= \frac{2}{N_L + 1} \sum_{k_L} \sin^2(k_L) \delta(\varepsilon - \varepsilon_{k_L}) = \frac{2}{N_L + 1} \sum_{k_L} [1 - \cos^2(k_L)] \delta(\varepsilon - 2t_L \cos(k_L)) \\ &= 2[1 - (\varepsilon/2t_L)^2] \frac{1}{N_L + 1} \sum_{k_L} \delta(\varepsilon - 2t_L \cos(k_L)). \end{aligned} \quad (9.20)$$

In the limit $N_L \rightarrow \infty$, the sum can be replaced by an integral. We identify the integral as the DOS of a one-dimensional lattice

$$\rho_{1D}(\varepsilon) = \frac{1}{\pi 2t} \frac{1}{\sqrt{1 - (\varepsilon/2t)^2}} \Theta(2t - |\varepsilon|), \quad (9.21)$$

where t is the hopping amplitude and $\Theta(\varepsilon)$ the Heaviside step function. Therefore, the surface DOS writes

$$\rho_L(\varepsilon) = 2 \left[1 - (\varepsilon/2t_L)^2 \right] \rho_{1D}(\varepsilon) = \frac{2}{\pi 2t_L} \sqrt{1 - (\varepsilon/2t_L)^2} \Theta(2t - |\varepsilon|). \quad (9.22)$$

We note that the surface DOS coincides with the semicircular DOS of the Bethe lattice for the half-bandwidth $D = 2t_L$. Alternatively, the surface Green's function can be derived by a recursion relation for the semi-infinite lead. As the lead is non-interacting, the Green's function of the decoupled lead can be calculated from the resolvent $\mathbf{g}_L(z) = [\mathbf{1}z - \mathbf{H}_L]^{-1}$. The surface Green's function is the right-most matrix element ($l = -1$) of the left lead; defining $\mathbf{L}(z) = \mathbf{1}z - \mathbf{H}_L$, it can be calculated as the inverse of the block matrix:

$$\begin{aligned} g_L^s(z) &= (\mathbf{L}^{-1})_{[-1,-1]} = \left[\begin{pmatrix} \mathbf{L}_{[: -1, : -1]} & \mathbf{t} \\ \mathbf{t}^\dagger & L_{[-1,-1]} \end{pmatrix}^{-1} \right]_{[-1,-1]} = \left[L_{[-1,-1]} - \mathbf{t}^\dagger (\mathbf{L}_{[: -1, : -1]})^{-1} \mathbf{t} \right]^{-1} \\ &= \left[L_{[-1,-1]} - |t_L|^2 [(\mathbf{L}_{[: -1, : -1]})^{-1}]_{[-1,-1]} \right]^{-1}, \end{aligned} \quad (9.23)$$

where we omit the frequency argument z for readability, and \mathbf{t} is the vector of hopping elements $\mathbf{t}^\dagger = (t_L^* \ 0 \ \dots \ 0)$. In the limit $N_L \rightarrow \infty$, the left lead remains a semi-infinite stack of layers after removing one layer; thus the matrix inverse with the right-most layer removed is identical to the surface Green's function:

$$[(\mathbf{L}_{[: -1, : -1]})^{-1}]_{[-1,-1]} = [\mathbf{L}^{-1}]_{[-1,-1]} = g_L^s(z). \quad (9.24)$$

We obtain the quadratic equation for the surface Green's function

$$|t_L|^2 [g_L^s(z)]^2 - L_{[-1,-1]}(z) g_L^s(z) + 1 = 0. \quad (9.25)$$

Again, the equation coincides with the Green's function of the Bethe lattice. We define the surface Green's function $g_L^s(z)$ excluding the on-site energies:

$$g_L^s(z) = \frac{z}{2|t_L|^2} \left(1 - \sqrt{1 - \left(\frac{2|t_L|}{z} \right)^2} \right); \quad (9.26)$$

to the on-site energies in the calculations we shift the frequency argument.

9.1.2. Meir–Wingreen formula for the transmission

In the following, we outline the main ideas of Meir–Wingreen [195] to obtain the transmission, we mainly follow the more detailed derivation found in the book of Haug and Jauho [201].

The current from the left lead L with $l < 0$ to the central region C with $l = 0$ is given by the continuity equation

$$J_L = -\frac{ie}{\hbar} \langle [\hat{H}, \hat{N}_L] \rangle \quad \text{with} \quad \hat{N}_L = \sum_{l < 0, \mathbf{k}_\parallel, \sigma} \hat{n}_{l\mathbf{k}_\parallel\sigma}, \quad (9.27)$$

where \hat{N}_L is the total particle number of the left lead. Using the diagonal form of the left lead eq. (9.11), we obtain the following expression for the current:

$$\begin{aligned} J_L &= \frac{2ie}{\hbar} \sqrt{\frac{2}{N_L + 1}} \sum_{k_L \mathbf{k}_{\parallel} \sigma} \left[\sin(-k_L) t_{-10} \langle \hat{c}_{k_L \mathbf{k}_{\parallel} \sigma}^\dagger \hat{c}_{0 \mathbf{k}_{\parallel} \sigma} \rangle - \text{H.c.} \right] \\ &= \frac{2e}{\hbar} \sqrt{\frac{2}{N_L + 1}} \Re \sum_{k_L \mathbf{k}_{\parallel} \sigma} \sin(-k_L) t_{-10} i \langle \hat{c}_{k_L \mathbf{k}_{\parallel} \sigma}^\dagger \hat{c}_{0 \mathbf{k}_{\parallel} \sigma} \rangle. \end{aligned} \quad (9.28)$$

The static expectation value $\langle \hat{c}_{k_L \mathbf{k}_{\parallel} \sigma}^\dagger \hat{c}_{0 \mathbf{k}_{\parallel} \sigma} \rangle$ can be expressed in terms of the lesser Green's function at times $t = 0$

$$\mathcal{G}_{0, k_L; \mathbf{k}_{\parallel} \sigma}^<(0, 0) = i \langle \hat{c}_{k_L \mathbf{k}_{\parallel} \sigma}^\dagger(0) \hat{c}_{0 \mathbf{k}_{\parallel} \sigma}(0) \rangle. \quad (9.29)$$

Due to the fact that we consider non-interacting leads, the equation of motion for the Green's function $G_{0, k_L; \mathbf{k}_{\parallel} \sigma}(z) = \langle\langle \hat{c}_{0 \mathbf{k}_{\parallel} \sigma} | \hat{c}_{k_L \mathbf{k}_{\parallel} \sigma}^\dagger \rangle\rangle(z)$ generates no higher-order Green's functions. The diagonal structure eq. (9.11) of the lead Hamiltonian yields the equation of motion

$$z G_{0, k_L; \mathbf{k}_{\parallel} \sigma}(z) = (\epsilon_{L\sigma} + \epsilon_{\mathbf{k}_{\parallel}} + \epsilon_{k_L}) G_{0, k_L; \mathbf{k}_{\parallel} \sigma}(z) + \sqrt{\frac{2}{N_L + 1}} \sin(-k_L) t_{-10}^* G_{0, 0; \mathbf{k}_{\parallel} \sigma}(z). \quad (9.30)$$

This equation connects the current from the left lead J_L to the Green's function of the central region $G_{0, 0; \mathbf{k}_{\parallel} \sigma}(z) = \langle\langle \hat{c}_{0 \mathbf{k}_{\parallel} \sigma} | \hat{c}_{0 \mathbf{k}_{\parallel} \sigma}^\dagger \rangle\rangle(z)$. We identify the Green's function of the *uncoupled* left lead

$$g_{k_L \mathbf{k}_{\parallel} \sigma}(z) = \langle\langle \hat{c}_{k_L \mathbf{k}_{\parallel} \sigma} | \hat{c}_{k_L \mathbf{k}_{\parallel} \sigma}^\dagger \rangle\rangle_{\hat{H}_L}(z) = [z - (\epsilon_{L\sigma} + \epsilon_{\mathbf{k}_{\parallel}} + \epsilon_{k_L})]^{-1} \quad (9.31)$$

and write the equation of motion eq. (9.30) in the compact form

$$g_{k_L \mathbf{k}_{\parallel} \sigma}^{-1}(z) G_{0, k_L; \mathbf{k}_{\parallel} \sigma}(z) = \sqrt{\frac{2}{N_L + 1}} \sin(-k_L) t_{-10}^* G_{0, 0; \mathbf{k}_{\parallel} \sigma}(z). \quad (9.32)$$

For the calculation of the lesser Green's function we refer to Haug and Jauho [201] and state only the result for the left current:

$$J_L = \frac{2e}{\hbar} \frac{2}{N_L + 1} \Re \sum_{k_L \mathbf{k}_{\parallel} \sigma} \sin^2(k_L) |t_{-10}|^2 \int_{-\infty}^{\infty} \frac{d\omega}{2\pi} \left[G_{00; \mathbf{k}_{\parallel} \sigma}^r(\omega) g_{k_L \mathbf{k}_{\parallel} \sigma}^<(\omega) + G_{00; \mathbf{k}_{\parallel} \sigma}^<(\omega) g_{k_L \mathbf{k}_{\parallel} \sigma}^a(\omega) \right]. \quad (9.33)$$

Only the lead Green's functions depend on k_L , therefore the k_L -summation can be moved into the integral and evaluated for the lead Green's functions. This yields the current

$$J_L = \frac{2e}{\hbar} \Re \sum_{\mathbf{k}_{\parallel} \sigma} |t_{-10}|^2 \int_{-\infty}^{\infty} \frac{d\omega}{2\pi} \left[G_{00; \mathbf{k}_{\parallel} \sigma}^r(\omega) g_{-1 \mathbf{k}_{\parallel} \sigma}^<(\omega) + G_{00; \mathbf{k}_{\parallel} \sigma}^<(\omega) g_{-1 \mathbf{k}_{\parallel} \sigma}^a(\omega) \right] \quad (9.34)$$

in terms of the Green's function $g_{l \mathbf{k}_{\parallel} \sigma}(z) = \langle\langle \hat{c}_{l \mathbf{k}_{\parallel} \sigma} | \hat{c}_{l \mathbf{k}_{\parallel} \sigma}^\dagger \rangle\rangle_{\hat{H}_L}(z)$ of the surface layer $l = -1$. Since the central region is just a *single* layer, the effect of the leads is characterized by the *scalar* level-width function

$$\Gamma_{\sigma}^L(\omega, \epsilon_{\mathbf{k}_{\parallel}}) = -2|t_{01}|^2 \Im g_{l \mathbf{k}_{\parallel} \sigma}^r(\omega) = -2|t_{01}|^2 \Im g_L^s(\omega^+ - \epsilon_{L\sigma} - \epsilon_{\mathbf{k}_{\parallel}}), \quad (9.35)$$

where $\omega^+ = \omega + i0^+$, and $g_L^s(z)$ is the leads' surface Green's function eq. (9.26). The lesser Green's functions in eq. (9.34) are purely imaginary; evaluating the real part yields [201]

$$J_L = \frac{e}{\hbar} \sum_{\mathbf{k}_{\parallel\sigma}} \int_{-\infty}^{\infty} \frac{d\omega}{2\pi} \Gamma_{\sigma}^L(\omega, \varepsilon_{\mathbf{k}_{\parallel}}) \left[f_L(\omega) \Im G_{00;\mathbf{k}_{\parallel}\sigma}^r(\omega) + i G_{00;\mathbf{k}_{\parallel}\sigma}^<(\omega) \right]. \quad (9.36)$$

Analogous, an expression for the right current J_R can be derived, replacing all indices L by R . In steady state the left and right current have the same magnitude $J_L = -J_R = J$. The level-width functions Γ_{σ} are scalar and identical for the left and right lead. Therefore, by considering the symmetrized current

$$J = \frac{1}{2}(J_L - J_R), \quad (9.37)$$

the lesser Green's functions $G_{00;\mathbf{k}_{\parallel}\sigma}^<(\omega)$ in eq. (9.36) can be eliminated, as the corresponding contributions of the left and right current cancel.

Applying the Meir–Wingreen formalism [195] to the present, highly symmetric heterostructure, therefore yields a particularly simple expression for the charge current perpendicular to the layers:

$$J = -\frac{e}{\hbar} N_{\parallel} \sum_{\sigma} \int \frac{d\omega}{2\pi} [f_L(\omega) - f_R(\omega)] \int d\varepsilon_{\parallel} \rho_{\parallel}(\varepsilon_{\parallel}) \Gamma_{\sigma}^L(\omega, \varepsilon_{\parallel}) \Im G_{00\sigma}(\omega^+, \varepsilon_{\parallel}), \quad (9.38)$$

where $G_{00\sigma}$ is the Green's function of the central region, $G_{00\sigma}(z, \varepsilon_{\mathbf{k}_{\parallel}}) = \langle\langle \hat{c}_{0\mathbf{k}_{\parallel}\sigma} | \hat{c}_{0\mathbf{k}_{\parallel}\sigma}^{\dagger} \rangle\rangle(z)$, and N_{\parallel} the number of sites within a layer (going to infinity). The layer DOS is given by

$$\rho_{\parallel}(\varepsilon_{\parallel}) = \frac{1}{N_{\parallel}} \sum_{\mathbf{k}_{\parallel}} \delta(\varepsilon_{\parallel} - \varepsilon_{\mathbf{k}_{\parallel}}) = \frac{2}{\pi^2 D} K(1 - \varepsilon_{\parallel}^2/D^2) \Theta(|\varepsilon_{\parallel}| - D), \quad (9.39)$$

where $\Theta(\varepsilon)$ is the Heaviside step function. For the square lattice [164], it can be written in terms of the complete elliptic integral of the first kind:

$$K(m) = \int_0^{\pi/2} dt [1 - m \sin^2(t)]^{-1/2}. \quad (9.40)$$

From the above quantities, the normalized transmission for the spin channel σ can be computed as follows:

$$\begin{aligned} T_{\sigma}(\omega) &= - \int d\varepsilon_{\parallel} \rho_{\parallel}(\varepsilon_{\parallel}) \Gamma_{\sigma}^L(\omega, \varepsilon_{\parallel}) \Im G_{00\sigma}(\omega^+, \varepsilon_{\parallel}) \\ &= 2|t_{01}|^2 \int d\varepsilon_{\parallel} \rho_{\parallel}(\varepsilon_{\parallel}) \Im g_L^s(\omega^+ - \varepsilon_{\parallel} - \varepsilon_{L\sigma}) \Im G_{00\sigma}(\omega^+, \varepsilon_{\parallel}). \end{aligned} \quad (9.41)$$

Within DMFT, the local self-energy, $\Sigma_{\sigma}(z)$, is included in the central region Green's function:

$$G_{00\sigma}(z, \varepsilon_{\parallel}) = \frac{1}{z - \varepsilon_{\parallel} - \varepsilon_{0\sigma} - \Sigma_{\sigma}(z) - 2|t_{01}|^2 g_L^s(z - \varepsilon_{L\sigma} - \varepsilon_{\parallel})}. \quad (9.42)$$

The DMFT self-energy $\Sigma_{\sigma}(z)$ is obtained by numerically solving a self-consistently determined reference system, which is interacting but local, see section 9.2.3.

In the next section, we discuss the behavior of the spin-resolved spectral functions, and contrast it with the spin-resolved transmissions, when varying the hopping to/from the central region, as well as the strength of the local interaction on the central layer.

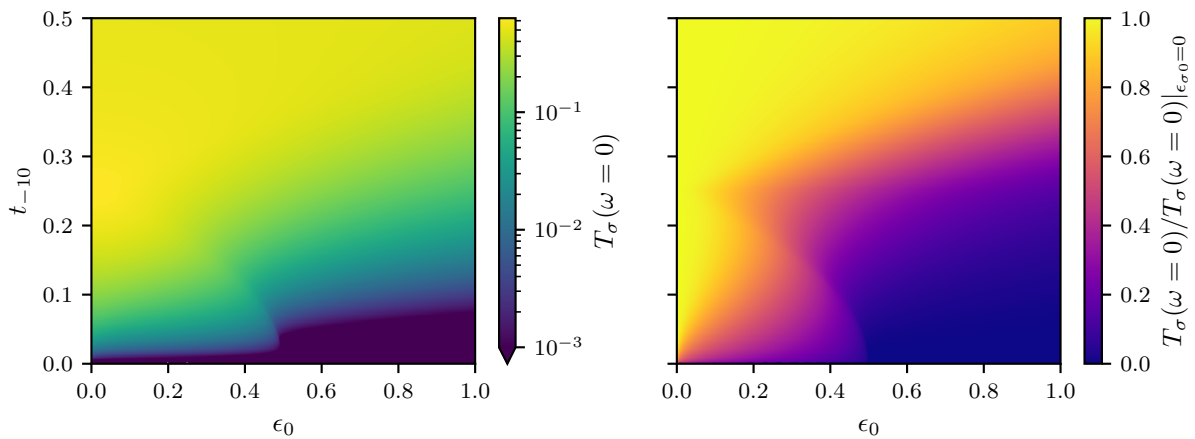


Figure 9.2.: Dependence of the transmission at the Fermi level $T_\sigma(\omega = 0)$ on t_{01} and $\epsilon_{0\sigma}$. On the left, a logarithmic color scale is used, on the right, the transmission is normalized to the value $T_\sigma(\omega = 0)$ for $\epsilon_{0\sigma} = 0$ and a linear color scale is used.

9.2. Results [W4]

We consider the setup as shown in fig. 9.1. In the following, we consider the leads to be identical, but keep the notation ‘ L ’ which henceforth refers to ‘lead’. As discussed above, our model consists of non-magnetic (non-spin-polarized) metallic leads in contact with a single layer of a ferromagnetic metal. The Hamiltonian describing the leads (at half-filling) is specified by the on-site energies, $\epsilon_{L\sigma} = 0$, and the electrons’ hopping matrix elements t_L in the direction of transport. The latter are fixed at $t_L = 0.25D$, where D denotes the parallel (in-plane) half-bandwidth. Furthermore, the square-lattice parallel hopping matrix elements, t_{\parallel} , are assumed to have the same value. From now on, D ($= 4t_{\parallel}$) will be our energy unit, i.e., formally $D = 1$, and $t_L = t_{\parallel} = 0.25$.

According to eq. (9.41), the transmission is determined by the product of the surface spectral functions of the uncoupled leads and that of the central region. The surface Green’s function is given above, eq. (9.26). The corresponding spectral function

$$A_L^s(\omega - \varepsilon_{\parallel}) = -\frac{1}{\pi} \Im g^s(\omega^+ - \varepsilon_{\parallel}) \quad (9.43)$$

has a semicircular shape and vanishes at the band edges, $\pm 2|t_L| = \pm 0.5$. The lead spectral function A_L^s is independent of the parameters of the central layer; in the following, we focus on the spectral function of the central region.

First, we present our results for the non-interacting case, i.e., we discuss how the spectral function of the central region and the transmission depend on the parameters on-site energy ($\epsilon_{0\sigma}$) and coupling (t_{01}), cf. figs. 9.3 to 9.5. In the second part of this section, we discuss the modifications induced by a local interaction (U_0) within the central layer: We vary t_{01} for fixed U_0 , see fig. 9.7, as well as U_0 for fixed t_{01} , see fig. 9.8.

9.2.1. Non-interacting central layer [W4]

For the non-interacting case, the two spin directions are independent and can be discussed separately. Figure 9.2 shows the dependence of the transmission on the coupling t_{-10} and

the on-site energy for $\omega = 0$. For small coupling t_{-10} we observe a dome of increased transmission extending till $\epsilon_0 = 0.5 = 2|t_L|$ at $t_{-10} = 0$. Tuning the on-site energy close to the edge of this dome, transmission and its polarization can be strongly modified. Therefore, we are interested in parameters in the vicinity of this dome. In the following, we explain the origin of this feature by investigating the spectral function of the central region.

In the non-interacting case, the Green's function depends only on the difference between frequency and dispersion, $G_{00\sigma}(\omega, \varepsilon_{\mathbf{k}_\parallel}) = G_{00\sigma}(\omega - \varepsilon_{\mathbf{k}_\parallel})$. The corresponding spectral function reads

$$A_{00\sigma}(\omega - \varepsilon_\parallel) = -\frac{1}{\pi} \Im \frac{1}{\omega^+ - \varepsilon_\parallel - \epsilon_{0\sigma} - 2|t_{01}|^2 g_L^s(\omega^+ - \varepsilon_\parallel)}. \quad (9.44)$$

In addition, the spin directions are decoupled. We define $\xi_\sigma = \omega - \varepsilon_\parallel$ as the (generally complex) root of the denominator of the right-hand side of eq. (9.44), i.e.,

$$\xi_\sigma - \epsilon_{0\sigma} - 2|t_{01}|^2 g_L^s(\xi_\sigma) = 0, \quad (9.45)$$

which leads to

$$(1 - 2r)\xi_\sigma^2 - 2(1 - r)\epsilon_{0\sigma}\xi_\sigma + \epsilon_{0\sigma}^2 + 4r^2|t_L|^2 = 0, \quad (9.46)$$

where $r = |t_{01}/t_L|^2$ characterizes the hopping to the central region relative to the hopping in the leads. First, we consider energies outside the lead band, $|\omega - \varepsilon_\parallel| > 2|t_L| = 0.5$. Then the lead Green's function g_L^s is real, implying that the spectral function is a sum over delta functions:

$$A_{00\sigma}(\omega - \varepsilon_\parallel) \propto \sum_{\xi_\sigma} \delta(\omega - \varepsilon_\parallel - \xi_\sigma). \quad (9.47)$$

The corresponding ξ_σ -solutions of eq. (9.46) are

$$\xi_\sigma^\pm = \frac{(1 - r)\epsilon_{0\sigma} \pm r\sqrt{\epsilon_{0\sigma}^2 - 4(1 - 2r)|t_L|^2}}{1 - 2r}. \quad (9.48)$$

Note that this expression also contains spurious solutions belonging to the unphysical branch of the square root in $g_L^s(z)$. On the other hand, inside the bandwidth of the lead, $|\omega - \varepsilon_\parallel| < 2|t_L| = 0.5$, the denominator of eq. (9.44) has an imaginary part stemming from $g_L^s(\omega^+ - \varepsilon_\parallel)$, eq. (9.26). In this case the spectral function of the central region reads

$$\begin{aligned} A_{00\sigma}(\omega - \varepsilon_\parallel) &= \frac{1}{\pi} \frac{r\sqrt{(2|t_L|)^2 - (\omega - \varepsilon_\parallel)^2}}{\left[(1 - r)(\omega - \varepsilon_\parallel) - \varepsilon_\parallel\right]^2 + r^2 \left[(2|t_L|)^2 - (\omega - \varepsilon_\parallel)^2\right]} \\ &= \frac{1}{\pi} \frac{r\sqrt{(2|t_L|)^2 - (\omega - \varepsilon_\parallel)^2}}{(1 - 2r)(\omega - \varepsilon_\parallel)^2 - 2(1 - r)(\omega - \varepsilon_\parallel)\epsilon_{0\sigma} + \epsilon_{0\sigma}^2 + 4r^2|t_L|^2}. \end{aligned} \quad (9.49)$$

Hence, within the band of the lead the spectral function $A_{00\sigma}(\omega - \varepsilon_\parallel)$ is finite. The real part of the roots ξ_σ^\pm , eq. (9.48), indicates resonances of increased amplitude in the spectrum.

The results are summarized in fig. 9.3 which shows the spectral function, eq. (9.44), as a function of the energy and the coupling, t_{01} . We consider the on-site energies $\epsilon_{0\sigma} = 0, 0.25$ and 0.75 ; the value $\epsilon_{0\sigma} = 0.25$ crosses the dome in fig. 9.2, the value $\epsilon_{0\sigma} = 0.75$ lies outside. Note that the horizontal axis refers to $\omega - \varepsilon_{\parallel}$; in this representation the information about the lattice structure drops out, as it is only encoded in the dispersion argument ε_{\parallel} of the spectral function $A_{00\sigma}(\omega - \varepsilon_{\parallel})$ eq. (9.44).

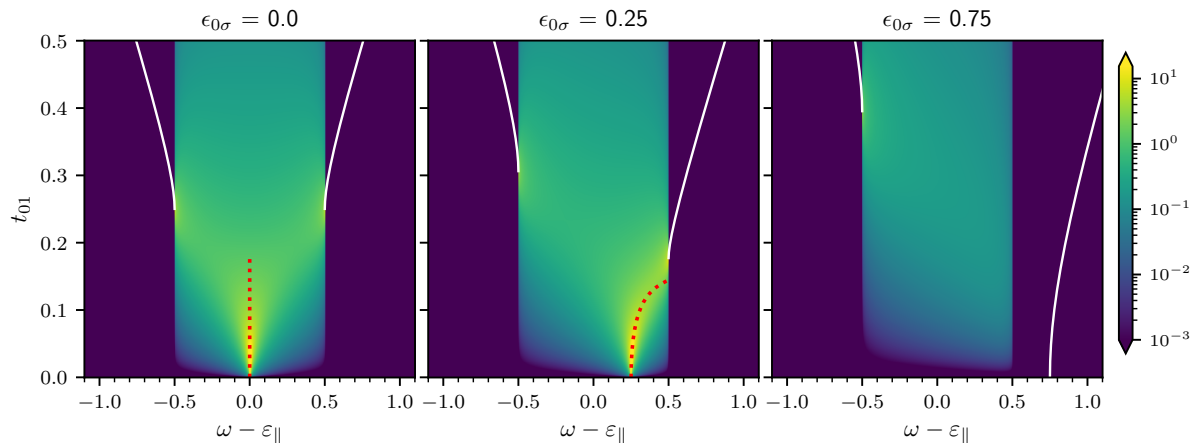


Figure 9.3.: Dependence of the spectral function of the central region, $A_{00\sigma}(\omega, \varepsilon_{\parallel})$, on t_{01} for a selection of $\epsilon_{0\sigma}$. The parameters are $\epsilon_{L\sigma} = 0$, $t_L = 0.25$, and $U_0 = 0$. For a non-interacting system, the spectral function is a function of $\omega - \varepsilon_{\parallel}$ only: $A_{00\sigma}(\omega, \varepsilon_{\parallel}) = A_{00\sigma}(\omega - \varepsilon_{\parallel})$. The white line indicates the position of the delta peak outside the band, $|\omega - \varepsilon_{\parallel}| > 2t_L$, while the red-dotted line is determined by the real part of ξ_{σ} within the band $|\omega - \varepsilon_{\parallel}| < 2t_L$, $\omega - \varepsilon_{\parallel} = \Re\xi_{\sigma}$, resulting in an enhanced spectral intensity; cf. eq. (9.48). Figure adapted from ref. [W4] (fig. 2).

The representative feature of the spectral function is a continuum band in the energy range of $[-2t_L, +2t_L] = [-0.5, +0.5]$, which corresponds to the band of the leads. The left graph in the figure ($\epsilon_{0\sigma} = 0$) includes the homogeneous ‘bulk’ case, namely the setup in which $t_{01} = t_L (= 0.25)$, i.e., all hopping parameters as well as the on-site energies in each layer are the same, $\epsilon_{0\sigma} = \epsilon_L (= 0)$. At this coupling strength $t_{01} = 0.25$, the spectral function $A_{00\sigma}(\omega - \varepsilon_{\parallel})$ diverges at the edges of the continuum band $|\omega - \varepsilon_{\parallel}| = 2t_L = 0.5$. The homogeneous case is an infinite stack of equivalent layers, therefore the $A_{00\sigma}(\omega - \varepsilon_{\parallel})$ corresponds to the DOS of a one-dimensional lattice.

In addition to the continuum, the spectral function displays a set of up to two high-intensity lines. The existence of these states entails an enhancement of the spectral function, and corresponds to bound and resonance states generated by the coupling of the semi-infinite leads and the central region. We note that a similar distinction between bound and resonance states can be made within the single impurity Anderson model [202, 203]. The analysis of bound versus resonance states can also be based on the assessment of the poles of the spectral function, eq. (9.44).

For larger values of the coupling, $|t_{01}|^2 > |t_L|^2/2 - \epsilon_{0\sigma}^2/8$, bound states are located outside the continuum (white line). Since the transmission is determined by the overlap of the spectral functions of the leads with that of the central region, the bound states outside the continuum do not contribute to transmission. With decreasing t_{01} values, the high-intensity states approach the continuum, and depending on the on-site energy $\epsilon_{0\sigma}$ they may enter the continuum region. This leads to an enhancement of the transmission,

as is apparent in fig. 9.4, where we show the transmission for a given on-site energy of $\epsilon_{0\sigma} = 0.25$ in the central square-lattice layer. Up to $t_{01} \approx 0.1$, the maximum of the transmission is determined by the position of the resonance, which is indicated by the black line with red dots. This line represents the transmission strength at the resonance as a function of t_{01} , i.e., $t_{01} \mapsto T_{\sigma}(\omega = \Re\xi_{\sigma}(t_{01}), t_{01})$.

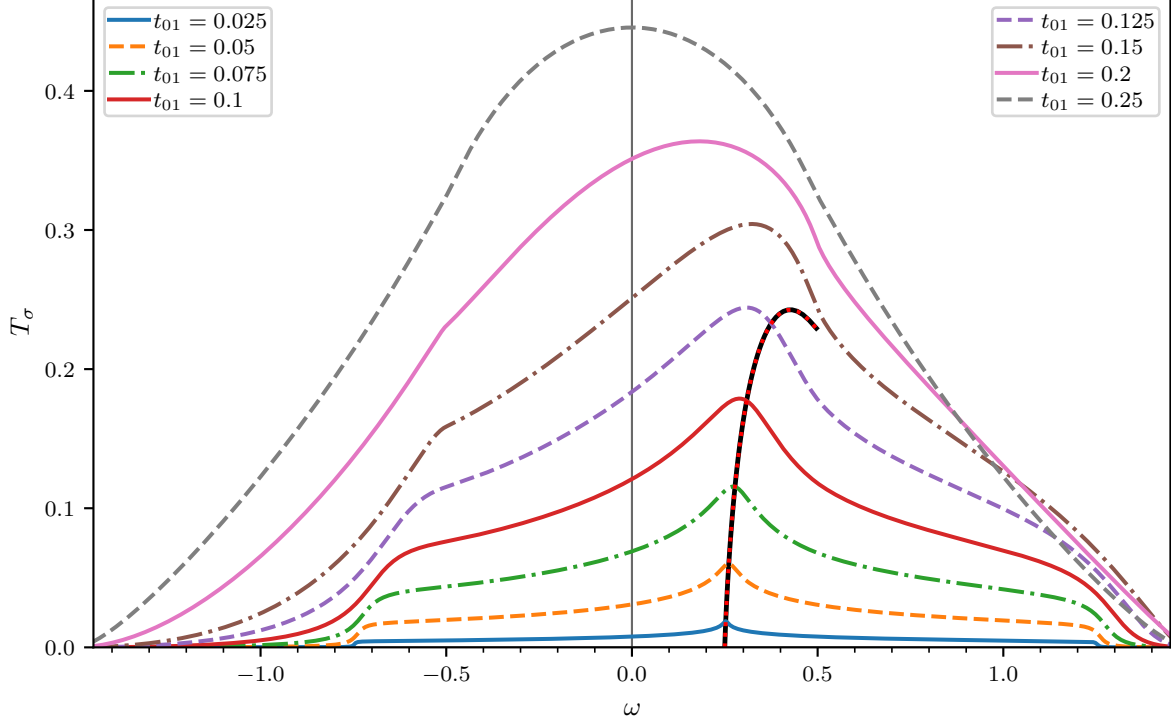


Figure 9.4.: Transmission $T_{\sigma}(\omega)$ versus frequency ω for various values of t_{01} for $\epsilon_{0\sigma} = 0.25$, corresponding to the central plot of fig. 9.3. The black line with red dots is the transmission at the position of the resonance (red dotted line in fig. 9.3). For small coupling, up to $t_{01} \approx 0.1$, the maximum of transmission corresponds to the position of the resonance. Figure adapted from ref. [W4] (fig. 3).

Based on these results, we can discuss the model parameters for which the investigated setup acts as an efficient spin filter. Clearly, choosing an on-site energy $\epsilon_{0\sigma}$ within the continuum for one spin channel and outside the continuum for the other, a high spin polarization of the transmission can be achieved due to the resonant states only present in one spin channel. As an example, we consider the parameters $\epsilon_0 = 0.5$ and $h_0 = 0.5$ ($\epsilon_{0\uparrow} = 0.25$, $\epsilon_{0\downarrow} = 0.75$). These are the same values used for the half-metallic layer in the bilayers investigated in section 8.2. In spite of a finite spectral weight at the Fermi level for the down-spin, for very small values of t_{01} we obtain a complete spin polarization in transmission, albeit with a small magnitude. Thus, mediated by the resonant state, an enhancement of the spin polarization of the transmission is found. This becomes apparent in fig. 9.5 which shows the \mathbf{k}_{\parallel} -resolved spectral function for the lead and the central region at $\omega = 0$ for a square lattice. The left (right) graph corresponds to $t_{01} = 0.05$ ($t_{01} = 0.25$), the upper (lower) part of each graph shows the spectral function of the up-spins (down-spins), and the left (right) part of each graph displays the lead (central region) spectral function, respectively. The Brillouin zone (BZ) extends from $[-\pi, \pi]$ (with

the lattice constant $a = 1$); the plots are taken in one of the four (identical) quadrants of the BZ.

The surface spectral function of the leads, $A_L^s(\omega - \varepsilon_{\mathbf{k}_{\parallel}})$ (left half of each graph), is identical for up- and down-spin since the leads are non-magnetic. The lead spectral function A_L^s is independent of t_{01} , as it is calculated for the case where the lead is decoupled from the central layer. The right half of each graph in fig. 9.5 shows the momentum resolved spectral function $A_{00\sigma}(\omega - \varepsilon_{\mathbf{k}_{\parallel}})$ in the central region; $A_{00\sigma}$ is calculated in the presence of the leads and therefore depends on t_{01} .

For $t_{01} = 0.05$, the maximum intensity of the spectral function is located within the continuum for $\sigma = \uparrow$, respectively outside the continuum for the $\sigma = \downarrow$ electrons. In spite of significant spectral weight in the central region $\int d\varepsilon_{\parallel} \rho_{\parallel}(\varepsilon_{\parallel}) A_{00\downarrow}(\omega - \varepsilon_{\parallel})$, the transmission for the down-spin almost vanishes. This spectral weight originates from the bound states which do not contribute to the current. Thus, we obtain a high polarization over a large frequency range.

Increasing the coupling strength to $t_{01} = 0.25$, we find that the spectral function of the central region significantly changes. The high-intensity states of the spin-up electrons are shifted out of the continuum, becoming sharp delta peaks. Similarly, the sharp states (white line) in the down-spin channel are repelled by the continuum and shift towards the edge of the Brillouin zone. Now for both spin channels only the continuous spectrum contributes, which is of similar magnitude for both spins.

This analysis shows that a change in the hopping amplitude between leads and central region, t_{01} , significantly affects the central region spectral function and consequently modifies the transmission qualitatively, beyond a mere change of the prefactor $|t_{01}|^2$ in eq. (9.41). In real materials such a situation is likely to happen as electronic states are significantly influenced by structural reconstructions at the surfaces.

9.2.2. Effect of lattice mismatch

So far we have considered epitaxial layers: In the transport direction $\hat{\mathbf{e}}_z$, every lattice site has exactly one site in each adjacent layer, see fig. 9.1. The neighboring sites in transport direction are at the same position in the x - y -plane, thus the hopping between layers t_{l+1} is independent of \mathbf{k}_{\parallel} . We focus on a particular simple mismatch between the central and the lead layers: a shift of half a lattice constant in x and y directions.

If the interface between leads and central region is not epitaxial, the hopping processes t_{-10} and t_{01} are not parallel to the transport direction, therefore these hopping amplitudes gain \mathbf{k}_{\parallel} -dependent phase factors. We assume the central region to be shifted diagonally by $\mathbf{r}^T = (\delta \ \delta \ 0)$. The in-plane Fourier transform of the hopping from the left to the central layer yields

$$t_{-10} \sum_{\alpha} \hat{c}_{-1\alpha\sigma}^{\dagger} \hat{c}_{0\alpha+r\sigma} = t_{-10} \sum_{k_x k_y} \hat{c}_{-1\mathbf{k}_{\parallel}\sigma}^{\dagger} \hat{c}_{0\mathbf{k}_{\parallel}\sigma} e^{-i\delta(k_x+k_y)}. \quad (9.50)$$

For small shifts $|\mathbf{r}| = \sqrt{2}\delta$, the transmission eq. (9.41) does not change as it depends only on the absolute square of the hopping amplitudes. For larger shifts, however, we need to consider the hopping amplitudes to different sites in the adjacent layer. We consider $\mathbf{r}^T = (1/2 \ 1/2 \ 0)$, in this case electrons should be able to hop to four different sites in the adjacent layer positioned at $\pm\mathbf{r}$ as well as $\pm\mathbf{r}'^T = (-1/2 \ 1/2 \ 0)$. We have to

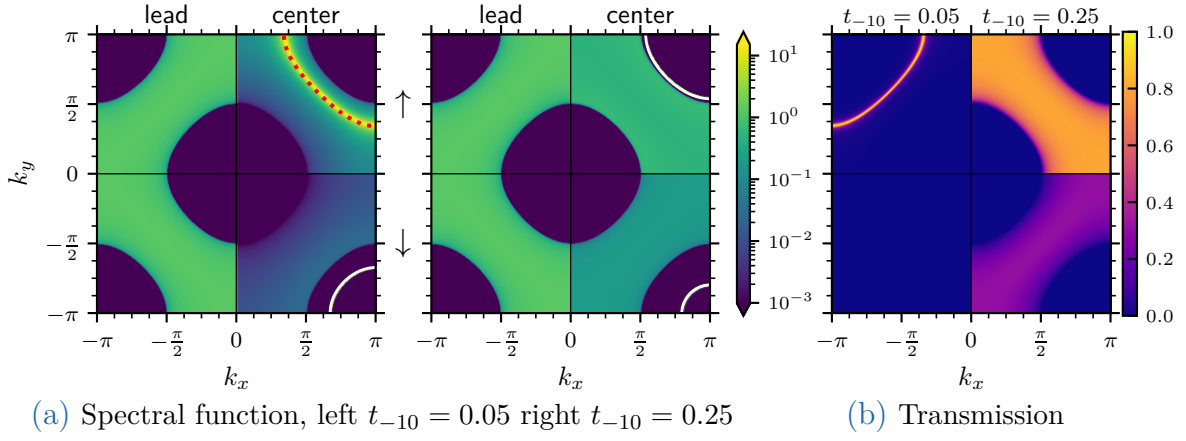


Figure 9.5: (a) Spectral functions of the non-interacting setup at the Fermi level $\omega = 0$. The left-hand-side, $k_x \in [-\pi, 0)$, of each graph shows the surface spectral function of the uncoupled lead, $A_L^s(0 - \varepsilon_{k_{\parallel}})$, and the right-hand-side, $k_x \in (0, +\pi]$, shows the spectral function of the central region, $A_{00\sigma}(0 - \varepsilon_{k_{\parallel}})$, respectively. The top half, $k_y \in (0, +\pi]$, and the bottom half, $k_y \in [-\pi, 0)$, parts correspond to the respective spin directions, as indicated. First graph: weak coupling, $t_{01} = 0.05$; second graph: strong coupling, $t_{01} = 0.25$. Other parameters are: $\epsilon_0 = 0.5$, $h_0 = 0.5$. Figure adapted from ref. [W4] (fig. 4). (b) Corresponding \mathbf{k}_{\parallel} -resolved transmission at frequency $\omega = 0$. The left-hand-side, $k_x \in [-\pi, 0)$, shows the result for $t_{-10} = 0.05$, and the right-hand-side, $k_x \in (0, +\pi]$, shows the result for $t_{-10} = 0.25$. The transmission is proportional to the product of the lead and the central region spectral function.

consider the following terms:

$$\begin{aligned}
 t_{-10} & \sum_{\alpha} [\hat{c}_{-1\alpha\sigma}^{\dagger} \hat{c}_{0\alpha+r\sigma} + \hat{c}_{-1\alpha\sigma}^{\dagger} \hat{c}_{0\alpha-r\sigma} + \hat{c}_{-1\alpha\sigma}^{\dagger} \hat{c}_{0\alpha+r'\sigma} + \hat{c}_{-1\alpha\sigma}^{\dagger} \hat{c}_{0\alpha-r'\sigma}] \\
 & = t_{-10} \sum_{k_x k_y} \hat{c}_{-1k_{\parallel}\sigma}^{\dagger} \hat{c}_{0k_{\parallel}\sigma} [e^{-i(k_x+k_y)/2} + e^{i(k_x+k_y)/2} + e^{-i(k_x-k_y)/2} + e^{i(k_x-k_y)/2}] \quad (9.51) \\
 & = 4t_{-10} \sum_{k_x k_y} \hat{c}_{-1k_{\parallel}\sigma}^{\dagger} \hat{c}_{0k_{\parallel}\sigma} [\cos(k_x/2) \cos(k_y/2)].
 \end{aligned}$$

Thus, we should modify the hopping amplitude $t_{-10} \rightarrow 4t_{-10} \cos(k_x/2) \cos(k_y/2)$. In general, the bare hopping amplitude t_{-10} should also change in a realistic system as the distance between the sites increased. Here, we employ the typical $1/\sqrt{Z} = 1/2$ scaling and define

$$\tilde{t}_{-10}(k_x, k_y) = 2t_{-10} \cos(k_x/2) \cos(k_y/2). \quad (9.52)$$

Thus, we adapt the transport eqs. (9.41) and (9.42) to the lattice mismatch using the effective hopping $\tilde{t}_{-10}(k_x, k_y)$. As the hopping explicitly depends on the k_x and k_y , the integration over the layer DOS has to be replaced by the two k -summations. The transmission for this lattice mismatch reads

$$T_{\sigma}(\omega) = \frac{2}{N_{\parallel}} \sum_{k_x k_y} |\tilde{t}_{-10}(k_x, k_y)|^2 \Im g_L^s(\omega^+ - \varepsilon_{k_{\parallel}} - \varepsilon_{L\sigma}) \Im G_{00k_{\parallel}\sigma}(\omega) \quad (9.53)$$

with the Green's function for the central region

$$G_{00k_{\parallel}\sigma}(z) = \frac{1}{z - \varepsilon_{k_{\parallel}} - \epsilon_{0\sigma} - \Sigma_{\sigma}(z) - 2|\tilde{t}_{-10}(k_x, k_y)|^2 g_{\sigma}^L(z - \varepsilon_{L\sigma} - \varepsilon_{k_{\parallel}})}. \quad (9.54)$$

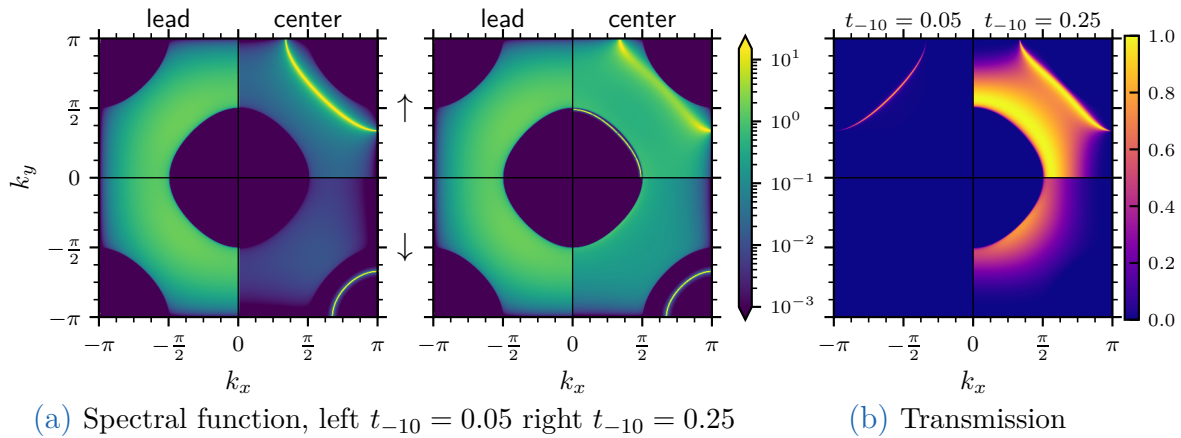


Figure 9.6.: (a) Spectral functions of the non-interacting setup with lattice mismatch at the Fermi level $\omega = 0$. The plot is analogous to fig. 9.5, the right-hand-side of each graph shows the spectral function of the central region eq. (9.54), and left-hand-side shows the surface spectral function $A_L^s(0 - \varepsilon_{\mathbf{k}_{\parallel}})$ multiplied by the $|\tilde{t}_{-10}(k_x, k_y)/t_{-10}|^2$. Compared to fig. 9.5, the factor $|\tilde{t}_{-10}(k_x, k_y)/t_{-10}|^2$ was included, such that the transmission is obtained as the product of the left and right half. Left graph: weak coupling, $t_{01} = 0.05$; right graph: strong coupling, $t_{01} = 0.25$. Other parameters are: $\epsilon_0 = 0.5$, $h_0 = 0.5$. (b) Corresponding \mathbf{k}_{\parallel} -resolved transmission at frequency $\omega = 0$. The transmission is proportional to $\tilde{t}_{-10}(k_x, k_y)$ times the product of the lead and the central region spectral function.

Just like in the epitaxial case, the modified transmission is determined by the product of the surface spectral functions of the uncoupled leads and that of the central region.

Results. Figure 9.6 illustrates the differences to the epitaxial case shown in fig. 9.5. It shows the \mathbf{k}_{\parallel} -resolved spectral function for the lead and the central region at $\omega = 0$ for a square lattice. Again, the left (right) graph corresponds to $t_{01} = 0.05$ ($t_{01} = 0.25$). The right part of each graph displays the central region spectral function eq. (9.54), left part shows the leads spectral function times the \mathbf{k}_{\parallel} -modulation, $|\tilde{t}_{-10}(k_x, k_y)/t_{-10}|^2 A_L^s(0 - \varepsilon_{\mathbf{k}_{\parallel}})$. We have to use an imaginary shift $\eta = 10^{-5}$ broadening the spectra, in order to make the sharp bound states visible.

For small coupling $t_{01} = 0.05$, the resonant and bound states are unchanged compared to fig. 9.5. Only continuum band is modulated by the \mathbf{k}_{\parallel} -dependent hopping $\tilde{t}(k_x, k_y)$. Increasing the coupling strength to $t_{01} = 0.25$, we find significant deviations compared to the epitaxial lattice in fig. 9.5. The bound state of the spin-down electron is closer to the continuum. For the spin-up electrons the difference is more drastic: a bound state for small \mathbf{k}_{\parallel} is obtained as well as a resonant state, whereas the epitaxial lattice shows only a bound state for large \mathbf{k}_{\parallel} .

The transmission eq. (9.53) remains a product of the surface spectral functions of the uncoupled leads and that of the central region. While the position of bound and resonant states changes with the lattice mismatch; qualitatively, the bound and resonant states affect the transmission in the same way as for the epitaxial lattice. Thus, we focus only on epitaxial layers in the following section.

9.2.3. Local electronic interaction in the central region [W4]

We treat the local electronic interaction in the central layer employing DMFT [59, 62, 63], see chapter 3. In combination with materials-specific input, the density functional theory + DMFT [204] technique was applied to heterostructures, more recently using supercells [199, 200]. While these studies were based on a perturbative impurity solver, in this thesis the recently developed fork tensor-product states (FTPS) solver [120] is employed, which is non-perturbative and allows for the accurate computation of spectral functions. Note that this solver works at zero temperature, and that there is no need to perform an analytic continuation of the spectral function which is otherwise a difficult technical issue [205, 206]. The hybridization function of the SIAM is discretized using 249 bath sites per spin. The ground state of the finite-size impurity problem is calculated using the DMRG [21, 207]. Subsequently, the time evolution is performed using the TDVP [145–147, 180] to obtain the local Green’s function. The time evolution is performed using time steps of 0.1 up to a maximal time $t_{\max} = 250$.

We apply the computational scheme outlined above to the setup described in section 9.1, including the Hubbard term U_0 in the central region, see eq. (9.7). Again, we consider the planes to be square lattices, the leads are non-magnetic and half-filled, $\epsilon_{L\sigma} = 0$, with hopping $t_L = 0.25$; in the central layer, we choose the parameters $\epsilon_0 = 0.5$ and $h_0 = 0.5$.

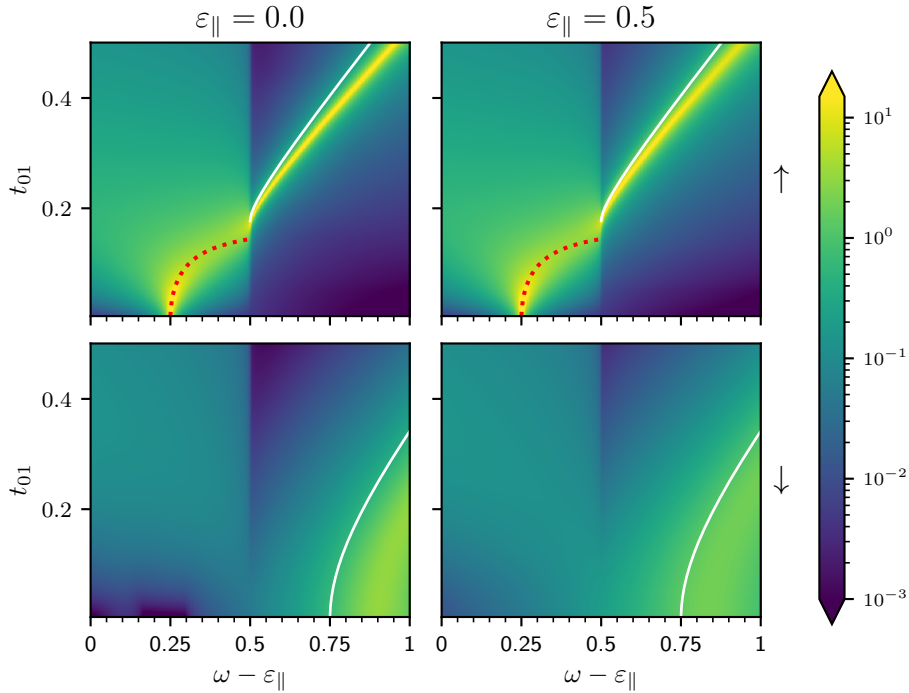


Figure 9.7.: Dependence of the spectral function of the central region, $A_{00\sigma}(\omega, \epsilon_{\parallel})$, on t_{01} . The parameters are $\epsilon_{L\sigma} = 0$, $t_L = 0.25$, $D = 1$, $\epsilon_0 = 0.5$, $h_0 = 0.5$, and $U_0 = 2$. The red dotted line corresponds to the real part of eq. (9.48) within the band of the leads for the *non-interacting* system, $U_0 = 0$. Figure adapted from ref. [W4] (fig. 5).

The spectral function of the central region is given by the imaginary part of eq. (9.42) on the real axis, $z = \omega^+$. This requires the knowledge of the many-body self-energy for the various coupling strengths t_{01} for a fixed interaction strength, here $U_0 = 2$. We

calculate the self-energy for different values of t_{01} in steps of 0.05 and linearly interpolate in-between to obtain a continuous function. Figure 9.7 shows the spectral function. To contrast it with the non-interacting case, we plot the delta peak outside the lead band (white line) and the resonance within the band (red dotted) line for $U_0 = 0$, which are given by the real part of eq. (9.48). We observe that the resonance in the up-spin is hardly affected by the interaction. In the regime of small t_{01} the down-spin is almost depleted, consequently there are only small interaction effects for the up-spin. On the other hand, the slope of the up-spin bound state changes compared to the non-interacting case. For the down-spin, we observe the bound state to be shifted to higher frequencies ω and to be considerably broadened.

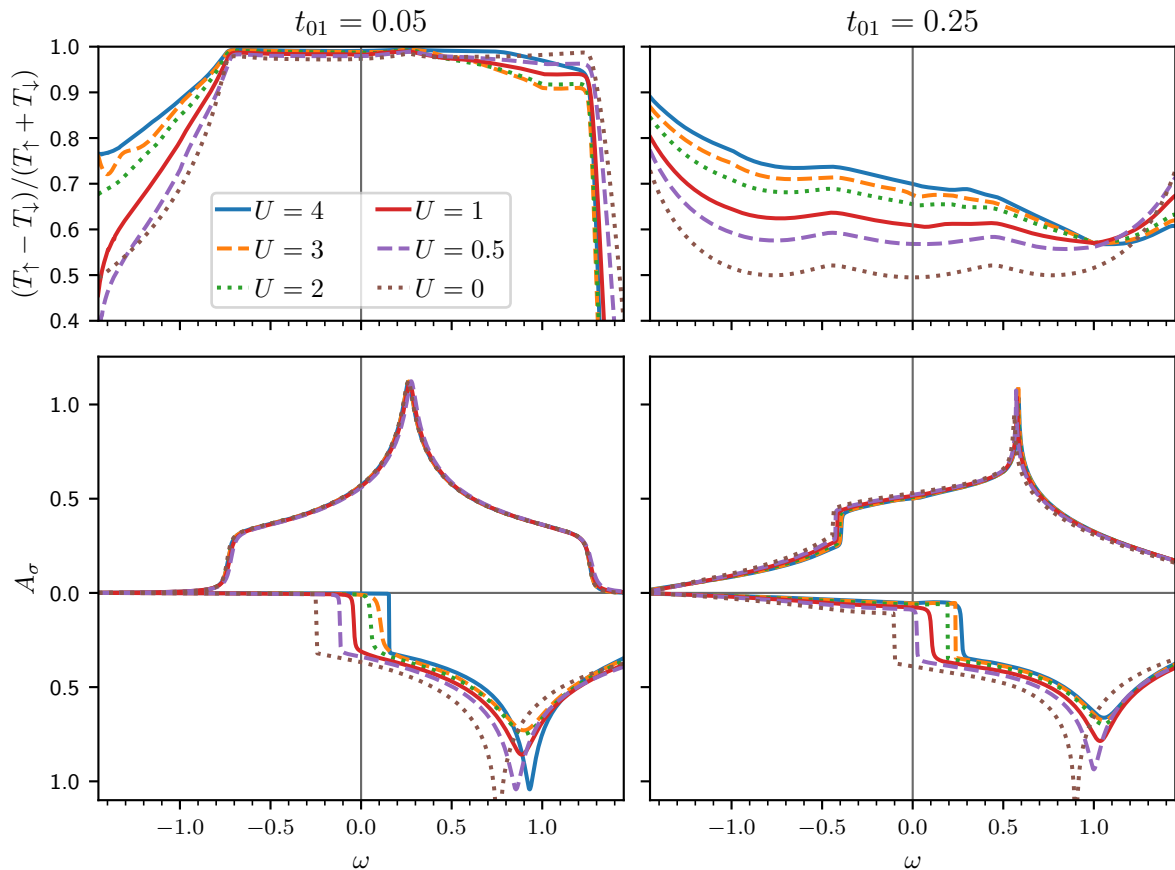


Figure 9.8.: Polarization of the transmission (top row) and local spectral function (bottom row) for an interacting central layer with varying on-site interaction U_0 . Left column: small coupling, $t_{01} = 0.05$; right column: intermediate coupling, $t_{01} = 0.25$. The spectral function for the down-spin varies strongly with U_0 at the Fermi level $\omega = 0$; the polarization of transmission, on the other hand, varies strongly only for $t_{01} = 0.25$. Figure adapted from ref. [W4] (fig. 6).

Figure 9.8 shows the local spectral functions of the central region, $A_{00\sigma}(\omega)$ (bottom), as well as the transmission polarization (top) for weak, $t_{01} = 0.05$ (left column), and strong, $t_{01} = 0.25$ (right column), coupling between leads and central region, for various interaction strengths U_0 . The local Coulomb interaction in the central region leads to an increased polarization of the spectral function, because the minority spin states are shifted towards higher energies. If the central region is decoupled, $t_{01} = 0$, the spectral

function is fully polarized for $U_0 \geq 2$ due to the Hartree shift, which means that the layer is a half-metallic ferromagnet, see chapter 8 and compare figs. 8.1 and 8.5(a). While for larger values of t_{01} the leads induce states for minority electrons in the central region, the spectral functions remain strongly polarized. For both couplings, $t_{01} = 0.05$ and $t_{01} = 0.25$, the majority spectral function remains largely unchanged in the presence of the interaction. This is a consequence of the almost depleted spin-down channel. Away from the Fermi energy tails of the spectral functions are formed, which are contributing to the high-energy satellite as discussed in chapter 8.

The polarization of the transmission, however, shows a behavior different from that of the local spectral function. For $t_{01} = 0.05$, in spite of the significant change of the minority spectral function at the Fermi energy ($\omega = 0$), the polarization remains above 95% for all values of U_0 , and changes only by a few percent. In this regime, the transmission of the majority spin is dominated by the resonance, while the spectral weight in the minority spin originates from the bound state which does not contribute to the current. In contrast to the small coupling $t_{01} = 0.05$, for $t_{01} = 0.25$ the polarization of transmission follows the interaction-induced change of the local spectral function. It increases from $\approx 50\%$ at $U_0 = 0$ to $\approx 70\%$ at $U_0 = 4$.

9.3. Summary [W4]

In this chapter we study a one-band generic model for transmission through metallic heterostructures. This model consists of two non-interacting leads sandwiching a central region that can be subject to local Coulomb interactions. The spin-dependent transmission is computed within the Meir–Wingreen formalism. The left and right leads in our model are assumed to be identical, and the central region consists only of a single layer, therefore the transmission decomposes into a product of the spectral function of the central region and the surface spectral function of the uncoupled leads. Independent of the presence of the local electronic interaction, small variations of the on-site energies and the hopping amplitude between leads and central region may strongly affect the shape of the spectral functions in the central region, and hence the conductance.

We identify bound and resonant states that may appear in this model, depending on the coupling strength between the leads and the central region. Generally speaking, resonance phenomena reveal themselves in the electronic conduction of mesoscopic condensed matter systems, however, a direct characterization of the resonance energy and the line width remains non-trivial. As a result, for a large coupling between the leads and the central region bound states are formed outside the continuum spectrum of the leads. These states do not contribute to the transmission, thus we expect them to be localized. In contrast, for the weak-coupling resonant state, the complex poles of the Green’s function entail an enhancement of the spin polarization of the transmission.

For the interacting central region, accurate results for the spectral functions and for the position of the bound and resonant states are obtained using the tensor network methods from chapter 5. For a certain set of parameters, electronic interactions lead to an enhanced spin polarization of the spectral function, as the minority electrons are shifted away from the Fermi level. As a consequence, a reduction of electronic correlations for the majority spins is found. For the bound states outside the continuum of the leads’ spectral function, electronic correlations lead to a significant broadening.

10. Conclusion and outlook

For many solids, the properties of electrons can be well approximated by an independent particle picture. This is, in particular, the case for itinerant electrons with broad energy bands; for such electrons, Bloch waves extending over the entire lattice are an appropriate description. For narrow bands, on the other hand, a particle-like picture is more appropriate since electrons may localize around atoms. Narrow bands are generally associated with partially filled d - and f -bands, which can, e.g., be found in transition metal oxides and rare earths. Particularly interesting phenomena occur if localization effects on larger energy scales compete with the itinerant character of electrons on smaller energy scales. In this case, intermediate energy scales become relevant, and diverse material-dependent properties emerge. A prime example is the metal-to-Mott-insulator transition where the energy cost of Coulomb repulsion competes against the kinetic energy, which favors delocalization. Theoretically, this is a most challenging problem, as the many-body problem of interacting electrons has to be solved. In this context, the thesis contributes to the development of numerical methods and applies them to models of half-metallic ferromagnets.

Methodological developments. We consider the local approximation to the problem of interacting electrons: the dynamical mean-field theory (DMFT). We summarize the derivation of DMFT and present the two complementary state-of-the-art algorithms to solve the impurity problem: continuous-time quantum Monte Carlo and tensor network methods.

We outline the continuous-time quantum Monte Carlo algorithm for the hybridization expansion CT-HYB (section 4.1). Appendix A provides an error-estimate related to the required number of Matsubara frequencies, as well as a more accurate Fourier transform for large Matsubara frequencies based on the Filon method. As the Monte Carlo algorithms are formulated in imaginary time, an analytic continuation is required to obtain spectral functions. We formulate an alternative version of the N -point Padé algorithm (section 4.2.2). The standard Padé algorithm is based on an exact interpolation of all data points. We employ the algorithm by Ito and Nakatsukasa [114]: Instead of determining the polynomial coefficients of the approximant, this algorithm directly calculates the position of the poles. It is formulated in a least-squares sense and therefore allows for incorporating uncertainties in the input data.

We also summarize the ideas of the density matrix renormalization group (DMRG) algorithm and the time evolution using the time-dependent variational principle (TDVP), employing the diagrammatic notation instead of explicit formulas (chapter 5). Appendix B discusses the Padé-Fourier algorithm for the Laplace transformation, for which a shorter time evolution suffices compared to a discrete Fourier transform. Therefore, the algorithm allows for reducing the computation time. We relate the Padé-Fourier algorithm to the commonly used linear prediction, identifying it with the linear prediction z -transform, which considers infinitely large times.

Further, we discuss the combination of DMFT for interacting electrons with the single-site approximation for disorder, the coherent potential approximation (CPA), and extend the combined scheme to off-diagonal disorder. For this purpose, we review the Blackman–Esterling–Berk (BEB) formulation of the CPA (section 6.4). We illustrate its ideas using tensor diagrams and provide an efficient implementation. The structure of the BEB effective medium is discussed, and we propose a concentration scaling that resolves some of its peculiarities. The limit of independent components for vanishing hopping between different components is discussed and solved analytically for the Bethe lattice with a general coordination number. We obtain the same concentration scaling of the bandwidth as found in the split-band limit for large disorder strength. While not providing a formal proof, we show how the BEB formulation can intuitively be combined with DMFT to treat interacting electrons in multicomponent alloys on a local level (chapter 7). As an example, we apply the algorithm to a Bethe lattice with an infinite coordination number, showing results that exhibit alloy band insulator to correlated metal to Mott insulator transitions.

Application to half-metallic ferromagnets. We apply the presented methods to models of half-metallic ferromagnets (chapter 8). We consider a Bethe lattice with a static spin splitting to produce a half-metal and investigate its spectral function. This problem was studied previously using a simplified Monte Carlo method. Applying the Padé analytic continuation to the self-energy instead of the Green’s function, we are able to produce reliable spectral functions. These spectra agree with zero-temperature results obtained by the DMRG+TDVP tensor network method, which produces results directly on the real axis without the need for an analytic continuation. Further, we investigate half-metallic ferromagnets in bilayers interfaced with a metallic, band insulating, or Mott insulating layer. Charge reconstruction at the interface of the layers induces metallicity; in spite of a large Hubbard U , we observe quasiparticle states in the Mott insulating layer.

Further, we study the transport through a single half-metallic layer sandwiched by metallic non-magnetic leads within the Meir–Wingreen formalism (chapter 9). This allows for a transparent calculation of the transmission in the presence of the Hubbard interaction. We identify bound and resonant states by analyzing the poles of the Green’s function in the central layer. For small coupling between the leads and the central layer, we find resonant states which enhance the transmission. For large coupling, on the other hand, we find bound states which do not contribute to the transmission. As a result, by modifying the doping of the weakly coupled central region, the transmission can be tuned to be strongly polarized.

Outlook. The BEB+DMFT algorithm could be further formalized by providing a rigorous derivation. Due to its similarity with the well-known CPA+DMFT algorithm, it should be feasible to generalize the existing proofs to off-diagonal disorder. Further investigations of the phase diagram of the Anderson–Hubbard model for off-diagonal disorder will be interesting. For vanishing hopping between the components, the self-consistency equations decouple in the components. Thus, it becomes clear that in this limit, a phase exists where one component is Mott insulating while the other remains metallic. The Mott insulator transition can also be tuned by the concentration, as it modifies the effective bandwidth of the components. It would be interesting to study

the evolution of this phase in terms of the hopping parameter between the different components. Combining the present formalism with band-structure calculations, it can be extended to real materials.

More realistic models of half-metallic ferromagnets could be investigated, like the frustrated face-centered cubic lattice, as the ferromagnetic phase can be stabilized for this lattice without a static magnetic splitting. Furthermore, half-metallic alloys could be studied using the BEB+DMFT algorithm as we expect interesting physics in the presence of both, disorder and interaction.

The transmission calculations could also be extended to larger central regions. In this case, the coupling between the leads and the interacting region is described by matrices which break the proportionality condition of the Meir–Wingreen formalism. Therefore, it is decisive to employ the transmission formula for the general case.

A. Matsubara sum and Fourier transform

The DMFT self-consistency equations are algebraic in the frequency domain; the CT-QMC impurity solver, on the other hand, works in imaginary time. Thus, the self-consistency equations on the imaginary axis require the transformation between Matsubara frequencies and imaginary times. The imaginary time Green's function

$$\mathcal{G}_{\hat{A},\hat{B}}(\tau - \tau') := -\langle \mathcal{T} \hat{A}(\tau) \hat{B}(\tau') \rangle = -\langle \mathcal{T} \hat{A}(\tau - \tau') \hat{B} \rangle, \quad (\text{A.1})$$

where \mathcal{T} denotes the time ordering, is by definition periodic in (imaginary) time. Mathematically, a clear recipe is given by the Fourier transform:

$$\overline{G}^{(n)} = \frac{1}{2} \int_{-\beta}^{\beta} d\tau \mathcal{G}(\tau) e^{i\overline{\omega}_n \tau} \quad (\text{A.2})$$

and its inverse

$$\mathcal{G}(\tau) = \frac{1}{\beta} \sum_{n=-\infty}^{\infty} \overline{G}^{(n)} e^{-i\overline{\omega}_n \tau}, \quad (\text{A.3})$$

with the Matsubara frequencies $i\overline{\omega}_n = i\pi n/\beta$. We focus on anti-periodic fermionic Green's functions, where only the odd frequencies, $i\omega_n = (2n+1)\pi/\beta$, contribute; these are accordingly referred to as fermionic Matsubara frequencies. Therefore, the Fourier transforms of fermionic Green's functions simplify: The Fourier integral can be reduced to an integration over half the interval

$$G^{(n)} := \overline{G}^{(2n+1)} = \int_0^{\beta} d\tau \mathcal{G}(\tau) e^{i\omega_n \tau} \quad (\text{A.4})$$

and the Fourier sum contains only the odd frequencies

$$\mathcal{G}(\tau) = \frac{1}{\beta} \sum_{n=-\infty}^{\infty} G^{(n)} e^{-i\omega_n \tau}. \quad (\text{A.5})$$

Static quantities can be calculated from the Matsubara sum of the corresponding Green's functions

$$\langle \hat{B} \hat{A} \rangle = \mathcal{G}_{\hat{A},\hat{B}}(0^-) = \frac{1}{\beta} \sum_{n=-\infty}^{\infty} G_{\hat{A},\hat{B}}^{(n)} e^{-i\omega_n 0^-}; \quad (\text{A.6})$$

like for example the occupation $\langle \hat{n} \rangle = \mathcal{G}_{\hat{c},\hat{c}^\dagger}(0^-)$ with $\hat{A} = \hat{c}$ and $\hat{B} = \hat{c}^\dagger$.

While these equations seem simple enough, they have to be treated with care in numerics. The main issues are the following:

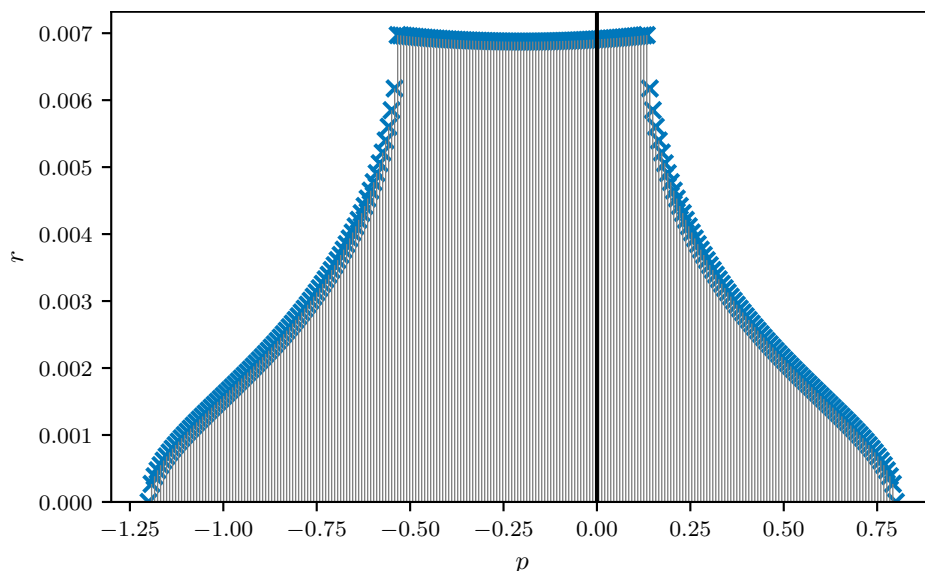


Figure A.1.: Poles ϵ_m and corresponding residues r_m of the example Green's functions given by 250 equidistant poles. The crosses mark the value of the residues r_m , the vertical lines indicate their position ϵ_m .

1. We can only calculate a finite number of Matsubara frequencies, thus the Matsubara and Fourier sum eq. (A.5) have to be truncated.
2. We calculate the imaginary time Green's function $\mathcal{G}(\tau)$ only on a grid, discretizing the Fourier integral eq. (A.4).

Alternative techniques exist, most notably sampling the Matsubara Green's function $G^{(n)}$ directly using nonuniform fast Fourier transform (NUFFT) [98]. Another approach is working with a polynomial basis like Legendre polynomials [97]. Here, we only focus on the simple approach of transforming a sampled imaginary-time Green's function. The algorithms discussed in this appendix are implemented in [C2].

Test case. Throughout this chapter we use the same example problem, which is analytically solvable, to benchmark the numerical algorithms. We choose an example Green's function

$$G(z) = \sum_{m=1}^{250} \frac{r_m}{z - \epsilon_m} \quad (\text{A.7})$$

given by 250 equidistant poles. The residues are chosen according to the simple cubic DOS [172, 208, 209], shifted by the chemical potential $\mu = 0.2$ and normalized to $\sum_m r_m = 1$. Figure A.1 shows its poles and residues. The particular choice of example Green's function does not affect the general results. However, it is essential that the example is away from particle whole symmetry. The symmetry leads to error cancellations, and would give the impression that the algorithms are more accurate.

A.1. Matsubara and Fourier sum

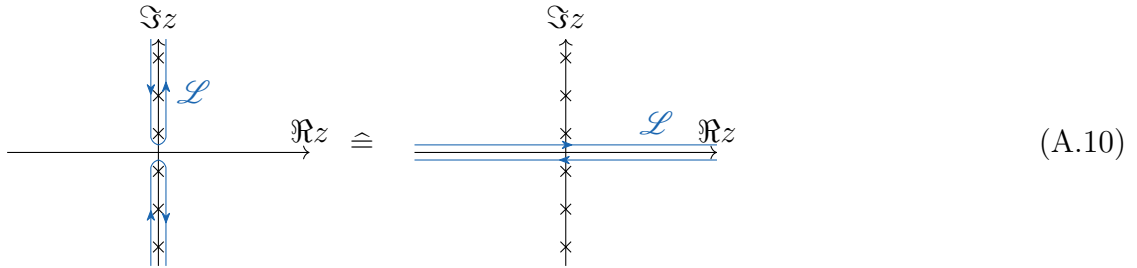
The Fourier summation eq. (A.4) can be expressed as the contour integral

$$\mathcal{G}(\tau) = \frac{1}{\beta} \sum_{n=-\infty}^{\infty} G^{(n)} e^{-i\omega_n \tau} = \begin{cases} -\frac{1}{2\pi i} \oint_{\mathcal{L}} dz G(z) f(z) e^{-z\tau} & \text{if } \tau \in (-\beta, 0) \\ \frac{1}{2\pi i} \oint_{\mathcal{L}} dz G(z) [1 - f(z)] e^{-z\tau} & \text{if } \tau \in (0, +\beta) \end{cases} \quad (\text{A.8})$$

via the analytic continuation $G(z)$ of the Matsubara Green's function $G^{(n)} = G(i\omega_n)$, where $f(z)$ is the Fermi function

$$f(z) = \frac{1}{e^{\beta z} + 1}. \quad (\text{A.9})$$

The contour \mathcal{L} can be chosen parallel to the real axis



where the shift into the imaginary half-planes η has to be smaller than the zeroth Matsubara frequency $\eta < \omega_0 = \pi/\beta$. The contour integral is helpful, to check the accuracy of the sums, as it can be evaluated exactly for simple Green's functions.

A.1.1. Example: occupation of the single-pole Green's function

The prime example for a static Matsubara sum is the occupation number

$$\langle \hat{n} \rangle = \mathcal{G}_{\hat{c}, \hat{c}^\dagger}(\tau = 0^-) = \frac{1}{\beta} \sum_{n=-\infty}^{\infty} G_{\hat{c}, \hat{c}^\dagger}^{(n)} e^{i\omega_n 0^+}, \quad (\text{A.11})$$

where $G^{(n)}$ is the diagonal one-particle Green's function. The Matsubara Green's function is asymptotic equivalent to $G^{(n)} \sim 1/i\omega_n$ as $n \rightarrow \pm\infty$, thus the convergence of the summation is problematic. It is instructive to consider the simplest Green's function $G(z) = 1/z$ as an example.

Using the analytic continuation, eq. (A.11), it is trivial to evaluate the occupation number of the single-pole Green's function $G(z) = 1/z$ exactly:

$$\langle \hat{n} \rangle = f(0) = \frac{1}{2}. \quad (\text{A.12})$$

If we symmetrically truncate the Matsubara sum after N positive and negative frequencies, we obtain, on the other hand,

$$\frac{1}{\beta} \sum_{n=-N}^{N-1} \frac{1}{i\omega_n} e^{i\omega_n 0^+} = \frac{1}{\beta} \sum_{n=-N}^{N-1} \frac{1}{i\omega_n} = \frac{1}{\beta} \sum_{n=0}^{N-1} \left[\frac{1}{i\omega_n} + \frac{1}{-i\omega_n} \right] = 0. \quad (\text{A.13})$$

No matter, how many frequencies we take into account, the truncated sum yields the wrong result $\langle \hat{n} \rangle \approx 0$. We cannot expect naively truncated Matsubara summations to yield the correct result. In this example, the entire weight of $1/2$ comes from the infinitely large frequencies combined with the convergence generating factor $\exp(i\omega_n 0^+)$. It is essential, to first take the limit $N \rightarrow \infty$, and to afterwards let 0^+ go to 0, dropping the convergence generating phase factor.

Integral test. The truncation error can be estimated using the *integral test* [210]. Let $h(x)$ be a monotonously decreasing function, then

$$\int_N^\infty dx h(x) \leq \sum_{n=N}^\infty h(n) \leq h(N) + \int_N^\infty dx h(x). \quad (\text{A.14})$$

Note that the function has to be non-negative $h \geq 0$ for the integrals and sum to converge. The first inequality approximates the integral by the left Riemann sum with unit steps; this is an upper bound as the function is monotonously decreasing. Analogously, the second inequality corresponds to the right Riemann sum, as can be seen by subtracting the term $h(N)$. The integral test eq. (A.14) allows calculating boundaries of the truncation error if the asymptotic limit of $G(z)$ has been reached. We assume the Green's function in consideration decays like $1/i\omega_n$ for large Matsubara frequencies. Ignoring the convergence generating factor $\exp(i\omega_n 0^+)$, the weight of the truncation after any finite N is logarithmically divergent

$$\frac{1}{\beta} \sum_{n=N}^\infty \frac{1}{\omega_n} \geq \frac{1}{2\pi} \int_N^\infty dx \frac{1}{x + 1/2} = \frac{1}{2\pi} \ln x \Big|_{N+1/2}^\infty. \quad (\text{A.15})$$

In fact, the integral test yields the exact value of $f(0) = 1/2$ for the truncated weight. We split the summation in the three parts

$$\begin{aligned} \frac{1}{\beta} \sum_{n=-\infty}^\infty \frac{1}{i\omega_n} e^{i\omega_n 0^+} &= \frac{1}{\beta} \sum_{n=-N}^{N-1} \frac{1}{i\omega_n} + \frac{1}{\beta} \sum_{n=N}^\infty \frac{1}{i\omega_n} e^{i\omega_n 0^+} + \frac{1}{\beta} \sum_{n=-\infty}^{-N-1} \frac{1}{i\omega_n} e^{i\omega_n 0^+} \\ &= \frac{2}{\beta} \sum_{n=N}^\infty \frac{1}{\omega_n} \sin(\omega_n 0^+). \end{aligned} \quad (\text{A.16})$$

We can neglect the convergence generating factor in the first addend because it is a finite sum. As shown before in eq. (A.13), this sum vanishes by symmetry. The remaining term of eq. (A.16) can be estimated using the integral test.¹ We calculate the integral

$$\lim_{\eta \searrow 0} \frac{2}{\beta} \int_N^\infty dx \frac{\sin(\omega_x \eta)}{\omega_x} = \lim_{\eta \searrow 0} \frac{1}{\pi} \int_{\omega_N \eta}^\infty dy \frac{\sin(y)}{y} = \frac{1}{2}, \quad (\text{A.17})$$

where we keep the order of the limits: first integrating till infinity and then letting η go to zero. The result is independent of N , as for any finite N we perform the full integration from zero to infinity. Thus, the integral test yields the sharp bounds

$$\frac{1}{2} \leq \left[\frac{1}{\beta} \sum_{n=N}^\infty \frac{1}{i\omega_n} e^{i\omega_n 0^+} + \frac{1}{\beta} \sum_{n=-N-1}^{-\infty} \frac{1}{i\omega_n} e^{i\omega_n 0^+} \right] \leq \frac{1}{2} + \frac{2 \sin(\omega_N 0^+)}{\beta \omega_N} = \frac{1}{2}, \quad (\text{A.18})$$

therefore, the whole contribution comes from frequencies at infinity. Therefore, at least the $1/z$ asymptote of the Green's function has to be treated analytically.

¹For any finite value instead 0^+ , the summand is in fact not monotonously decreasing. We neglect mathematical rigor here, and simply ignore this fact.

A.1.2. Truncation error estimate

In the following, we provide an error estimate, that enables us to judge the number of Matsubara frequencies which is necessary for an accurate summation. In the following, we assume that we know at least how to handle the high-frequency asymptote $1/z$ of the Green's functions. More precisely, we assume that $\tilde{G}^{(n)} \sim a(i\omega_n)^{-k-1}$ as $n \rightarrow \infty$, with $k > 0$; in this case the convergence generating factor $\exp(i\omega_n 0^+)$ does not contribute and can be omitted. We define the truncation error

$$T(N) = \left| \frac{1}{\beta} \sum_{n=-\infty}^{\infty} \tilde{G}^{(n)} - \frac{1}{\beta} \sum_{n=-N}^{N-1} \tilde{G}^{(n)} \right|. \quad (\text{A.19})$$

For simplicity, we restrict the calculations to diagonal Green's function elements with the symmetry $G(-i\omega_n) = G^*(i\omega_n)$, thus we can simplify the truncation error to the sum over the real parts at positive Matsubara frequencies

$$T(N) = \frac{2}{\beta} \left| \sum_{n=N}^{\infty} \Re \tilde{G}^{(n)} \right|. \quad (\text{A.20})$$

Again, we employ the integral test eq. (A.14), however, $\tilde{G}^{(n)}$ is unknown for $n \geq N$. Knowing the high-frequency behavior, we can however find a function $g(x) > 0$ with $|\tilde{G}^{(n)}| \leq g(x) \forall x > N$. Thus, eq. (A.14) provides an upper limit of the truncation error:

$$T(N) \leq \frac{2}{\beta} \sum_{n=N}^{\infty} |\Re \tilde{G}^{(n)}| \leq \frac{2}{\beta} \sum_{n=N}^{\infty} g(n) \leq \frac{2}{\beta} \int_{N-1}^{\infty} dx g(x). \quad (\text{A.21})$$

We assume, that for large enough n , $\tilde{G}^{(n)}$ is asymptotic to $\tilde{G}^{(n)} \sim a(i\omega_n)^{-k-1}$. Thus, assuming N is large enough, there is a constant $c \geq a$ such that $|\tilde{G}^{(n)}| \leq c\omega_n^{-k-1} = g(n) \forall n \geq N$. The integral test yields the estimate

$$\begin{aligned} T(N+1) &\leq \frac{2}{\beta} \int_N^{\infty} dx c\omega_x^{-k-1} = \frac{1}{\pi} \int_{\omega_N}^{\infty} d\omega c\omega^{-k-1} \\ &= \frac{c}{\pi k \omega_N^k} = \frac{c\beta^k}{k\pi^{k+1}(2N+1)^k} = \mathcal{O}\left((\beta/N)^k\right). \end{aligned} \quad (\text{A.22})$$

To obtain a truncation error smaller than δ , we thus need to include at least

$$N \geq \sqrt[k]{\frac{c}{k\delta}} \frac{\beta}{2\pi} + \frac{1}{2} \quad (\text{A.23})$$

positive Matsubara frequencies. We remind, this estimate assumes that we have reached the asymptotic limit $\tilde{G}^{(n)} \sim i\omega_n^{-k-1}$. The constant c can be estimated in practice by fitting the function $g(n)$ to the available data points $\tilde{G}^{(n)}$. If applied correctly, the error estimate is an upper bound for all imaginary times τ , not just the static sum at $\tau = 0^-$, as the absolute in eq. (A.21) is applied to every summand, ignoring the phase factor. For τ approaching $\beta/2$, the exact truncation error eq. (A.19) is typically much smaller than the estimate, as the phase factors cause cancellations.

A.1.3. Treatment of high-frequency behavior

To improve the accuracy of the Fourier summation, we need to treat the high-frequency behavior of the Green's function exactly. We propose a simple function $g(x)$, which can be summed exactly and rewrite the sum

$$\frac{1}{\beta} \sum_{n=-\infty}^{\infty} G^{(n)} e^{-i\omega_n \tau} = \frac{1}{\beta} \sum_{n=-\infty}^{\infty} [G^{(n)} - g(i\omega_n)] e^{-i\omega_n \tau} + \frac{1}{\beta} \sum_{n=-\infty}^{\infty} g(i\omega_n) e^{i\omega_n \tau} \quad (\text{A.24})$$

The function $g(x)$ needs to be chosen such that it cancels the high-frequency behavior of $G^{(n)}$. We truncate only the sum over the difference $[G^{(n)} - g(i\omega_n)]$, reducing the error as shown in the previous section. To treat the $1/z$ asymptote, we can choose $g_1(x) = 1/x$ which sums up

$$\frac{1}{\beta} \sum_{n=-\infty}^{\infty} \frac{1}{i\omega_n} e^{-i\omega_n \tau} = \begin{cases} +\frac{1}{2} & \text{if } \tau \in (-\beta, 0), \\ -\frac{1}{2} & \text{if } \tau \in (0, +\beta). \end{cases} \quad (\text{A.25})$$

To additionally include a c/z^2 behavior, the function $g_2(x) = 1/(x - c)$ can be used which sums to

$$\frac{1}{\beta} \sum_{n=-\infty}^{\infty} \frac{1}{i\omega_n - c} e^{-i\omega_n \tau} = \begin{cases} f(c) e^{-c\tau} & \text{if } \tau \in (-\beta, 0), \\ -[1 - f(c)] e^{-c\tau} & \text{if } \tau \in (0, +\beta). \end{cases} \quad (\text{A.26})$$

In general, the Green's function $G(z)$ has the high-frequency behavior

$$G(z) = \sum_{k=0}^{\infty} \frac{m_k}{z^{k+1}}, \quad (\text{A.27})$$

with the high-frequency moments m_k . These moments can e.g. be calculated via the equation of motion. They also equal the frequency integral

$$m_k = -\frac{1}{2\pi i} \int_{\mathcal{L}} dz G(z) z^k = \int_{-\infty}^{\infty} d\omega A(\omega) \omega^k, \quad (\text{A.28})$$

with the spectral function $2\pi i A(\omega) = \lim_{\eta \searrow 0} [G(\omega - i\eta) - G(\omega + i\eta)]$. Thus, the high-frequency moments are the moments of the spectral function. Furthermore, the moments describe the discontinuity at $\tau = 0$ on the imaginary axis:

$$\begin{aligned} \lim_{\epsilon \searrow 0} [\mathcal{G}^{(k)}(-\epsilon) - \mathcal{G}^{(k)}(+\epsilon)] &= -\frac{1}{2\pi i} \lim_{\epsilon \searrow 0} \int_{\mathcal{L}} dz G(z) z^k \{f(z) e^{+z\epsilon} + [1 - f(z)] e^{-z\epsilon}\} \\ &= m_k, \end{aligned} \quad (\text{A.29})$$

where $\mathcal{G}^{(k)}(\tau)$ is the k -th derivative $\mathcal{G}^{(k)} = \frac{d^k}{d\tau^k} \mathcal{G}(\tau)$.

To treat a larger number of moments m_k a linear superposition of functions $g_2(x)$ with different constants is adequate. The moments of $g_2(x)$ are the powers of the constant $m_k = c^k$. Thus, the function

$$g_M(x) = \sum_{m=1}^M \frac{r_m}{x - \epsilon_m} \quad (\text{A.30})$$

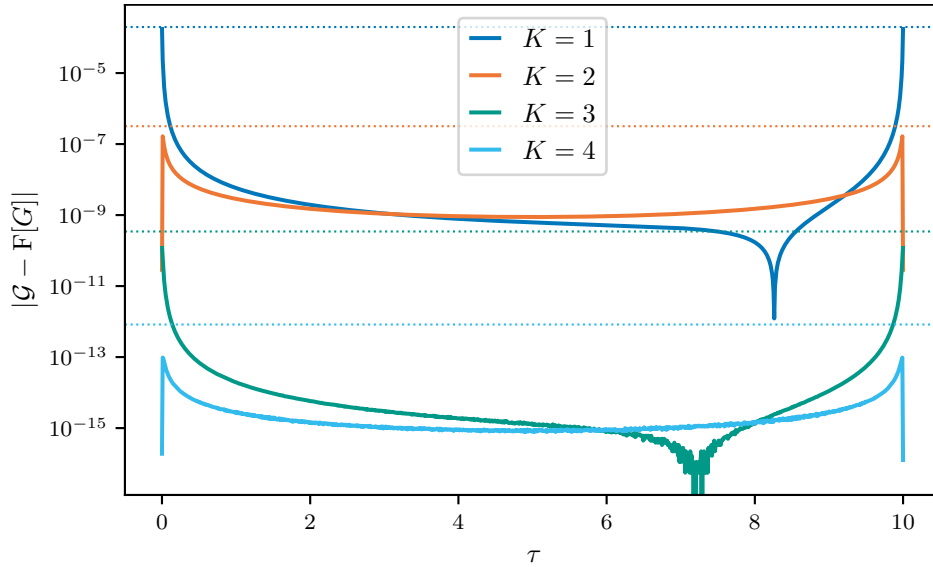


Figure A.2.: Accuracy of Fourier sum including the first K moments. The inverse temperature is $\beta = 10$, 512 positive Matsubara frequencies are used; the Green's function is given by fig. A.1. The dotted line shows the corresponding error estimate eq. (A.22) using the moment $c = m_{K+1}$.

has the moments $m_k = \sum_m r_m \epsilon_m^k$. Let \mathbf{m} be the vector of desired moments $(\mathbf{m})_k = m_k$, then the moments are given by the matrix equation

$$\mathbf{m} = \mathbf{V}^T \mathbf{r} \quad (\mathbf{V})_{mk} = \epsilon_m^k \quad (\text{A.31})$$

where \mathbf{r} is the vector of residues $(\mathbf{r})_m = r_m$, and \mathbf{V} is the Vandermonde matrix of the poles ϵ_m . For a given set of poles ϵ_m , the linear equation can easily be solved. The Vandermonde matrix is known to be ill conditioned, as we consider only a few moments and therefore small matrices, the condition number is unproblematic. The problem is similar to polynomial interpolation, for which the Chebyshev points are known to be a good choice. We choose the Chebyshev points [211], that are the nodes of the Chebyshev polynomials, as poles ϵ_m

$$\epsilon_m = \cos\left(\frac{2m-1}{2M}\pi\right) = \sin\left(\frac{M-2m+1}{2M}\pi\right) \quad m \in \{1, \dots, M\}. \quad (\text{A.32})$$

For these points, the Vandermonde matrix is better conditioned [212, 213] than for equidistant points. Specific algorithms for solving Vandermonde systems are known, also in particular on the Chebyshev points [115, 213–215]. We consider only small matrices, therefore we directly solve eq. (A.31) using a standard algorithm instead of an algorithm tailored to the Vandermonde system. Figure A.2 shows the absolute error for the example Green's function eq. (A.7). For the chosen parameters, using $N = 4$ moments yields an accuracy of 10^{-13} close to machine precision. Using more moments $N > 4$, the Fourier transform becomes numerically exact. For numbers $N \geq 15$ numerical errors start to accumulate, and the results gradually get worse.

If not enough moments are known, additional moments can be fit using an equality-constrained least-squares algorithm [115]. We define the kernel matrix

$$(\mathbf{K})_{nm} = \frac{1}{i\omega_n - \epsilon_m}. \quad (\text{A.33})$$

The residues r_m of a function $g_M(x)$ can be determined by solving the linear equation

$$\mathbf{g} \approx \mathbf{K}\mathbf{r} \quad \text{constrained to } \mathbf{m} = \mathbf{V}^\top \mathbf{r}, \quad (\text{A.34})$$

where \mathbf{g} is the vector of known values $(\mathbf{g})_n = G^{(n)}$. This is a least-squares problem with equality constraints, for its solution, Golub and Van Loan [115] provide an algorithm using the QR-decomposition. Of course, $g_M(x)$ needs to reproduce the tail of the Green's function $G^{(n)}$, not the whole function itself. For this purpose, we weight the rows of the least-squares problem eq. (A.34) by left-multiplying the diagonal matrix $\mathbf{W} = \text{diag}(\omega_n^M)$. If error estimates for the Green's function $G^{(n)}$ are available, they can also be incorporated into the matrix \mathbf{W} . To obtain real-valued residues and thus moments, the kernel \mathbf{K} and \mathbf{g} in eq. (A.34) can be split into real and imaginary part to obtain the real equation

$$[\mathbf{W}\Re\mathbf{g}, \mathbf{W}\Im\mathbf{g}]^\top \approx [\mathbf{W}\Re\mathbf{K}, \mathbf{W}\Im\mathbf{K}]^\top \mathbf{r} \quad \text{constrained to } \mathbf{m} = \mathbf{V}^\top \mathbf{r}. \quad (\text{A.35})$$

Solving this equation yields the function $g_M(x)$, eq. (A.30), that exactly matches the known moments m_k , additional moments are approximate by the least-squares fit of the tail of $G^{(n)}$.

We conclude, that the truncation error for Fourier sum eq. (A.3) can be reduced by using eq. (A.24) with a suitable auxiliary function $g_M(z)$, eq. (A.30). For known high-frequency moments m_k eq. (A.31) provides $g_M(z)$, additional moments can be fit using eq. (A.35).

A.1.4. Gibbs oscillation of Fourier sum

Truncating the Fourier sum after N Matsubara frequencies equals approximating $G^{(n)} \stackrel{!}{=} 0$ for $n \geq N$. Thus, we introduce an artificial jump. Such a jump or step function is known to cause oscillations for the Fourier transform, this is known as the Gibbs phenomenon. Using a truncated Fourier sum, we observe oscillations around $\tau = 0$ and $\tau = \beta$. This effect can be reduced, if $G^{(n)} \stackrel{!}{=} 0$ is replaced by a tail explicitly going to 0 at finite $n > N$. E.g. we choose

$$G^{(n)} \stackrel{!}{=} \frac{G^{(N-1)}}{2} \left[\cos\left(\pi \frac{n-N}{N+1}\right) + 1 \right] \quad \text{for } 2N > n > N. \quad (\text{A.36})$$

While this tail is not physically motivated, it is a better heuristic than the truncation, which amounts to the equally unphysical choice of setting all elements 0. Figure A.3 shows that the heuristic choice reduces the errors.

A.1.5. Truncation as approximate Fermi function

From the analytic continuation eq. (A.8), we realize that the truncation of the Matsubara sum is equivalent to the approximation of the Fermi function by a finite number of poles. The Fermi function has simple poles at the Matsubara frequencies with residue $-\beta$; it can be written as the infinity sum

$$f(z) = \frac{1}{2} - \sum_{n=-\infty}^{\infty} \frac{\beta}{z - i\omega_n}. \quad (\text{A.37})$$

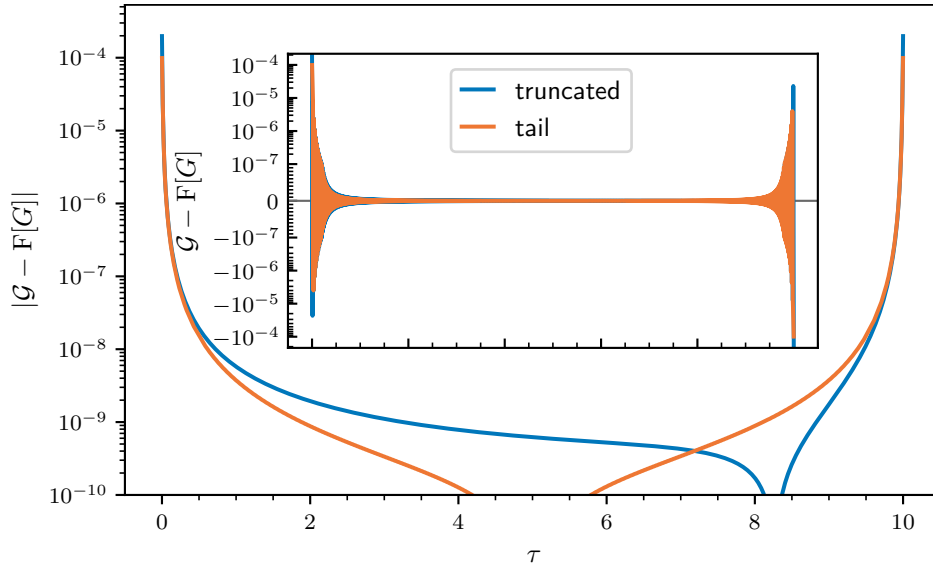


Figure A.3.: Absolute error of the truncated Fourier sums (blue) compared to the tail (orange) eq. (A.36). The inverse temperature is $\beta = 10$, 512 positive Matsubara frequencies are used; the Green's function is given by fig. A.1. The inset shows the difference between the exact Green's function using a symmetric logarithmic scale to show the oscillations.

Truncating the Matsubara sum after N positive and negative Matsubara frequencies amounts to approximating the Fermi function by $2N$ poles:

$$f(z) \simeq f_N(z) = \frac{1}{2} - \sum_{n=-N}^{N-1} \frac{\beta}{z - i\omega_n}. \quad (\text{A.38})$$

While the Fermi function is a strictly monotonous decreasing function, the approximation $f_N(z)$ has a local maximum and minimum on the real axis. The approximation $f_N(z)$ is converging only slowly, requiring large N for a decent approximation.

Instead of using the exact $2N$ poles, one can search for a given N the $2N$ poles which approximate the Fermi function best. In essence this is finding the $[2N/2N]$ Padé approximant [216, 217]. Ozaki [216] provides the poles iz_p and corresponding residues $-\beta r_p$. Just like the Matsubara frequencies, the poles iz_p are purely imaginary. We denote iz_p Padé frequencies. This approximation writes

$$f(z) \simeq f_N^p(z) = \frac{1}{2} - \sum_{p=-N}^{N-1} \frac{\beta r_p}{z - iz_p}. \quad (\text{A.39})$$

Figure A.4 compares the approximation using Matsubara frequencies $i\omega_n$, eq. (A.38), and Padé frequencies iz_p , eq. (A.39). The left plot compares the exact result (black) on the interval $\omega/\beta \in [0, 100]$. The Matsubara approximation $f_N(z)$ agrees only close to the Fermi level, thus the approximation is only applicable for small band-widths or high temperature. The Padé approximation converges much faster, already for $N = 25$ it follows the exact result until machine precision is reached. It is instructive to consider the error integrated from to Fermi level $\omega = 0$ up to the distance $\omega = d$

$$\epsilon(d) = \int_0^d d\omega [f_N(\omega) - f(\omega)] = \frac{d}{2} - \beta \sum_{n=0}^N \ln(1 + (d/\omega_n)^2) - \beta \ln\left(\frac{1}{1 + \exp(-\beta d)}\right) - \beta \ln(2),$$

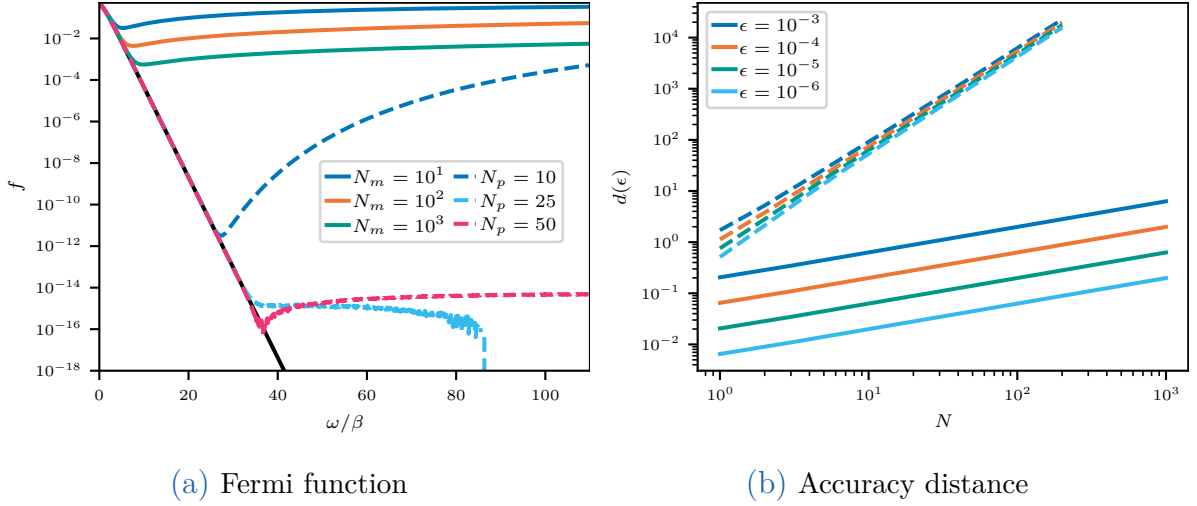


Figure A.4.: (a) Approximations of the Fermi function using $2N$ poles. Solid lines use N_m positive Matsubara frequencies eq. (A.38), dashed lines use N_p positive Padé frequencies eq. (A.39); the black solid line is the exact Fermi function. (b) Distance $d(\epsilon)$ till integrated error eq. (A.40) reaches ϵ .

(A.40)

or rather its inverse, the accuracy distance $d(\epsilon)$. This is the distance up to which integrals are accurate up to ϵ ; for a desired accuracy we require the bandwidth to be less than $d(\epsilon)$. Figure A.4(b) shows the accuracy distance for both approximations. Padé frequencies (dashed) exhibit much larger accuracy distances even for small numbers of poles, and the distance grows faster with the number of poles. For the Matsubara approximation the distance is roughly proportional to $d(\epsilon) \propto N^{1/2}$; while for the results shown in fig. A.4(b), the Padé approximation exhibits an asymptote $d(\epsilon) \sim c(\epsilon)N^{1.9}$.

The frequencies and residues can be calculated as the generalized eigenvalue problem [216, 217]

$$\mathbf{A}\mathbf{v}_p = (\beta z_p)\mathbf{B}\mathbf{v}_p, \quad \text{with} \quad A_{ij} = -\delta_{ij}(2i+1), \quad B_{ij} = \frac{1}{2}(\delta_{ij+1} + \delta_{i+1j}); \quad (\text{A.41})$$

the corresponding residues are given by

$$r_p = \frac{1}{4}\mathbf{V}_{[0,:]}(\mathbf{V}^{-1})_{[:,0]}(\beta z_p)^2, \quad (\text{A.42})$$

where \mathbf{V} is the matrix of right eigenvectors $\mathbf{V}_{[:,p]} = \mathbf{v}_p$. Roughly the first 61% of the Padé frequencies coincide with the Matsubara frequencies, the rest of the frequencies are located at increasing distances, such that large imaginary frequencies are covered [216]. Such frequencies are suitable for an integral over the Green's functions: The poles of the Green's function are located on the real axis, therefore it becomes featureless for large imaginary frequencies. A suitable imaginary mesh should have many points close to the real axis, and few points deep in the imaginary plane.

Compared with the Matsubara frequencies, the usage of Padé frequencies yields extremely accurate results for static quantities, that is the limit $\tau = 0^+$ of the integral

eq. (A.8):

$$-\frac{1}{2\pi i} \oint_{\mathcal{L}} dz g(z) f(z) e^{-z0^+} \approx \sum_{p=-N}^{N-1} r_p g(iz_p). \quad (\text{A.43})$$

The transformation to and from imaginary time, however, is not as simple. Formally, the imaginary time Green's function for $\tau > 0$ can be expressed as the linear equation

$$\mathcal{G}(\tau) = \frac{1}{2\pi i} \int_{\mathcal{L}} dz G(z) [1 - f(z)] e^{-z\tau} \approx \frac{1}{\beta} \sum_{p=-N}^{N-1} r_p G(iz_p) e^{-iz_p\tau}, \quad (\text{A.44})$$

which can readily be inverted. In practice, this approximation turns out to be rather poor for small N , as the Fourier basis is strongly truncated. Furthermore, it does not fulfill the periodicity $\exp(-i\omega_n[\tau + \beta]) = -\exp(-i\omega_n\tau)$ of the imaginary time Green's function. While the Green's function $G(z)$ becomes featureless deep in the imaginary plane, the phase factor $\exp(-z\tau)$ rapidly oscillates. These oscillations are not captured by the mesh iz_p , which is sparse for large imaginary frequencies. Thus, $f(z)$ should not be treated on its own, instead an accurate approximation for

$$f(z) \exp(-z\tau) = \frac{e^{-z\tau}}{e^{z\beta} + 1} \quad (\text{A.45})$$

has to be sought.

To circumvent the problem, we propose the use of a basis for the Fourier transform. We consider single-pole functions as basis functions. In principle, an infinite number of poles and therefore basis functions would be necessary to describe a Green's function in the thermodynamic limit. Finding the correct poles is equivalent to the hard problem of analytic continuation. For our purpose, this is not an issue as we evaluate the equation only in the imaginary plane far away from the poles. The main difficulty of analytic continuation is precisely that there is an infinite number of spectral functions that match the imaginary time/frequency data for a given accuracy. We are only interested in the data on the imaginary axis, therefore the precise pole structure is of little relevance.

We introduce the single-pole basis functions

$$g(z, \epsilon_m) = \frac{1}{z - \epsilon_m}, \quad g(\tau, \epsilon_m) = -[1 - f(\epsilon_m)] e^{-\epsilon_m\tau} \quad \text{for } \tau \in (0, \beta). \quad (\text{A.46})$$

For a given set of poles ϵ_m , the coefficients w_m are fit to the Green's function

$$G(iz_p) \approx \sum_m w_m g(iz_p, \epsilon_m) \quad (\text{A.47})$$

which is a standard linear least-squares problem. Equality constraints can readily be included [115], to fix known high-frequency moments (e.g. $\sum_m \omega_m = 1$) or the occupation, cf. appendix A.1.3. The imaginary time Green's function is reconstructed from the basis functions

$$\mathcal{G}(\tau) \approx \sum_m \omega_m g(\tau, \epsilon_m). \quad (\text{A.48})$$

The inverse transformation is analog, fitting the imaginary time Green's function $\mathcal{G}(\tau)$. The fitting of the weights ω_m is analogous to that of high-frequency moments in appendix A.1.3.

Therefore, we choose the same poles, the Chebyshev points. We fix the number of poles to the number of Padé frequencies. For the transformation $i\omega_n \rightarrow \tau$, this results in an overfitting of factor 2, as we get a separate equation for real and imaginary part. Additionally, we scale the poles by a widening factor $W > 0$, which is left as an optimization parameter. The least-squares problem can be weighted by the inverse variance $1/\sigma$ of the data points, to account for errors in QMC data.

A.2. Fourier integral

We assume $\mathcal{G}(\tau)$ to be sampled at equidistant time points τ_l . We approximate the integral by a weighted sum over these sample points. Writing these sums in the form of a discrete Fourier transform (DFT), the fast Fourier transform (FFT) algorithm can be employed for an efficient evaluation. We define the inverse discrete Fourier transform (iDFT)

$$a_n = \text{iDFT}[A_l] = \frac{1}{N} \sum_{l=0}^{N-1} A_l e^{i2\pi nl/N}. \quad (\text{A.49})$$

Note that we obtain $\mathcal{G}(\tau)$ from a Monte Carlo algorithm, therefore we require algorithms which are stable against noise.

Riemann sum. The standard approach is to approximate the Fourier integral eq. (A.4) by the Riemann sum. To apply it to eq. (A.4), we discretize the interval $[-\beta, \beta]$ into $N + 1$ τ -points, with

$$\tau_l = -\beta + 2\beta l/N, = -\beta + l\Delta\tau \quad l \in \{0, 1, \dots, N\}. \quad (\text{A.50})$$

With this mesh, the Riemann sum for the full Fourier integral eq. (A.2) reads

$$\overline{G}^{(n)} = \frac{1}{2} \int_{-\beta}^{\beta} d\tau \mathcal{G}(\tau) e^{i\overline{\omega}_n \tau} \approx \frac{\beta}{N} \sum_{l=0}^{N-1} \mathcal{G}_l e^{i\overline{\omega}_n \tau_l}, \quad (\text{A.51})$$

where \mathcal{G}_l is the sample $\mathcal{G}_l \approx \mathcal{G}(\tau_l)$ and $i\overline{\omega}_n = i\pi n/\beta$. Note that the integral contains a jump of size $\langle\{A, B\}\rangle$ at $\tau = 0$; this jump needs to be removed by hand else the approximation is very crude. With $\tau_l = -\beta + l\Delta\tau$, we can shift the constant $-\beta$ in the prefactor $\exp(-i\overline{\omega}_n \beta) = \pm 1$. The bosonic Matsubara frequencies vanish by symmetry, so we can use the negative sign for the whole expression

$$\overline{G}^{(n)} \approx -\frac{\beta}{N} \sum_{l=0}^{N-1} \mathcal{G}_l \exp(i\overline{\omega}_n \Delta\tau l) = -\beta \frac{1}{N} \sum_{l=0}^{N-1} \mathcal{G}_l e^{i2\pi nl/N} = -\beta \text{iDFT}[\mathcal{G}_l]. \quad (\text{A.52})$$

We have approximately written the Matsubara Green's function in terms of a iDFT. The values at the bosonic Matsubara frequency vanish and can be discarded. Equation (A.52) can be efficiently evaluated using FFT algorithms; algorithms exploiting the Hermitian symmetry $G^{(-n)} = [G^{(n)}]^*$ of local Green's functions are available.

The accuracy of the Riemann sum eq. (A.52) is determined by the discretization $\Delta\tau$. The method is stable against the noise of quantum Monte Carlo. However, the error grows with frequency as seen in fig. A.5. Increasing the number of mesh points, accuracy

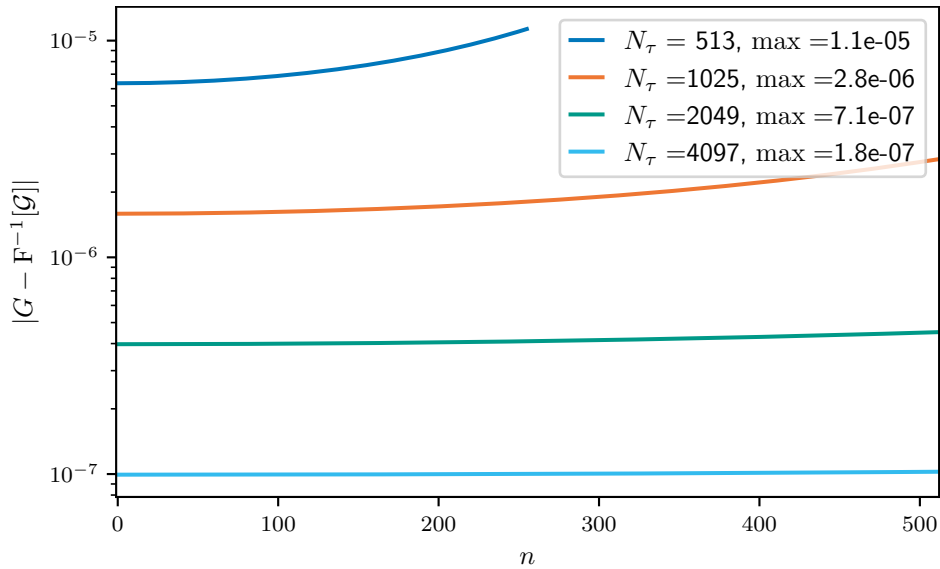


Figure A.5.: Accuracy of Riemann sum to approximate the Fourier integral. The inverse temperature is $\beta = 10$, the interval $[0, \beta]$ is discretized using N_{τ} τ -points; the Green's function is given by fig. A.1. The legend provides the maximum error, which is not shown as the plot is truncated for large Matsubara frequencies.

improves and the increase in error shifts to higher frequencies.² Accurate Matsubara sums, however, need large numbers of Matsubara frequencies and therefore large frequencies. This problem can be amended employing Filon integration [218–220], which is a technique to integrate fast oscillating integrals.

Filon integration. We can employ standard techniques for oscillating integrals to improve accuracy for large frequencies. Filon methods are a particular simple approach, which come with little additional cost. Considering the continuous integral eq. (A.2), we observe that for large frequencies $|i\bar{\omega}_n| \gg \Delta\tau$, the phase $\exp(i\bar{\omega}_n\tau)$ oscillates rapidly in τ , even on the scale of a discretization $\Delta\tau$; the Green's function $\mathcal{G}(\tau)$ on the other hand varies only slowly. At the Nyquist frequency $i\bar{\omega}_{N/2} = i\pi/2\Delta\tau$, the phase function performs a quarter oscillation $\exp(i\bar{\omega}_{N/2}\Delta\tau) = i$ for every discretization step. Filon methods account for the oscillating function by only approximating $\mathcal{G}(\tau)$ and integrating the phase $\exp(i\bar{\omega}_n\tau)$ analytically. Thus, the Filon method takes more information into account than the Riemann sum, which uses the known phase only at the sample points τ_l .

We split the integral at the sample points τ_l into intervals of the length $\Delta\tau$

$$G^{(\bar{n})} = \frac{1}{2} \sum_{l=0}^{N-1} \int_{\tau_l}^{\tau_{l+1}} d\tau \mathcal{G}(\tau) e^{i\bar{\omega}_n\tau} =: \frac{1}{2} \sum_{l=0}^{N-1} I_l. \quad (\text{A.53})$$

As mentioned before, in the limit of high frequencies, the phase factor oscillates rapidly on the interval $[\tau_l, \tau_{l+1}]$, while $\mathcal{G}(\tau)$ changes little for a sufficiently dense τ -mesh. Thus, we approximate $\mathcal{G}|_{[\tau_l, \tau_{l+1}]}(\tau)$ by a simple function and evaluate the integral analytically.

²For setups symmetric with respect to the Fermi level, the Riemann sum is extremely accurate. In this scenario it is the method of choice; in practice, however, this is a rather rare situation.

We choose a linear interpolation for the Green's function:

$$\mathcal{G}\Big|_{[\tau_l, \tau_{l+1}]}(\tau) \approx \frac{\tau_{l+1} - \tau}{\tau_{l+1} - \tau_l} \mathcal{G}(\tau_l) + \frac{\tau - \tau_l}{\tau_{l+1} - \tau_l} \mathcal{G}(\tau_{l+1}). \quad (\text{A.54})$$

Higher order interpolations are not suitable for noisy Monte Carlo data, as they tend to enhance the noise. Within this approximation, the integrals can be evaluated explicitly

$$\begin{aligned} I_l &\approx \int_{\tau_l}^{\tau_{l+1}} d\tau \mathcal{G}\Big|_{[\tau_l, \tau_{l+1}]}(\tau) e^{i\bar{\omega}_n \tau} \\ &= w_n \mathcal{G}_l \Delta\tau e^{i\bar{\omega}_n \tau_l} + \frac{\exp(i\bar{\omega}_n \Delta\tau) - w_n}{\Delta\tau i\bar{\omega}_n} \Delta\mathcal{G}_l \Delta\tau e^{i\bar{\omega}_n \tau_l}, \end{aligned} \quad (\text{A.55})$$

with the weights $w_n = [\exp(i\bar{\omega}_n \Delta\tau) - 1]/i\bar{\omega}_n \Delta\tau$ and the difference $\Delta\mathcal{G}_l = \mathcal{G}_{l+1} - \mathcal{G}_l$. The sum eq. (A.53) over these approximations (A.55) for the integrals yields the approximation

$$G^{(\bar{n})} \approx -\beta \left(w_n \text{iDFT}[\mathcal{G}_l] - \frac{\exp(i\bar{\omega}_n \Delta\tau) - w_n}{\Delta\tau i\bar{\omega}_n} \text{iDFT}[\Delta\mathcal{G}_l] \right). \quad (\text{A.56})$$

Again, we can employ the inverse FFT algorithm for an efficient evaluation. The Filon method is therefore of the same complexity as the Riemann sum, the computation is only slightly more involved, as we have to perform two separate iDFTs and calculate two weight factors. In the static limit $i\omega_n \rightarrow 0$, the weights are all one $\lim_{i\omega_n \rightarrow 0} w_n = 1$, and we recover the Riemann sum eq. (A.52).

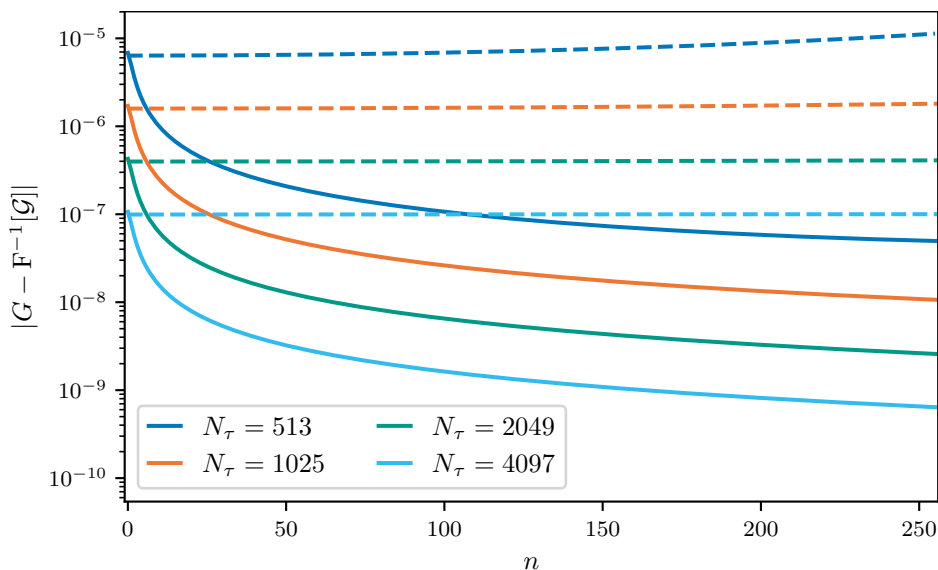


Figure A.6.: Accuracy of Filon method (solid line) compared to Riemann sum (dashed line) to approximate the Fourier integral. The inverse temperature is $\beta = 10$, the interval $[0, \beta]$ is discretized using N_τ τ -points; the Green's function is given by fig. A.1.

Figure A.6 compares the accuracy of the Filon method with the Riemann sum. For the first few Matsubara frequencies, the accuracy of the two methods is comparable. For larger Matsubara frequencies, however, the Filon method is orders of magnitudes

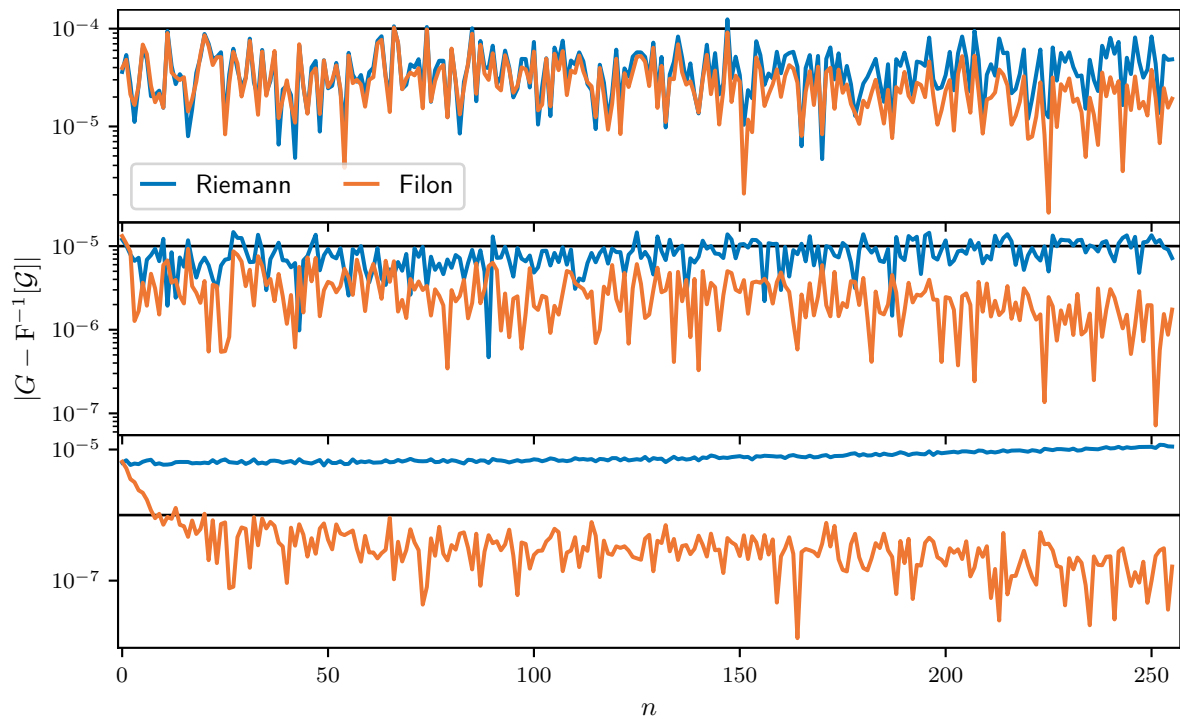


Figure A.7.: Accuracy of Filon method (orange) compared to Riemann sum (blue) to approximate the Fourier integral in the presence of Gaussian noise. The black line indicates the variance of the noise. The inverse temperature is $\beta = 10$, the interval $[0, \beta]$ is discretized using 513 τ -points; the Green's function is given by fig. A.1.

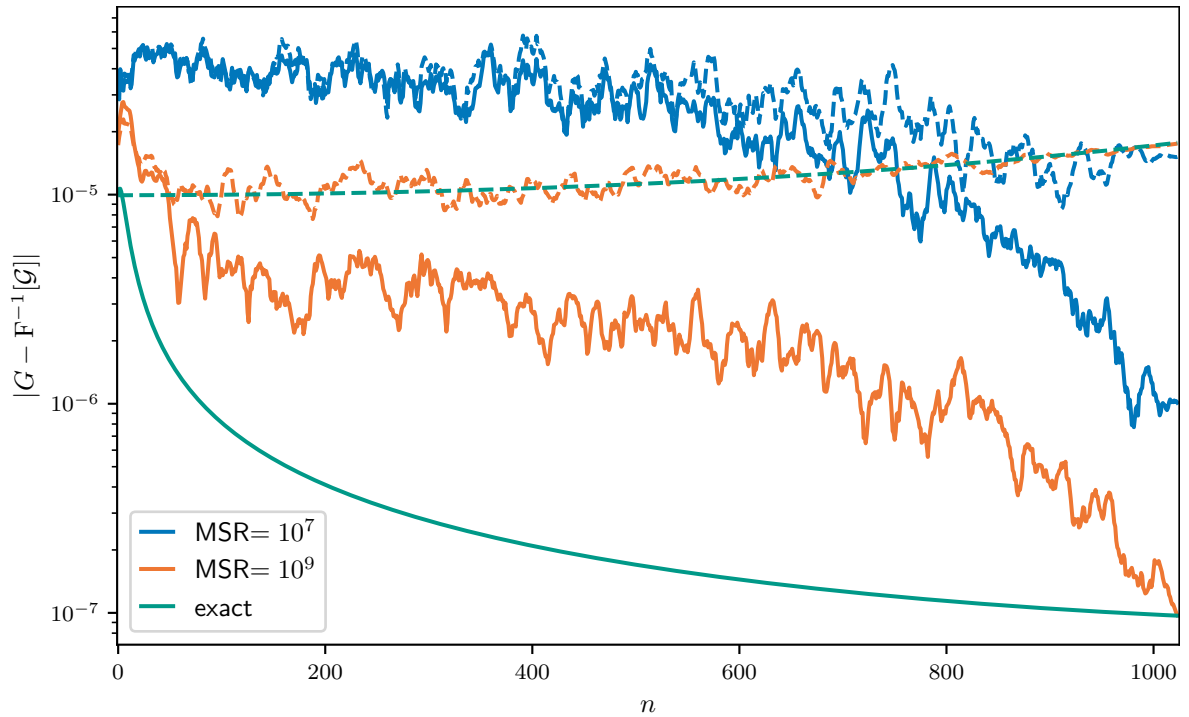


Figure A.8.: Accuracy of Filon method compared to Riemann sum (dashed) to approximate the Fourier integral for noisy QMC data, the rolling average over 10 frequencies is plotted to increase readability. The QMC data is produced using 64 bins, the blue line corresponds to 10^7 measurements, the orange to 10^9 measurements, and the green is calculated from exact data as comparison. The inverse temperature is $\beta = 50$, the interval $[0, \beta]$ is discretized using 2049 τ -points; the Green's function is given by fig. A.1.

more accurate. Thus, this is the preferred method to obtain accurate high-frequency data. This is also true for noisy data as shown by fig. A.7 for normal noise. If the noise is larger than the accuracy of the approximation of the Fourier integral (first row), it dominates the overall error and there is little difference between the methods. If the noise is of the same magnitude or smaller than the accuracy of the approximation, the Filon method is significantly more accurate for large frequencies. Figure A.8 shows real QMC data: We calculate the non-interacting ($U = 0$) Green's function $\mathcal{G}(\tau_l)$ for eq. (A.7) using the CT-HYB code. This provides realistic test data that can be compared to the exact solution. Qualitatively the results are the same as in fig. A.7. For large frequencies the Filon method significantly improves the accuracy of the Fourier integral. We conclude, that Filon method should in general be preferred over a Riemann sum.

B. Laplace transform

We consider the retarded-/advanced-time Green's function $\mathcal{G}^{r/a}(t)$ obtained from real-time evolution. The Laplace transform yields the retarded/advanced Green's function $G^{r/a}(z)$ in frequency domain:

$$G^{r/a}(z) = \int_{-\infty}^{\infty} dt \mathcal{G}^{r/a}(t) e^{izt/\hbar} \quad \text{with} \quad \begin{cases} \Im z > 0 & \text{for } G^r, \\ \Im z < 0 & \text{for } G^a. \end{cases} \quad (\text{B.1})$$

This equation defines the retarded/advanced Green's function in the upper/lower complex half-plane. We write the complex frequencies as $z = \omega + i\eta$, where ω denotes real frequencies and η the shift into the imaginary plane. The retarded/advanced Green's function on the real-axis is defined by the limit

$$G^{r/a}(\omega) := \lim_{\eta \searrow 0} G^{r/a}(\omega \pm i\eta). \quad (\text{B.2})$$

This appendix discusses only the retarded Green's function, the advanced Green's function can be treated analogous. We set $\hbar = 1$ as usual, such that frequencies are given in units of energy and times in units of inverse energy.

B.1. Test cases: analytic examples

Before discussing the numerical treatment of the Laplace transform eq. (B.1), we provide examples with known analytic expressions. These examples allow to validate the accuracy of numerical approximations. A main interest is the evaluation of spectral functions, which requires knowledge of the Green's function on the real-axis. Therefore, the pole structure of the examples is relevant. We consider the three examples, simple poles, a square-root branch cut, and a logarithmic branch cut with a finite jump of the spectral function.

For the simple poles, we consider a Green's function given by 10 poles with random position ϵ_m and residue r_m :

$$\mathcal{G}^r(t) = -i\Theta(t) \sum_{m=1}^{10} r_m e^{-i\epsilon_m t}, \quad (\text{B.3a})$$

$$G(z) = \sum_{m=1}^{10} \frac{r_m}{z - \epsilon_m}. \quad (\text{B.3b})$$

For the branch cut, we consider the Bethe lattice with infinite coordination, with the known analytic expression for the retarded-time Green's function

$$\mathcal{G}^r(t) = -i\Theta(t) \frac{2J_1(Dt)}{Dt} e^{i\mu t}, \quad (\text{B.4a})$$

$$G(z - \mu) = \frac{2z}{D^2} \left(1 - \sqrt{1 - z^2/D^2} \right), \quad (\text{B.4b})$$

where D is the half-bandwidth, μ the chemical potential which determines the center of the spectral function, and $J_1(t)$ is the Bessel function of first kind. We fix the energy scale as $D \equiv 1$, and consider the asymmetric spectrum centered around $\omega = 0.2 = -\mu$.

For the logarithmic branch cut, we consider the Green's function corresponding to a box-shaped DOS:

$$\mathcal{G}^r(t) = -i\Theta(t)\frac{\sin(Dt)}{Dt}e^{i\mu t}, \quad (\text{B.5a})$$

$$G(z - \mu) = \frac{1}{2D} \ln\left(\frac{z/D + 1}{z/D - 1}\right). \quad (\text{B.5b})$$

The numerical treatment of the Laplace transform is particularly hard for this example, as it contains a finite jump at the band-edge $\omega - \mu = \pm D$.

Note, that the Green's function for a finite number of simple poles oscillates without decaying till infinite times, while the Green's function for the two continuous DOSs decays like $1/t$ (or faster) in time. Therefore, in the case of simple poles larger times are relevant for the Laplace transform of the Green's function than in the case of continuous DOSs.

B.2. Discretization

The time-evolution algorithms we employ are based on an equidistant time discretization, thus we approximate the Laplace integral by the discrete Riemann sum

$$G^r(z) = \int_0^\infty dt \mathcal{G}^r(t) e^{izt} \approx \sum_{l=0}^{\infty} \Delta t \mathcal{G}^r(t_l) e^{izt_l}, \quad (\text{B.6})$$

with $t_l = l\Delta t$. This discretization in time of the Laplace transform yields a function which is periodic in real frequencies. The approximate Green's function fulfills the periodicity condition $G^r(\omega + 2\pi/\Delta t + i\eta) = G^r(\omega + i\eta)$. Therefore, such a discretized Laplace transform only approximates the Green's function on an interval $\omega \in [-\pi/\Delta t, +\pi/\Delta t]$, and the approximation is expected to be of poor quality around the boundaries due to the artificial periodicity.

Figure B.1 shows the effect of discretization for the Bethe Green's function eq. (B.4). We approximate eq. (B.6) by 10^4 time points using a trapezoidal rule, and evaluate the transform for a large shift, $\eta = 10^{-2}$, into the imaginary plane to focus on the discretization error. The blue line shows a reasonable discretization of $\Delta t = 0.1$, the relative error is below 10^{-3} . Visually, it is indistinguishable from the exact solution (black). Increasing the discretization by a factor of 20 (orange) to $\Delta t = 2$ hardly affects the imaginary part, the real part on the other hand deviates strongly; the error increases to the order 0.1 to 1. The imaginary part is hardly affected by the discretization $\Delta t = 2$, as it is contained in the interval $[-0.8, 1.2] \subset [-\pi/\Delta t, +\pi/\Delta t]$ (up to small tails due to the imaginary shift η). The real part, on the other hand, is long-ranged, thus it is affected by the periodicity due to the discretization. Increasing Δt further by a factor of two (green), the imaginary part exceeds the periodicity interval, and side lobes start to appear.

The discretized Laplace transform is closely related to the Z -transform in signal processing. We introduce the new variable

$$y(z) = \exp(iz\Delta t). \quad (\text{B.7})$$

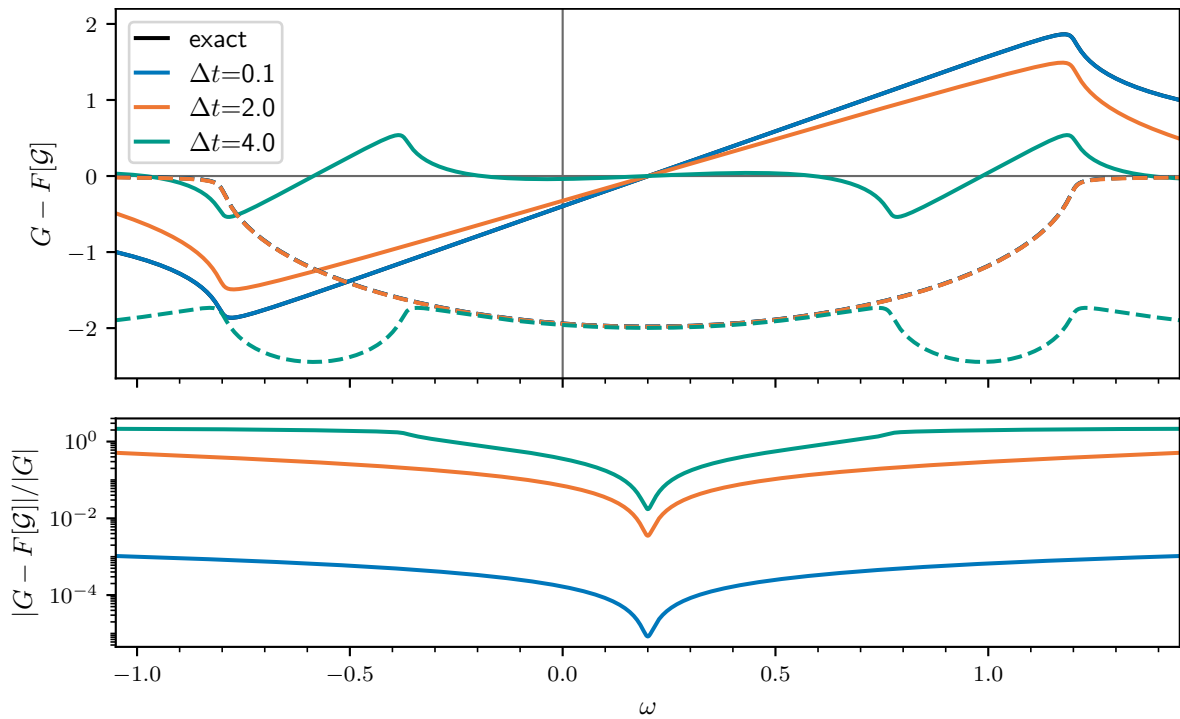


Figure B.1.: Discretized Laplace transform eq. (B.6) for a Bethe Green's function eq. (B.4) centered at $-\mu = 0.2$. The solid lines show the imaginary part, the dashed lines the real part. The Trapezoid rule is used with 10^4 time points, the shift is $\eta = 10^{-2}$.

The discretized Laplace transform eq. (B.6) reads

$$G^r(y(z)) \approx \sum_{l=0}^{\infty} \Delta t G^r(l\Delta t) y^l. \quad (\text{B.8})$$

Its structure is analogous to a (unilateral¹) Z -transform, which is typically written in terms of a variable z replacing y^{-1} . The change of variable $y(z)$ maps contours parallel to the real axis $z = \omega + i\eta$ onto circles in the complex plane:

$$y : \left[-\frac{\pi}{\Delta t}, \frac{\pi}{\Delta t} \right] \rightarrow \left[-1, 1 \right] \quad (\text{B.9})$$

The radius of the circles is given by $\exp(-\eta\Delta t)$, for large shifts $\eta \rightarrow \infty$ the circles shrink to a single point at the origin $y = 0$. This mapping encodes the periodicity in real frequencies ω , caused by the discretization of the Laplace transform: $y(z + 2\pi/\Delta t) = y(z)$. Thus, the band $-\pi/\Delta t < \Re z < +\pi/\Delta t$ of the upper complex half-plane is mapped to the unit ball in the y -plane. Both, the Padé-Fourier algorithm appendix B.5, and the linear prediction appendix B.6 employ this structure.

¹That is, the sum contains only the non-negative values of l .

In practice, the discretization error poses no problem because typical values of Δt are sufficiently small. Keep in mind, that the discretization tends to affect the real part stronger than the imaginary part as seen in fig. B.1. Instead of the Riemann sum in eq. (B.6), more accurate quadrature schemes for the sampling points t_l should be chosen. The corresponding weights are assumed to be included in $\mathcal{G}^r(t_l)$ to keep the notation simple. The examples we present only consider the trapezoidal rule; that is the first, $l = 0$, and last, $l = \infty$, point are weighted by 1/2. Other quadrature schemes like the Simpson rule can readily be chosen, to reduce the discretization error.

Throughout the rest of this appendix, we will use the discretization $\Delta t = 0.1$ using a trapezoidal rule. Thus, fig. B.1 is the reference for the discretization error (blue). Errors of the same magnitude can be attributed to the discretization.

B.3. Truncation

More crucial than the discretization eq. (B.6), is the fact, that we can only evolve up to a maximal time t_L :

$$G^r(z) \approx \sum_{l=0}^L \Delta t_l \mathcal{G}^r(t_l) e^{izt_l}; \quad (\text{B.10})$$

we have to truncate the series after the time point $t_L < \infty$. This corresponds to the approximation $\mathcal{G}^r(t_{l>L}) \stackrel{!}{=} 0$ and causes oscillation similar to the Gibbs phenomenon. Evidently, the truncated sum does not capture the high frequency behavior, as the limit reads

$$\lim_{z \rightarrow i\infty} \sum_{l=0}^L \Delta t_l \mathcal{G}^r(t_l) e^{izt_l} = \Delta t_0 \mathcal{G}^r(0) \neq 0, \quad (\text{B.11})$$

but we are mainly interested in the opposite limit $\Im z \searrow 0$.

Let's investigate the truncation error of the Laplace transform for the example of a single-pole Green's function

$$\mathcal{G}^r(t) = -i\Theta(t)e^{-i\epsilon t}, \quad G(z) = \frac{1}{z - \epsilon}. \quad (\text{B.12})$$

Truncating the Laplace integral eq. (B.1) at a finite time t_L , yields the approximation

$$G^{\text{approx}}(z) = \int_0^{t_L} dt \mathcal{G}^r(t) e^{izt} = G(z) - \frac{e^{i(z-\epsilon)t_L}}{z - \epsilon} = G(z)[1 - e^{i(z-\epsilon)t_L}]. \quad (\text{B.13})$$

The magnitude of the error is determined by the product of the shift η and the maximal time t_L , and error oscillates with real frequencies ω :

$$\frac{G(z) - G^{\text{approx}}(z)}{G(z)} = e^{i(\omega-\epsilon)t_L} e^{-\eta t_L}. \quad (\text{B.14})$$

If the error is large, the oscillations are problematic as the imaginary part of eq. (B.13) can change its sign:

$$\Im G^{\text{approx}}(z) = \Im G(z) [1 - \cos([\omega - \epsilon]t_L) e^{-\eta t_L}] - \Re G(z) \sin([\omega - \epsilon]t_L) e^{-\eta t_L}. \quad (\text{B.15})$$

This is especially relevant where the spectral weight is small, e.g., around band-edges. To keep the truncation error small, a contour $z = \omega + i\eta$ with a sufficiently large shift η into the upper complex half-plane is necessary.

For large shifts η the error of truncating $\mathcal{G}^r(t)$ is exponentially suppressed by the factor $\exp(-\eta t)$ for large times. However, to obtain spectra, we need to evaluate the retarded Green's function $G^r(z)$ at the real axis $A(\omega) = -\frac{1}{\pi}\Im G(\omega + i0^+)$. Therefore, we analyze the difference between the Green's function $G(\omega + i0^+)$ we are interested in and the Green's function $G(\omega + i\eta)$ on the shifted contour. A finite shift η into the complex plane acts as a broadening of the Green's function $G(z)$; this can be shown using the convolution theorem. We define the auxiliary function

$$h_\eta(t) = \exp(-\eta|t|); \quad (\text{B.16})$$

the absolute $|t|$ is necessary for the existence of the Fourier transform $\text{F}[h_\eta](\omega)$. In terms of this helper function, we can interpret the Laplace transform eq. (B.1) as the Fourier transform

$$G(\omega + i\eta) = \int_{-\infty}^{\infty} dt \mathcal{G}^r(t) h_\eta(t) e^{i\omega t} =: \text{F}[\mathcal{G}^r \cdot h_\eta](\omega), \quad (\text{B.17})$$

where we omit the infinitesimal shift $i0^+$ to shorten the notation. Applying the convolution theorem, we can write the Green's function

$$\begin{aligned} G(\omega + i\eta) &= (\text{F}[h_\eta] * G)(\omega) = \frac{1}{2\pi} \int_{-\infty}^{\infty} d\omega' \text{F}[h_\eta](\omega - \omega') G(\omega') \\ &= \int_{-\infty}^{\infty} d\omega' \frac{1}{\pi} \frac{\eta}{(\omega - \omega')^2 + \eta^2} G(\omega'), \end{aligned} \quad (\text{B.18})$$

this is the convolution of the Green's function at the real axis $G(\omega + i0^+)$ with the Cauchy distribution (also known as Lorentz distribution).

To summarize, for an accurate evaluation of the Laplace transform a sufficiently large shift η is necessary to keep the truncation error small; on the other hand, the Green's function $G(\omega + i\eta)$ on the shifted contour yields a broadened spectrum compared to $G(\omega + i0^+)$ as it is convoluted with the Cauchy distribution. In the following, we present three algorithms to reduce the truncation error, with the goal to obtain good spectra, that is good approximations for the imaginary part of the Green's function at the real axis $\eta \searrow 0$. The first algorithm is based on a Taylor expansion in a finite shift η giving sharper spectra in spite of η . The second algorithm employs a Padé algorithm, and the third extends the time points by linear prediction; these algorithms reduce the truncation errors allowing for smaller shifts η .

B.4. Expansion to the real axis

We assume, that the truncation error is kept small by using a sufficient large shift η into the upper complex half-plane. To improve the spectra obtained from the Green's functions evaluated at this finite shift η , an expansion in η can be performed as I proposed in [W3]. The retarded Green's function $G^r(\omega + i\eta)$ on the contour parallel to the real axis

shifted by a fixed $\eta > 0$ into the upper complex half-plane corresponds to the Laplace transform:

$$G(\omega + i\eta) = \int_0^\infty dt \mathcal{G}^r(t) e^{i(\omega + i\eta)t} = F[\mathcal{G}^r \cdot h_\eta](\omega) =: F_\eta[\mathcal{G}^r](\omega). \quad (\text{B.19})$$

This Laplace transform can be interpreted as the Fourier transform of the Green's function $\mathcal{G}^r(t)$ damped by the factor $\exp(-\eta t)$; we denote this transformation by F_η . The spectrum is given by the retarded Green's function on the real axis $G(\omega + i0^+)$. Introducing an arbitrary finite parameter η , the Green's function on the real axis can be written in terms of the damped Fourier transform F_η :

$$G(\omega + i0^+) = \lim_{\eta' \searrow 0} F_{\eta'}[\mathcal{G}^r(t)](\omega) = F_\eta[e^{t\eta^-} \mathcal{G}^r(t)](\omega) \quad (\text{B.20})$$

where $\eta^- = \eta - 0^+$. The second equality replaces the limit $\eta' \searrow 0$ by the finite shift η :

$$\lim_{\eta' \searrow 0} e^{-\eta' t} = e^{-\eta t} e^{\eta^- t}. \quad (\text{B.21})$$

Next, we rewrite the exponential function $\exp(\eta^- t)$ as its series representation:

$$G(\omega + i0^+) = F_\eta[e^{t\eta^-} \mathcal{G}^r(t)](\omega) = \sum_k \frac{1}{k!} (\eta^-)^k F_\eta[t^k \mathcal{G}^r(t)](\omega). \quad (\text{B.22})$$

Truncating the sum after a finite order $k = K < \infty$, we can drop the infinitesimal shift in η^- and write η instead. The first term, $k = 0$, corresponds to the Green's function on the shifted contour $G(\omega + i\eta)$, higher order terms give systematic corrections:

$$G(\omega + i0^+) = G(\omega + i\eta) + \eta F_\eta[t \mathcal{G}^r(t)](\omega) + \frac{\eta^2}{2} F_\eta[t^2 \mathcal{G}^r(t)](\omega) + \mathcal{O}(\eta^3). \quad (\text{B.23})$$

For a given contour determined by the shift η , this equation allows to systematically calculate corrections to approach the real axis $z = \omega + i0^+$. We retain the exponential damping factor $\exp(-\eta t)$, in return we have to include the k th power t^k for the k th expansion order. The expansion is systematic in η , for the expansion order K we can estimate the 'error' of our spectra by $\eta^{K+1}/(K+1)!$. We can also calculate the next order $K+1$ and visually inspect the changes, to see if features exist which might be washed out by the shift η . Equation (B.23) can be interpreted as an approximate deconvolution of eq. (B.18). We note, that the factor t^k can be generated by differentiating with respect to the shift η ,

$$\frac{\partial^k}{\partial \eta^k} G(\omega + i\eta) = F_\eta[(-t)^k \mathcal{G}^r(t)], \quad (\text{B.24})$$

thus the expansion is indeed a Taylor expansion in η .

B.4.1. Examples

Figure B.2 compares the truncated Fourier transform eq. (B.10) with the expansion algorithm eq. (B.22) for a Green's function given by 10 poles with random position ϵ_m and residue r_m , eq. (B.3). A maximal time $t_L = 150$ and a shift $\eta = 5 \times 10^{-2}$ are used,

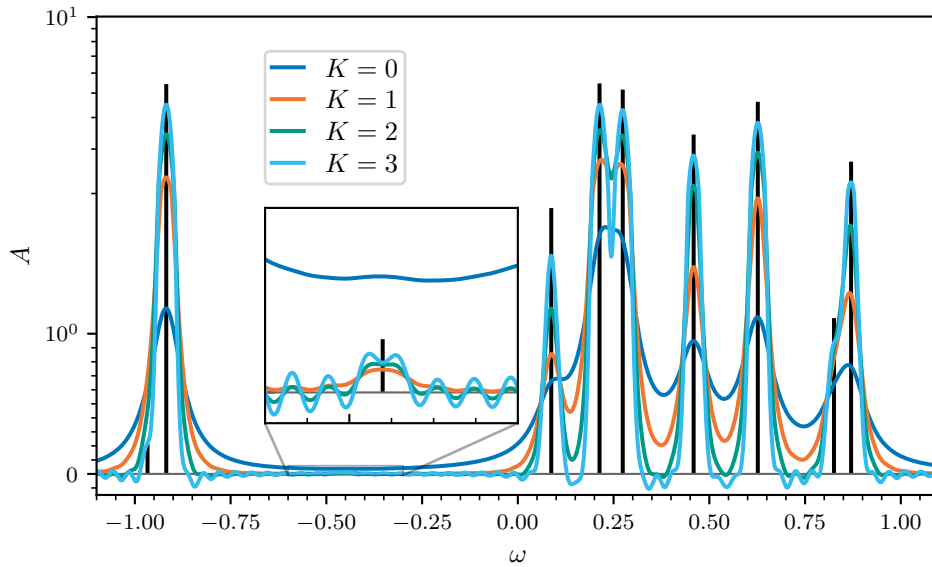


Figure B.2.: Comparison of Laplace transforms for 10 poles eq. (B.3). The vertical black lines indicate the position of the poles ϵ_m , their height equals $30r_m$. Time steps of $\Delta t = 0.1$ are used up to a maximal time of $t_L = 150$, the shift is $\eta = 5 \times 10^{-2}$. The trapezoid rule is used for the finite DFT eq. (B.10) and the expansion algorithm eq. (B.22).

such that $\exp(-\eta t_L) \approx 6 \times 10^{-4}$. The shift is chosen approximately as the smallest shift that produces no unphysical oscillations; the accuracy for the truncated Fourier transform eq. (B.10) is of the order $|G(\omega + i\eta) - \text{F}[\mathcal{G}](\omega + i\eta)| \approx 10^{-3}$. Including corrections in η according to eq. (B.22), the peaks become sharper. From the second order corrections $k = 2$, visible oscillations start to appear especially where the spectral function approaches 0. Increasing the order to $k = 3$, these oscillations increase producing more negative spectral weight. Another problem becomes apparent: We cannot adequately compare the results with an exact solution, which consists of delta-peaks at the real axis. The expansion of the form eq. (B.23) is an approximation to the real axis, but does not correspond to a particular contour $z = \omega + i\eta'$ in the complex plane. Therefore, if we want to evaluate the DMFT self-consistency equation closer to the real axis than the bare contour $z = \omega + i\eta$, the usage of the corrections eq. (B.23) to the Green's function introduce ambiguity. On the other hand, this is not relevant if the expansion is used only as a post-processing step to obtain sharper spectra. Furthermore, there is no clear criteria for choosing the shift η . Larger shifts could be used, allowing higher order corrections before unphysical oscillations are generated.

Figure B.3 compares the algorithms for the Bethe lattice with infinite coordination number eq. (B.4). A maximal time $t_L = 50$ and a shift $\eta = 5 \times 10^{-2}$ are used. The Green's function on this contour is a poor approximation to the spectrum as the shift η is relatively large. The first correction $k = 1$, however, yields already a good approximation of the spectrum away from the band-edge. Higher orders further improve the spectrum, but the corrections are rather minor. At the band-edge, however, the higher order corrections start to overshoot, yielding a negative spectral weight outside the band-edges.

Figure B.4 compares the algorithms for the Green's function corresponding to a box-shaped DOS eq. (B.5). Compared to the Bethe Green's function, a larger maximal time

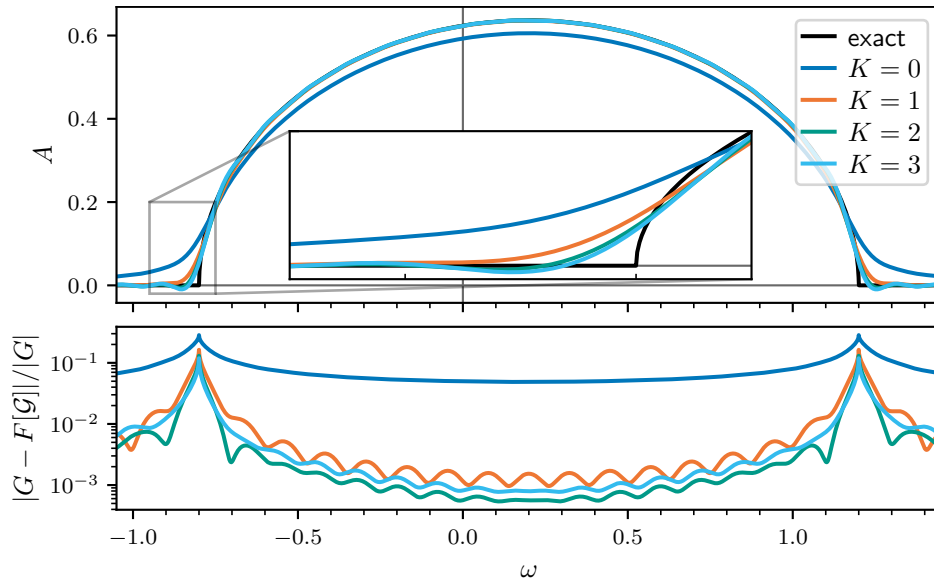


Figure B.3.: Comparison of Laplace transforms for a Bethe Green's function at $-\mu = 0.2$ eq. (B.4). Time steps of $\Delta t = 0.1$ are used up to a maximal time of $t_L = 50$, the shift is $\eta = 5 \times 10^{-2}$. The trapezoid rule is used for the finite DFT eq. (B.10) and the expansion algorithm eq. (B.22).

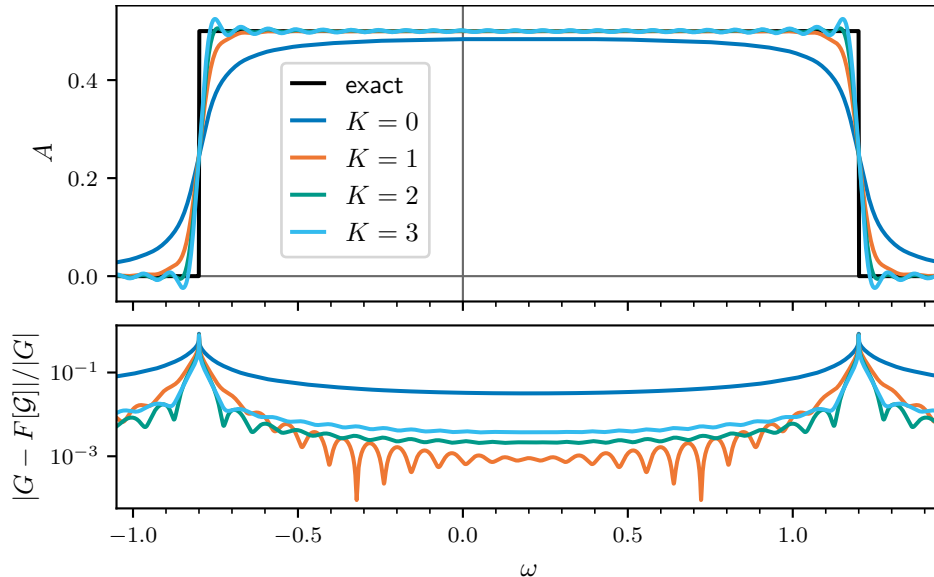


Figure B.4.: Comparison of Laplace transforms for a box-shaped Green's function at $-\mu = 0.2$ eq. (B.5). Time steps of $\Delta t = 0.1$ are used up to a maximal time of $t_L = 75$, the shift is $\eta = 5 \times 10^{-2}$. The trapezoid rule is used for the finite DFT eq. (B.10) and the expansion algorithm eq. (B.22).

$t_L = 75$ is necessary to avoid oscillations for the shift $\eta = 5 \times 10^{-2}$. Apparently the finite jump is much harder to approximate. The expansion yields little improvement for the jump, and higher order corrections $k > 1$ are plagued by overshooting the spectrum. Oscillations are also visible within the spectrum.

B.5. Padé-Fourier approximation

The Padé-Fourier approximation [104, 221] provides a significant improvement for small number of time points. It is essential that the time points are equidistant, to employ eq. (B.8) with $y = \exp(iz\Delta t)$. In terms of $y(z)$, the truncated series eq. (B.10) reads

$$G^r(y(z)) \approx \sum_{l=0}^L \Delta t \mathcal{G}^r(l\Delta t) y^l. \quad (\text{B.25})$$

We recognize this as a truncated Taylor expansion in y . A typical approach to improve Taylor expansions is the Padé algorithm, we search for polynomials $p(y)$ and $q(y)$ of degrees N and M , fulfilling

$$q(y)G^r(y) - p(y) = \mathcal{O}(y^{N+M+1}). \quad (\text{B.26})$$

Substituting the polynomial forms of the functions, yields the linear system of equations

$$\begin{pmatrix} -\mathbf{1} & \mathbf{C}_1 \\ \mathbf{0} & \mathbf{C}_2 \end{pmatrix} \begin{pmatrix} \mathbf{p} \\ \mathbf{q} \end{pmatrix} = \mathbf{0}, \quad (\text{B.27})$$

where \mathbf{p} and \mathbf{q} are the vectors of polynomial coefficients, and \mathbf{C} is the Toeplitz matrix containing the function values $C_{ll'} = \Delta t \mathcal{G}^r([l - l']\Delta t)$, which is partitioned in the two rows $\mathbf{C}^T = (\mathbf{C}_1 \quad \mathbf{C}_2)$. The system is underdetermined, it has $N + M + 1$ rows from eq. (B.26), but $N + M + 2$ coefficients. We first solve the second row, determining \mathbf{q} as the null-vector of the $M \times M + 1$ matrix \mathbf{C}_2 , in a second step we get $\mathbf{p} = \mathbf{C}_1 \mathbf{q}$. This is the Padé-Fourier algorithm: The improved approximation of the retarded Green's function reads

$$G^r(z) \approx \frac{p(e^{iz\Delta t})}{q(e^{iz\Delta t})}. \quad (\text{B.28})$$

The rational polynomial $p(y)/q(y)$ is evidently especially suitable to resolve a finite number of poles, where the number of sampling points should be at least two times the number of poles. Note that the high-frequency limit $z \rightarrow i\infty$ corresponds to the center $y = 0$ of the y -plane, thus

$$\lim_{z \rightarrow i\infty} G^r(z) \approx \lim_{y \rightarrow 0} \frac{p(0)}{q(0)} = \frac{p_0}{q_0} = \Delta t \mathcal{G}^r(0) \quad (\text{B.29})$$

as eq. (B.11) pointed out.

The remaining task is to fix the degrees N and M . For Green's functions, we know the high-frequency asymptote from the equation of motion, e.g., a diagonal one-particle

Green's function is asymptotic $G(z) \sim 1/z$ for $|z| \rightarrow \infty$. For a finite system, the Lehmann representation of the Green's function can be expressed as a rational polynomial in z

$$G(z) \stackrel{!}{=} \frac{\tilde{p}(z)}{\tilde{q}(z)} \quad (\text{B.30})$$

with polynomials $\tilde{p}(z)$ of degree N and $\tilde{q}(z)$ of degree M . To satisfy the asymptote $1/z$, the degrees have to fulfill $M = N + 1$. This means the Green's function has M poles and N zeros on the real axis. Assuming that our discretization Δt spans the relevant region containing these poles and zeros, they are mapped by $y(z)$, eq. (B.7), to the unit-circle. Therefore, the rational approximant $p(y)/q(y)$ should be of the same degree $[N/M]$. In practice, this produces suboptimal results, as the example of a one-pole Green's function will demonstrate in the next paragraph. The approximant improves if an additional zero is included to reduce the discretization error. This zero can be placed at the boundary of the periodicity interval (generated by the discretization), which reduces the error due to the discretization periodicity. This requires to use a higher order quadrature scheme than the Riemann sum, else the additional coefficient q_{N+1} vanishes.

It is instructive to consider the simplest example, the one-pole Green's function

$$G(z) = \frac{1}{z - \epsilon}, \quad \mathcal{G}^r(t) = -i\Theta(t)e^{-i\epsilon t}. \quad (\text{B.31})$$

First, we consider a single time step $L = 1$ of size Δt and calculate the $[0/1]$ approximant. The approximant is determined by the linear system of equations

$$\begin{pmatrix} -1 & \Delta t \mathcal{G}^r(0) & 0 \\ 0 & \Delta t \mathcal{G}^r(\Delta t) & \Delta t \mathcal{G}^r(0) \end{pmatrix} \begin{pmatrix} p_0 \\ q_0 \\ q_1 \end{pmatrix} = \mathbf{0}. \quad (\text{B.32})$$

Fixing the constant term in the denominator $q_0 = 1$, we obtain $q_1 = -\exp(-i\epsilon\Delta t)$ and $p_0 = -i\Delta t$:

$$\mathcal{G}^r(z) \approx \frac{-i\Delta t}{1 - e^{i(z-\epsilon)\Delta t}} = \frac{-i\Delta t}{1 - e^{-i\epsilon\Delta t}y(z)} = [0/1](y(z)). \quad (\text{B.33})$$

The approximant correctly yields a single pole with residue 1 at $z = \epsilon$, and due to periodicity all equivalent points $z = \epsilon + 2\pi n/\Delta t$ which map to the same point on the unit circle in $y(z)$. We can rewrite the rational polynomial as the sum

$$[0/1](z) = \frac{-i\Delta t}{1 - e^{i(z-\epsilon)\Delta t}} = -\frac{i\Delta t}{2} + \sum_{n=-\infty}^{\infty} \frac{1}{z - \epsilon + 2\pi n/\Delta t}. \quad (\text{B.34})$$

Ignoring the small off-set $-i\Delta t/2$, a single time step is enough to exactly reproduce the single-pole Green's function up to the periodicity introduced by the discretization Δt . The off-set is a discretization error, for $\Delta t \rightarrow 0$ we recover the exact result. For large broadening, the spectral weight of the 'mirror' poles at $\epsilon + 2\pi n/\Delta t$ will spill, causing excess spectral weight. In practice, this is no problem as we are interested in results close to the real axis, not for large shifts η . As mentioned in appendix B.2, the long-ranged real part on the other hand is affected by the periodicity.

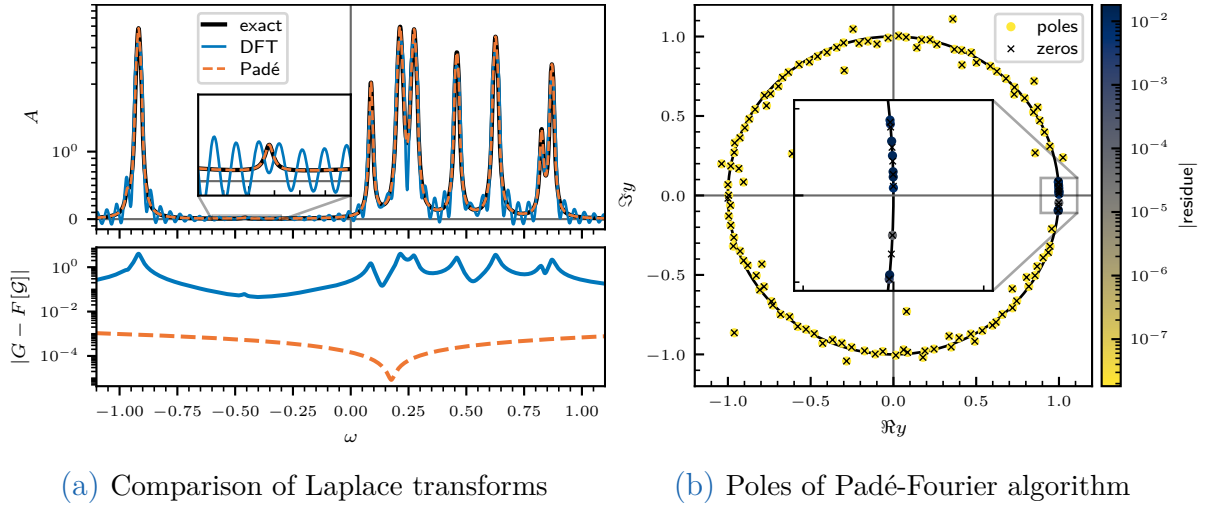


Figure B.5.: Laplace transforms for 10 poles eq. (B.3). Time steps of $\Delta t = 0.1$ are used up to a maximal time of $t_L = 150$, the shift is $\eta = 10^{-2}$. The trapezoid rule is used for the finite DFT eq. (B.10) and the Padé-Fourier algorithm eq. (B.28). For (b) a maximal time of $t_L = 25$ is used which is sufficient for the Padé-Fourier algorithm.

Adding an additional zero, that is increasing the numerator degree by 1, fixes the off-set. We need an additional time point, and employ the trapezoidal rule

$$\begin{pmatrix} -1 & 0 & \frac{\Delta t}{2} \mathcal{G}^r(0) & 0 \\ 0 & -1 & \Delta t \mathcal{G}^r(\Delta t) & \frac{\Delta t}{2} \mathcal{G}^r(0) \\ 0 & 0 & \Delta t \mathcal{G}^r(2\Delta t) & \Delta t \mathcal{G}^r(\Delta t) \end{pmatrix} \begin{pmatrix} p_0 \\ p_1 \\ q_0 \\ q_1 \end{pmatrix} = \mathbf{0}. \quad (\text{B.35})$$

Setting $q_0 = 1$ and solving the equation yields $q_1 = -\exp(-i\epsilon\Delta t)$, $p_0 = -i\Delta t/2$, and $p_1 = -i\Delta t \exp(-i\epsilon\Delta t)/2$:

$$G(z) \approx -i \frac{\Delta t}{2} \frac{1 + e^{i(z-\epsilon)\Delta t}}{1 - e^{i(z-\epsilon)\Delta t}} = [1/1](z) \quad (\text{B.36})$$

This Padé approximant produces the same poles and residues, but without any off-set:

$$[1/1](z) = -i \frac{\Delta t}{2} \frac{1 + e^{i(z-\epsilon)\Delta t}}{1 - e^{i(z-\epsilon)\Delta t}} = \sum_{n=-\infty}^{\infty} \frac{1}{z - \epsilon + 2\pi n/\Delta t}. \quad (\text{B.37})$$

The zero $[1/1](z_0) = 0$ is placed periodically between the poles $z_0 = \epsilon + (2n + 1)\pi/\Delta t$. If we place the periodicity interval around the pole ϵ , i.e. consider $\omega \in \epsilon + [-\pi/\Delta t, +\pi/\Delta t]$, the zero is placed at the interval boundary.

To conclude, the Padé-Fourier algorithm yields the exact result up to the discretization error using only 3 time points. Numerically we found that using a $[M-1/M]$ approximant for the Padé-Fourier algorithm the coefficient q_M is nearly zero. This is further evidence that the $[M/M]$ approximant is indeed the correct choice for the Padé-Fourier algorithm.

Figure B.5(a) compares the truncated Laplace transform eq. (B.10) with the Padé-Fourier algorithm for a Green's function given by 10 poles with random position ϵ_m and residue r_m , eq. (B.3). The maximal time is $t_L = 150$ and the shift in the imaginary plane is $\eta = 10^{-2}$. As expected the truncated sum eq. (B.10) is inaccurate for such a small

shift η . Green's functions given by simple poles, eq. (B.3a), oscillate in time without decaying, thus long times t_L are necessary to resolve them. The truncated Laplace transform eq. (B.10) yields unphysical oscillations, causing negative spectral weight. The Padé-Fourier algorithm, on the other hand, resolves the peaks to the discretization error of order 10^{-3} ; by eye we see no difference to the exact solution. A maximal time of $t_L = 25$ suffices to obtain results of similar accuracy, and much smaller shifts η are accessible. The Padé-Fourier algorithm is expected to excel at resolving small numbers of poles, as this corresponds to the assumed rational approximant. This becomes obvious by investigating the pole structure of the rational polynomial approximation (B.28). Figure B.5(b) shows the poles in the complex y -plane, they are colored according to the absolute of their residuum. Most poles have negligible residues, they cancel with zeros of the numerator. Only the 10 poles on the unit-circle shown in the inset significantly contribute; these poles approximate the true poles of eq. (B.3).

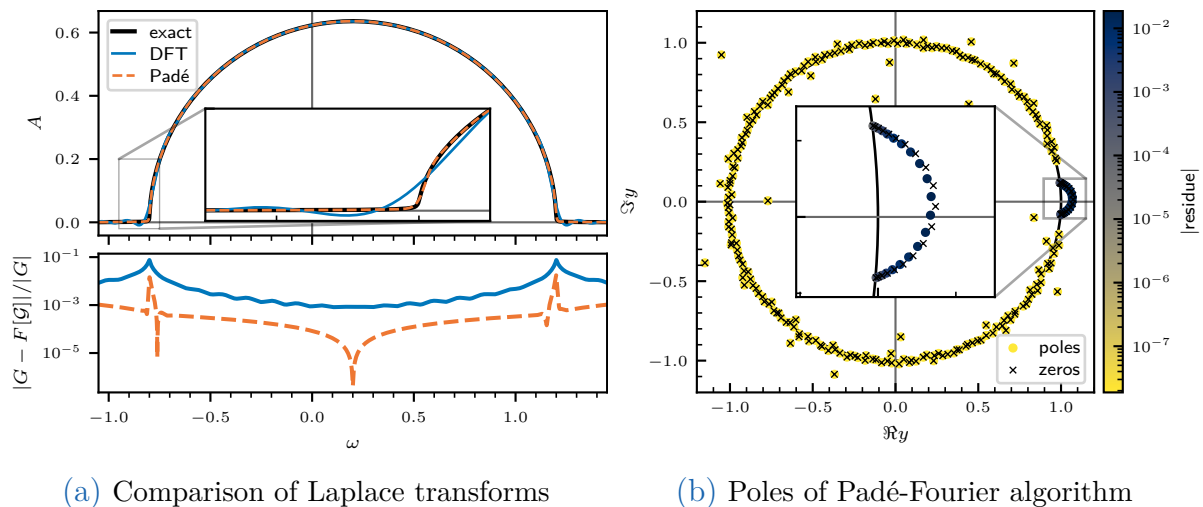


Figure B.6.: Laplace transforms for a Bethe Green's function at $-\mu = 0.2$ eq. (B.4). Time steps of $\Delta t = 0.1$ are used up to a maximal time of $t_L = 50$, the shift is $\eta = 10^{-3}$. The trapezoid rule is used for the finite DFT eq. (B.10) and the Padé-Fourier algorithm eq. (B.28).

For Green's functions in the thermodynamic limit with branch cuts, the quality of the Padé-Fourier algorithm is less obvious, as Padé cannot reproduce branch cuts exactly. We consider the Bethe lattice with infinite coordination eq. (B.4). The retarded-time Green's functions eq. (B.4a) decays in time, thus the error due to truncation is smaller. Figure B.6(a) shows, that the Padé-Fourier algorithm is also in this case superior. A relative small maximal time $t_L = 50$ and shift $\eta = 10^{-3}$ are used, but also for larger parameters, where eq. (B.10) performs better, the Padé-Fourier is more accurate. For the chosen parameters, we see that it is an order of magnitude more accurate. But the algorithm also has problems reproducing the band-edges. This is to be expected, as Padé cannot reproduce the branch cut. However, unlike eq. (B.10) the Padé-Fourier algorithm does not produce unphysical oscillations, the spectral function is non-negative even around the band-edge. Again, we investigate the pole structure in the y -plane shown in fig. B.6(b). As before the majority of poles have negligible weight as they cancel with zeros of the numerator. For the Bethe Green's function, however, the relevant poles shown in the inset lie outside the unit circle. Thus, they do not lie on the real z -axis, but in the lower complex half-plane. This is the correct behavior to approximate the continuous

branch cut. We further note, that the physical poles are well separated from the spurious poles in real energy ω .

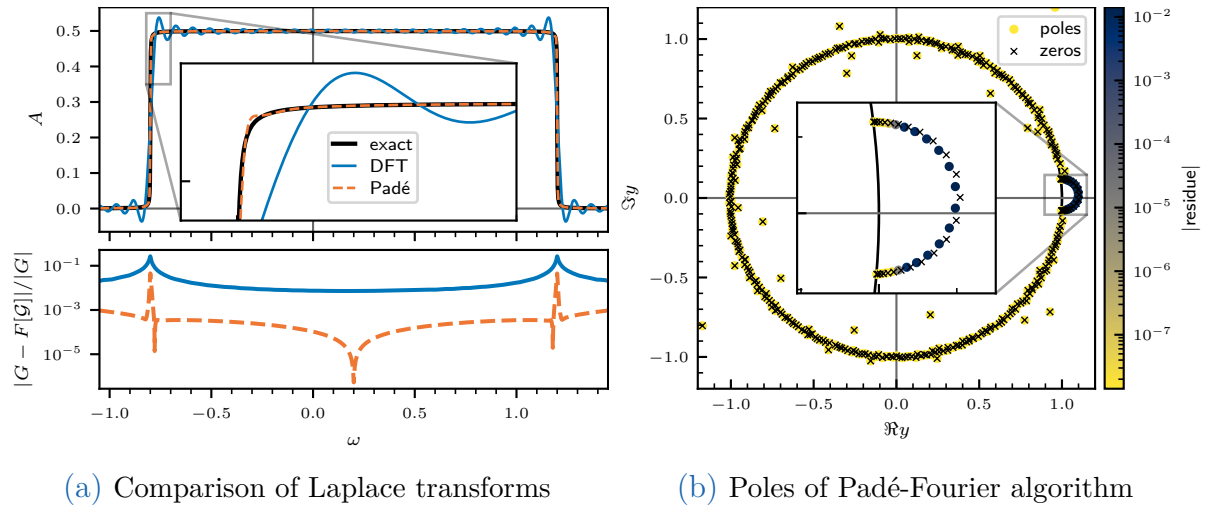


Figure B.7.: Laplace transforms for a box-shaped Green's function at $-\mu = 0.2$ eq. (B.5). Time steps of $\Delta t = 0.1$ are used up to a maximal time of $t_L = 75$, the shift is $\eta = 10^{-3}$. The trapezoid rule is used for the finite DFT eq. (B.10) and the Padé-Fourier algorithm eq. (B.28).

Furthermore, we test the Padé-Fourier algorithm against the Green's function with the box-shaped DOS eq. (B.5). Figure B.7(a) shows, the algorithm can even handle finite jumps reasonable well. The inset shows, however, a small spurious shoulder inside the band near the edge. Reducing the shift η further, this shoulder becomes sharper and turns into a spurious peak. For smaller times t_L the Padé-Fourier algorithm still performs well, however, the spurious peak at the edge becomes even sharper. Like for the Bethe example, the errors appear locally at the band-edge, and the spectral function is non-negative.

The rational polynomial given by the Padé-Fourier algorithm eq. (B.28) is a global approximation in the whole upper complex half-plane. Therefore, it is instructive to investigate the method not only on a contour for a fixed shift η , but in the upper complex half-plane. Figures B.8(a) to B.8(c) show the results for the test cases eqs. (B.3) to (B.5) in the upper complex half-plane, note the symlog scale of the error. The parameters are the same as in figs. B.5(a), B.6(a) and B.7(a). We plot not the absolute error, but the error in the imaginary part, $-\frac{1}{\pi}\Im[F(\mathcal{G}) - G]$, to resolve oscillations. Note, that the discretization error mainly affects the real part, thus errors of the imaginary part can get smaller than the error of 10^{-3} due to discretization. Evaluating eq. (B.10), we observe the existence of a rough threshold for η . For shifts smaller than this threshold, the approximate is unemployable. For shifts around the threshold, reasonable results can be obtained, however unphysical oscillations occur. With increasing shift, the approximation becomes more and more accurate. For the example of poles, fig. B.8(a), the Padé-Fourier algorithm performs well for the full shown range of η . For the Bethe and the box Green's function with continuous DOSs, below a certain threshold η , the inaccuracies around the band-edges appear. In principle the methods is applicable for the full range of η again, the error is localized at the band-edge.

We conclude that Padé-Fourier algorithm using a $[M/M]$ approximant substantially improves the quality of the numerical Laplace transform. It yields accurate results for

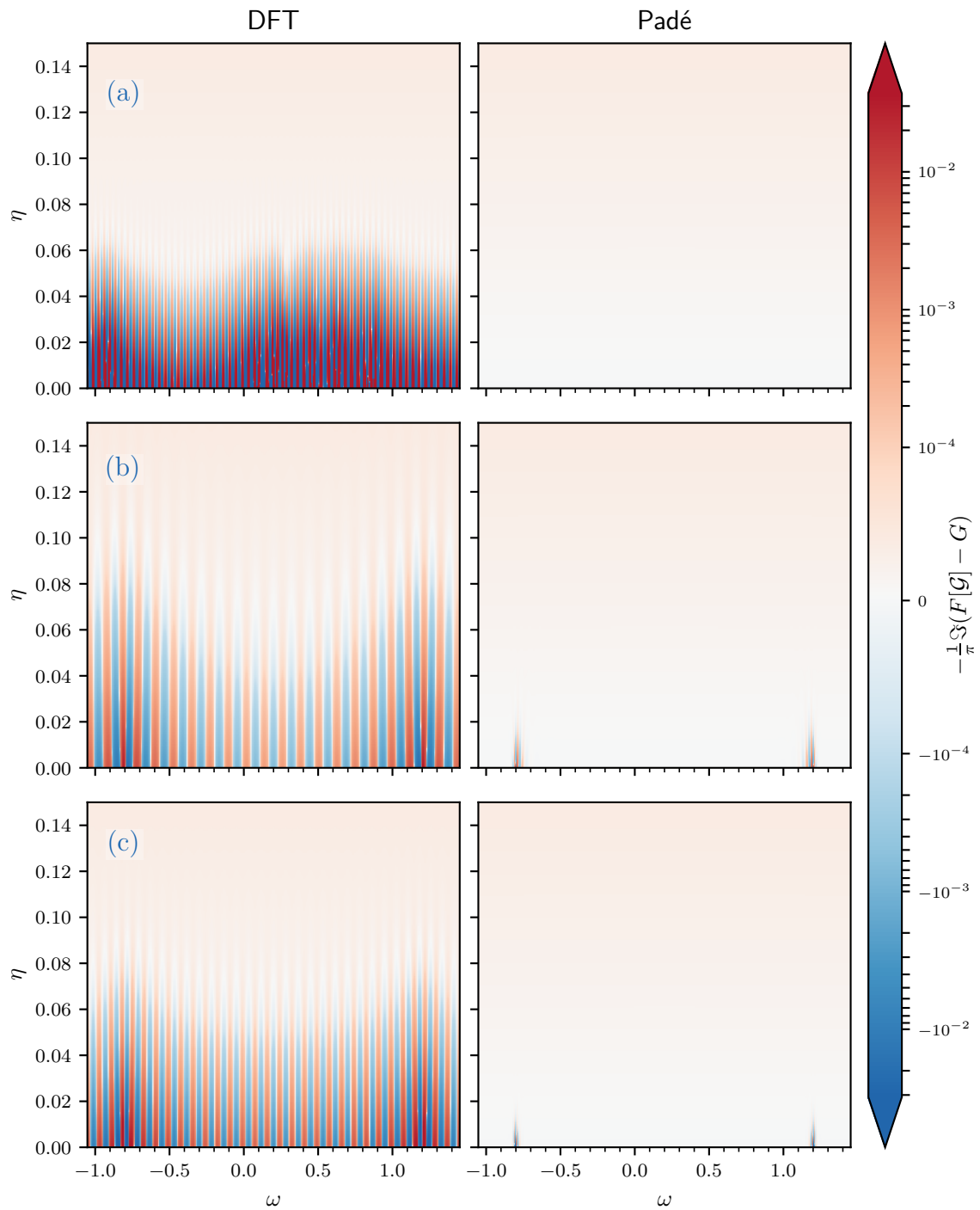


Figure B.8.: Error of Laplace transform in the complex plane $z = \omega + i\eta$. (a) Pole Green's function corresponding to fig. B.5(a). (b) Bethe Green's function corresponding to fig. B.6(a). (c) Box-shaped Green's function corresponding to fig. B.7(a). The same parameters, in particular the different maximal times t_L , are chosen as in the corresponding figs. B.5(a), B.6(a) and B.7(a).

smaller sampling times t_L , and makes the real axis limit $\eta \searrow 0$ accessible. Errors are mostly located at the band-edges and associated with the branch cuts. We found the Padé-Fourier transform to be stable against small normal noise. It might be possible to employ the Padé algorithm to determine the necessary sampling time t_L by investigating the necessary degree M ; criteria to determine the degree M are given, e.g., by Gonnet et al. [222] or Mishonov and Varonov [223].

B.5.1. Quadratic Hermite-Padé approximant

To improve the Padé-Fourier algorithm for branch cuts, Driscoll and Fornberg [221] suggests explicitly including a logarithmic branch cut. In our case, their algorithm seems unpractical as it requires knowledge of the position of the branch cut. Instead, the Padé approximant can be further generalized to the so-called Hermite-Padé approximants [104, 224], which introduces square-root (or higher order root) branch cuts. We generalize eq. (B.26) to the equation

$$\sum_{j=0}^J p_j(y) f^j(y) = \mathcal{O}\left(y^{\sum_j (N_j+1)-1}\right), \quad (\text{B.38})$$

where $p_j(y)$ are polynomials of order N_j and $f^j(y)$ is the j -th power of the function $f(y) = G^r(y)$. We identify the definition eq. (B.26) of the (linear) Padé approximant as a special case of eq. (B.38) with $J = 1$, $N_0 = N$, $N_1 = M$, $p_0(y) = -p(y)$, and $p_1(y) = q(y)$. Theoretical details can be found the book by Baker and Graves-Morris [104], we focus only on the practical application to our problem, following Fasondini et al. [225].

The first order beyond Padé is the quadratic Hermite-Padé approximant $J = 2$:

$$p(y) + q(y)f(y) + r(y)f^2(y) = \mathcal{O}\left(z^{N_p+N_q+N_r+2}\right) \quad (\text{B.39})$$

with polynomials $p(y)$, $q(y)$, $r(y)$ of orders N_p , N_q , N_r . Analogous to the Padé approximant, we find the diagonal Hermite-Padé approximant $N_p = N_q = N_r$ to be suitable, which we validate numerically by inspecting the coefficients p_{N_p} , q_{N_q} , and r_{N_r} . The linear system of equations can be solved just like Padé using standard methods to obtain the polynomials. Substituting the polynomial forms of the functions yields the linear system of equations

$$\begin{pmatrix} \mathbf{1} & \mathbf{C}_{[:N_p+1, :N_q+1]} & (\mathbf{C}^2)_{[:N_p+1, :N_r+1]} \\ \mathbf{0} & \mathbf{C}_{[N_p+1:, :N_q+1]} & (\mathbf{C}^2)_{[N_p+1:, :N_r+1]} \end{pmatrix} \begin{pmatrix} \mathbf{p} \\ \mathbf{q} \\ \mathbf{r} \end{pmatrix} = \mathbf{0} \quad (\text{B.40})$$

where \mathbf{C} is the Toeplitz matrix $C_{ll'} = \Delta t \mathcal{G}^r([l - l'] \Delta t)$. Solving the quadratic eq. (B.39) for $f(y)$ yields the quadratic Hermite-Padé approximant F_2 which has two branches

$$F_2^\pm(y) = \frac{-q(y) \pm \sqrt{q^2(y) - 4p(y)r(y)}}{2r(y)}. \quad (\text{B.41})$$

Compared to the Padé approximant, the quadratic Hermite-Padé approximant can represent not only simple poles but square-root branch cuts. Thus, the Bethe Green's function eq. (B.4) can be accurately represented. Additional structure, like finite jumps,

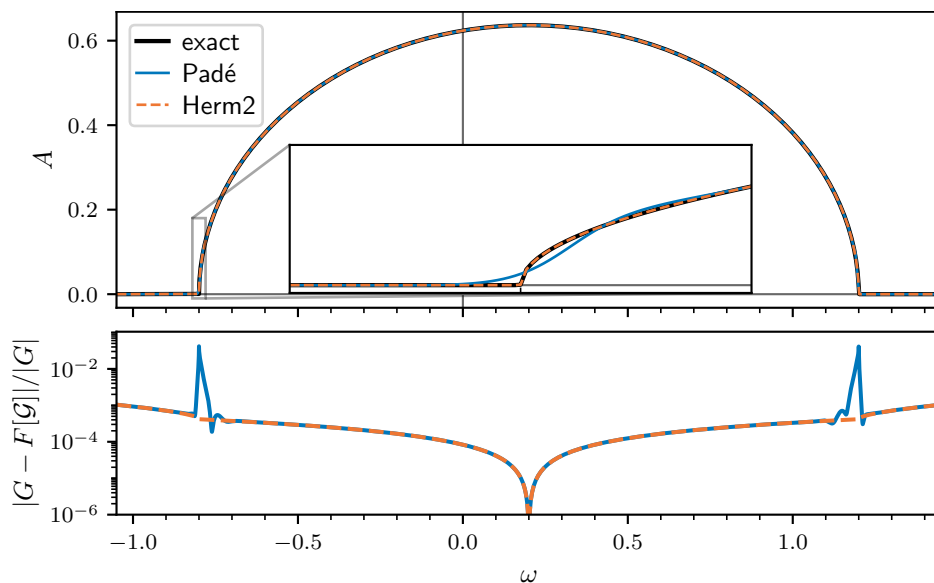


Figure B.9.: Comparison of Laplace transforms for a Bethe Green's function at $-\mu = 0.2$ eq. (B.4). Time steps of $\Delta t = 0.1$ are used up to a maximal time of $t_L = 50$, the shift is $\eta = 10^{-6}$. The trapezoid rule is used for Padé-Fourier algorithm eq. (B.28) and the Hermite-Padé algorithm.

can be generated by switching between the two branches $F_2^+(y)$ and $F_2^-(y)$. This poses, however, an additional difficulty compared to Padé: The appropriate branch of $F_2^\pm(y)$ has to be determined (locally for every y). In some case, this might be done according to the properties of the function $F_2(y) \stackrel{!}{=} G^r(y)$; the imaginary part has to be negative. If one branch corresponds to the advanced and the other to the retarded Green's function, the correct branch can be picked. In practice, we assume that the linear Padé approximant $[M/M](y)$ is a reasonable approximation, and accordingly choose the branch F_2^\pm that differs less from it [225], that is

$$F_2(y) = \begin{cases} F_2^+(y) & \text{if } |F_2^+(y) - [M/M](y)| \leq |F_2^-(y) - [M/M](y)|, \\ F_2^-(y) & \text{if } |F_2^-(y) - [M/M](y)| < |F_2^+(y) - [M/M](y)|. \end{cases} \quad (\text{B.42})$$

Test cases. We revisit the test cases we studied using the Padé-Fourier transform. The pole Green's function eq. (B.3) is already correctly treated by the Padé-Fourier transform, the Hermite-Padé algorithm also yields accurate results. As expected, for the Bethe Green's function eq. (B.4), the Hermite-Padé removes the errors at the band-edge. Only the discretization error remains, which mainly affects the real part. This is shown by fig. B.9. For the Padé-Fourier algorithms, we can use a tiny shift of $\eta = 10^{-6}$, evaluating the Green's function almost at the real axis.

For the box-shaped DOS eq. (B.5) shown in fig. B.10, the improvement of the Hermite-Padé algorithm is less significant. While the error is located in a smaller region around the jump, and the frequency-integrated error is accordingly smaller, the Hermite-Padé algorithm suffers the same deficiencies as the Padé algorithm. A spurious peak is present at the band-edge, and we get negative spectral weight. For larger shifts, e.g., $\eta = 10^{-3}$, Hermite-Padé correctly reproduces the spectrum, while for Padé a spurious shoulder

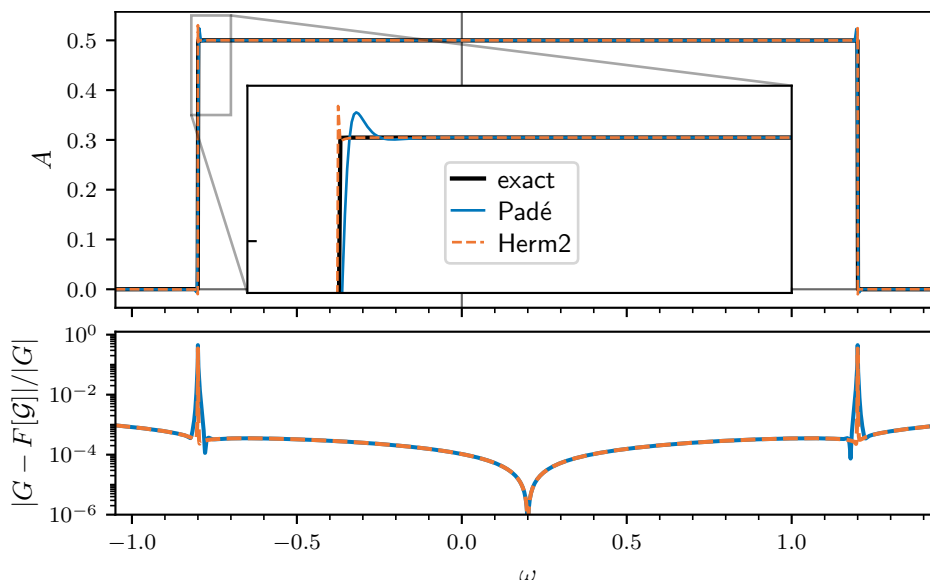


Figure B.10.: Comparison of Laplace transforms for a box-shaped Green's function at $-\mu = 0.2$ eq. (B.5). Time steps of $\Delta t = 0.1$ are used up to a maximal time of $t_L = 75$, the shift is $\eta = 10^{-3}$. The trapezoid rule is used for the Padé-Fourier algorithm eq. (B.28) and the Hermite-Padé algorithm.

remains and the band edge is not represented correctly.

B.6. Linear prediction

Linear prediction (LP) can be used to predict values at later or previous time points (forward and backward prediction), interpolate missing data, or compress signals. It is a widely used technique, e.g., for nuclear magnetic resonance signals or speech processing [226]. In the context of the Laplace transform, we focus only on the forward prediction, to extend eq. (B.10) beyond the maximum sampled time $\mathcal{G}^r(t_L)$. The LP predicts the next time point of a signal \hat{x}_l as *linear* combination of the past K time points x_l :

$$\hat{x}_l = - \sum_{k=1}^K a_{K,k} x_{l-k}, \quad (\text{B.43})$$

where K is the prediction order, and $a_{K,k}$ are the prediction coefficients. We drop the subscript K for the coefficients, which indicates that they depend on the prediction order. LP is routinely used to obtain accurate spectra from time evolution, e.g. [119, 227]. The review on tensor-network time-evolution methods [20] lists it as an ‘additional trick’. An accessible introduction to LP is given, e.g., by Vaidyanathan [228], or the detailed review by Makhoul [229].

B.6.1. Validity for Green's functions

The retarded Green's function can also be written in the form of a linear prediction (also known as autoregressive processes), as shown by Koehl [226]. We consider a Green's

function given by K simple poles ϵ_m with residue r_m

$$G(z) = \sum_{m=1}^K \frac{r_m}{z - \epsilon_m}, \quad \mathcal{G}^r(t) = -i\Theta(t) \sum_{m=1}^K r_m e^{-i\epsilon_m t}. \quad (\text{B.44})$$

While the Lehmann representation yields strictly real poles $\epsilon_m \in \mathbb{R}$, for the retarded Green's function we allow also effective complex poles $\Im\epsilon_m \leq 0$ in the lower half plane. Similar to the Padé-Fourier transform, we assume an equidistant discretization of time and define the new variable

$$y_m = y(-\epsilon_m) = \exp(-i\epsilon_m \Delta t), \quad (\text{B.45})$$

in terms of the poles ϵ_m , and not of the complex frequency z like for the Padé-Fourier algorithm in appendix B.5. For non-negative times $l\Delta t \geq 0$, the time-discretized Green's function reads

$$\mathcal{G}^r(l\Delta t) = -i \sum_{m=1}^K r_m y_m^l. \quad (\text{B.46})$$

Next, we define a complex polynomial $P(y)$ with the roots y_m :

$$P(y) = \prod_{m=1}^K (y - y_m) = \sum_{k=0}^K b_k y^k \stackrel{k \rightarrow K-k}{=} \sum_{k=0}^K a_k y^{K-k}, \quad (\text{B.47})$$

where b_k are the coefficients from expanding the product, which depend on all y_m . The second equality is just a relabeling $a_k = b_{K-k}$. We point out, the roots $y_m = y(-\epsilon_m)$ lie inside the unit-circle of the complex y -plane, they are the reciprocal $y_m = 1/y(\epsilon_m)$ of the poles $y(\epsilon_m)$ we encounter in the Padé-Fourier algorithm appendix B.5. By definition y_m are the roots of $P(y)$, i.e. $P(y_m) = 0$, and the 0-th coefficient is $a_0 = b_K = 1$, therefore solving eq. (B.47) for y_m^K yields the expression

$$y_m^K = - \sum_{k=0}^{K-1} b_k y_m^k = - \sum_{k=1}^K a_k y_m^{K-k} \quad (\text{B.48})$$

for the K -th power. Multiplying this equation by y_m^{l-K} with $l \geq K$ generalizes this result to

$$y_m^l = - \sum_{k=1}^K a_k y_m^{l-k}. \quad (\text{B.49})$$

Inserting this expression in the Green's function eq. (B.46), we obtain

$$\mathcal{G}^r(l\Delta t) = i \sum_{m=1}^K r_m \sum_{k=1}^K a_k y_m^{l-k} = - \sum_{k=1}^K a_k \left(-i \sum_{m=1}^K r_m y_m^{l-k} \right) = - \sum_{k=1}^K a_k \mathcal{G}^r([l-k]\Delta t). \quad (\text{B.50})$$

This is the linear prediction eq. (B.43) for the retarded Green's function: Knowing the K previous time points $\mathcal{G}^r([l-k]\Delta t)$, we can predict the next time point $\mathcal{G}^r(l\Delta t)$.

B.6.2. Linear prediction coefficients

We follow Vaidyanathan [228] to determine the LP coefficients a_k . The number of available data points $L + 1$ is considered to be larger than the prediction order K , i.e. $L + 1 > K$. The prediction coefficients a_k are chosen to minimize the error in the 2-norm

$$\delta = \sum_{l=K}^L |x_l - \hat{x}_l|^2 = \sum_{l=K}^L \left| x_l + \sum_{k=1}^K a_k x_{l-k} \right|^2 =: \sum_{l=K}^L |\delta_l|^2. \quad (\text{B.51})$$

The error δ is minimal, if the individual difference δ_l are orthogonal to the previous data points [228]

$$\sum_{l=K}^L \delta_l x_{l-k}^* = 0 \quad \forall k \in \{1, \dots, K\}. \quad (\text{B.52})$$

We proof that the orthogonality condition indeed minimizes the error. Let \tilde{a}_k be a different choice of parameters which yields the prediction \tilde{x}_l . The difference $\tilde{\delta}_l$ between the true data points x_l and the prediction \tilde{x}_l is

$$\tilde{\delta}_l = x_l - \tilde{x}_l = x_l + \sum_{k=1}^K \tilde{a}_k x_{l-k}. \quad (\text{B.53})$$

Using the difference $\delta_l = x_l - \hat{x}_l$, the 2-norm error of the prediction can be expanded as

$$\tilde{\delta} = \sum_{l=K}^L |x_l - \tilde{x}_l|^2 = \sum_{l=K}^L |\delta_l + \hat{x}_l - \tilde{x}_l|^2 = \delta + \sum_{l=K}^L |\hat{x}_l - \tilde{x}_l|^2 + \sum_{l=K}^L [\delta_l (\hat{x}_l^* - \tilde{x}_l^*)] + \sum_{l=K}^L [(\hat{x}_l - \tilde{x}_l) \delta_l^*]. \quad (\text{B.54})$$

The two cross-terms vanish due to the orthogonality eq. (B.52):

$$\sum_{l=K}^L [\delta_l (\hat{x}_l^* - \tilde{x}_l^*)] = - \sum_{l=K}^L [\delta_l \sum_{k=1}^K (a_k^* - \tilde{a}_k^*) x_{l-k}^*] = - \sum_{k=1}^K (a_k^* - \tilde{a}_k^*) \sum_{l=K}^L \delta_l x_{l-k}^* = 0. \quad (\text{B.55})$$

Hence, the error is indeed minimal; any different choice \tilde{a}_k yields a larger error

$$\tilde{\delta} = \delta + \sum_{l=K}^L |\hat{x}_l - \tilde{x}_l|^2 \geq \delta. \quad (\text{B.56})$$

Substituting the difference δ_l by its explicit form in terms of the prediction coefficients a_k in eq. (B.52) yields the equation

$$\sum_{k'=1}^K a_{k'} \sum_{l=K}^L x_{l-k'} x_{l-k}^* = - \sum_{l=K}^L x_l x_{l-k}^* \quad \forall k \in \{1, \dots, K\}, \quad (\text{B.57})$$

or equivalently written as the matrix equation

$$\mathbf{R}\mathbf{a} = -\mathbf{r} \quad \text{with} \quad R_{kk'} = \sum_{l=K}^L x_{l-k}^* x_{l-k'}, \quad r_k = \sum_{l=K}^L x_{l-k}^* x_l \quad (\text{B.58})$$

with the Hermitian covariance matrix \mathbf{R} and the cross-covariance vector \mathbf{r} (not to be confused with the previously defined residues). Accordingly, this method is denoted *covariance method* [229]. The covariance matrix can be expressed as the matrix product

$$\mathbf{R} = \mathbf{X}^\dagger \mathbf{X} \quad \text{with} \quad (\mathbf{R})_{kk'} = \sum_{l=0}^{L-K} X_{lk}^* X_{lk'}, \quad (\mathbf{X})_{lk} = x_{l+K-k}, \quad (\text{B.59})$$

where the $L+1-K \times K$ matrix \mathbf{X} is the Toeplitz matrix containing all measured values x_l . Therefore, \mathbf{R} is positive semi-definite. Likewise, the cross-covariance vector can be expressed as

$$\mathbf{r} = \mathbf{X}^\dagger \mathbf{x}^K \quad \text{with} \quad (\mathbf{x}^K)_l = x_{l+K}. \quad (\text{B.60})$$

We identify the LP eq. (B.58) as the normal equation to

$$\mathbf{X} \mathbf{a} = -\mathbf{x}^K. \quad (\text{B.61})$$

Therefore, it is better to solve eq. (B.61) in a least-squares sense, as it is better conditioned than its normal equation eq. (B.58). Thus, we obtain the LP coefficients a_k using the covariance method as the least-squares solution of the matrix eq. (B.61). Typically, the solution is regularized by truncating singular values smaller than a given threshold.

Equation (B.61) is identical to determining the poles of the Padé-Fourier approximant eq. (B.27). We add the coefficient $a_0 = 1$ and find

$$\mathbf{0} = \mathbf{x}^K a_0 + \mathbf{X} \mathbf{a} = \begin{pmatrix} \mathbf{x}^K & \mathbf{X} \end{pmatrix} \begin{pmatrix} a_0 \\ \mathbf{a} \end{pmatrix} \equiv \mathbf{C}_2 \mathbf{q}, \quad (\text{B.62})$$

where the numerator degree of the Padé approximant is $N = K-1$, the denominator degree is $M = K$, and the total number of points is twice the prediction order $L+1 = 2K+1$.

For completeness, we also mention the *autocorrelation method* [228, 229]. If the time series x_l was completely known for all $l \in \mathbb{Z}$ (this is never the case for retarded Green's functions), the sum in eq. (B.58) could be extended over all l . The elements of the matrix \mathbf{R} depend only on the time difference $R_{kk'} = R(k-k')$, with $R(-k) = R^*(k)$. This is \mathbf{R} is the autocorrelation matrix, which is a Hermitian Toeplitz matrix. As only the finite signal x_l $l \in \{0, \dots, L\}$ is known, a window function has to be applied, setting unknown values to 0.

The autocorrelation method is inadequate for our purpose, see the comparisons of the methods by Vaidyanathan [228] and the references mentioned therein. We employ the covariance method and obtain the LP coefficients by solving eq. (B.61) using a least-squares algorithm.

B.6.3. Pole-structure of Green's function from prediction roots

The polynomial $P(y)$ eq. (B.47) relates the prediction coefficients $a_k = b_{K-k}$ to the poles ϵ_m of the Green's function eq. (B.44). Numerically, the roots of the polynomial $P(y)$ are calculated as the eigenvalues of the companion matrix [115, 230]

$$A_{kk'} = \delta_{k+1k'} - a_{K-k+1} \delta_{k'K}, \quad \mathbf{A} = \begin{pmatrix} 0 & 0 & \dots & 0 & -a_K \\ 1 & 0 & \dots & 0 & -a_{K-1} \\ 0 & 1 & & 0 & -a_{K-2} \\ \vdots & & \ddots & & \vdots \\ 0 & 0 & \dots & 1 & -a_1 \end{pmatrix}, \quad (\text{B.63})$$

the matrix of eigenvectors is the Vandermonde matrix of the eigenvalues. The roots are $y_m = y(-\epsilon_m) = \exp(-i\epsilon_m \Delta t)$, thus the eigenvalues should be all in the unit circle $|y_m| \leq 1$. Eigenvalues outside the unit circle correspond to poles in the upper complex half-plane, and thus an exponentially growing contribution in the Green's function. The exponential growing contribution of poles in the upper half-plane is also reflected by the linear prediction. The transpose companion matrix \mathbf{A}^\top generates the linear prediction:

$$\mathbf{A}^\top \begin{pmatrix} x_{l-K} \\ x_{l-K+1} \\ \vdots \\ x_{l-1} \end{pmatrix} = \begin{pmatrix} x_{l-K+1} \\ x_{l-K+2} \\ \vdots \\ -\sum_{k=1}^K a_k x_{l-k} \end{pmatrix} = \begin{pmatrix} x_{l-K+1} \\ x_{l-K+2} \\ \vdots \\ \hat{x}_l \end{pmatrix}, \quad (\text{B.64})$$

the ones on the sub-diagonal of eq. (B.63) shift the vector elements, the last column generates the LP eq. (B.43). Defining the data vector $(\mathbf{x})_l = x_l$, the predicted value \hat{x}_{K+l} is generated by applying l times the companion matrix \mathbf{A}^\top to \mathbf{x} . Thus, \hat{x}_{K+l} can be calculated as the K -th vector element

$$\hat{x}_{K+l} = ([\mathbf{A}^\top]^l \mathbf{x})_K = (\mathbf{x}^\top \mathbf{A}^l)_K. \quad (\text{B.65})$$

We diagonalize the companion matrix $\mathbf{A} = \mathbf{V}^{-1} \mathbf{\Lambda} \mathbf{V}$ to write the predicted value as

$$\hat{x}_{K+l} = \sum_{l'=1}^K x_{l'-1} \sum_{k=1}^K (\mathbf{V}^{-1})_{l'k} \lambda_k^l (\mathbf{V})_{kK} = \sum_{k=1}^K \lambda_k^l V_{kK} \sum_{l'=1}^K x_{l'-1} (\mathbf{V}^{-1})_{l'k}. \quad (\text{B.66})$$

Defining $\tilde{r}_k = V_{kK} \sum_{l'=1}^K x_{l'-1} (\mathbf{V}^{-1})_{l'k}$ and using $\lambda_k = \exp(-i\epsilon_k \Delta t)$, the prediction can be written in the form

$$\hat{x}_{K+l} = \sum_{k=1}^K \lambda_k^l \tilde{r}_k = \sum_{k=1}^K e^{-i\epsilon_k l \Delta t} \tilde{r}_k. \quad (\text{B.67})$$

While in principle this equation allows to reconstruct the Green's function by reading of the residues \tilde{r}_k and poles ϵ_k , in practice this yields highly inaccurate results. Equation (B.67) can be used to produce a stable prediction, by omitting the exponential growing terms $|\lambda_k| > 1$, which correspond to poles in the upper half-plane.

B.6.4. Linear prediction z -transform

The linear prediction (LP) allows in principle to extend the Green's function $\mathcal{G}^r(l\Delta t)$ till infinite times. Thus, it is not necessary to truncate the discrete Laplace transform eq. (B.6), the infinite summation can be performed. We write the full series for the discretized Laplace transform eq. (B.6) in the form eq. (B.8):

$$G^r(y) \approx \sum_{l=0}^{\infty} \Delta t \mathcal{G}^r(l\Delta t) y^l, \quad (\text{B.68})$$

with $y = \exp(iz\Delta t)$ eq. (B.7), see also eq. (B.25) for the Padé-Fourier transform appendix B.5. We shorten the notation using $\mathcal{G}_l^r = \mathcal{G}^r(l\Delta t)$ and define

$$S(y) := \sum_{l=0}^{\infty} \mathcal{G}_l^r y^l = \sum_{l=0}^{K-1} \mathcal{G}_l^r y^l + \sum_{l=K}^{\infty} \mathcal{G}_l^r y^l, \quad (\text{B.69})$$

where K is the prediction order. Such an equation is known as Z -transform, we used the variable y instead of z^{-1} , as the variable name z is already taken for the complex frequency. We partition $S(y)$ into the first K Green's function points, which are sampled, and the rest which will be replaced by the prediction. For now, we focus on the second sum, in which we replace the unknown Green's function values \mathcal{G}_l^r by their predicted function $\hat{\mathcal{G}}_l^r$. In the following, we drop the hat and do not distinguish between measured \mathcal{G}_l^r and predicted $\hat{\mathcal{G}}_l^r$ values. We insert the prediction expression eq. (B.43):

$$\sum_{l=K}^{\infty} \mathcal{G}_l^r y^l = - \sum_{l=K}^{\infty} y^l \sum_{k=1}^K a_k \mathcal{G}_{l-k}^r = - \sum_{k=1}^K a_k \sum_{l=K}^{\infty} \mathcal{G}_{l-k}^r y^l = - \sum_{k=1}^K a_k y^k \sum_{l=K-k}^{\infty} \mathcal{G}_l^r y^l, \quad (\text{B.70})$$

in the second equality we exchange the order of the summations, in the third equality we shifted the summation index l . We extend the l -summation to start at $l = 0$ yielding the full summation of $S(y)$, and subtract the added terms $l = 0$ to $l = K - k - 1$:

$$\sum_{l=K}^{\infty} \mathcal{G}_l^r y^l = - \sum_{k=1}^K a_k y^k \left[S(y) - \sum_{l=0}^{K-k-1} \mathcal{G}_l^r y^l \right] = -S(y) \sum_{k=1}^K a_k y^k + \sum_{k=1}^K \sum_{l=0}^{K-k-1} a_k y^{k+l} \mathcal{G}_l^r. \quad (\text{B.71})$$

Next, we shift the summation $l \rightarrow l - k$, and thereafter exchange the order of the k and l summation to pull the free variable y out of the double summation:

$$\sum_{l=K}^{\infty} \mathcal{G}_l^r y^l = -S(y) \sum_{k=1}^K a_k y^k + \sum_{k=1}^K \sum_{l=k}^{K-1} a_k y^l \mathcal{G}_{l-k}^r = -S(y) \sum_{k=1}^K a_k y^k + \sum_{l=1}^{K-1} y^l \sum_{k=1}^l a_k \mathcal{G}_{l-k}^r \quad (\text{B.72})$$

The summation over l can be extended to include $l = 0$, as the term with $\mathcal{G}_{-k}^r = 0$ does not contribute. The formula for the full $S(y)$, eq. (B.69), yields

$$\begin{aligned} S(y) &= -S(y) \sum_{k=1}^K a_k y^k + \sum_{l=0}^{K-1} y^l \left[\mathcal{G}_l^r + \sum_{k=1}^l a_k \mathcal{G}_{l-k}^r \right] = \frac{\sum_{l=0}^{K-1} y^l \left[\mathcal{G}_l^r + \sum_{k=1}^l a_k \mathcal{G}_{l-k}^r \right]}{1 + \sum_{k=1}^K a_k y^k} \\ &= \frac{\sum_{l=0}^{K-1} y^l \sum_{k=0}^l a_k \mathcal{G}_{l-k}^r}{\sum_{k=0}^K a_k y^k}, \end{aligned} \quad (\text{B.73})$$

where we included $a_0 = 1$ to write the result more compactly. This is the linear prediction z -transform (LPZ) by Tang and Norris [231–233]. A similar expression is given by Ni and Scheraga [234] including all sampled times \mathcal{G}_l^r . The retarded Green's function vanishes for negative times, thus the upper limit of the k -summation can be extended from l to K . The numerator of $S(y)$ is the truncated Laplace transform of the convolution of the LP coefficients with the sampled Green's function $a * \mathcal{G}^r$; the denominator is the truncated Laplace transform of the LP coefficients a_k . Thus, defining $L_K[x](y) = \sum_{l=0}^{K-1} x_l y^l$, we can write eq. (B.73) in the form

$$S(y) = L_K[a * \mathcal{G}^r] / L_{K+1}[a]. \quad (\text{B.74})$$

The formula for the Green's function eq. (B.68) reads

$$G^r(z) \approx \Delta t S(y(z)) = \frac{\sum_{l=0}^{K-1} e^{izl\Delta t} \sum_{k=0}^l a_k \Delta t \mathcal{G}^r([l-k]\Delta t)}{\sum_{k=0}^K a_k e^{izl\Delta t}}. \quad (\text{B.75})$$

The result can be interpreted as truncation of the convolution theorem. In the limit $K \rightarrow \infty$, we recover the infinite discretized Laplace transform eq. (B.6) according to the convolution theorem, as the transform turns the convolution of Green's function and prediction coefficients into a product.

The LPZ is in fact equivalent to the Padé-Fourier algorithm [235]. As shown in appendix B.6.2, the prediction coefficients and the denominator of eq. (B.75) are identical to the denominator polynomial $q(z)$ of the $[K - 1/K](z)$ Padé approximant for $L = 2K$. Likewise, we identify the numerator of eq. (B.75) with the numerator polynomial $p(z)$ with the first line of Padé equation eq. (B.27). Thus, choosing the (maximal) prediction order $K = L/2$, the Padé-Fourier approximant $[K - 1/K](z)$ and the LPZ algorithm are in fact identical. In principle, this allows to transfer knowledge between the two methods. Methods to calculate LP coefficients can be used to calculate the denominator polynomial of Padé. Furthermore, LP readily defines least-squares versions of Padé for overdetermined systems $N + M < L$. On the other hand, we can use the flexibility of Padé to use different polynomial degrees; the $[K/K](z)$ approximant is better suited for the Padé-Fourier algorithm. There is literature for both algorithms how to choose a suitable order.

As mentioned before, the LPZ transform takes only the first K time points directly into account, the rest of the L time points only enter the prediction coefficients. We modify the above derivation to include all available time points on equal footing. In this case, we split the Z -transform eq. (B.69) after the L time points, not the prediction order K :

$$S(y) = \sum_{l=0}^L \mathcal{G}_l^r y^l + \sum_{l=L+1}^{\infty} \mathcal{G}_l^r y^l. \quad (\text{B.76})$$

We follow the analogous steps till eq. (B.72), which reads in this case

$$\sum_{l=L+1}^{\infty} \mathcal{G}_l^r y^l = -S(y) \sum_{k=1}^K a_k y^k + \sum_{k=1}^K \sum_{l=k}^L a_k y^l \mathcal{G}_{l-k}^r = -S(y) \sum_{k=1}^K a_k y^k + \sum_{l=0}^L y^l \sum_{k=1}^K a_k \mathcal{G}_{l-k}^r. \quad (\text{B.77})$$

For the second equation, we again employed the fact that the retarded Green's function vanishes for negative times, $G_{l<0} = 0$. This allows us to extend the lower limit of the l -summation to 0, and exchange the summations over k and l . The summation for the full summation eq. (B.76) yields

$$S(y) = -S(y) \sum_{k=1}^K a_k y^k + \sum_{l=0}^L y^l [\mathcal{G}_l^r + \sum_{k=1}^K a_k \mathcal{G}_{l-k}^r] = \frac{\sum_{l=0}^L y^l \sum_{k=0}^K a_k \mathcal{G}_{l-k}^r}{\sum_{k=0}^K a_k y^k}, \quad (\text{B.78})$$

where we included $a_0 = 1$. Surprisingly, we recover the same structure as in the LPZ, however, we sum over all available time points

$$G^r(z) \approx \Delta t S(y(z)) = \frac{\sum_{l=0}^L y^l \sum_{k=0}^K a_k \Delta t \mathcal{G}^r([l-k]\Delta t)}{\sum_{k=0}^K a_k y^k}. \quad (\text{B.79})$$

B.7. Comparison

We compare the different methods for Laplace transform for a realistic example. We calculate the retarded Green's function for a simple cubic lattice [172, 208, 209] with $\mu = 0.2$, where the hybridization function is discretized using 250 bath sites. The time evolution is calculated using the TDVP with time steps of $\Delta t = 0.1$. While the non-interacting example is non-trivial using tensor-network methods, we should keep in mind that the results are simpler. The up and down spins decouple, which is reflected in the bond dimension between the impurity sites. We consider the integrated error

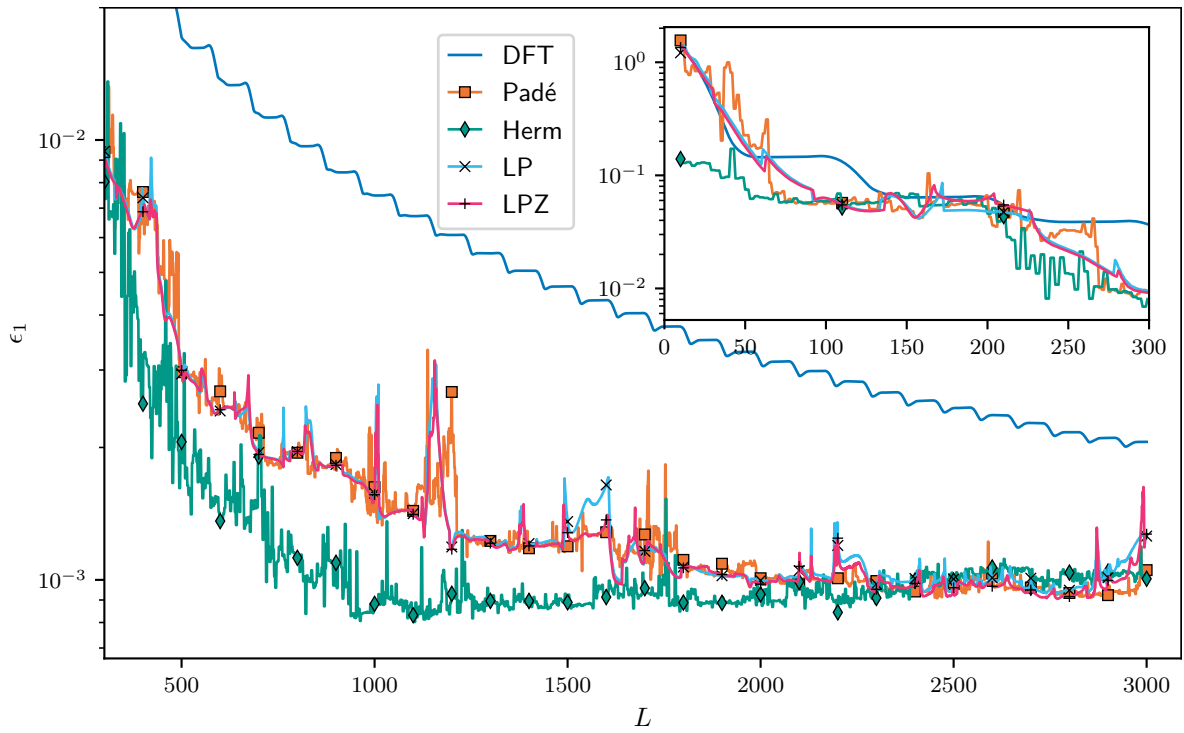
$$\epsilon_n := \sqrt[n]{\frac{1}{W} \int_{-W/2}^{W/2} d\omega |G^r(\omega + i\eta) - F[\mathcal{G}^r](\omega + i\eta)|^n} \quad \text{with } W = 3, \quad (\text{B.80})$$

where $F[\mathcal{G}^r]$ denotes our approximation for the Laplace transform. Note that $G^r(z)$ is the continuous Green's function for the simple cubic lattice, not the discretized Green's function calculated from the bath parameters.

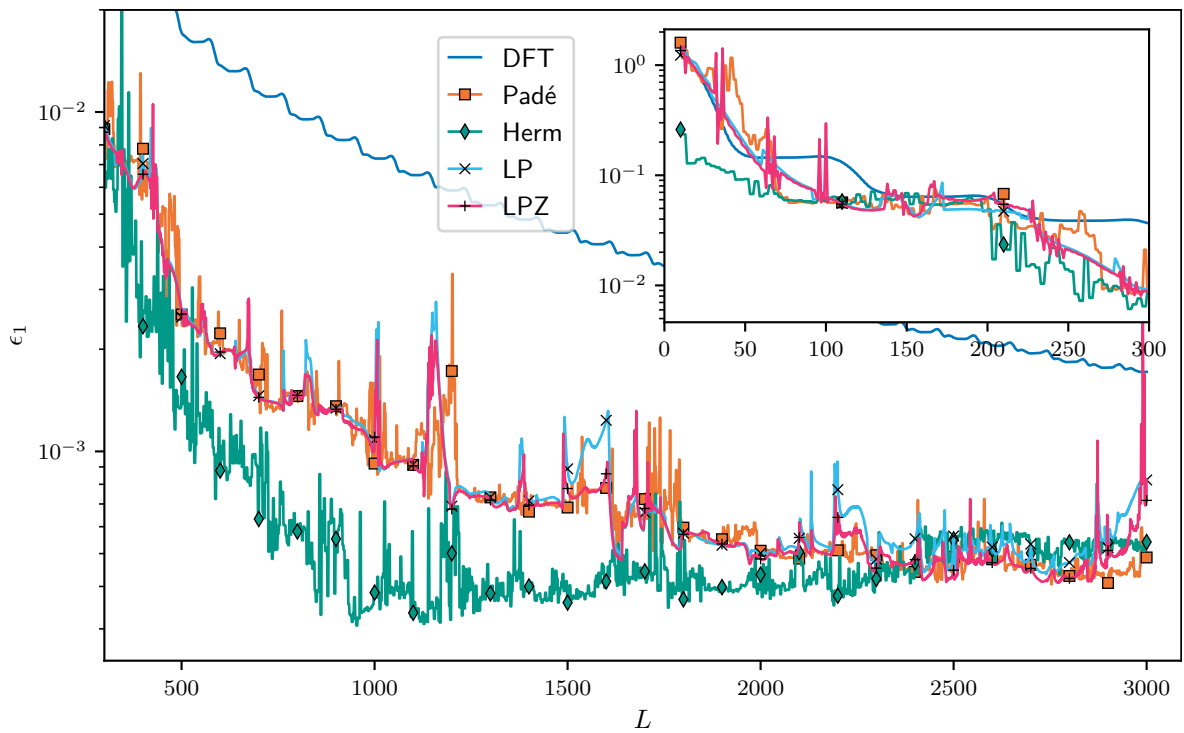
Figure B.11(a) shows the errors ϵ_1 of the different methods for $\eta = 10^{-6}$ using a trapezoidal rule. The error is plotted against the number of time points included in the Laplace transform. The inset shows the error for the first few time points $L \leq 300$, i.e., $t_L \leq 30$. The blue line DFT is the reference for the truncated summation of eq. (B.10). The error of DFT decreases nearly monotonously in the number of time points L , showing a step-like structure. The convergence is, however, slow. Even $L = 3000$ time points are not sufficient to reach an error smaller than 10^{-3} .

The error of the $[\frac{L}{2}/\frac{L}{2}]$ Padé-Fourier approximant eq. (B.28) changes rather erratically. In the region $L \in \{200, \dots, 1500\}$, it decreases rapidly, converging against a value of $\epsilon_1 \approx 10^{-3}$, which is determined by the discretization $\Delta t = 0.1$. The usage of larger numbers of time points $L > 2000$ cannot decrease the error further; instead, it increases slightly. The Hermite-Padé algorithm, eqs. (B.40) and (B.41), which additionally includes square-root branch cuts further improves the Laplace transform. Except for some outliers, it is more accurate for all values of L and converges faster than the Padé-Fourier and the LPZ algorithm. It also converges to the discretization error of 10^{-3} . Values of $L > 2000$ yield no further improvement, in fact, the error slightly grows, and the (linear) Padé-Fourier algorithm yields slightly more accurate results.

Next, we consider the LP algorithms. To determine the LP coefficients, we use a relative threshold of 10^{-6} , truncating singular values σ_k smaller than $\sigma_0 10^{-6}$. This truncation considerably smooths the error, especially for small numbers of time points $L \leq 200$. Increasing this relative threshold leads to similar behavior as seen for the Padé-Fourier algorithm. For the LP algorithm we choose the maximal prediction order $K = L/2$, predict the Green's function till t_{10L} , and remove zeros outside the unit circle, which would generate exponentially growing terms. The same prediction order $K = L/2$ is used for the LPZ algorithm; it is, however, not necessary to remove zeros outside the unit circle. These zeros result in poles in the upper complex half-plane, but they do not generate relevant errors as their residue is small. LP and LPZ result in comparable errors. In general, the Padé-Fourier, LP, and LPZ algorithms all yield comparable results, as they are all based on simple poles. The Hermite-Padé algorithm, on the other hand, is a better approximation for this example. Considering the error ϵ_2 instead of ϵ_1 shows qualitatively the same picture; however, the advantage over the basic DFT is smaller. The improved algorithms tend to produce more localized errors resulting in small ϵ_1 errors.



(a) Trapezoidal rule



(b) Simpson rule

Figure B.11.: Comparison of different methods for the Laplace transform using (a) the trapezoidal rule and (b) the Simpson rule. The time steps are $\Delta t = 0.1$ and the shift is $\eta = 10^{-6}$. Note the different limits for the vertical axis ϵ_1 . The markers are just a guide to the eye.

Figure B.11(b) shows the error using the Simpson rule instead of the trapezoidal rule. Qualitatively, the picture remains the same. For the Simpson rule, lower errors are reachable due to the smaller discretization error. Consequently, the difference between the error of DFT and the other algorithms is bigger. The Hermite-Padé algorithm reaches its minimal error already at $L \approx 1000$; the error grows for larger numbers of time points. For large values $L \approx 3000$, the error of LPZ shows large peaks. The prediction coefficients of LPZ are calculated from the Green's function weighted by the Simpson coefficients, while for LP, we can predict the bare Green's function. This difference explains the larger error of LPZ compared to LP. However, for this example, both algorithms perform worse than the Padé-Fourier algorithm for large values $L \approx 3000$.

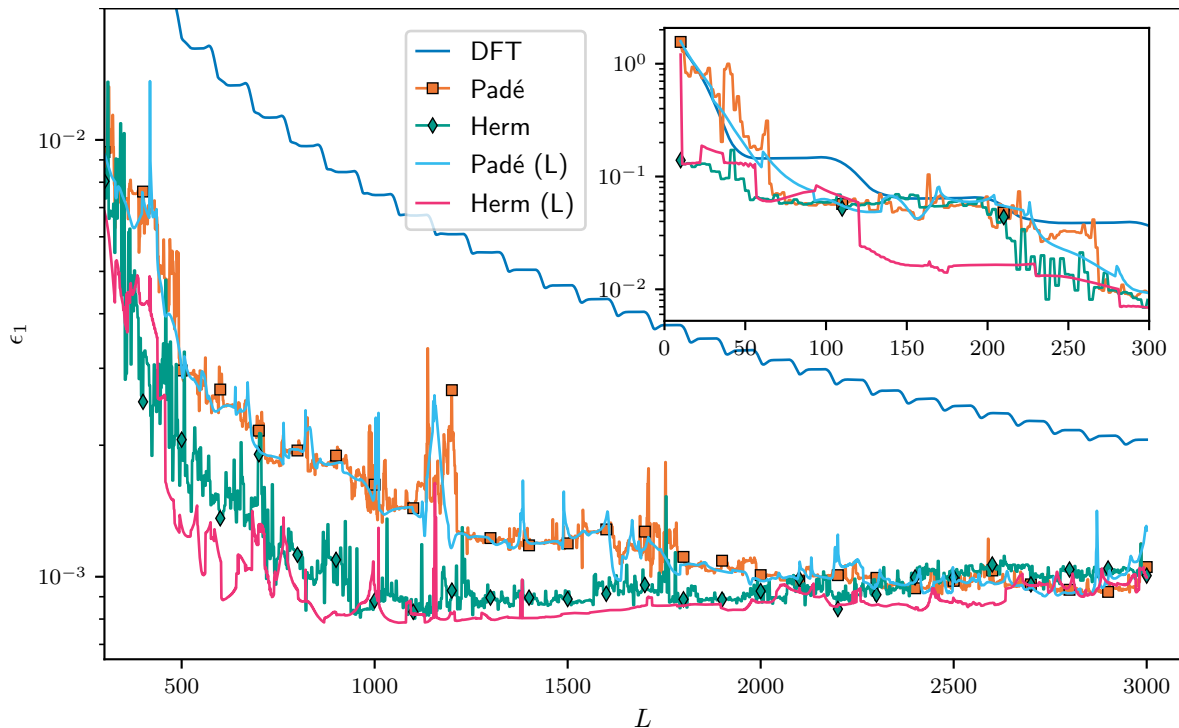


Figure B.12.: Comparison of the Padé-Fourier algorithms for the Laplace transform using the trapezoidal rule. The time steps are $\Delta t = 0.1$ and the shift is $\eta = 10^{-6}$. The lines without marker correspond to using a least-squares solution (L) truncating singular values σ_k smaller than $\sigma_0 10^{-6}$, where σ_0 is the largest singular value.

We conclude all algorithms discussed in this low for accurate Laplace transforms for much shorter maximal times t_L than the basic DFT algorithm. We find the Padé-Fourier-based algorithms, in particular using the square Hermite-Padé, to produce the best results. However, the error as a function of the number of time points $\epsilon_1(L)$ shows many peaks, unlike the DFT. Instead of calculating the Padé coefficients as the null vector of the second row in eqs. (B.27) and (B.40), we can use a least-squares solution analogous to the LP algorithm. We fix one parameter and calculate the other parameters truncating the smaller singular values. For the linear Padé algorithm, we can, e.g., set $q_0 = 1$ and calculate the other parameters as

$$(\mathbf{C}_2)_{[:, 1:]} \mathbf{q}_{[1:]} = -(\mathbf{C}_2)_{[:, 0]} q_0, \quad (\text{B.81})$$

cf. eq. (B.27). This approach yields a smoother error $\epsilon_1(L)$, as seen in fig. B.12. For large values of L , this yields more accurate results for the quadratic Hermite-Padé approximants. The error still contains several peaks; hence, it could be useful to take the average (or median) over several approximants for different values of L .

Conclusion. Both the Padé-Fourier and the LP algorithm significantly reduce the truncation error compared to the DFT, allowing for shorter time evolutions and, thereby, shorter computation times. This is in particular relevant as the bond dimension typically grows, which limits the maximal time t_L that can be computed.

Instead of using the LP to predict the Green's function until a finite time $t_{LP} > t_L$, the LPZ algorithm can be employed, corresponding to an infinitely large time $t_{LP} \rightarrow \infty$. Therefore, the LPZ algorithm eliminates the arbitrary parameter t_{LP} . The LPZ with prediction order $K = L/2$ is identical to the $[K - 1/K]$ approximant of the Padé-Fourier algorithm; both algorithms yield comparable results. Out of the considered algorithms, we find the quadratic Hermite-Padé approximant $[L/3, L/3, L/3]$ to give the most accurate results for the Laplace transform.

Acronyms

- BEB** Blackman–Esterling–Berk. 4, 82, 84, 88, 89, 92–94, 97, 98, 138, 139
- BZ** Brillouin zone. 130, 131
- CPA** coherent potential approximation. 4, 76–82, 86, 87, 89, 95, 97, 98, 102, 104, 138
- CT-AUX** auxiliary field continuous-time quantum Monte Carlo. 19
- CT-HYB** continuous-time quantum Monte Carlo in hybridization expansion. v, 16, 19, 44, 110, 113–116, 137, 157
- CT-INT** continuous-time quantum Monte Carlo in interaction expansion. 19
- CT-QMC** continuous-time quantum Monte Carlo. v, 2, 4, 11, 19, 32, 137, 141
- DFT** discrete Fourier transform. 137, 152, 165, 166, 169–171, 182, 184, 185
- DMFT** dynamical mean-field theory. 1, 2, 4, 6, 11, 12, 15, 17, 19, 97–99, 102, 104, 108, 110, 113–117, 119, 126, 134, 137–139, 141, 165
- DMRG** density matrix renormalization group. 2, 4, 47, 53, 57–61, 66, 67, 69, 99, 107, 134, 137, 138
- DOS** density of states. 7, 15, 16, 43, 89, 92, 95, 108, 111, 123, 124, 126, 129, 132, 142, 160, 165, 171, 174
- FFT** fast Fourier transform. 152, 154
- FTPS** fork tensor-product states. 134
- HF** Hartree-Fock. 108, 110, 112–116
- HMF** half-metallic ferromagnet. 4, 107, 109, 111–117, 138, 139
- iDFT** inverse discrete Fourier transform. 152, 154
- LASSO** least absolute shrinkage and selection operator. 36
- LP** linear prediction. 137, 161, 163, 175–182, 184, 185
- LPZ** linear prediction z -transform. 137, 180–182, 184, 185
- MaxEnt** maximum entropy. 33–35

NUFFT nonuniform fast Fourier transform. 28, 142

QMC quantum Monte Carlo. 2, 33, 34, 45, 107, 108, 152, 156, 157

QP quasiparticle. 113

SIAM single-impurity Anderson model. 4, 8, 9, 11, 14–16, 47, 54, 56, 59, 134

SOM stochastic optimization method. 33, 35

SpM sparse modeling. 33, 35, 36

SVD singular value decomposition. 34, 36, 47–50, 52, 57, 58, 60–62, 89, 91

TDVP time-dependent variational principle. 4, 16, 47, 62, 63, 66, 67, 69, 99, 107, 134, 137, 138, 182

TEBD time-evolving block decimation. 62, 110

Own publications

- [W1] A. Weh, J. Otsuki, and L. Chioncel, “Finite temperature many-body effects in half-metallic ferromagnets”, in *Proceedings of the international conference on strongly correlated electron systems (SCES2019)*, Vol. 30 (Journal of the Physical Society of Japan, Mar. 2020), p. 011005 (cit. on p. v).
- [W2] A. Weh, J. Otsuki, H. Schnait, H. G. Evertz, U. Eckern, A. I. Lichtenstein, and L. Chioncel, “Spectral properties of heterostructures containing half-metallic ferromagnets in the presence of local many-body correlations”, *Phys. Rev. Research* **2**, 043263 (2020) (cit. on pp. v, 107–117).
- [W3] A. Weh, Y. Zhang, A. Östlin, H. Terletska, D. Bauernfeind, K.-M. Tam, H. G. Evertz, K. Byczuk, D. Vollhardt, and L. Chioncel, “Dynamical mean-field theory of the Anderson-Hubbard model with local and nonlocal disorder in tensor formulation”, *Phys. Rev. B* **104**, 045127 (2021) (cit. on pp. v, 71–74, 76, 78, 80, 82–105, 163).
- [W4] A. Weh, W. H. Appelt, A. Östlin, L. Chioncel, and U. Eckern, “Spin-polarization and resonant states in electronic conduction through a correlated magnetic layer”, *Phys. Status Solidi B*, 2100157 (2021) (cit. on pp. v, 119–136).

Codes

- [C1] M. Wallerberger, A. Hausoel, P. Gunacker, A. Kowalski, N. Parragh, F. Goth, K. Held, and G. Sangiovanni, “w2dynamics: Local one- and two-particle quantities from dynamical mean field theory”, *Comput. Phys. Commun.* **235**, 388–399 (2019) (cit. on pp. v, 19, 110).
- [C2] A. Weh and A. Östlin, *DerWeh/gftools: GfTool 0.11.0 release*, Zenodo <https://doi.org/10.5281/zenodo.4744545>, version 0.11.0, Apr. 2022 (cit. on pp. v, 43, 98, 142).
- [C3] K. Yoshimi, J. Otsuki, Y. Motoyama, M. Ohzeki, and H. Shinaoka, “SpM: Sparse modeling tool for analytic continuation of imaginary-time Green’s function”, *Comput. Phys. Commun.* **244**, 319–323 (2019) (cit. on pp. v, 36, 110).
- [C4] D. Bergeron and A.-M. S. Tremblay, “Algorithms for optimized maximum entropy and diagnostic tools for analytic continuation”, *Phys. Rev. E* **94**, 023303 (2016) (cit. on pp. v, 34).
- [C5] J. Nordström, J. Schött, I. L. Loch, and I. Di Marco, “A GPU code for analytic continuation through a sampling method”, *SoftwareX* **5**, 178–182 (2016) (cit. on pp. v, 35).
- [C6] M. Fishman, S. R. White, and E. M. Stoudenmire, *The ITensor software library for tensor network calculations*, 2020, arXiv:2007.14822 (cit. on p. v).
- [C7] O. Parcollet, M. Ferrero, T. Ayrat, H. Hafermann, I. Krivenko, L. Messio, and P. Seth, “TRIQS: a toolbox for research on interacting quantum systems”, *Comput. Phys. Commun.* **196**, 398–415 (2015) (cit. on p. v).
- [C8] P. Seth, I. Krivenko, M. Ferrero, and O. Parcollet, “TRIQS/CTHYB: a continuous-time quantum Monte Carlo hybridisation expansion solver for quantum impurity problems”, *Comput. Phys. Commun.* **200**, 274–284 (2016) (cit. on p. 19).
- [C9] A. Weh, *DMRG lecture code using tensor trains*, <https://github.com/DerWeh/tensortrain>, 2022 (cit. on p. 47).

Bibliography

- [1] N. F. Mott, “Metal-insulator transition”, *Rev. Mod. Phys.* **40**, 677–683 (1968) (cit. on p. 1).
- [2] N. Mott, *Metal-insulator transitions* (CRC Press, London, Aug. 20, 1990), p. 296, 296 pp. (cit. on p. 1).
- [3] M. Imada, A. Fujimori, and Y. Tokura, “Metal-insulator transitions”, *Rev. Mod. Phys.* **70**, 1039–1263 (1998) (cit. on p. 1).
- [4] P. Hohenberg and W. Kohn, “Inhomogeneous electron gas”, *Phys. Rev.* **136**, B864–B871 (1964) (cit. on pp. 1, 2).
- [5] W. Kohn, “Nobel lecture: Electronic structure of matter—wave functions and density functionals”, *Rev. Mod. Phys.* **71**, 1253–1266 (1999) (cit. on pp. 1, 2).
- [6] R. O. Jones and O. Gunnarsson, “The density functional formalism, its applications and prospects”, *Rev. Mod. Phys.* **61**, 689–746 (1989) (cit. on pp. 1, 2).
- [7] R. O. Jones, “Density functional theory: Its origins, rise to prominence, and future”, *Rev. Mod. Phys.* **87**, 897–923 (2015) (cit. on pp. 1, 2).
- [8] H. Lin, J. Gubernatis, H. Gould, and J. Tobochnik, “Exact diagonalization methods for quantum systems”, *Comput. Phys.* **7**, 400 (1993) (cit. on p. 2).
- [9] C. Lanczos, “An iteration method for the solution of the eigenvalue problem of linear differential and integral operators”, *J. RES. NATL. BUR. STAN.* **45**, 255–282 (1950) (cit. on pp. 2, 57, 58).
- [10] J. W. Negele and H. Orland, *Quantum many-particle systems*, 1st ed. (CRC Press, Boca Raton, 1998) (cit. on pp. 2, 9, 12–14).
- [11] A. Altland and B. D. Simons, *Condensed matter field theory*, 2nd ed. (Cambridge University Press, 2009) (cit. on pp. 2, 9, 10, 12, 28).
- [12] J. E. Hirsch and R. M. Fye, “Monte Carlo method for magnetic impurities in metals”, *Phys. Rev. Lett.* **56**, 2521–2524 (1986) (cit. on p. 2).
- [13] E. Gull, A. J. Millis, A. I. Lichtenstein, A. N. Rubtsov, M. Troyer, and P. Werner, “Continuous-time Monte Carlo methods for quantum impurity models”, *Rev. Mod. Phys.* **83**, 349–404 (2011) (cit. on pp. 2, 19, 20).
- [14] L. Mühlbacher and E. Rabani, “Real-time path integral approach to nonequilibrium many-body quantum systems”, *Phys. Rev. Lett.* **100**, 176403 (2008) (cit. on pp. 2, 19).
- [15] E. Gull, D. R. Reichman, and A. J. Millis, “Bold-line diagrammatic Monte Carlo method: General formulation and application to expansion around the noncrossing approximation”, *Phys. Rev. B* **82**, 075109 (2010) (cit. on p. 2).

- [16] G. Cohen, E. Gull, D. R. Reichman, and A. J. Millis, “Taming the dynamical sign problem in real-time evolution of quantum many-body problems”, *Phys. Rev. Lett.* **115**, 266802 (2015) (cit. on p. 2).
- [17] K. G. Wilson, “The renormalization group: Critical phenomena and the Kondo problem”, *Rev. Mod. Phys.* **47**, 773–840 (1975) (cit. on p. 2).
- [18] R. Bulla, T. A. Costi, and T. Pruschke, “Numerical renormalization group method for quantum impurity systems”, *Rev. Mod. Phys.* **80**, 395–450 (2008) (cit. on p. 2).
- [19] U. Schollwöck, “The density-matrix renormalization group in the age of matrix product states”, *Ann. Phys. (New York)* **326**, 96–192 (2011) (cit. on pp. 2, 57).
- [20] S. Paeckel, T. Köhler, A. Swoboda, S. R. Manmana, U. Schollwöck, and C. Hubig, “Time-evolution methods for matrix-product states”, *Annals of Physics* **411**, 167998 (2019) (cit. on pp. 2, 62, 63, 175).
- [21] S. R. White, “Density matrix formulation for quantum renormalization groups”, *Phys. Rev. Lett.* **69**, 2863–2866 (1992) (cit. on pp. 2, 47, 57, 60, 99, 134).
- [22] S. R. White, “Density-matrix algorithms for quantum renormalization groups”, *Phys. Rev. B* **48**, 10345–10356 (1993) (cit. on pp. 2, 47, 57, 60, 62, 99).
- [23] M. I. Katsnelson, V. Y. Irkhin, L. Chioncel, A. I. Lichtenstein, and R. A. de Groot, “Half-metallic ferromagnets: From band structure to many-body effects”, *Rev. Mod. Phys.* **80**, 315–378 (2008) (cit. on pp. 2, 3, 107, 109, 110, 114).
- [24] I. Žutić, J. Fabian, and S. Das Sarma, “Spintronics: Fundamentals and applications”, *Rev. Mod. Phys.* **76**, 323–410 (2004) (cit. on pp. 2, 107).
- [25] R. A. de Groot, F. M. Mueller, P. G. van Engen, and K. H. J. Buschow, “New class of materials: Half-metallic ferromagnets”, *Phys. Rev. Lett.* **50**, 2024–2027 (1983) (cit. on p. 2).
- [26] T. Moriya, *Spin fluctuations in itinerant electron magnetism*, Springer Series in Solid-State Sciences (Springer Berlin Heidelberg, 1985) (cit. on p. 3).
- [27] D. M. Edwards and J. A. Hertz, “Electron-magnon interactions in itinerant ferromagnetism. II. Strong ferromagnetism”, *J. Phys. F: Met. Phys.* **3**, 2191–2205 (1973) (cit. on pp. 3, 107, 109, 110).
- [28] V. Y. Irkhin and M. I. Katsnelson, “Charge-carriers in the narrow-band Hubbard ferromagnet in the spin-wave temperature-range”, *Fiz. Tverd. Tela* **25**, 3383–3388 (1983) (cit. on pp. 3, 109, 110).
- [29] W. P. Pratt, S.-F. Lee, J. M. Slaughter, R. Loloee, P. A. Schroeder, and J. Bass, “Perpendicular giant magnetoresistances of Ag/Co multilayers”, *Phys. Rev. Lett.* **66**, 3060–3063 (1991) (cit. on p. 3).
- [30] Z. Q. Bai, Y. H. Lu, L. Shen, V. Ko, G. C. Han, and Y. P. Feng, “Transport properties of high-performance all-heusler $\text{Co}_2\text{CrSi}/\text{Cu}_2\text{CrAl}/\text{Co}_2\text{CrSi}$ giant magnetoresistance device”, *J. Appl. Phys.* **111**, 093911 (2012) (cit. on p. 3).
- [31] W. Rotjanapittayakul, J. Prasongkit, I. Rungger, S. Sanvito, W. Pijitrojana, and T. Archer, “Search for alternative magnetic tunnel junctions based on all-heusler stacks”, *Phys. Rev. B* **98**, 054425 (2018) (cit. on p. 3).

-
- [32] J. Hubbard, “Electron correlations in narrow energy bands”, Proc. R. Soc. Lond. A **276**, 238–257 (1963) (cit. on pp. 5, 104).
- [33] M. C. Gutzwiller, “Effect of correlation on the ferromagnetism of transition metals”, Phys. Rev. Lett. **10**, 159–162 (1963) (cit. on p. 5).
- [34] J. Kanamori, “Electron correlation and ferromagnetism of transition metals”, Prog. Theor. Phys. **30**, 275–289 (1963) (cit. on p. 5).
- [35] A. Mielke, “The Hubbard model and its properties”, in *Many-body physics: from Kondo to Hubbard*, edited by E. Pavarini, E. Koch, and P. Coleman, Modeling and Simulation 5 (Forschungszentrum Jülich, Sept. 2015) Chap. 11 (cit. on p. 5).
- [36] R. T. Scalettar, “An introduction to the Hubbard Hamiltonian”, in *Quantum materials: experiments and theory*, edited by E. Pavarini, E. Koch, J. van den Brink, and G. Sawatzky, Modeling and simulation 6 (Forschungszentrum Jülich, Sept. 2016) Chap. 4 (cit. on pp. 5, 6).
- [37] R. Eder, “Introduction to the Hubbard model”, in *The physics of correlated insulators, metals, and superconductors*, edited by E. Pavarini, E. Koch, R. Scalettar, and R. Martin, Modeling and Simulation 7 (Forschungszentrum Jülich, Sept. 2017) Chap. 6 (cit. on p. 5).
- [38] E. H. Lieb and F. Y. Wu, “Absence of Mott transition in an exact solution of the short-range, one-band model in one dimension”, Phys. Rev. Lett. **20**, 1445–1448 (1968) (cit. on p. 6).
- [39] F. H. L. Essler, V. E. Korepin, and K. Schoutens, “Complete solution of the one-dimensional Hubbard model”, Phys. Rev. Lett. **67**, 3848–3851 (1991) (cit. on p. 6).
- [40] J. Hubbard, “Electron correlations in narrow energy bands III. An improved solution”, Proc. R. Soc. Lond. A **281**, 401–419 (1964) (cit. on p. 6).
- [41] D. Vollhardt, N. Blümer, K. Held, M. Kollar, J. Schlipf, M. Ulmke, and J. Wahle, “Metallic ferromagnetism: Progress in our understanding of an old strong-coupling problem”, in *Advances in solid state physics 38* (Springer Berlin Heidelberg, 1999), pp. 383–396 (cit. on p. 6).
- [42] A. Sekiyama, H. Fujiwara, S. Imada, S. Suga, H. Eisaki, S. I. Uchida, K. Takegahara, H. Harima, Y. Saitoh, I. A. Nekrasov, G. Keller, D. E. Kondakov, A. V. Kozhevnikov, T. Pruschke, K. Held, D. Vollhardt, and V. I. Anisimov, “Mutual experimental and theoretical validation of bulk photoemission spectra of $\text{Sr}_{1-x}\text{Ca}_x\text{VO}_3$ ”, Phys. Rev. Lett. **93**, 156402 (2004) (cit. on p. 6).
- [43] I. A. Nekrasov, G. Keller, D. E. Kondakov, A. V. Kozhevnikov, T. Pruschke, K. Held, D. Vollhardt, and V. I. Anisimov, “Comparative study of correlation effects in CaVO_3 and SrVO_3 ”, Phys. Rev. B **72**, 155106 (2005) (cit. on p. 6).
- [44] I. A. Nekrasov, K. Held, G. Keller, D. E. Kondakov, T. Pruschke, M. Kollar, O. K. Andersen, V. I. Anisimov, and D. Vollhardt, “Momentum-resolved spectral functions of SrVO_3 calculated by LDA + DMFT”, Phys. Rev. B **73**, 155112 (2006) (cit. on p. 6).

- [45] R. Jördens, N. Strohmaier, K. Günter, H. Moritz, and T. Esslinger, “A Mott insulator of fermionic atoms in an optical lattice”, *Nature* **455**, 204–207 (2008) (cit. on p. 6).
- [46] U. Schneider, L. Hackermüller, S. Will, T. Best, I. Bloch, T. A. Costi, R. W. Helmes, D. Rasch, and A. Rosch, “Metallic and insulating phases of repulsively interacting fermions in a 3D optical lattice”, *Science* **322**, 1520–1525 (2008) (cit. on p. 6).
- [47] K. A. Chao, J. Spałek, and A. M. Oles, “Kinetic exchange interaction in a narrow s-band”, *J. Phys. C: Solid State Phys.* **10**, L271–L276 (1977) (cit. on p. 7).
- [48] K. A. Chao, J. Spałek, and A. M. Oles, “Canonical perturbation expansion of the Hubbard model”, *Phys. Rev. B* **18**, 3453–3464 (1978) (cit. on p. 7).
- [49] J. Spałek, “t-J model then and now: a personal perspective from the pioneering times”, *Acta Phys. Pol. A* **111**, 409–424 (2007) (cit. on pp. 7, 8).
- [50] M. Ma, “Renormalization-group study of the Anderson-Hubbard model”, *Phys. Rev. B* **26**, 5097–5102 (1982) (cit. on p. 8).
- [51] M. Ulmke, V. Janiš, and D. Vollhardt, “Anderson-Hubbard model in infinite dimensions”, *Phys. Rev. B* **51**, 10411–10426 (1995) (cit. on p. 8).
- [52] R. Chitra and G. Kotliar, “Effect of long range Coulomb interactions on the Mott transition”, *Phys. Rev. Lett.* **84**, 3678–3681 (2000) (cit. on p. 8).
- [53] P. Sun and G. Kotliar, “Extended dynamical mean-field theory and GW method”, *Phys. Rev. B* **66**, 085120 (2002) (cit. on p. 8).
- [54] A. Amaricci, A. Camjayi, K. Haule, G. Kotliar, D. Tanasković, and V. Dobrosavljević, “Extended Hubbard model: Charge ordering and Wigner-Mott transition”, *Phys. Rev. B* **82**, 155102 (2010) (cit. on p. 8).
- [55] P. W. Anderson, “Localized magnetic states in metals”, *Phys. Rev.* **124**, 41–53 (1961) (cit. on p. 8).
- [56] J. R. Schrieffer and P. A. Wolff, “Relation between the Anderson and Kondo Hamiltonians”, *Phys. Rev.* **149**, 491–492 (1966) (cit. on p. 10).
- [57] J. Kondo, “Resistance minimum in dilute magnetic alloys”, *Prog. Theor. Phys.* **32**, 37–49 (1964) (cit. on p. 10).
- [58] M. Plischke and B. Bergersen, *Equilibrium statistical physics*, 3rd (World Scientific, Apr. 2006) (cit. on p. 11).
- [59] W. Metzner and D. Vollhardt, “Correlated lattice fermions in $d = \infty$ dimensions”, *Phys. Rev. Lett.* **62**, 324–327 (1989) (cit. on pp. 11, 14, 97, 134).
- [60] A. Georges and G. Kotliar, “Hubbard model in infinite dimensions”, *Phys. Rev. B* **45**, 6479–6483 (1992) (cit. on pp. 11, 16).
- [61] M. Jarrell, “Hubbard model in infinite dimensions: a quantum Monte Carlo study”, *Phys. Rev. Lett.* **69**, 168–171 (1992) (cit. on p. 11).
- [62] A. Georges, G. Kotliar, W. Krauth, and M. J. Rozenberg, “Dynamical mean-field theory of strongly correlated fermion systems and the limit of infinite dimensions”, *Rev. Mod. Phys.* **68**, 13–125 (1996) (cit. on pp. 11, 14, 97, 109, 134).

-
- [63] G. Kotliar and D. Vollhardt, “Strongly correlated materials: Insights from dynamical mean-field theory”, *Phys. Today* **57**, 53–59 (2004) (cit. on pp. 11, 97, 134).
- [64] V. Janiš, “A new construction of thermodynamic mean-field theories of itinerant fermions: Application to the Falicov-Kimball model”, *Z. Phys. B Condens. Matter* **83**, 227–235 (1991) (cit. on p. 11).
- [65] V. Janiš and D. Vollhardt, “Comprehensive mean field theory for the Hubbard model”, *Int. J. Mod. Phys. B* **06**, 731–747 (1992) (cit. on p. 11).
- [66] D. Vollhardt, “Dynamical mean-field theory of electronic correlations in models and materials”, in *Lectures on the physics of strongly correlated systems XIV*, Vol. 1297, edited by A. Avella and F. Mancini (2010), p. 339 (cit. on pp. 11, 97).
- [67] A. Weh, “Charge reconstruction in magnetic heterostructures, A real space dynamical mean-field approach”, MA thesis (Augsburg University, Mar. 2018) (cit. on pp. 11, 15).
- [68] W. Greiner and J. Reinhardt, *Field quantization* (Springer Berlin Heidelberg, 1996) (cit. on p. 13).
- [69] W. Metzner, “Linked-cluster expansion around the atomic limit of the Hubbard model”, *Phys. Rev. B* **43**, 8549–8563 (1991) (cit. on p. 14).
- [70] E. Müller-Hartmann, “The Hubbard model at high dimensions: Some exact results and weak coupling theory”, *Z. Physik B - Condensed Matter* **76**, 211–217 (1989) (cit. on p. 15).
- [71] R. Bulla, A. C. Hewson, and T. Pruschke, “Numerical renormalization group calculations for the self-energy of the impurity Anderson model”, *J. Phys.: Condens. Matter* **10**, 8365–8380 (1998) (cit. on pp. 16, 99, 107).
- [72] H. Hafermann, K. R. Patton, and P. Werner, “Improved estimators for the self-energy and vertex function in hybridization-expansion continuous-time quantum Monte Carlo simulations”, *Phys. Rev. B* **85**, 205106 (2012) (cit. on pp. 16, 107).
- [73] T. Maier, M. Jarrell, T. Pruschke, and M. H. Hettler, “Quantum cluster theories”, *Rev. Mod. Phys.* **77**, 1027–1080 (2005) (cit. on pp. 17, 19).
- [74] M. H. Hettler, A. N. Tahvildar-Zadeh, M. Jarrell, T. Pruschke, and H. R. Krishnamurthy, “Nonlocal dynamical correlations of strongly interacting electron systems”, *Phys. Rev. B* **58**, R7475–R7479 (1998) (cit. on p. 17).
- [75] A. I. Lichtenstein and M. I. Katsnelson, “Antiferromagnetism and d-wave superconductivity in cuprates: a cluster dynamical mean-field theory”, *Phys. Rev. B* **62**, R9283–R9286 (2000) (cit. on p. 17).
- [76] G. Kotliar, S. Y. Savrasov, G. Pálsson, and G. Biroli, “Cellular dynamical mean field approach to strongly correlated systems”, *Phys. Rev. Lett.* **87**, 186401 (2001) (cit. on p. 17).
- [77] G. Rohringer, H. Hafermann, A. Toschi, A. A. Katanin, A. E. Antipov, M. I. Katsnelson, A. I. Lichtenstein, A. N. Rubtsov, and K. Held, “Diagrammatic routes to nonlocal correlations beyond dynamical mean field theory”, *Rev. Mod. Phys.* **90**, 025003 (2018) (cit. on p. 17).

- [78] A. Toschi, A. A. Katanin, and K. Held, “Dynamical vertex approximation: a step beyond dynamical mean-field theory”, *Phys. Rev. B* **75**, 045118 (2007) (cit. on pp. 17, 19).
- [79] A. N. Rubtsov, M. I. Katsnelson, and A. I. Lichtenstein, “Dual fermion approach to nonlocal correlations in the Hubbard model”, *Phys. Rev. B* **77**, 033101 (2008) (cit. on pp. 17, 19).
- [80] P. Werner, T. Oka, and A. J. Millis, “Diagrammatic Monte Carlo simulation of nonequilibrium systems”, *Phys. Rev. B* **79**, 035320 (2009) (cit. on p. 19).
- [81] A. N. Rubtsov, V. V. Savkin, and A. I. Lichtenstein, “Continuous-time quantum Monte Carlo method for fermions”, *Phys. Rev. B* **72**, 035122 (2005) (cit. on p. 19).
- [82] P. Werner, A. Comanac, L. de’Medici, M. Troyer, and A. J. Millis, “Continuous-time solver for quantum impurity models”, *Phys. Rev. Lett.* **97**, 076405 (2006) (cit. on pp. 19, 21).
- [83] P. Werner and A. J. Millis, “Hybridization expansion impurity solver: General formulation and application to Kondo lattice and two-orbital models”, *Phys. Rev. B* **74**, 155107 (2006) (cit. on p. 19).
- [84] E. Gull, P. Werner, O. Parcollet, and M. Troyer, “Continuous-time auxiliary-field Monte Carlo for quantum impurity models”, *Europhys. Lett.* **82**, 57003 (2008) (cit. on p. 19).
- [85] P. Werner, “Continuous-time impurity solvers”, in *The LDA+DMFT approach to strongly correlated materials*, edited by E. Pavarini, E. Koch, A. Lichtenstein, and D. Vollhardt, Modeling and Simulation 1 (Forschungszentrum Jülich, 2011) Chap. 10 (cit. on p. 19).
- [86] F. F. Assaad, “Continuous-time QMC solvers for electronic systems in fermionic and bosonic baths”, in *DMFT at 25: infinite dimensions*, edited by E. Pavarini, E. Koch, D. Vollhardt, and A. Lichtenstein, Modeling and simulation 4 (Forschungszentrum Jülich, Sept. 2014) Chap. 7 (cit. on p. 19).
- [87] M. Wallerberger, “w2dynamics: Continuous time quantum Monte Carlo calculations of one-and two-particle propagators”, PhD thesis (Wien, 2016) (cit. on pp. 19, 20, 28, 29).
- [88] K. Haule, “Quantum Monte Carlo impurity solver for cluster dynamical mean-field theory and electronic structure calculations with adjustable cluster base”, *Phys. Rev. B* **75**, 155113 (2007) (cit. on pp. 20, 21).
- [89] N. Parragh, A. Toschi, K. Held, and G. Sangiovanni, “Conserved quantities of $SU(2)$ -invariant interactions for correlated fermions and the advantages for quantum Monte Carlo simulations”, *Phys. Rev. B* **86**, 155158 (2012) (cit. on p. 21).
- [90] A. M. Läuchli and P. Werner, “Krylov implementation of the hybridization expansion impurity solver and application to 5-orbital models”, *Phys. Rev. B* **80**, 235117 (2009) (cit. on p. 21).
- [91] H. Shinaoka, M. Dolfi, M. Troyer, and P. Werner, “Hybridization expansion Monte Carlo simulation of multi-orbital quantum impurity problems: Matrix product formalism and improved sampling”, *J. Stat. Mech.* **2014**, P06012 (2014) (cit. on p. 21).

-
- [92] N. Metropolis, A. W. Rosenbluth, M. N. Rosenbluth, A. H. Teller, and E. Teller, “Equation of state calculations by fast computing machines”, *J. Chem. Phys.* **21**, 1087–1092 (1953) (cit. on p. 23).
- [93] W. K. Hastings, “Monte Carlo sampling methods using Markov chains and their applications”, *Biometrika* **57**, 97–109 (1970) (cit. on p. 23).
- [94] D. A. Harville, *Matrix algebra from a statistician’s perspective* (Springer New York, 1997) (cit. on p. 26).
- [95] N. J. Higham, *Accuracy and stability of numerical algorithms*, Other Titles in Applied Mathematics (Society for Industrial and Applied Mathematics, Jan. 2002) (cit. on pp. 26, 38, 48, 78).
- [96] D. S. Bernstein, *Scalar, vector, and matrix mathematics, Theory, facts, and formulas - revised and expanded edition* (Princeton University Press, Feb. 2018) (cit. on p. 27).
- [97] L. Boehnke, H. Hafermann, M. Ferrero, F. Lechermann, and O. Parcollet, “Orthogonal polynomial representation of imaginary-time Green’s functions”, *Phys. Rev. B* **84**, 075145 (2011) (cit. on pp. 28, 142).
- [98] P. Staar, T. A. Maier, and T. C. Schulthess, “Efficient non-equidistant FFT approach to the measurement of single- and two-particle quantities in continuous time quantum Monte Carlo methods”, *J. Phys.: Conf. Ser.* **402**, 012015 (2012) (cit. on pp. 28, 142).
- [99] P. Gunacker, M. Wallerberger, E. Gull, A. Hausoel, G. Sangiovanni, and K. Held, “Continuous-time quantum Monte Carlo using worm sampling”, *Phys. Rev. B* **92**, 155102 (2015) (cit. on pp. 29–31).
- [100] E. Y. Loh, J. E. Gubernatis, R. T. Scalettar, S. R. White, D. J. Scalapino, and R. L. Sugar, “Sign problem in the numerical simulation of many-electron systems”, *Phys. Rev. B* **41**, 9301–9307 (1990) (cit. on p. 31).
- [101] B. Efron, *The jackknife, the bootstrap and other resampling plans* (Society for Industrial and Applied Mathematics, Jan. 1982) (cit. on p. 32).
- [102] G. A. Baker, *Essentials of Padé approximants* (Academic Press, 1975) (cit. on pp. 32, 36, 108).
- [103] H. J. Vidberg and J. W. Serene, “Solving the Eliashberg equations by means of N-point Padé approximants”, *J. Low Temp. Phys.* **29**, 179–192 (1977) (cit. on pp. 32, 108).
- [104] G. A. Baker and P. Graves-Morris, *Padé approximants second edition* (Cambridge University Press, 1996) (cit. on pp. 32, 36, 108, 167, 173).
- [105] J. Fei, C.-N. Yeh, and E. Gull, “Nevanlinna analytical continuation”, *Phys. Rev. Lett.* **126**, 056402 (2021) (cit. on p. 32).
- [106] R. N. Silver, D. S. Sivia, and J. E. Gubernatis, “Maximum-entropy method for analytic continuation of quantum Monte Carlo data”, *Phys. Rev. B* **41**, 2380–2389 (1990) (cit. on p. 33).

- [107] M. Jarrell and J. Gubernatis, “Bayesian inference and the analytic continuation of imaginary-time quantum Monte Carlo data”, *Phys. Rep.* **269**, 133–195 (1996) (cit. on p. 33).
- [108] M. Jarrell, “The maximum entropy method: Analytic continuation of QMC data”, in *Correlated electrons: from models to materials*, edited by E. Pavarini, E. Koch, F. Anders, and M. Jarrell, Modeling and simulation 2 (Forschungszentrum Jülich, 2012) Chap. 13 (cit. on pp. 33, 34).
- [109] A. S. Mishchenko, N. V. Prokof’ev, A. Sakamoto, and B. V. Svistunov, “Diagrammatic quantum Monte Carlo study of the Fröhlich polaron”, *Phys. Rev. B* **62**, 6317–6336 (2000) (cit. on p. 35).
- [110] A. S. Mishchenko, “Stochastic optimization method for analytic continuation”, in *Correlated electrons: from models to materials*, edited by E. Pavarini, E. Koch, F. Anders, and M. Jarrell, Modeling and simulation 2 (Forschungszentrum Jülich, 2012) Chap. 14 (cit. on p. 35).
- [111] J. Otsuki, M. Ohzeki, H. Shinaoka, and K. Yoshimi, “Sparse modeling approach to analytical continuation of imaginary-time quantum Monte Carlo data”, *Phys. Rev. E* **95**, 061302(R) (2017) (cit. on pp. 35, 36, 110).
- [112] T. Hastie, R. Tibshirani, and J. Friedman, *The elements of statistical learning* (Springer New York, 2009) (cit. on p. 36).
- [113] Y. Motoyama, K. Yoshimi, and J. Otsuki, “Robust analytic continuation combining the advantages of the sparse modeling approach and the padé approximation”, *Phys. Rev. B* **105**, 035139 (2022) (cit. on p. 36).
- [114] S. Ito and Y. Nakatsukasa, “Stable polefinding and rational least-squares fitting via eigenvalues”, *Numer. Math.* **139**, 633–682 (2018) (cit. on pp. 37, 40, 137).
- [115] G. H. Golub and C. F. Van Loan, *Matrix computations*, Vol. 3 (JHU press, 2013) (cit. on pp. 40, 42, 43, 48, 49, 147, 148, 151, 178).
- [116] S. Nishimoto and E. Jeckelmann, “Density-matrix renormalization group approach to quantum impurity problems”, *J. Phys. Condens. Matter* **16**, 613–625 (2004) (cit. on p. 47).
- [117] R. Peters, “Spectral functions for single- and multi-impurity models using density matrix renormalization group”, *Phys. Rev. B* **84**, 075139 (2011) (cit. on p. 47).
- [118] M. Ganahl, P. Thunström, F. Verstraete, K. Held, and H. G. Evertz, “Chebyshev expansion for impurity models using matrix product states”, *Phys. Rev. B* **90**, 045144 (2014) (cit. on p. 47).
- [119] M. Ganahl, M. Aichhorn, H. G. Evertz, P. Thunström, K. Held, and F. Verstraete, “Efficient DMFT impurity solver using real-time dynamics with matrix product states”, *Phys. Rev. B* **92**, 155132 (2015) (cit. on pp. 47, 99, 107, 175).
- [120] D. Bauernfeind, M. Zingl, R. Triebl, M. Aichhorn, and H. G. Evertz, “Fork tensor-product states: Efficient multiorbital real-time DMFT solver”, *Phys. Rev. X* **7**, 031013 (2017) (cit. on pp. 47, 49, 59, 99, 134).

-
- [121] H. G. Evertz, “DMRG for multiband impurity solvers”, in *DMFT: from infinite dimensions to real materials*, edited by E. Pavarini, E. Koch, A. Lichtenstein, and D. Vollhardt, Reihe modeling and simulation 8 (Forschungszentrum Jülich, Sept. 2018) Chap. 9 (cit. on p. 47).
- [122] A. E. Feiguin and S. R. White, “Finite-temperature density matrix renormalization using an enlarged Hilbert space”, *Phys. Rev. B* **72**, 220401 (2005) (cit. on p. 47).
- [123] E. Jeckelmann, “Density-matrix renormalization group methods for momentum- and frequency-resolved dynamical correlation functions”, *Prog. Theor. Phys., Suppl.* **176**, 143–164 (2008) (cit. on p. 47).
- [124] T. D. Kühner and S. R. White, “Dynamical correlation functions using the density matrix renormalization group”, *Phys. Rev. B* **60**, 335–343 (1999) (cit. on p. 47).
- [125] E. Jeckelmann, “Dynamical density-matrix renormalization-group method”, *Phys. Rev. B* **66**, 045114 (2002) (cit. on p. 47).
- [126] J. C. Bridgeman and C. T. Chubb, “Hand-waving and interpretive dance: An introductory course on tensor networks”, *J. Phys. A: Math. Theor.* **50**, 223001 (2017) (cit. on p. 47).
- [127] I. V. Oseledets, “Tensor-train decomposition”, *SIAM J. Sci. Comput.* **33**, 2295–2317 (2011) (cit. on p. 49).
- [128] Q. Zhao, G. Zhou, S. Xie, L. Zhang, and A. Cichocki, *Tensor ring decomposition*, 2016, arXiv:1606.05535 [cs.NA] (cit. on p. 49).
- [129] C. Eckart and G. Young, “The approximation of one matrix by another of lower rank”, *Psychometrika* **1**, 211–218 (1936) (cit. on p. 50).
- [130] L. Mirsky, “Symmetric gauge functions and unitarily invariant norms”, *Q. J. Math.* **11**, 50–59 (1960) (cit. on p. 50).
- [131] D. Bauernfeind, “Fork tensor product states: Efficient multi-orbital impurity solver for dynamical mean field theory”, PhD thesis (TU Graz, Feb. 2018) (cit. on pp. 54, 55).
- [132] C. Hubig, I. P. McCulloch, and U. Schollwöck, “Generic construction of efficient matrix product operators”, *Phys. Rev. B* **95**, 035129 (2017) (cit. on p. 57).
- [133] J. K. Cullum and R. A. Willoughby, *Lanczos algorithms for large symmetric eigenvalue computations, Vol. I: Theory* (Society for Industrial and Applied Mathematics, Jan. 2002) (cit. on pp. 57, 58).
- [134] E. R. Davidson, “The iterative calculation of a few of the lowest eigenvalues and corresponding eigenvectors of large real-symmetric matrices”, *J. Comput. Phys.* **17**, 87–94 (1975) (cit. on pp. 57, 58).
- [135] M. Yang and S. R. White, “Time-dependent variational principle with ancillary Krylov subspace”, *Phys. Rev. B* **102**, 094315 (2020) (cit. on pp. 59, 69).
- [136] M. Yang and S. R. White, “Density-matrix-renormalization-group study of a one-dimensional diatomic molecule beyond the Born-Oppenheimer approximation”, *Phys. Rev. A* **99**, 022509 (2019) (cit. on p. 59).
- [137] S. R. White, “Density matrix renormalization group algorithms with a single center site”, *Phys. Rev. B* **72**, 180403 (2005) (cit. on p. 59).

- [138] C. Hubig, I. P. McCulloch, U. Schollwöck, and F. A. Wolf, “Strictly single-site DMRG algorithm with subspace expansion”, *Phys. Rev. B* **91**, 155115 (2015) (cit. on pp. 59, 60).
- [139] S. V. Dolgov and D. V. Savostyanov, “Alternating minimal energy methods for linear systems in higher dimensions”, *SIAM J. Sci. Comput.* **36**, A2248–A2271 (2014) (cit. on p. 60).
- [140] R. P. Feynman, *Statistical mechanics, A set of lectures* (CRC Press, Mar. 26, 1998), p. 368 (cit. on p. 61).
- [141] H. F. Trotter, “On the product of semi-groups of operators”, *Proc. Amer. Math. Soc.* **10**, 545–551 (1959) (cit. on p. 62).
- [142] M. Suzuki, “Generalized Trotter’s formula and systematic approximants of exponential operators and inner derivations with applications to many-body problems”, *Commun. Math. Phys.* **51**, 183–190 (1976) (cit. on p. 62).
- [143] G. Vidal, “Efficient classical simulation of slightly entangled quantum computations”, *Phys. Rev. Lett.* **91**, 147902 (2003) (cit. on p. 62).
- [144] G. Vidal, “Efficient simulation of one-dimensional quantum many-body systems”, *Phys. Rev. Lett.* **93**, 040502 (2004) (cit. on p. 62).
- [145] J. Haegeman, J. I. Cirac, T. J. Osborne, I. Pižorn, H. Verschelde, and F. Verstraete, “Time-dependent variational principle for quantum lattices”, *Phys. Rev. Lett.* **107**, 070601 (2011) (cit. on pp. 62, 99, 134).
- [146] J. Haegeman, C. Lubich, I. Oseledets, B. Vandereycken, and F. Verstraete, “Unifying time evolution and optimization with matrix product states”, *Phys. Rev. B* **94**, 165116 (2016) (cit. on pp. 62–66, 69, 99, 134).
- [147] C. Lubich, I. V. Oseledets, and B. Vandereycken, “Time integration of tensor trains”, *SIAM J. Numer. Anal.* **53**, 917–941 (2015) (cit. on pp. 62–64, 66, 99, 134).
- [148] C. Lubich, *From quantum to classical molecular dynamics: Reduced models and numerical analysis* (European Mathematical Society Publishing House, Sept. 2008) (cit. on pp. 62, 63).
- [149] P. A. M. Dirac, “Note on exchange phenomena in the Thomas atom”, *Mathematical Proceedings of the Cambridge Philosophical Society* **26**, 376–385 (1930) (cit. on p. 62).
- [150] P. Kramer and M. Saraceno, “Geometry of the time-dependent variational principle in quantum mechanics”, in *Group theoretical methods in physics* (Springer Berlin Heidelberg, Berlin, Heidelberg, 1980), pp. 112–121 (cit. on p. 62).
- [151] H. Feldmeier and J. Schnack, “Molecular dynamics for fermions”, *Reviews of Modern Physics* **72**, 655–688 (2000) (cit. on p. 62).
- [152] J. Haegeman, T. J. Osborne, and F. Verstraete, “Post-matrix product state methods: To tangent space and beyond”, *Phys. Rev. B* **88**, 075133 (2013) (cit. on p. 64).
- [153] C. Moler and C. Van Loan, “Nineteen dubious ways to compute the exponential of a matrix, twenty-five years later”, *SIAM Rev.* **45**, 3–49 (2003) (cit. on p. 67).

-
- [154] A. H. Al-Mohy and N. J. Higham, “Computing the action of the matrix exponential, with an application to exponential integrators”, *SIAM J. Sci. Comput.* **33**, 488–511 (2011) (cit. on p. 67).
- [155] K. Koepernik, B. Velický, R. Hayn, and H. Eschrig, “Self-consistent LCAO-CPA method for disordered alloys”, *Phys. Rev. B* **55**, 5717–5729 (1997) (cit. on pp. 72, 82).
- [156] K. Koepernik, B. Velický, R. Hayn, and H. Eschrig, “Analytic properties and accuracy of the generalized blackman-esterling-berk coherent-potential approximation”, *Phys. Rev. B* **58**, 6944–6962 (1998) (cit. on pp. 72, 82).
- [157] S. Karlin and H. E. Taylor, *A first course in stochastic processes*, 2nd ed. (Elsevier, New York, 1975) (cit. on pp. 74, 78, 85).
- [158] A. Gonis, *Green functions for ordered and disordered systems* (North-Holland, Amsterdam, 1992) (cit. on pp. 74, 76, 81).
- [159] J. M. Ziman, *Models of disorder: The theoretical physics of homogeneously disordered system* (Cambridge University Press, 1979) (cit. on p. 76).
- [160] P. Soven, “Coherent-potential model of substitutional disordered alloys”, *Phys. Rev.* **156**, 809–813 (1967) (cit. on p. 76).
- [161] D. W. Taylor, “Vibrational properties of imperfect crystals with large defect concentrations”, *Phys. Rev.* **156**, 1017–1029 (1967) (cit. on p. 76).
- [162] B. Velický, S. Kirkpatrick, and H. Ehrenreich, “Single-site approximations in the electronic theory of simple binary alloys”, *Phys. Rev.* **175**, 747–766 (1968) (cit. on pp. 76, 81).
- [163] R. J. Elliott, J. A. Krumhansl, and P. L. Leath, “The theory and properties of randomly disordered crystals and related physical systems”, *Rev. Mod. Phys.* **46**, 465–543 (1974) (cit. on p. 76).
- [164] E. N. Economou, *Green’s functions in quantum physics*, Vol. 7 (Springer Science & Business Media, 2006) (cit. on pp. 76, 90, 94, 95, 126).
- [165] J. A. Blackman, D. M. Esterling, and N. F. Berk, “Generalized Locator—Coherent-potential approach to binary alloys”, *Phys. Rev. B* **4**, 2412–2428 (1971) (cit. on p. 82).
- [166] D. M. Esterling, “Simplified derivation of the matrix coherent-potential approximation for off-diagonal random alloys”, *Phys. Rev. B* **12**, 1596–1599 (1975) (cit. on p. 82).
- [167] A. Gonis and J. W. Garland, “Rederivation and proof of analyticity of the blackman-esterling-berk approximation”, *Phys. Rev. B* **16**, 1495–1502 (1977) (cit. on p. 82).
- [168] H. Shiba, “A reformulation of the coherent potential approximation and its applications”, *Prog. Theor. Phys.* **46**, 77–94 (1971) (cit. on p. 89).
- [169] J. Noble, M. Lubasch, J. Stevens, and U. Jentschura, “Diagonalization of complex symmetric matrices: Generalized householder reflections, iterative deflation and implicit shifts”, *Comput. Phys. Commun.* **221**, 304–316 (2017) (cit. on p. 90).

- [170] T. Morita and T. Horiguchi, “Calculation of the lattice Green’s function for the bcc, fcc, and rectangular lattices”, *J. Math. Phys.* **12**, 986–992 (1971) (cit. on p. 90).
- [171] T. Horiguchi, “Lattice Green’s functions for the triangular and honeycomb lattices”, *J. Math. Phys.* **13**, 1411–1419 (1972) (cit. on p. 90).
- [172] R. Delves and G. Joyce, “On the Green function for the anisotropic simple cubic lattice”, *Ann. Phys. (New York)* **291**, 71–133 (2001) (cit. on pp. 90, 142, 182).
- [173] V. K. Varma and H. Monien, “Lattice Green’s functions for kagome, diced, and hyperkagome lattices”, *Phys. Rev. E* **87**, 032109 (2013) (cit. on p. 90).
- [174] E. Kogan and G. Gumbs, “Green’s functions and DOS for some 2D lattices”, *Graphene* **10**, 1–12 (2021) (cit. on p. 90).
- [175] E. H. Moore, “On the reciprocal of the general algebraic matrix”, *Bull. Am. Math. Soc.* **26**, 394–395 (1920) (cit. on p. 92).
- [176] R. Penrose, “A generalized inverse for matrices”, *Math. Proc. Camb. Phil. Soc.* **51**, 406–413 (1955) (cit. on p. 92).
- [177] S. A. Gershgorin, “Über die Abgrenzung der Eigenwerte einer Matrix”, *Bull. Acad. Sci. URSS* **1931**, 749–754 (1931) (cit. on pp. 94, 100).
- [178] K. Byczuk, W. Hofstetter, and D. Vollhardt, “Mott-Hubbard metal-insulator transition at noninteger filling”, *Phys. Rev. B* **69**, 045112 (2004) (cit. on p. 95).
- [179] V. Janiš and D. Vollhardt, “Coupling of quantum degrees of freedom in strongly interacting disordered electron systems”, *Phys. Rev. B* **46**, 15712–15715 (1992) (cit. on p. 97).
- [180] D. Bauernfeind and M. Aichhorn, “Time dependent variational principle for tree tensor networks”, *SciPost Phys.* **8**, 24 (2020) (cit. on pp. 99, 134).
- [181] S. Burdin and P. Fulde, “Random kondo alloys investigated with the coherent potential approximation”, *Phys. Rev. B* **76**, 104425 (2007) (cit. on pp. 100, 101).
- [182] P. Lombardo, R. Hayn, and G. I. Japaridze, “Insulator-metal-insulator transition and selective spectral-weight transfer in a disordered strongly correlated system”, *Phys. Rev. B* **74**, 085116 (2006) (cit. on p. 104).
- [183] L. Chioncel, M. I. Katsnelson, R. A. de Groot, and A. I. Lichtenstein, “Nonquasi-particle states in the half-metallic ferromagnet NiMnSb”, *Phys. Rev. B* **68**, 144425 (2003) (cit. on p. 109).
- [184] V. Y. Irkhin and M. I. Katsnelson, “Spin waves in narrow band ferromagnet”, *J. Phys. C: Solid State Phys.* **18**, 4173–4188 (1985) (cit. on pp. 109, 110).
- [185] Y. Ohnuma, M. Matsuo, and S. Maekawa, “Spin transport in half-metallic ferromagnets”, *Phys. Rev. B* **94**, 184405 (2016) (cit. on p. 109).
- [186] A. Fuhrmann, D. Heilmann, and H. Monien, “From Mott insulator to band insulator: a dynamical mean-field theory study”, *Phys. Rev. B* **73**, 245118 (2006) (cit. on p. 113).
- [187] S. S. Kancharla and S. Okamoto, “Band insulator to Mott insulator transition in a bilayer Hubbard model”, *Phys. Rev. B* **75**, 193103 (2007) (cit. on p. 113).

-
- [188] R. W. Helmes, T. A. Costi, and A. Rosch, “Kondo proximity effect: How does a metal penetrate into a Mott insulator?”, *Phys. Rev. Lett.* **101**, 066802 (2008) (cit. on p. 114).
- [189] R. Nourafkan and F. Marsiglio, “Surface effects in doping a Mott insulator”, *Phys. Rev. B* **83**, 155116 (2011) (cit. on p. 114).
- [190] S. Okamoto and A. J. Millis, “Theory of Mott insulator–band insulator heterostructures”, *Phys. Rev. B* **70**, 075101 (2004) (cit. on p. 114).
- [191] R. Landauer, “Spatial variation of currents and fields due to localized scatterers in metallic conduction”, *IBM J. Res. & Dev.* **1**, 223–231 (1957) (cit. on p. 119).
- [192] R. Landauer, “Spatial variation of currents and fields due to localized scatterers in metallic conduction”, *IBM J. Res. Dev.* **32**, 306–316 (1988) (cit. on p. 119).
- [193] M. Büttiker, “Four-terminal phase-coherent conductance”, *Phys. Rev. Lett.* **57**, 1761–1764 (1986) (cit. on p. 119).
- [194] M. Buttiker, “Symmetry of electrical conduction”, *IBM J. Res. Dev.* **32**, 317–334 (1988) (cit. on p. 119).
- [195] Y. Meir and N. S. Wingreen, “Landauer formula for the current through an interacting electron region”, *Phys. Rev. Lett.* **68**, 2512–2515 (1992) (cit. on pp. 119, 121, 124, 126).
- [196] J. Rammer and H. Smith, “Quantum field-theoretical methods in transport theory of metals”, *Rev. Mod. Phys.* **58**, 323–359 (1986) (cit. on p. 119).
- [197] C. Caroli, R. Combescot, P. Nozieres, and D. Saint-James, “Direct calculation of the tunneling current”, *J. Phys. C: Solid State Phys.* **4**, 916–929 (1971) (cit. on p. 119).
- [198] C. Caroli, R. Combescot, D. Lederer, P. Nozieres, and D. Saint-James, “A direct calculation of the tunnelling current. II. Free electron description”, *J. Phys. C: Solid State Phys.* **4**, 2598–2610 (1971) (cit. on p. 119).
- [199] L. Chioncel, C. Morari, A. Östlin, W. H. Appelt, A. Droghetti, M. M. Radonjić, I. Rungger, L. Vitos, U. Eckern, and A. V. Postnikov, “Transmission through correlated Cu_nCoCu_n heterostructures”, *Phys. Rev. B* **92**, 054431 (2015) (cit. on pp. 119, 134).
- [200] C. Morari, W. H. Appelt, A. Östlin, A. Prinz-Zwick, U. Schwingenschlögl, U. Eckern, and L. Chioncel, “Spin-polarized ballistic conduction through correlated Au-NiMnSb-Au heterostructures”, *Phys. Rev. B* **96**, 205137 (2017) (cit. on pp. 119, 134).
- [201] H. Haug and A.-P. Jauho, *Quantum kinetics in transport and optics of semiconductors*, Vol. 2 (Springer Berlin Heidelberg, 2008) (cit. on pp. 124–126).
- [202] A. C. Hewson, *The kondo problem to heavy fermions* (Cambridge University Press, Cambridge, Jan. 1993) (cit. on p. 129).
- [203] N. Vogiatzis and J. M. Rorison, “Single impurity Anderson model and band anti-crossing in the $\text{Ga}_{1-x}\text{In}_x\text{N}_y\text{As}_{1-y}$ material system”, *phys. stat. sol. (a)* **205**, 120–128 (2008) (cit. on p. 129).

- [204] G. Kotliar, S. Y. Savrasov, K. Haule, V. S. Oudovenko, O. Parcollet, and C. A. Marianetti, “Electronic structure calculations with dynamical mean-field theory”, *Rev. Mod. Phys.* **78**, 865–951 (2006) (cit. on p. 134).
- [205] A. Östlin, L. Chioncel, and L. Vitos, “One-particle spectral function and analytic continuation for many-body implementation in the exact muffin-tin orbitals method”, *Phys. Rev. B* **86**, 235107 (2012) (cit. on p. 134).
- [206] A. Östlin, L. Vitos, and L. Chioncel, “Analytic continuation-free Green’s function approach to correlated electronic structure calculations”, *Phys. Rev. B* **96**, 125156 (2017) (cit. on p. 134).
- [207] U. Schollwöck, “The density-matrix renormalization group”, *Rev. Mod. Phys.* **77**, 259–315 (2005) (cit. on p. 134).
- [208] S. Katsura, S. Inawashiro, and Y. Abe, “Lattice Green’s function for the simple cubic lattice in terms of a Mellin-Barnes type integral”, *J. Math. Phys.* **12**, 895–899 (1971) (cit. on pp. 142, 182).
- [209] G. S. Joyce, “On the simple cubic lattice Green function”, *Philosophical Transactions of the Royal Society of London. Series A, Mathematical and Physical Sciences* **273**, 583–610 (1973) (cit. on pp. 142, 182).
- [210] K. Knopp, *Infinite sequences and series*, Dover Books on Mathematics (Dover Publications, 1956) (cit. on p. 144).
- [211] K. Xu, “The Chebyshev points of the first kind”, *Appl. Numer. Math.* **102**, 17–30 (2016) (cit. on p. 147).
- [212] W. Gautschi, “Norm estimates for inverses of Vandermonde matrices”, *Numer. Math.* **23**, 337–347 (1974) (cit. on p. 147).
- [213] M. Kuian, L. Reichel, and S. V. Shiyankovskii, “Fast factorization of rectangular Vandermonde matrices with Chebyshev nodes”, *Numer. Algorithms* **81**, 547–559 (2018) (cit. on p. 147).
- [214] A. Eisenberg, G. Franzé, and P. Pugliese, “Vandermonde matrices on Chebyshev points”, *Linear Algebra Appl.* **283**, 205–219 (1998) (cit. on p. 147).
- [215] A. Eisenberg, G. Franzé, and N. Salerno, “Rectangular Vandermonde matrices on Chebyshev nodes”, *Linear Algebra Appl.* **338**, 27–36 (2001) (cit. on p. 147).
- [216] T. Ozaki, “Continued fraction representation of the Fermi-Dirac function for large-scale electronic structure calculations”, *Phys. Rev. B* **75**, 035123 (2007) (cit. on pp. 149, 150).
- [217] J. Hu, R.-X. Xu, and Y. Yan, “Communication: Padé spectrum decomposition of Fermi function and Bose function”, *J. Chem. Phys.* **133**, 101106 (2010) (cit. on pp. 149, 150).
- [218] L. N. G. Filon, “III.—On a quadrature formula for trigonometric integrals”, *Proc. R. Soc. Edinb.* **49**, 38–47 (1930) (cit. on p. 153).
- [219] E. A. Flinn, “A modification of Filon’s method of numerical integration”, *J. ACM* **7**, 181–184 (1960) (cit. on p. 153).

-
- [220] A. Iserles, S. Nørsett, and S. Olver, “Highly oscillatory quadrature: The story so far”, in *Numerical mathematics and advanced applications*, edited by A. B. de Castro, D. Gómez, P. Quintela, and P. Salgado (Springer Berlin Heidelberg, Berlin, Heidelberg, 2006), pp. 97–118 (cit. on p. 153).
- [221] T. A. Driscoll and B. Fornberg, “A Padé-based algorithm for overcoming the Gibbs phenomenon”, *Numer. Algorithms* **26**, 77–92 (2001) (cit. on pp. 167, 173).
- [222] P. Gonnet, S. Güttel, and L. N. Trefethen, “Robust Padé approximation via SVD”, *SIAM Rev.* **55**, 101–117 (2013) (cit. on p. 173).
- [223] T. M. Mishonov and A. M. Varonov, “Robust formula for N-point Padé approximant calculation based on Wynn identity”, *Appl. Numer. Math.* **157**, 291–306 (2020) (cit. on p. 173).
- [224] H. Stahl, “From Taylor to quadratic Hermite-Padé polynomials”, *Electron. Trans. Numer. Anal.* **25**, 480–510 (2006) (cit. on p. 173).
- [225] M. Fasoldini, N. Hale, R. Spoerer, and J. Weideman, “Quadratic Padé approximation: Numerical aspects and applications”, *Comput. Res. Model.* **11**, 1017–1031 (2019) (cit. on pp. 173, 174).
- [226] P. Koehl, “Linear prediction spectral analysis of NMR data”, *Prog. Nucl. Mag. Res. Sp.* **34**, 257–299 (1999) (cit. on p. 175).
- [227] T. Barthel, U. Schollwöck, and S. R. White, “Spectral functions in one-dimensional quantum systems at finite temperature using the density matrix renormalization group”, *Phys. Rev. B* **79**, 245101 (2009) (cit. on p. 175).
- [228] P. P. Vaidyanathan, “The theory of linear prediction”, *Synthesis Lectures on Signal Processing* **2**, 1–184 (2007) (cit. on pp. 175, 177, 178).
- [229] J. Makhoul, “Linear prediction: a tutorial review”, *Proc. IEEE* **63**, 561–580 (1975) (cit. on pp. 175, 178).
- [230] A. Edelman and H. Murakami, “Polynomial roots from companion matrix eigenvalues”, *Math. Comput.* **64**, 763–776 (1995) (cit. on p. 178).
- [231] J. Tang and J. R. Norris, “LPZ spectral analysis using linear prediction and the z transform”, *J. Chem. Phys.* **84**, 5210–5211 (1986) (cit. on p. 180).
- [232] J. Tang and J. Norris, “Two-dimensional LPZ spectral analysis with improved resolution and sensitivity”, *Journal of Magnetic Resonance* (1969) **69**, 180–186 (1986) (cit. on p. 180).
- [233] J. Tang and J. Norris, “Spectral analysis using linear prediction z-transform and autoregression”, *Chem. Phys. Lett.* **131**, 252–255 (1986) (cit. on p. 180).
- [234] F. Ni and H. A. Scheraga, “Phase-sensitive spectral analysis by maximum entropy extrapolation”, *Journal of Magnetic Resonance* (1969) **70**, 506–511 (1986) (cit. on p. 180).
- [235] J. Tang and J. Norrist, “Linear prediction z-transform (LPZ) method, Padé rational approximation, and the burg maximum entropy extrapolation”, *Journal of Magnetic Resonance* (1969) **78**, 23–30 (1988) (cit. on p. 181).

Acknowledgments

At this point, I want to thank all the people who helped me in one way or another. Without them, writing this thesis would not have been possible.

My first and foremost thanks go to my supervisors, Prof. Dr. Ulrich Eckern and Prof. Dr. Liviu Chioncel, for offering me this opportunity. Without their support, this dissertation would certainly not have been possible. They created a harmonious working atmosphere, allowing me freedom as well as providing guidance. It was a great help to be able to rely on their various expertises. I have to thank Liviu for supporting me long before my Ph.D. studies and always providing me with opportunities to learn. Already after my Bachelor's, he arranged for me to visit our collaborator Prof. Dr. Junya Otsuki in Sendai during my semester abroad. During my Master's, he sent me to summer and autumn schools.

I am grateful to all the professors and groups that hosted and took the time to teach me. Prof. Dr. Junya Otsuki taught me a lot about quantum Monte Carlo and was always open to questions, whether on-site in Japan or via E-mail. I am thankful to Prof. Dr. Karsten Held for hosting me in Vienna and especially to Dr. Markus Wallerberger, who took so much time to teach me the details of their 'w2dynamics' code. Dr. Daniel Bauernfeind played a similar role with the tensor-network methods by teaching me the 'ForkTPS' code. Unfortunately, we could not meet in person due to Corona, but I am grateful for our educational video chats. I am thankful to Prof. Dr. André-Marie Tremblay, Prof. Dr. Milos Radonjić, and Prof. Dr. Krzysztof Byczuk for making research visits possible, allowing for stimulating discussions and scientific as well as cultural exchange.

I am also grateful to the group of Dr. Wilhelm Appelt, Dr. Andreas Östlin, Dr. Mikheil Sekania, and Farzad Schafiqpur, even though our group got scattered during my studies, and most left the University in Augsburg. Willi was always open to discussions and, even after leaving science, readily jumped in to publish a paper together. Andreas was always available for coffee-room discussions that eventually came back to the topic of physics after some smaller or bigger detours. Even though Misha was farther away, he always had answers at hand and was a standard reference for computational questions. I still remember mathematical tutorials during my Bachelor's that he moved to his office to explain everything in great detail when the regular time did not suffice. And Fasi was the important organizing element. He helped keep us grounded, proving our academic world with a reality check.

I would also like to thank Ralf Utermann for keeping the computers running and readily fixing technical problems, as well as Dr. Michael Dzierzawa for crosschecking from time to time some of my calculations.

I am grateful to Misha, Willi, Dylan Jones, and my father for proofreading my thesis, providing valuable comments, and pointing out minor or bigger mistakes.

Finally, I thank my parents for providing me with a suitable environment, and especially my father for always listening and discussing no matter the topic. I want to dedicate this thesis to my late grandmother; I will always remain grateful for your unconditional love and support.